Doctoral Thesis

Mass Measurement of s-shell Lambda Hypernuclei via Decay Pion Spectroscopy

（崩壊パイ中間子分光法による s 殻ラムダハイパー核の質量測定実験）

TOHOKU
UNIVERSITY

A thesis submitted in fulfillment of the requirements
for the degree of Doctor of Philosophy

Ryoko KINO

2025

Abstract

We have conducted a high-precision measurement of the Λ binding energy (B_Λ) of the hypertriton (${}^{3}_{\Lambda}\mathrm{H}$) using decay pion spectroscopy at the Mainz Microtron (MAMI). Although ${}^{3}_{\Lambda}\mathrm{H}$, the lightest Λ hypernucleus, has long served as a benchmark in hypernuclear physics, its fundamental properties such as B_Λ and lifetime, have remained uncertain, with recent heavy-ion collision experiments reporting conflicting results. This longstanding discrepancy, known as the "hypertriton puzzle," has highlighted the need for a more direct and precise measurement.

To address this, we upgraded the previous experimental method used in the successful ${}^{4}_{\Lambda}\mathrm{H}$ spectroscopy at MAMI. In particular, a natural lithium (${}^{\mathrm{nat}}\mathrm{Li}$) target with low atomic number and density was adopted to reduce both electromagnetic and hyperfragment-induced backgrounds. The target was elongated to 45 mm along the beam axis to ensure high luminosity, while its transverse thickness was limited to 0.75 mm to minimize pion energy loss. As a result, this method enabled the first observation of a distinct ${}^{3}_{\Lambda}\mathrm{H}$ decay π^- momentum peak exceeding the 3σ significance level. Decay π^- from ${}^{4}_{\Lambda}\mathrm{H}$ was also observed, as well as in the previous study.

This thesis provides a detailed explanation of the experimental methods and data analysis. The decay π^- momentum was calibrated based on the previous study at MAMI, which reported a reference value of $p_{\pi^-}({}^{4}_{\Lambda}\mathrm{H}) = 132.867 \pm 0.013\ (\mathrm{stat.}) \pm 0.107\ (\mathrm{syst.})$ MeV/c [Sch+16]. As a result, the following values were obtained:

- $p_{\pi^-}({}^{3}_{\Lambda}\mathrm{H}) = 113.789 \pm 0.020\ (\mathrm{stat.}) \pm 0.112\ (\mathrm{syst.})\mathrm{MeV}/c$
- $B_\Lambda({}^{3}_{\Lambda}\mathrm{H}) = 0.523 \pm 0.013\ (\mathrm{stat.}) \pm 0.075\ (\mathrm{syst.})$ MeV

The calibration using electron elastic scattering at $E_b = 420$ MeV was also performed. The measured momenta were:

- $p_{\pi^-}({}^{3}_{\Lambda}\mathrm{H}) = 113.661 \pm 0.020\ (\mathrm{stat.}) \pm 0.245\ (\mathrm{syst.})$ MeV/c,
- $p_{\pi^-}({}^{4}_{\Lambda}\mathrm{H}) = 132.718 \pm 0.007\ (\mathrm{stat.}) \pm 0.246\ (\mathrm{syst.})$ MeV/c.

The corresponding Λ binding energies were determined as:

- $B_\Lambda(^3_\Lambda\mathrm{H}) = 0.609 \pm 0.013$ (stat.) ± 0.165 (syst.) MeV,
- $B_\Lambda(^4_\Lambda\mathrm{H}) = 2.265 \pm 0.005$ (stat.) ± 0.178 (syst.) MeV.

The statistical precision achieved is ten times better than that of previous measurements of $B_\Lambda(^3_\Lambda\mathrm{H})$. The associated systematic uncertainty currently dominates the result. During calibration data taking of electron elastic scattering, a novel method of beam energy measurement based on undulator interferometry was also conducted. It is expected to be reduced to below 30 keV once the undulator analysis is completed.

These results, including the clearly resolved momentum difference between $^3_\Lambda\mathrm{H}$ and $^4_\Lambda\mathrm{H}$, provide crucial input for understanding the $\Lambda-N$ interaction and resolving the hypertriton puzzle.

Acknowledgement

This doctoral dissertation could not have been completed without the invaluable support of many people. I would like to take this opportunity to express my deepest gratitude to all those who have helped me throughout this journey.

I am sincerely grateful to Prof. Satoshi Nue Nakamura, my academic advisor, for accepting me into the graduate program and setting me on this path. Over the course of nearly five years, from before my enrollment to the completion of this dissertation, he has provided thoughtful and consistent guidance. I deeply appreciate the opportunities he gave me to gain experience in international environments, such as experiments in Germany and various international conferences. His weekly meetings and advice on my progress and analysis challenges were particularly invaluable. Prof. Nakamura's uncompromising pursuit of difficult research topics and his deep and broad intellectual curiosity have greatly influenced my own approach to research. I will carry his teachings with me as I move forward into the next stage of my career.

I am also deeply indebted to Prof. Sho Nagao, who has guided me in every fundamental aspect of research—from detector operation and data analysis methods to experiment management—since my master's program through to this doctoral dissertation. This study is closely related to his own doctoral work, and I benefited greatly from it. He not only allowed me to refer extensively to his thesis, but also offered real-time advice during the experiment from Japan via daily online meetings with Germany. I consulted with him on every detail of the data analysis as well. His mentorship has been instrumental not only technically but also in shaping my attitude toward research.

Prof. Josef Pochodzalla at the Johannes Gutenberg University Mainz, kindly welcomed me when I first joined the experiment during my master's studies. He served as my on-site supervisor during the experiment and continued to provide detailed feedback on data analysis through weekly online meetings after my return to Japan.

Prof. Patrick Achenbach of Jefferson Lab provided valuable guidance during

the preparation and beam time of the experiment. Even after moving to Jefferson Lab, he continued to follow up on my analysis progress and kindly offered me the opportunity to give a talk at the JPS-APS joint meeting of nuclear physics held in Hawaii in 2022.

This research experiment was carried out in collaboration with several students, to whom I am very grateful, especially Dr. Philipp Eckert Vonwirth, Dr. Tianhao Shao, Dr. Pascal Klag, and Mr. Kotaro Nishi. The experiment and subsequent analysis could not have been completed without their cooperation. I also owe a great deal to the local staff members who supported us throughout the experiment, particularly Dr. Anselm Esser, Dr. Ulrich Müller, Dr. Michael O. Distler, Dr. Michaela Thiel, Dr. Sören Schlimme, and Dr. Miha Mihovilovic, among many others. I am also thankful to the A1 staff and students who took beam time shifts, as well as the MAMI accelerator staff and students who contributed to the beam time operations.

The success of this international collaboration was also made possible by the administrative support of Ms. Ayumi Takahashi and Ms. Yukie Sasaki, the secretaries of the Nuclear Physics Laboratory, Mr. Hiroo Umetsu, the technical staff member, and Ms. Hiroko Lane Miwa, the secretary of GP-PU, as well as other GP-PU staff. I truly appreciate their support and patience through the many administrative procedures, which were often complicated. GP-PU also provided me with valuable learning opportunities through international schools and seminars, and generously supported my stay in Germany. I also gratefully acknowledge the financial support from the Japan Society for the Promotion of Science (JSPS) through a Research Fellowship for Young Scientists.

I have also learned much from Prof. Hirokazu Tamura, Prof. Koji Miwa, Prof. Masashi Kaneta, Prof. Yudai Ichikawa, Prof. Shuhei Hayakawa, and Prof. Toshiyuki Gogami through weekly meetings and numerous seminars in the group. I deeply appreciate their generous support and insightful guidance throughout my studies. Their dedication to research and thoughtful mentoring has left a strong impression on me, and I aspire to embody the same spirit in my future career.

I would like to thank all members and alumni of the ELS group—Dr. Yuichi Toyama, Dr. Kosuke Itabashi, Dr. Takeru Akiyama, Dr. Kazuki Okuyama, Mr. Tomomasa Fujiwara, Mr. Masaya Mizuno, Mr. Yuki Nakamura, Mr. Shintaro Nagano, Mr. Koga Tachibana, Mr. Tatsuhiro Ishige, Mr. Daigo Watanabe, Mr. Ken Nishida, Mr. Kaito Higashimoto, Mr. Shunsuke Niwa, Mr. Shota Toyama, Mr. Jin Takahashi, and Mr. Yuto Tsutsumi—for their support. In particular, the experiments at Tohoku University RARiS and the MAMI were excellent experiences made possible by our mutual cooperation and learning.

I am also deeply thankful to the current and former students of the Strengeness Nuclear Physics Group—Dr. Yuji Ishikawa, Dr. Tamao Sakao, Mr. Shunsuke Kajikawa, Mr. Kento Kamada, Mr. Fumiya Oura, Mr. Hayato Miyata, Mr. Kazuma Ohashi, Mr. Chesu Seong, Mr. Ryo Imamoto, Mr. Rintaro Kurata, Mr. Ryuta Saito, Mr. Koki Amamiya, Ms. Akari Haratani, Mr. Yuning Hong, Mr. Kaito Shimazaki, Mr. Zen Takano, Mr. Ryogo Akao, Mr. Yusuke Nakayama, Ms. Ruri Sasaki, and Ms. Miyu Yoshida. Sharing daily life, seminars, and meals with them made these five years incredibly fulfilling and enjoyable, both academically and personally.

Finally, I am profoundly grateful to my family and all those who supported me in my personal life. Their presence and encouragement sustained me throughout my academic path.

August 2025
Ryoko Kino

Contents

Chapter 1

Introduction

1.1 Strangeness nuclear physics

What constitutes the world around us, and where does the origin of matter lie? These are fundamental questions that humanity has pondered for generations. The Standard Model of modern physics, which represents the current pinnacle of our understanding, posits that quarks and leptons are the elementary building blocks of matter. Among them, quarks participate in strong interactions, and both quarks and leptons are organized into three generations (see Table 1.1).

Table 1.1: Quarks and Leptons

	Charge	Spin	First Gen.	Second Gen.	Third Gen.
Quark	$+\frac{2}{3}e$	$\frac{1}{2}$	u	c	t
	$-\frac{1}{3}e$	$\frac{1}{2}$	d	s	b
Lepton	0	$\frac{1}{2}$	ν_e	ν_μ	ν_τ
	$-e$	$\frac{1}{2}$	e	μ	τ

In each generation, quarks appear in pairs with electric charges of $+\frac{2}{3}e$ and $-\frac{1}{3}e$. In the strong interaction, the concept of color charge plays a central role. Quarks possess three colors—red, green, and blue—and form color-neutral bound states due to confinement. Composite particles formed through the strong interaction among quarks are called hadrons. Among these, hadrons composed of a quark and an antiquark are known as mesons, while those consisting of three quarks are called baryons.

All visible matter, including human beings, is composed of atoms, which consist of nuclei surrounded by electrons. The atomic nucleus itself is made up of protons and neutrons, which are baryons with quark compositions of uud and udd, respec-

tively. The strong interaction between protons and neutrons is called the nuclear force, and atomic nuclei are quantum many-body systems bound by this force.

Although the nuclear force is fundamentally based on the forces described by quantum chromodynamics (QCD), which governs the interactions between quarks and gluons, it is challenging to apply QCD directly because protons and neutrons are composite particles that do not carry net color charge. For this reason, phenomena in the low-energy regime (below the pion production threshold), where elastic scattering is dominant, have been described using potential models that consider nucleon-nucleon distances as well as spin and isospin degrees of freedom.

These potential models have been constructed based on thousands of nucleon-nucleon scattering data points and on the binding energy and electromagnetic structure of the deuteron, forming systematic frameworks of the so-called realistic nuclear forces, including the Bonn, Paris, and Argonne potentials.

Characteristic properties of the nuclear force include its attractive nature and short-range behavior, as well as its dependence on spin, its non-central (tensor) component, charge symmetry, and spin-orbit interactions. In this sense, the nuclear force has been well understood within the framework of isospin SU(2) symmetry, which reflects the approximate invariance under the exchange of u and d quarks, and has enabled systematic descriptions of nucleon-nucleon interactions, particularly in the long-range and intermediate-range regions dominated by pion exchanges.

However, it is also known that the nuclear force exhibits a strong short-range repulsive core, the origin of which remains to be fully understood. The repulsive core has been the subject of longstanding debate, with suggestions that the quark structure, such as quark Pauli blocking and color-magnetic interactions, plays a crucial role [OY81; FSN07; RNY10; IAH07]. Understanding the quark degrees of freedom in this context remains an important challenge in elucidating the short-range structure of the nuclear force.

One promising approach to connecting our understanding of the nuclear force to QCD and addressing its unresolved short-range behavior is to extend the framework from isospin SU(2) symmetry to flavor SU(3) symmetry by introducing hyperons containing strange quarks. Studying hyperon-nucleon and hyperon-hyperon interactions allows the quark-originated components of the short-range repulsive core to be distinguished from meson-exchange contributions. This approach is expected to play a crucial role in elucidating the fundamental nature of the nuclear force and in advancing our understanding of the strong interaction.

The s quark carries a quantum number called strangeness, $S = -1$. Quarks possess spin $1/2$ and baryon number $B = 1/3$, so baryons, composed of three quarks, have $B = 1$. A quantity called hypercharge Y is defined as:

$$Y = B + S \tag{1.1.1}$$

The electric charge Q of a quark is related to its isospin third component I_3 and hypercharge Y via the following relation:

$$Q = I_3 + \frac{Y}{2} \tag{1.1.2}$$

This relation is known as the GellMann-Nishijima formula.

Among baryons containing an s quark, those with spin-parity $J^P = \frac{1}{2}^+$ form the baryon octet shown in Fig. 1.1(a), while those with $J^P = \frac{3}{2}^+$ form the baryon decuplet shown in Fig. 1.1(b). In these figures, the vertical axis represents hypercharge Y and the horizontal axis denotes the third component of isospin I_3. The charge Q of each baryon is also indicated.

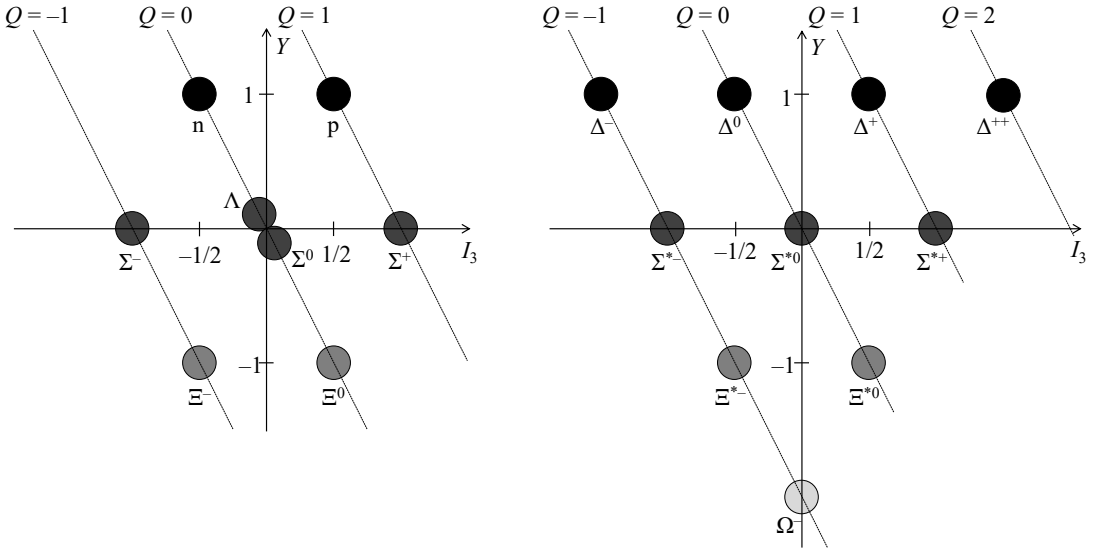

(a) Baryon octet with spin 1/2

(b) Baryon decuplet with spin 3/2

Figure 1.1: (a) The baryon octet with $J^P = \frac{1}{2}^+$, and (b) the baryon decuplet with $J^P = \frac{3}{2}^+$. Vertical axis: hypercharge Y; horizontal axis: isospin component I_3; numbers indicate the electric charge Q.

Table 1.2 summarizes the basic properties of hyperons with $J^P = \frac{1}{2}^+$ [Gro+22].

These hyperons primarily decay via the weak interaction and typically exhibit lifetimes on the order of $\sim 10^{-10}$ seconds. However, the short lifetime of hyperons makes hyperon-nucleon scattering experiments extremely challenging, resulting in

Table 1.2: Basic properties of hyperons with $J^P = \frac{1}{2}^+$ [Gro+22]

Hyperon	Mass (MeV/c^2)	Lifetime (s)	Decay Mode	Branching Ratio (%)
Λ	1115.683(6)	$2.632(20) \times 10^{-10}$	$p\pi^-$ $n\pi^0$	63.9(5) 35.8(5)
Σ^0	1192.642(24)	$7.4(7) \times 10^{-20}$	$\Lambda\gamma$	100
Σ^+	1189.37(6)	$8.018(26) \times 10^{-9}$	$p\pi^0$ $n\pi^+$	51.57(30) 48.31(30)
Σ^-	1197.45(4)	$1.479(11) \times 10^{-10}$	$n\pi^-$	99.848(5)
Ξ^0	1314.86(20)	$2.90(20) \times 10^{-10}$	$\Lambda\pi^0$	99.524(12)
Ξ^-	1321.71(7)	$1.639(15) \times 10^{-10}$	$\Lambda\pi^-$	99.887(35)

very limited available scattering data. Existing YN scattering data are restricted to specific beam momentum ranges and suffer from low statistics. This is mainly because hyperons often decay before detection, making it difficult to realize YN scattering experiments in practice. Recently, at J-PARC, progress has been made using high-intensity pion beams, where a novel method has been successfully employed in Σp scattering experiments. In this approach, Σ hyperons produced via the $\pi p \to K^+\Sigma$ reaction are scattered off protons within the target, and the identification of scattering events is achieved by detecting only the final-state particles and reconstructing the kinematics, offering a promising avenue for future developments.

In contrast, the strong interaction that dominates inside nuclei occurs on a much shorter timescale of $\sim 10^{-24}$ seconds. Therefore, even with their relatively short lifetimes, hyperons can be bound within nuclei and participate in nuclear interactions as constituent particles. Nuclei that contain one or more hyperons as constituents are referred to as hypernuclei.

If the mass $m({}^A_\Lambda Z)$ of a Λ hypernucleus is measured via spectroscopy, one can determine the Λ binding energy B_Λ, which quantifies the strength of the attractive force between the Λ and the nuclear core:

$$B_\Lambda = m_{\text{core}} + m_\Lambda - m({}^A_\Lambda Z) \tag{1.1.3}$$

Here, m_{core} is the mass of the core nucleus and m_Λ is the mass of the Λ hyperon. The value of B_Λ provides essential information about the hyperon-nucleon (YN) interaction. This interaction, as an extension of the conventional nucleon-nucleon (NN) force to the "baryon force," is expected to shed light on unresolved problems in nuclear forces, such as the origin of the short-range repulsive core.

Furthermore, it has been suggested that hyperons may emerge in high-density environments such as the cores of neutron stars, where the chemical potential of nuclear matter can exceed the mass difference between nucleons and hyperons. Thus, hyperons are of interest not only in conventional nuclear matter but also in extreme states of matter.

Additionally, since hyperons are distinguishable from nucleons and not subject to the Pauli exclusion principle with respect to them, they can occupy various quantum states within the nucleus. This feature allows hyperons to serve as probes for exploring nuclear structure, or conversely, to investigate how hadron properties are modified within the nuclear medium.

Due to their profound physical significance, hypernuclei have been actively studied since the first observation of a Λ hypernucleus decay event using nuclear emulsions in 1953 [DP53]. To date, approximately 40 types of Λ hypernuclei have been identified, with experimental efforts expanding to include Σ and double-Λ hypernuclei.

1.2 Recent hot topics of s-shell hypernuclear physics

This section outlines the current experimental status and surrounding issues of s-shell hypernuclei, ${}^{3}_{\Lambda}\mathrm{H}$ and ${}^{4}_{\Lambda}\mathrm{H}$.

1.2.1 Hypertriton puzzle

The hypertriton (${}^{3}_{\Lambda}\mathrm{H}$) is the lightest known hypernucleus, consisting of a three-body system composed of a Λ hyperon, a proton, and a neutron. It is characterized by several remarkable features: an extremely small binding energy of approximately 130 keV [Jur+73], a halo structure with an extended Λ wave function, and dominance of the S-wave component, which makes it highly sensitive to the ΛN interaction.

Notably, the hypertriton is the only three-body bound hypernuclear system in which the S-wave structure is well determined, providing a unique benchmark for extracting the parameters of the ΛN interaction, such as the scattering length and effective range. As the NN interaction is precisely determined from deuteron properties and other experimental scattering data, the binding energy of the hypertriton strongly depends on the details of the ΛN interaction. In particular, its weakly bound nature means that even small variations in the ΛN scattering length can significantly affect the binding energy, potentially leading to unbinding. Indeed, previous theoretical studies have shown that the calculated Λ binding en-

ergy, B_Λ, can vary by more than 100 keV depending on the YN interaction model employed [Hiy+00; GGM12; NAM03].

The dominance of the S-wave in the hypertriton arises from the fact that the relative motions of the $\Lambda-p$, $\Lambda-n$, and $p-n$ pairs can be described almost entirely by the $l=0$ component, while the D-wave admixture due to tensor forces is negligibly small compared to that in the deuteron. Few-body calculations have demonstrated that the D-wave admixture in the hypertriton is below 0.2%, confirming its S-wave dominance [Hiy+96]. This property ensures that the hypertriton is highly sensitive to the low-energy effective parameters of the ΛN interaction, including the scattering length and effective range.

Given these unique features, the hypertriton serves as a crucial benchmark for understanding hyperon-nucleon interactions and, by extension, the role of strangeness in nuclear forces. Determining its fundamental properties with high precision is therefore of critical importance for advancing our knowledge of baryonic forces and for exploring the role of quark degrees of freedom within nuclear systems. However, despite its significance, large experimental uncertainties still remain in measurements of both the Λ binding energy (B_Λ) and the lifetime (τ) of the hypertriton, underscoring the need for further precise experimental investigations.

Lambda hypernuclear decay and lifetime

Before addressing the puzzle, it is useful to briefly review the decay and lifetime of Λ hypernuclei.

Due to strangeness conservation, Λ hypernuclei cannot decay via the strong interaction. Instead, they decay through the weak interaction, which does not conserve strangeness ($S=-1 \to S=0$).

The decay of a free Λ particle is well understood, with a lifetime of (263.1 ± 2.0) ps and nearly 100% probability of decaying into a nucleon and a pion. The dominant decay modes are summarized in Table 1.3.

When a Λ is bound within a nucleus, it can decay via two primary channels. The mesonic weak decay involves emission of a pion, as shown in Table 1.3, where the emitted nucleons have momenta of about 100 MeV/c. Since this is below the Fermi momentum (approximately 270 MeV/c), Pauli blocking suppresses this decay.

On the other hand, a unique nuclear decay channel known as non-mesonic weak decay becomes possible: $\Lambda + N \to N + N$. In this mode, no meson is emitted, and the resulting nucleons have momenta around 420 MeV/c, above the Fermi momentum, so the decay is not Pauli suppressed. As a result, non-mesonic decay

Table 1.3: Decay modes of the Λ hyperon [Gro22]

Decay mode	Branching ratio	Decay momentum (MeV/c)
$p\pi^-$	$(63.9 \pm 0.5)\%$	101
$n\pi^0$	$(35.8 \pm 0.5)\%$	104
$n\gamma$	$(1.75 \pm 0.15) \times 10^{-3}$	162
$p\pi^-\gamma$	$(8.4 \pm 1.4) \times 10^{-4}$	101
$pe^-\bar{\nu}_e$	$(8.32 \pm 0.14) \times 10^{-4}$	163
$p\mu^-\bar{\nu}_\mu$	$(1.57 \pm 0.35) \times 10^{-4}$	131

becomes dominant in heavier hypernuclei.

The lifetimes of Λ hypernuclei are therefore shortened relative to the free Λ, and measured lifetimes for medium-heavy hypernuclei are typically around 200 ps [Bha+98].

World data of Hypertriton

Figure 1.2 summarizes the world data on the Λ binding energy and lifetime of ${}^{3}_{\Lambda}$H.

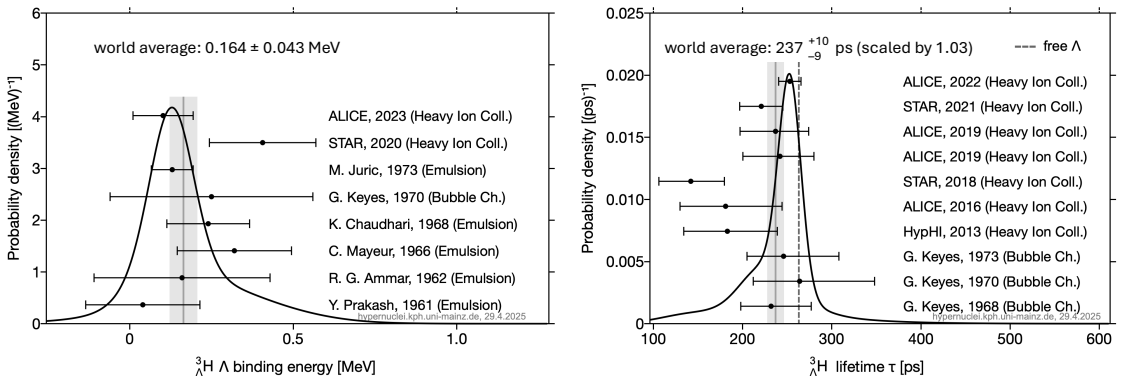

Figure 1.2: World data summary of ${}^{3}_{\Lambda}$H Λ binding energy (left) and lifetime (right), adapted from the hypernuclear chart compiled by the A1 Collaboration [EA+21].

B_Λ values of ${}^{3}_{\Lambda}$H were first measured in early experiments using nuclear emulsions and bubble chambers. In the 1970s, Jurič summarized these results [Jur+73], including a reanalysis of 122 events from Ref. [Boh+68]. The resulting value was:

$$B_\Lambda({}^{3}_{\Lambda}\mathrm{H}) = 0.13 \pm 0.05 \text{ MeV} \tag{1.2.1}$$

The small binding energy of ${}^{3}_{\Lambda}$H, in contrast to the several MeV binding seen in heavier hypernuclei, has led to its interpretation as a weakly bound Λ halo nucleus. This implies that the spatial separation between the Λ and the deuteron core is relatively large, resulting in a small overlap of their wave functions. Therefore, the lifetime of ${}^{3}_{\Lambda}$H is expected to be longer than that of typical hypernuclei and closer

to the free Λ lifetime. This interpretation is also supported by few-body theoretical calculations, such as those based on Faddeev calculations [Kam+98; GG19].

However, this understanding was challenged in the 2010s, when heavy-ion collision experiments reported significantly shorter lifetimes ($\tau \sim 200$ ps) [Rap+13; Ada+16; Ada+18]. This was surprising given the weak binding of ${}^{3}_{\Lambda}$H, and the discrepancy sparked interest as the so-called "hypertriton puzzle." More recent measurements by STAR and ALICE updated the reported values, with ALICE finding a lifetime closer to the free Λ value [Ach+23].

For B_Λ, conflicting results were also reported in the 2020s. ALICE reported $B_\Lambda = 102 \pm 63$ (stat.) ± 67 (syst.) keV [Ach+23], consistent with older measurements, while STAR reported a significantly deeper value of $B_\Lambda = 406 \pm 120$ (stat.) $\pm$ 110 (syst.) keV [Ada+20]. Additionally, an analysis using machine learning on nuclear emulsion data from the J-PARC E07 experiment reported $B_\Lambda = 0.23 \pm 0.11$ (stat.) ± 0.05 (syst.) MeV [Kas+25].

Resolving the hypertriton puzzle requires careful determination of both B_Λ and τ, and the topic remains an active area of research in both theoretical and experimental strangeness nuclear physics.

Theoretical calculations

Various theoretical approaches have been employed to calculate the Λ binding energy of ${}^{3}_{\Lambda}$H. In the classical work by Dalitz, the value was estimated as $B_\Lambda = 0.10$ MeV [Dal+72], consistent with the nuclear emulsion results available up to the 1970s. Since then, significant progress has been made in both the experimental data and the theoretical framework for describing hypernuclei.

A key development in theoretical hypernuclear physics is the recognition of the role played by $\Lambda N - \Sigma N$ coupling. Although the Λ and Σ hyperons differ in mass by about 80 MeV, they can couple via the strong interaction because they share the same strangeness and baryon number. In particular, the ΛN and ΣN channels can mix through tensor components of the baryon-baryon interaction, most notably in the ${}^3S_1 - {}^3D_1$ coupled channel, where one-pion exchange is allowed for ΣN but not for pure ΛN systems. This mixing effectively allows long-range pion exchange contributions to enter the ΛN interaction, which would otherwise be forbidden due to isospin symmetry.

Although the Σ admixture in the ${}^{3}_{\Lambda}$H wave function is only a few percent, its contribution–particularly through the tensor interaction–has been shown to be essential in achieving a bound state [Miy+95].

A prominent example is the work by Y. Akaishi *et al.* [Aka+00], they introduced

the concept of coherent $\Lambda N - \Sigma N$ coupling in s-shell hypernuclei. Using a model with strong $\Lambda N - \Sigma N$ coupling, they showed that the Σ component can account for more than 10% of the ${}^{4}_{\Lambda}$He wave function, playing an essential role in reproducing the spin-dependent energy splitting in s-shell systems.

Another important contribution is the work by E. Hiyama *et al.* [Hiy+01], who performed precise few-body calculations using a variational method with Gaussian basis functions in Jacobi coordinates. Using a model based on NSC97f that includes $\Lambda N - \Sigma N$ coupling, they demonstrated that the Σ admixture plays an important role in reproducing the structure of ${}^{4}_{\Lambda}$He and ${}^{4}_{\Lambda}$H, and obtained a $B_\Lambda = 0.19$ MeV for ${}^{3}_{\Lambda}$H. Their results highlight the importance of accounting for $\Lambda N - \Sigma N$ coupling effects in few-body calculations of light hypernuclei.

More recently, a variety of theoretical models have been employed to estimate the binding energy of ${}^{3}_{\Lambda}$H. For example, Fujiwara *et al.* reported $B_\Lambda = 0.262$ MeV using a quark-model SU(6) baryon-baryon interaction [Fuj+08], while an auxiliary field diffusion Monte Carlo (AFDMC) calculation yielded $B_\Lambda = 0.23$ MeV [LP17]. Calculations based on SU(3) chiral effective field theory (EFT) suggest shallower binding, typically in the range $B_\Lambda = 0.046 - 0.135$ MeV [Hai+20].

Recent rigorous Faddeev calculations incorporating repulsive ΛNN three-body forces generated via two-pion exchange processes have also been reported [Kam+23]. The calculation estimates the repulsive effect of the three-body interaction to be approximately $20 - 30$ keV, resulting in a theoretical value that tends to lie slightly below the experimental value of 148 ± 40 keV [Kam+23].

Overall, while theoretical predictions vary across models and treatments of baryon-baryon interactions, many results are broadly consistent with the earlier nuclear emulsion values and with the recent measurements by the ALICE Collaboration, which report B_Λ in the range of $100 - 130$ keV. Nonetheless, persistent discrepancies highlight the importance of a more precise and model-independent experimental determination.

1.2.2 Charge-symmetry breaking

Charge symmetry, the invariance of nuclear interactions under isospin inversion, is one of the most fundamental symmetries in nuclear physics. In ordinary nuclei, this symmetry is confirmed by the near equality of the proton-proton and neutron-neutron scattering lengths. The same concept applies to the Λ-nucleon (ΛN) interaction, where charge symmetry implies equivalence between the Λp and Λn systems. Although direct scattering experiments are still challenging due to technical limitations, recent progress is making such measurements increasingly feasible.

In the meantime, hypernuclei provide a powerful alternative means to probe this symmetry.

The $A = 4$ hypernuclei, ${}^{4}_{\Lambda}$H and ${}^{4}_{\Lambda}$He, are ideal systems for investigating ΛN charge symmetry breaking (CSB). These mirror hypernuclei consist of a Λ bound to ^{3}H and ^{3}He, respectively, and benefit from well-established theoretical frameworks for precision calculations. If charge symmetry in the ΛN interaction were exact, the Λ, being electrically neutral, would not distinguish between ^{3}H and ^{3}He, resulting in identical binding energies B_Λ.

However, experimental results tell a different story. Decay pion spectroscopy performed at MAMI (Mainz Microtron) and emulsion measurements report ground-state binding energies of $B_\Lambda({}^{4}_{\Lambda}\mathrm{H}) = 2.157 \pm 0.005(\mathrm{stat.}) \pm 0.077(\mathrm{syst.})$ MeV [Sch+16] and $B_\Lambda({}^{4}_{\Lambda}\mathrm{He}) = 2.39 \pm 0.04$ MeV [Jur+73], yielding a difference of $\Delta B^{4}_{\Lambda}(0^{+}_{\mathrm{g.s.}}) = B_\Lambda({}^{4}_{\Lambda}\mathrm{H}(0^+)) - B_\Lambda({}^{4}_{\Lambda}\mathrm{He}(0^+)) = -230$ keV. For the core nuclei ^{3}H and ^{3}He, the binding energy difference is $\Delta B(\mathrm{g.s.}) = 764$ keV, of which approximately 690 keV stems from electromagnetic effects and the remaining 70 keV is attributed to strong interaction contributions due to the u-d quark mass difference [Fri70; BCS78; Mil94]. Thus, the effect of strong interaction in the observed Λ binding energy difference is significantly larger than that in the core systems, suggesting an enhanced CSB effect in ΛN interactions.

Further insight comes from measurements of de-excitation gamma rays emitted in the $1^+ \to 0^+$ transition. For ${}^{4}_{\Lambda}$H, three measurements yield an average energy of 1.09 ± 0.02 keV [Bed+76; Bed+79; Kaw97]. In contrast, for ${}^{4}_{\Lambda}$He, the J-PARC E13 experiment reported a precision value of 1.406 ± 0.003 keV [Yam+15]. Figure 1.3 summarizes these level schemes in terms of Λ binding energy, excluding core binding energy differences. These findings clearly demonstrate the breaking of charge symmetry in the ΛN interaction. Notably, the 1^+ state shows a smaller difference, $\Delta B^{4}_{\Lambda}(1^{+}_{\mathrm{exc.}}) = -83 \pm 94$ keV, suggesting a strong spin dependence of the CSB.

In ordinary nuclei, binding energy differences between mirror nuclei primarily arise from Coulomb interactions. However, theoretical estimates show that in $A = 4$ hypernuclei, the Coulomb contribution to the Λ binding energy is relatively small [BU85], suggesting that $\Delta B_\Lambda(0^{+}_{\mathrm{g.s.}})$ originates predominantly from CSB in the strong interaction, with Λn and Λp interactions differing substantially.

The Λ hyperon, as a $T = 0$ state, can mix with the Σ^0 ($T = 1$ component) through isospin-breaking effects, known as Λ-Σ^0 mixing. This mixing enables one-pion exchange in ΛN interactions, which is otherwise forbidden by isospin symmetry, and can induce long-range CSB effects. However, in the Nijmegen NSC97 models, such effects account for only about 30% (100 keV) of the observed

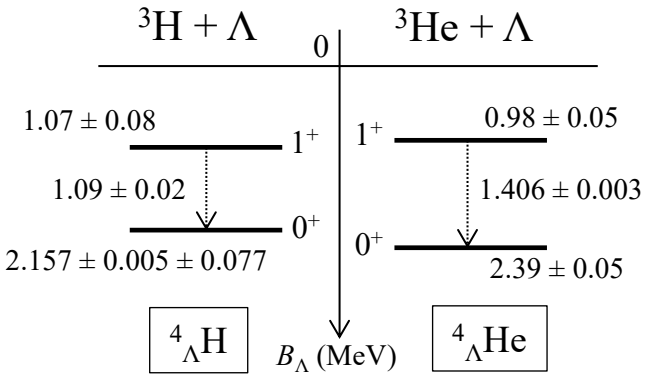

Figure 1.3: Energy level scheme of $^4_\Lambda$H and $^4_\Lambda$He showing charge symmetry breaking effects in the ΛN interaction.

$\Delta B^4_\Lambda(0^+_{\text{g.s.}})$ [Nog+02; Nog13]. In contrast, ab initio no-core shell model calculations incorporating Λ-Σ^0 mixing with Bonn-Jülich leading-order chiral EFT potentials reproduce $\Delta B^4_\Lambda(0^+_{\text{g.s.}}) \sim -270$ keV, albeit with momentum cutoff variations ($30 - 300$ keV) and an overestimation of the 1^+ state difference, $\Delta B^4_\Lambda(1^+_{\text{exc.}}) \sim -204$ keV [GG16].

Variational Monte Carlo calculations using realistic four-body wavefunctions predict smaller CSB values of $\Delta B^4_\Lambda(0^+_{\text{g.s.}}) \sim 50$ keV and $\Delta B^4_\Lambda(1^+_{\text{exc.}}) \sim 60$ keV [Coo+99]. More recently, chiral EFT calculations up to next-to-next-to-leading order have explored the impact of adjustable CSB contact terms, constrained by experimental data, to probe the nature of Λn interactions [Hai+21].

Despite these efforts, no existing theory fully explains the large experimental CSB observed in Λ binding energies, highlighting the need for further theoretical development and high-precision experiments. In particular, past measurements of the $1^+ \rightarrow 0^+$ transition in $^4_\Lambda$H were performed using NaI detectors in the 1970s and 1990s, with reported energies of 1.09 ± 0.03 MeV [Bed+76], 1.04 ± 0.04 MeV [Bed+79], and $1.114 \pm 0.015(\text{stat.}) \pm 0.015(\text{syst.})$ MeV [Kaw97], showing large discrepancies and limited precision. To address this, a high-precision gamma-ray measurement using Ge detectors, similar to that of $^4_\Lambda$He, is now being planned at J-PARC (E63) [Tam08].

While the Λ binding energy in $^4_\Lambda$H has been successfully measured at MAMI, its systematic uncertainties remain significant. Recent heavy-ion results from the STAR collaboration report $B_\Lambda(^4_\Lambda\text{H}) = 2.22 \pm 0.06(\text{stat.}) \pm 0.14(\text{syst.})$ MeV [T S22], and a machine-learning-based analysis of J-PARC E07 emulsion data yields $B_\Lambda(^4_\Lambda\text{H}) = 2.25 \pm 0.10(\text{stat.}) \pm 0.06(\text{syst.})$ MeV [Kas+25]. Although these results are less precise, they suggest a smaller $\Delta B^4_\Lambda(0^+_{\text{g.s.}})$ than previously reported. Nonetheless, de-

cay pion spectroscopy at MAMI remains the most effective method for determining absolute binding energies, and reducing its systematic uncertainties remains a top priority.

1.3 Experimental method to investigate s-shell hypernuclei

This section provides an overview of the experimental methods employed in previous studies to determine the Λ binding energies of s-shell hypernuclei.

1.3.1 Nuclear emulsion

As mentioned earlier, the experimental study of hypernuclei began with the discovery of a hypernucleus by M. Danysz and J. Pniewski in 1953 through the analysis of nuclear emulsions exposed to cosmic rays [DP53]. In the 1950s and 1960s, during the pioneering era of hypernuclear physics, hypernuclei were produced using cosmic rays in nuclear emulsions or bubble chambers, and the tracks of particles were analyzed. These studies enabled the determination of binding energies of relatively light hypernuclei with mass numbers $A \leq 16$, contributing significantly to the understanding of hypernuclear structure.

The emulsion contains silver bromide (AgBr) crystals, which react when charged particles pass through and lose energy, thereby recording their trajectories. A hypernucleus produced in the emulsion travels a few tens to hundreds of micrometers before decaying due to the recoil momentum at production, leaving a characteristic track with a displaced decay vertex. The darkness (i.e., density) of the track encodes information about energy loss, while its length provides information about range and total energy.

Nuclear emulsions serve as active target detectors with an unparalleled spatial resolution of a few to several tens of micrometers, and remain a powerful tool in modern experiments, such as those discovering double-Λ and Ξ hypernuclei [Tak+01; Hay+21].

However, the measurements of the Λ binding energy for s-shell hypernuclei conducted in the 1960s may lack a thorough discussion of systematic uncertainties. A recent report based on modern nuclear emulsion analysis [Kas+25] points out serious inconsistencies in the traditional energy calibration method using monochromatic α particle tracks. Specifically, a discrepancy of 3.9σ was found between the expected and observed momentum of π^- particles from the two-body decay

of ${}^{4}_{\Lambda}$H, based on calibration from monochromatic μ^+ tracks. This discrepancy was attributed to differences in stopping power treatment between α particles ($Z = 2$) and π^- mesons ($Z = 1$). In Ref. [Kas+25], systematic uncertainties in the Λ binding energy were successfully reduced to the 50 keV level by implementing density calibration using low-energy μ^+, precision calculations considering the elemental composition based on the modern stopping power calculation tool ATIMA, and correction for the Barkas effect.

1.3.2 Heavy ion collision

In heavy-ion collision experiments, ions are accelerated to GeV-scale energies per nucleon and collided either with fixed targets or in collider mode. One of the major goals is the formation of the quark-gluon plasma (QGP) under extreme conditions.

As an example, the experiment conducted by the ALICE collaboration at CERN' s Large Hadron Collider (LHC) is briefly introduced [Ach+23]. The collisions are Pb-Pb at a center-of-mass energy of $\sqrt{S_{NN}} = 5.02$ TeV. The ALICE detector setup includes a tracking system with a Time Projection Chamber (TPC) inside a 0.5 T solenoidal magnetic field, which enables precise tracking and particle identification. The energy resolution of the TPC is approximately 5%.

Various nuclei are produced through thermal coalescence during high-energy heavy-ion collisions. The one of them, ${}^{3}_{\Lambda}$H decays via ${}^{3}_{\Lambda}\mathrm{H} \rightarrow {}^{3}\mathrm{He} + \pi^-$. These decay products are identified within a $\pm 5\sigma$ window in dE/dx, and their momenta and tracks are used to reconstruct the decay topology and the invariant mass of the hypernucleus. The Λ binding energy is then obtained via Eq. 1.1.3.

This method allows for the accumulation of large statistics due to the abundant production of hypernuclei. However, the thermal and non-equilibrium nature of the production process and the unknown initial conditions are drawbacks for precise nuclear structure studies. Moreover, the reconstruction relies on Monte Carlo corrections for detector materials and magnetic fields, and is therefore not entirely self-contained. In Ref. [Ach+23], the dominant systematic uncertainty of approximately 60 keV arises from the correction δ_Λ due to differences between the measured and simulated Λ mass.

1.3.3 Decay pion spectroscopy

For light hypernuclei undergoing two-body mesonic weak decay, such as ${}^{4}_{\Lambda}\mathrm{H} \rightarrow {}^{4}\mathrm{He} + \pi^{-}$, the momentum of the emitted particles is monochromatic if the parent hypernucleus is at rest. From this, a relation can be derived between the mass of the hypernucleus before decay, ($m({}^{4}_{\Lambda}\mathrm{H})$), the masses of the decay products, $m({}^{4}\mathrm{He})$ and $m(\pi^{-})$, and their momenta, $p_{{}^{4}\mathrm{He}}$ and $p_{\pi^{-}}$, as follows:

$$\begin{aligned} m({}^{4}_{\Lambda}\mathrm{H}) &= \sqrt{m({}^{4}\mathrm{He})^{2} + p^{2}_{{}^{4}\mathrm{He}}} + \sqrt{m^{2}_{\pi^{-}} + p^{2}_{\pi^{-}}}, \\ |p_{{}^{4}\mathrm{He}}| &= |p_{\pi^{-}}|. \end{aligned} \tag{1.3.1}$$

Thus, measuring the momentum of either particle allows for the reconstruction of the hypernuclear mass. This approach is known as "decay pion spectroscopy," and further details are provided in Section 2.2.2.

In the 1980s, this experiments were conducted at KEK 12 GeV proton synchrotron (PS) using stopped K^{-} beams in light targets to produce hypernuclei and measure the momentum of the decay π^{-} [Tam+89]. Although a monochromatic peak from ${}^{4}_{\Lambda}\mathrm{H} \rightarrow {}^{4}\mathrm{He} + \pi^{-}$ was observed, the resolution was limited to $1.4 - 3.3$ MeV/c (FWHM).

In the 2000s, a breakthrough was achieved in this technique, driven by the establishment of a production method using electromagnetic interactions via the $(e, e'K^{+})$ reaction at Jefferson Lab (JLab). At MAMI (Mainz Microtron), electron beams up to 1.5 GeV are available, exceeding the threshold for strangeness-associated production. The spectrometers at MAMI A1 provide a momentum resolution of $\Delta p/p \sim 10^{-4}$ (σ) [Sch+16], enabling high-precision measurement of π^{-} momenta. To suppress the electromagnetic background, coincident detection of K^{+}–as used in JLab experiments–is employed.

The A1 hypernuclear collaboration, led by Tohoku University and Johannes Gutenberg University Mainz, initiated this experiment in 2011. An only 125 μm-thick ${}^{9}\mathrm{Be}$ target was irradiated with a 1.5 GeV electron beam totaling 20 C [ENS+15]. After electromagnetic production of excited hypernuclei like ${}^{9}_{\Lambda}\mathrm{Li}^{*}$, fragmentation and de-excitation lead to the formation of ${}^{4}_{\Lambda}\mathrm{H}$. The π^{-} from its decay has a monochromatic momentum. The momentum calibration was performed via electron elastic scattering off ${}^{181}\mathrm{Ta}$ and ${}^{12}\mathrm{C}$, achieving $\Delta p/p \sim 2 \times 10^{-4}$ (σ) [Sch16].

Experiments were conducted in 2012 and 2014, resulting in:

$$
\begin{aligned}
B_\Lambda &= 2.12 \pm 0.01\ (\text{stat.}) \pm 0.09\ (\text{syst.})\ \text{MeV}\ \ (2012), \\
B_\Lambda &= 2.157 \pm 0.005\ (\text{stat.}) \pm 0.077\ (\text{syst.})\ \text{MeV}\ \ (2014).
\end{aligned}
\tag{1.3.2}
$$

These results represent the most precise Λ binding energy measurements to date. Figure 1.4 shows the observed π^- spectra. Panel (a) presents the 2012 data, where approximately 30 events from ${}^{4}_{\Lambda}\mathrm{H}$ decay were identified [ENS+15], while panel (b) shows the 2014 high-resolution, high-statistics spectrum [Sch16].

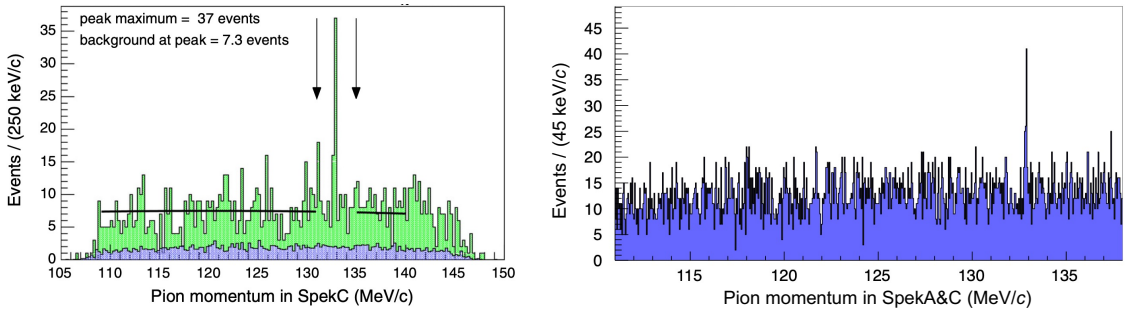

(a) MAMI 2012 (b) MAMI 2014

Figure 1.4: π^- spectra from the decay of ${}^{4}_{\Lambda}\mathrm{H}$ observed in the decay pion spectroscopy experiments at MAMI. Panel (a) shows the result from the 2012 measurement, identifying about 30 events corresponding to ${}^{4}_{\Lambda}\mathrm{H} \to {}^{4}\mathrm{He} + \pi^-$ [ENS+15]. Panel (b) presents the higher-resolution, higher-statistics result from the 2014 experiment [Sch16].

In the 2014 experiment, measurements were conducted using multiple spectrometers and targets of varying thicknesses, which not only confirmed the reproducibility of the results but also improved the statistical precision. These improvements were achieved by modifying the experimental setup—specifically, by connecting the target chamber and the spectrometers via vacuum pipes to suppress multiple scattering effects, and by implementing continuous magnetic field monitoring to ensure stability [Sch+16].

1.4 Purpose of this experiment

As described in the previous section, the decay pion spectroscopy established at MAMI provides excellent resolution and reliability for Λ binding energy measurements of light hypernuclei. Building upon this technique, the present experiment aims to further improve the precision of Λ binding energy measurements for s-shell

hypernuclei, thereby providing critical input for addressing the hypertriton puzzle and the charge symmetry breaking (CSB) problem.

However, two major limitations remain: (1) no events from ${}^{3}_{\Lambda}$H decays have been observed, and (2) despite achieving a statistical uncertainty of only 5 keV, the systematic uncertainty remains as large as 80 keV, thereby limiting the overall precision. In response, the following improvements were implemented.

(1) Non-observation of ${}^{3}_{\Lambda}$H decay π^- events

In the two-body decay ${}^{3}_{\Lambda}\mathrm{H} \rightarrow {}^{3}\mathrm{He} + \pi^-$, the π^- is expected to be emitted with a monochromatic momentum of approximately 114 MeV/c (see Section 2.2.2), which falls within the spectrometer acceptance in the 2012 and 2014 studies. If ${}^{3}_{\Lambda}$H had been produced via fragmentation reactions, this peak should have been visible, yet no significant structure was observed.

Given that ${}^{3}_{\Lambda}$H has a much smaller binding energy—roughly one-tenth that of ${}^{4}_{\Lambda}$H—the production probability is expected to be lower. Consequently, a reduction of background events is essential for observing such rare decays. Since the rate of electromagnetic background scales with the square of the target atomic number, lighter target nuclei are more suitable for electron-beam experiments.

Additionally, the ^{9}Be target used in previous studies is theoretically and experimentally known to have a $(2\alpha + n)$ cluster structure [RI18]. In the $(e, e'K^+)$ reaction, where a proton is converted into a Λ hyperon, this structure may play a role in the fragmentation process and could favor the production of ${}^{4}_{\Lambda}$H over ${}^{3}_{\Lambda}$H.

Therefore, the target material was changed to ^{7}Li. A new target system was developed, incorporating a water-cooling mechanism to handle the low melting point and geometric optimization to compensate for the reduced density. Details are provided in Section 2.3.5.

(2) Systematic uncertainty of ~ 80 keV limited overall precision

As previously discussed, momentum calibration relies on the known peaks from electron elastic scattering. The momentum of the scattered electron can be expressed as:

$$p_{e'} = \sqrt{E_{e'}^2 - m_e^2 c^4}/c, E_{e'} = \frac{E_b}{1 + \frac{E_b}{M_t}(1 - \cos\theta)}, \tag{1.4.1}$$

where the subscripts $_{e'}$ and $_b$ refer to the scattered and incident electrons (beam), respectively, and M_t is the mass of the target nucleus.

Thus, the scattered electron's momentum depends on the incident beam energy E_b, which in previous calibration runs carried an uncertainty of $\sigma = \pm 160$ keV. This uncertainty directly propagated to the reconstructed momenta and ultimately became the dominant source of systematic error.

To reduce this uncertainty, a new method utilizing synchrotron radiation interferometry with an undulator was developed [Kla+18]. This approach successfully constrained the uncertainty to $\Delta E_b/E_b = 18$ keV$/195$ MeV, roughly one-tenth of the previous level. (See Section 2.3.2 for the principle of this method.)

In the present experiment, this technique was employed for the first time in conjunction with the elastic scattering calibration, enabling simultaneous measurement of the beam energy and promising a significant reduction in systematic uncertainty. The analysis of this undulator-based beam energy measurement is currently ongoing.

Summary of the purpose

The aim of this experiment is to achieve world-leading precision in the Λ binding energy measurements of ${}^{3}_{\Lambda}$H and ${}^{4}_{\Lambda}$H by introducing two major improvements to the decay pion spectroscopy technique previously established at MAMI: (1) the development of a new ^{7}Li target system and (2) the implementation of a nobel electron beam energy measurement by undulator interferometry to suppress systematic uncertainties. The results are expected to provide crucial input not only for resolving the hypertriton puzzle and the charge symmetry breaking (CSB) issue, but also for deepening our understanding of baryon-baryon interactions under extreme conditions, thereby contributing to the theoretical modeling of dense baryonic matter, such as that found in neutron stars.

Goal of this thesis

This thesis presents the new decay pion spectroscopy experiment conducted at MAMI to fulfill these objectives, detailing the updated experimental methodology and subsequent data analysis. Since the analysis of the undulator-based beam energy measurement is still in progress, a preliminary calibration using the conventional beam energy measurement is adopted in this work. Accordingly, the final results reported here are subject to updates in their absolute values and systematic uncertainties once the undulator-based calibration is completed. Meanwhile, this thesis provides a robust outcome of determining the relative momenta of the decay π^- from ${}^{3}_{\Lambda}$H and ${}^{4}_{\Lambda}$H.

Chapter 2

Experiment

This chapter presents the experimental methodology and setup used for the high-precision mass measurement of light Λ hypernuclei via decay pion spectroscopy at the Mainz Microtron (MAMI). It begins with an overview of the MAMI electron accelerator (Section 2.1), followed by a detailed explanation of the experimental principle, including the electroproduction of hypernuclei and the detection method of decay pions (Section 2.2). The specific configuration of the experimental setup is then described, including the spectrometers used for detecting K^+ and decay π^-, the data acquisition system, and the specially designed lithium target (Section 2.3). The latter part of the chapter summarizes the beamtime operations (Section 2.4).

2.1 The Mainz Microtron MAMI

The experiment was conducted at the Mainz Microtron (MAMI) accelerator facility [Kai+08] of the Institute of Nuclear Physics, Johannes Gutenberg University Mainz, Germany. This facility was designed to provide high-quality, continuous electron beams for nuclear physics research. Figure 2.1 shows the overall view of the MAMI facility.

MAMI comprises three Race-Track Microtrons (RTM), which include linac and semi-circle dipoles. Figure 2.2 shows a schematic drawing of RTM. The beam injected into the RTM is repeatedly accelerated for each orbit by a single linear accelerator. The orbit radius of the two 180° bending magnets at both ends of the linear accelerator gradually increases according to the beam energy, which makes it possible to accelerate the beam with a single linear accelerator repeatedly. Electrons emitted from the ion source are accelerated to 855 MeV through three RTMs (RTM1, RTM2, RTM3) (MAMI-B).

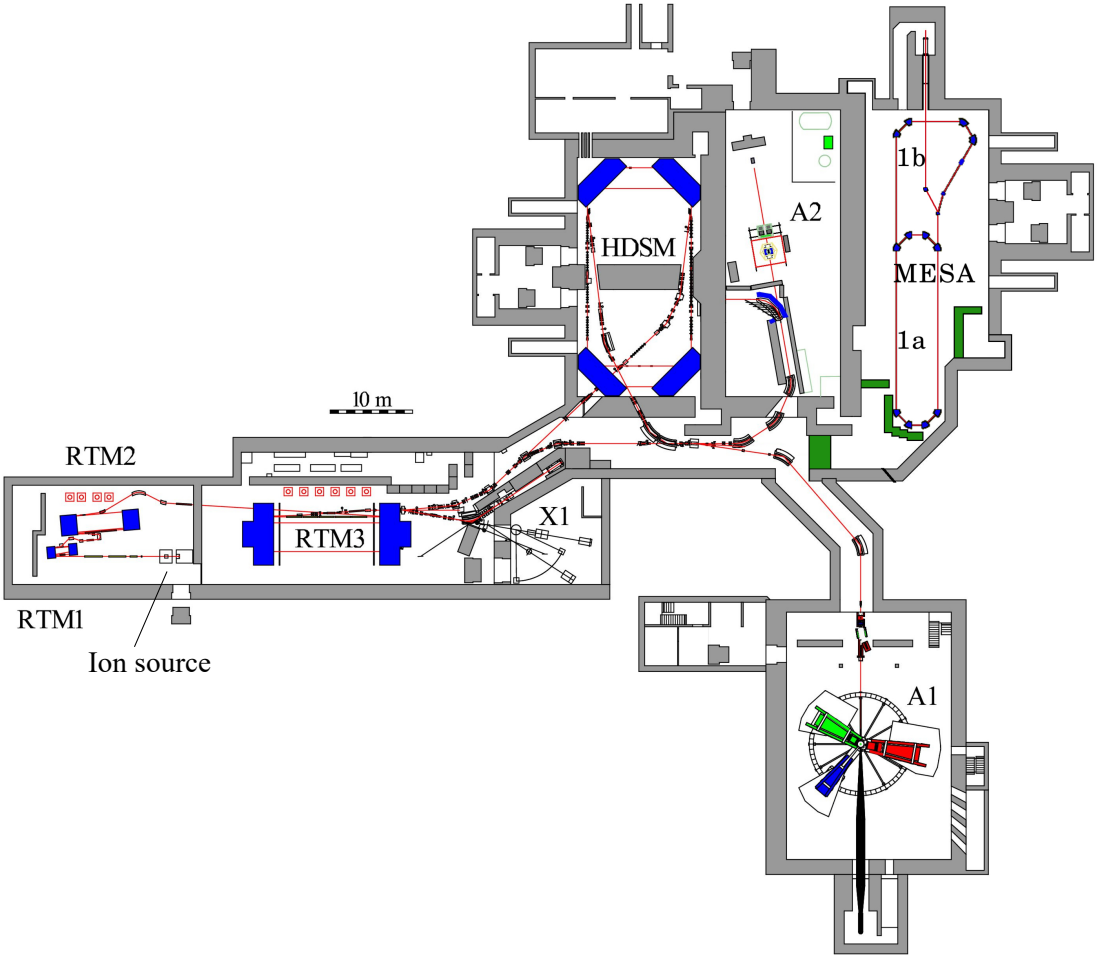

Figure 2.1: The floor plan of whole facility of Mainz Microtron [Sch16].Electrons emitted from the ion source at the bottom left are accelerated to 855 MeV in three stages of RTMs. After passing through the HDSM in the fourth stage, they are accelerated to 1.5 GeV. In addition to the A1 hall, where the main experiment is carried out, there are two experimental halls, A2 and X1. A new accelerator, MESA, is currently under construction.

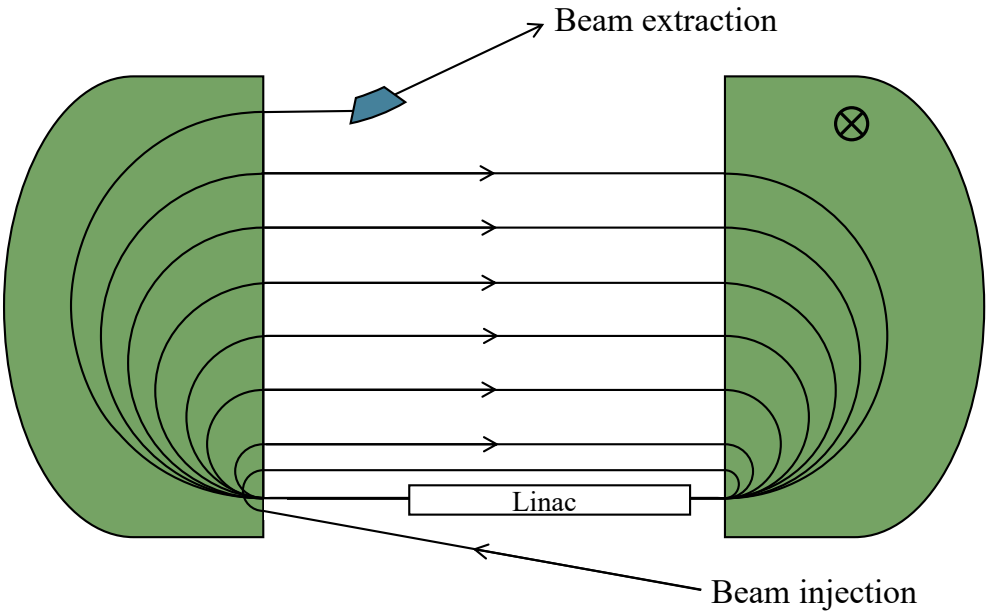

Figure 2.2: Schematic drawing of the RTM at MAMI. RTM consists of two 180° bending dipoles and a linear accelerator. The injected beam is accelerated by the linear accelerators for each orbit.

In 2006, a Harmonic Double-Sided Microtron (HDSM) [Kai+08] was installed (MAMI-C). The schematic drawing of the HDSM is shown in Figure 2.3. The HDSM is composed of two linacs and four $90°$ bending dipole magnets. The electron beam is accelerated from 855 MeV to 1.5 GeV over 43 orbits.

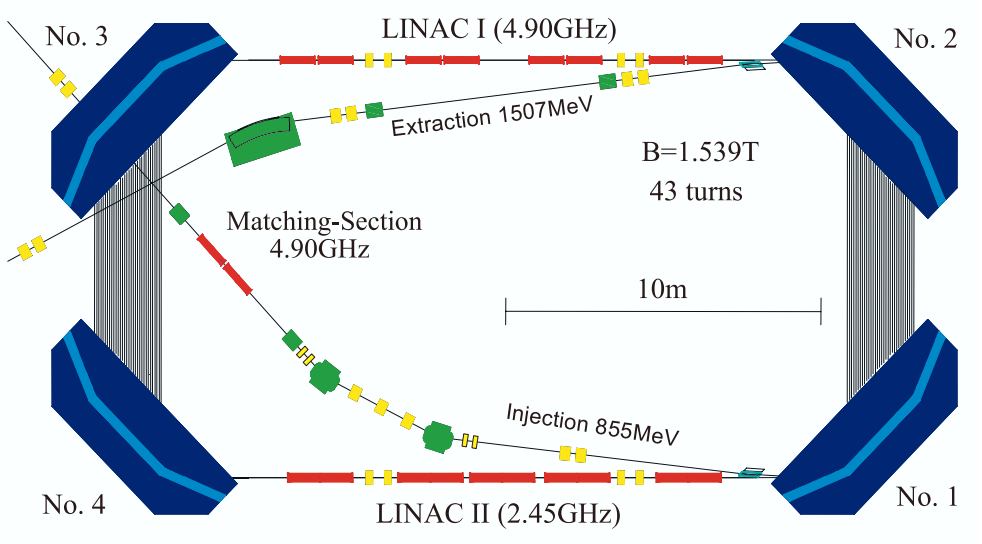

Figure 2.3: Schematic drawing of the HDSM at MAMI [Jan06]. HDSM, consisting of four $90°$ bending magnets and two linear accelerators, was newly constructed after RTM3 in 2006. It can further accelerate the electron beam accelerated by MAMI-B up to 1.5 GeV.

The high-energy electron beam from MAMI-C is transported to the A1 experimental hall, where this experiment was performed, or the A2 hall. Also, the Mainz Energy recovering Superconducting Accelerator (MESA) is currently under construction.

MAMI can operate continuously for more than $7,000$ hours per year [Kai+08], and is highly regarded for its energy stability and beam quality. Table 2.1 shows the main characteristics of the beams provided by MAMI-B and MAMI-C.

Figure 2.4 shows a photo of the A1 experimental hall. The hall has three large vertical bending spectrometers, named Spectrometer A (Spek-A, red), Spectrometer B (Spek-B, blue), and Spectrometer C (Spek-C, green). The three spectrometers are installed on a rotating platform, and the installation angle can be changed to match the kinematics of each experiment. A target chamber for placing the experimental target is installed in the center of the rotating platform. The features of these spectrometers and the target are described in Section 2.3.1 and 2.2.2.

Table 2.1: Characteristics of the electron beam provided by MAMI-B and MAMI-C [Kai+08]

Stage Name	RTM3 (MAMI-B)	HDSM (MAMI-C)
Maximum output energy (MeV)	855.1	1508
Maximum output current (μA)	100	100
Frequency (GHz)	2.45	4.90
Energy spread (keV)	13 (FWHM)	110 (FWHM)
Horizontal Emittance (μm·mrad)	13π (rms)	27π (rms)
Vertical Emittance (μm·mrad)	0.84π (rms)	1.2π (rms)

Figure 2.4: Picture of the A1 hall [Ber10]. From the left side, Spectrometer A (Spek-A, red one), Spectrometer B (Spek-B, blue one), and Spectrometer C (Spek-C, green one). These three vertical bending spectrometers are installed on the rolling stage. The radiation shielding doors of Spek-A and Spek-C are open in this picture.

2.2 Experimental principle and design

2.2.1 Electro-production of hyperons and hypernucleus

The upgrade to MAMI-C in 2006 brought the continuous beam energy to the threshold for $s\bar{s}$ production, allowing access to hadronic physics, including strangeness. This section will explain the electromagnetic production of hyperons by electron scattering.

The kinematics of the reaction:

$$e + p \rightarrow e' + K^+ + Y \tag{2.2.1}$$

is used to produce a hyperon in this experiment is shown in Figure 2.5, where $Y = \Lambda$. Here, we assume the One-Photon Exchange Approximation (OPEA).

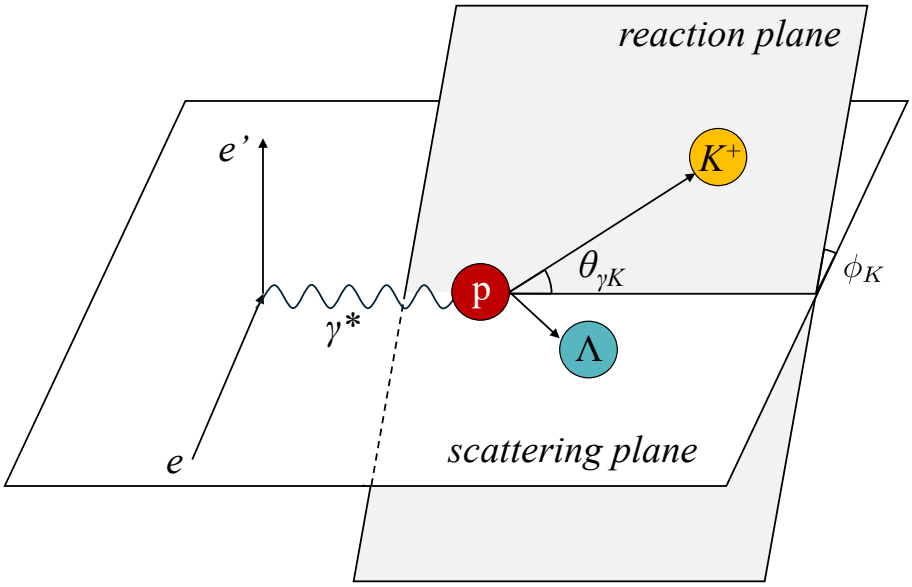

Figure 2.5: Kinematics of the $(e, e'K^+)$ reaction

The $(e, e'K^+)$ reaction uses an electron beam to generate $s\bar{s}$ quarks via virtual photons, as shown in Figure 2.5. Other representative reactions for producing hypernuclei include the (π^+, K^+) and (K^-, π^-) reactions. Diagrams of these elementary processes are shown in Figure 2.6.

The production cross sections of the strangeness exchange reaction: (K^-, π^-) reaction are the largest at about mb/sr, the strangeness-associated production reaction: (π^+, K^+) reaction at 100 μb/sr, and the $(e, e'K^+)$ reaction at $\sim$ 100 nb/sr.

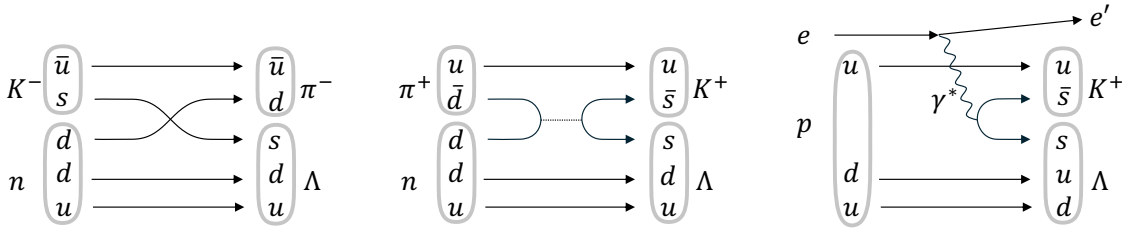

(a) (K^-, π^-) reaction (b) (π^+, K^+) reaction (c) (e, e'K^+) reaction

Figure 2.6: Feynman diagrams of the Λ particle production reaction. (a) Strangeness-exchange reaction (K^-, π^-), typically with a cross section of about mb/sr. (b) Strangeness-associated production reaction (π^+, K^+), with a cross section of approximately 100 μb/sr. (c) Electroproduction reaction $(e, e'K^+)$, with a cross section on the order of ~ 100 nb/sr.

Figure 2.7 shows the correlation between the recoil momentum of the hyperon and the incident momentum in the hyperon production reaction.

The (π^+, K^+) and $(e, e'K^+)$ reactions are endothermic reactions and have a threshold for Λ particle production (~ 900 MeV/c). In addition, the large momentum transfer to Λ particles makes it easy to observe hypernuclei with deeply bound hyperons. In the (π^+, K^+) and (K^-, π^-) reactions, the spins of the incident beams, π^+ and K^- mesons, are 0, so the spin of the Λ particle does not invert when viewed in the 0° direction relative to the beam. On the other hand, the virtual photon that mediates the $(e, e'K^+)$ reaction has a spin of 1, so it has the characteristic that Λ particles with spins inverted relative to the reacting nucleons can be produced even in the 0° direction where the production cross section is large.

The differential cross section for electromagnetically produced mesons can be written as

$$\frac{d^3\sigma}{dE'_e d\Omega'_e d\Omega_K^{\mathrm{CM}}} = \Gamma \frac{d\sigma_{\gamma^*}}{d\Omega_K^{\mathrm{CM}}}. \tag{2.2.2}$$

Here, Γ is called the virtual photon flux in the laboratory system, and $\frac{d\sigma_{\gamma^*}}{d\Omega_K^{\mathrm{CM}}}$ is the differential cross section in the center of mass system of the hadronic final state. Conventionally, hadronic quantities are treated in the center-of-mass system, and lepton quantities in the laboratory system. Quantities in the center-of-mass system are indicated with the subscript CM.

As shown in Equation 2.2.2, by separating Γ from the differential cross section and corresponding $\frac{d\sigma_{\gamma^*}}{d\Omega_K^{\mathrm{CM}}}$ to photoproduction (by virtual photon γ^*), we can consider

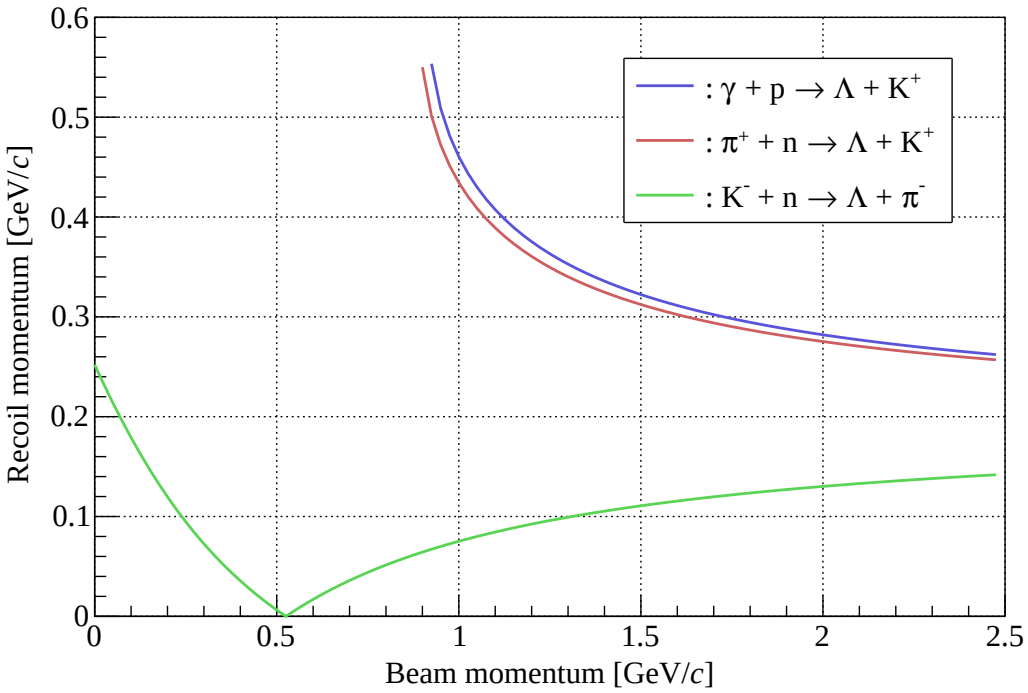

Figure 2.7: Correlation between the recoil momentum of the hyperon and the incident momentum in the hyperon production reaction. The figure shows the correlation when the observation angle is $\theta_{\text{lab}} = 0°$.

the corresponding behavior when photoproduction $(Q^2 = 0)$ becomes finite Q^2. In this case, Q^2 represents four-momentum transfer $(Q^2 > 0)$, and since the virtual photon four-momentum q^μ can be written as

$$q^\mu := (\omega, \mathbf{q}) = (E_e - E_{e'},\ \mathbf{p}_e - \mathbf{p}_{e'}) \tag{2.2.3}$$

it is a quantity that can be expressed as

$$\begin{aligned} Q^2 := -q^2 &= -\left[(E_e - E_{e'})^2 - (\mathbf{p}_e - \mathbf{p}_{e'})^2\right] \\ &= -2m_e^2 + 2E_e E_{e'} - 2|\mathbf{p}_e||\mathbf{p}_{e'}|\cos\theta_{ee'}. \end{aligned} \tag{2.2.4}$$

Additionally, Γ can be interpreted as the flux of virtual photons contributing to meson production. Since QED can well describe the electron scattering part, it can

be written as

$$\begin{aligned} \Gamma &= \frac{\alpha}{2\pi^2 Q^2}\frac{E_\gamma}{1-\epsilon}\frac{E_{e'}}{E_e} \\ \epsilon &:= \left[1+2\frac{|\mathbf{q}|^2}{Q^2}\tan^2\left(\frac{\theta_{ee'}}{2}\right)\right]^{-1} \\ \epsilon_L &:= \epsilon\frac{Q^2}{\omega^2} \end{aligned} \tag{2.2.5}$$

under the lowest-order contribution OPEA as shown in Figure 2.5. Here, ϵ and ϵ_L represent the polarization of the virtual photon, distinguishing between transverse and longitudinal polarities. In this way, the information of the virtual photon is determined only by the information of the lepton, and is handled in the laboratory system.

Also, the quantity E_γ that appears here is called the photon equivalent energy, which is the energy required to cause the same reaction when real photons $Q^2 = 0$ are used, and can be written by

$$E_\gamma := \frac{W^2 - m_p^2}{2m_p} = \omega + \frac{q^2}{2m_p}. \tag{2.2.6}$$

The differential cross-section Equation 2.2.2 can be decomposed into five parts according to the angle ϕ_K between the electron scattering plane and the hadron reaction plane (Figure 2.5), and the degree of polarization ϵ of the virtual photon as follows:

$$\frac{d\sigma_{\gamma^*}}{d\Omega_K^{\mathrm{CM}}} = \frac{d\sigma_T}{d\Omega_K^{\mathrm{CM}}} + \epsilon_L\frac{d\sigma_L}{d\Omega_K^{\mathrm{CM}}} + \sqrt{2\epsilon_L(1+\epsilon)}\frac{d\sigma_{LT}}{d\Omega_K^{\mathrm{CM}}}\cos\phi_K + \epsilon\frac{d\sigma_{TT}}{d\Omega_K^{\mathrm{CM}}}\cos 2\phi_K \tag{2.2.7}$$

The subscripts T and L represent the transverse and longitudinal wave components, respectively. The third term, LT, is related to the interference of the longitudinal and transverse amplitudes, and the fourth term, TT, is associated with the interference of the transverse amplitude. All structure functions depend on the momentum transfer Q^2, the center-of-mass polar angle $\theta_{\gamma K}$ of the emitted K^+, and the energy of the hadron system. Since the real photon has only a transverse wave component in the (γ, K^+) reaction, the L and LT contributions can only be measured by the $(e, e'K^+)$ reaction.

2.2.2 Principle of decay pion spectroscopy

Figure 2.8 depicts the principle of the decay pion spectroscopy.

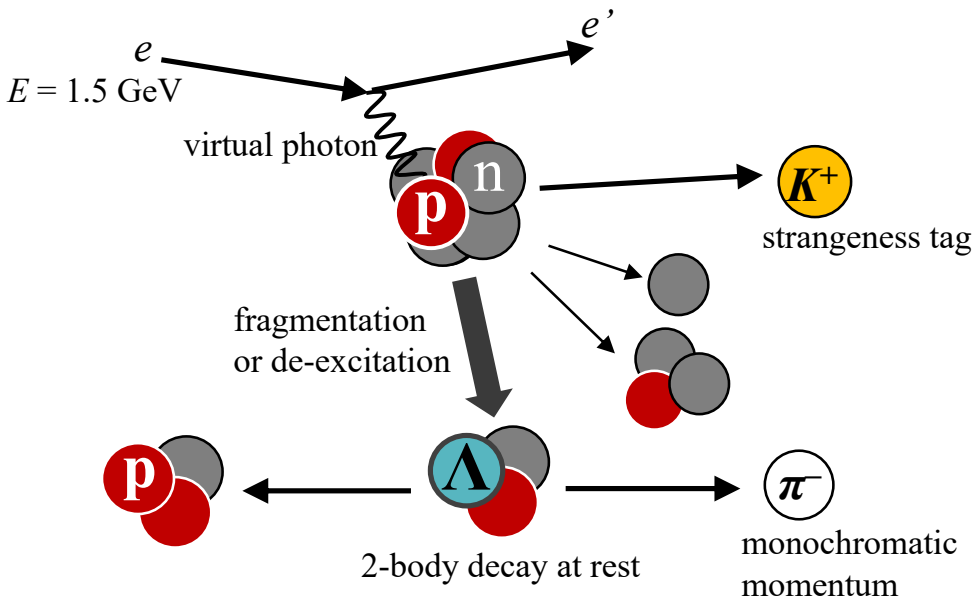

Figure 2.8: Principle of decay pion spectroscopy. When an electron beam with $E_b = 1.5$ GeV is incident on the target, protons in the target nuclei are converted into Λ hyperons. The produced Λ hypernuclei lose energy within the target material and subsequently undergo fragmentation reactions or de-excitation. Some of the resulting Λ hypernuclei eventually come to rest in the ground state of ${}^{3}_{\Lambda}\mathrm{H}$ or ${}^{4}_{\Lambda}\mathrm{H}$. These nuclei undergo two-body weak decays accompanied by the emission of a π^- meson. The emitted π^- carries a monochromatic momentum that depends on the mass of the parent hypernucleus. By measuring the monochromatic momentum of the decay π^-, the mass of the parent hypernucleus can be determined. In addition, by tagging the K^+ mesons emitted simultaneously with the production of strange quarks, strangeness production events can be identified amidst a large background.

An electron beam is irradiated, then Λ hyperons are produced from the protons in the target nuclei through the $(e, e'K^+)$ reaction according to the formula 2.2.1. The Λ hypernuclei produced in this process lose their energy in the target material by undergoing nuclear fragmentation reactions due to recoil momentum, or de-excitation. Eventually, some Λ hypernuclei come to rest in the ground state in the target material.

In this study, natural lithium was used as the target material (Section 2.3.5). As a result, hypernuclei such as excited states of ${}^{7}_{\Lambda}\mathrm{He}^{*}$ are first produced via the $(e, e'K^+)$ reaction. Among the Λ hypernuclei subsequently generated through fragmentation reactions, ${}^{4}_{\Lambda}\mathrm{H}$ and ${}^{3}_{\Lambda}\mathrm{H}$ are the primary focus of this study.

Light Λ hypernuclei such as ${}^{3}_{\Lambda}\mathrm{H}$ and ${}^{4}_{\Lambda}\mathrm{H}$ then undergo two-body decays by mesonic weak decays emitting π^-/π^+. In this experiment, we use the following decay modes:

$$\begin{aligned} {}^{3}_{\Lambda}\mathrm{H} &\rightarrow {}^{3}\mathrm{He} + \pi^- \\ {}^{4}_{\Lambda}\mathrm{H} &\rightarrow {}^{4}\mathrm{He} + \pi^-. \end{aligned} \tag{2.2.8}$$

There is another decay mode of $\Lambda \rightarrow \pi^0 + n$. However, this can not be observed due to the polarity setting of the spectrometers. In this decay, energy conservation is represented as:

$$E_{\mathrm{hyp}} = E_{\mathrm{nucl}} + E_{\pi^-}. \tag{2.2.9}$$

If the hypernucleus is in rest, e.g. $p_{\mathrm{hyp}} = 0$, this Equation 2.2.9 is turn to be:

$$m({}^{A}_{\Lambda}Z) = \sqrt{m({}^{A}(Z+1))^2 + p^2_{\pi^-}} + \sqrt{m^2_{\pi^-} + p^2_{\pi^-}} \tag{2.2.10}$$

where $m({}^{A}(Z+1))$ is the daughter nucleus after decay, m_{π^-} is the mass of the emitted pion, and p_{π^-} is the momentum of the decay pion. The case of Equation 2.2.10, the masses of the daughter nuclei ($m({}^{A}(Z+1))$), which are ^{3}He and ^{4}He, and the mass of the π^- (m_{π^-}) are experimentally well-known values, the accuracy of 2.42 eV, 0.06 eV [AWT03], and 0.35 keV [Ber+12], respectively. Therefore, the mass of the Lambda hypernucleus ($m({}^{A}_{\Lambda}Z)$) can be obtained by measuring the momentum of the π^- (p_{π^-}).

Besides, obviously, the p_{π^-} has a monochromatic value only depending on the species of parent hypernuclei; we can easily identify the parent hypernuclei from the p_{π^-} value.

In reality, a large number of background events are observed during beam irradiation. Still, detecting K^+ emitted simultaneously with the production of Λ particles and tagging the strangeness production events makes it possible to suppress many of the background events. In the present experiment, the π^- momentum is measured by SpekA (Section 2.3.1), and the emitted K^+ is detected by the dedicated spectrometer KAOS (Section 2.3.3).

The binding energy of Λ can be calculated from the mass of the Λ hypernucleus ($m({}^{A}_{\Lambda}Z)$) by the following definition:

$$B_{\Lambda} = m_{\mathrm{core}} + m_{\Lambda} - m({}^{A}_{\Lambda}Z). \tag{2.2.11}$$

To effectively gain light hypernuclear candidates through fragmentation reaction, the atomic number of the target material should be small. In addition, the target material needs to be easy to handle and mechanically stable, making solid-state targets more suitable for use in experimental hall A1. Due to these reasons, the ^{9}Be target was selected in the past experiment [ENS+15; Sch+16]. It was confirmed that the ^{9}Be is suited for deducing $^{4}_{\Lambda}$H; however, $^{3}_{\Lambda}$H-like events were not observed. We should suppress the background events and gain the fragmentation reaction to obtain the $^{3}_{\Lambda}$H produced events. For this reason, $^{\mathrm{nat}}$Li (natural lithium; 93.7 % of ^{7}Li, and 6.3 % of ^{6}Li) is selected as the target material in this present experiment. Section 2.2.2 will explain this lithium targeting system in more detail.

In the ^{7}Li case, the eight candidates, from $^{3}_{\Lambda}$H to $^{7}_{\Lambda}$He, for Λ hypernuclei will be produced by the nuclear fragmentation reaction, shown in Table 2.2. The table shows each decay mode that emits π^{-}, the expected momentum of the π^{-}, and the mass width of the resulting nucleus. The each expected momentum of the decay pions ($p_{\pi^{-}}$) are calculated as

$$p_{\pi^{-}} = \sqrt{\left(\frac{m(^{A}(Z+1))^2 + m(^{A}_{\Lambda}Z)^2 - m^2_{\pi^{-}}}{2m(^{A}_{\Lambda}Z)}\right)^2 - m(^{A}(Z+1))^2} \qquad (2.2.12)$$

by using Equation 2.2.10 and 2.2.12.

$^{5}_{\Lambda}$H is not able to estimate the decay π^{-} momentum because no value for the Λ binding energy has been reported. Of these fragment candidates, $^{5}_{\Lambda}$H, $^{4}_{\Lambda}$He, and $^{5}_{\Lambda}$He decay into the nuclei ^{5}He, ^{4}Li, and ^{5}Li by nucleon emission, with lifetimes of the order of 10^{-21}. Therefore, their mass width is on the order of several MeV, broadening the decay pion peak and making them unsuitable for measurement by decay pion spectroscopy. For $^{6}_{\Lambda}$H, the width is negligibly small, but the reported Λ binding energy is unclear [Hon+17; Agn+12], so experiments cannot be adjusted accordingly.

Figure 2.9 shows the predicted amount of hyperfragment production from ^{7}Li and ^{6}Li [BP07]. The routines underlying this model are based on a framework initially used to predict the fragmentation of normal nuclei in heavy-ion reactions [BGI90]. In principle, the system of excited nuclei in heavy-ion collisions behaves similarly to nuclei excited by an electron beam, so the model was later extended to handle hyperfragments as well [BP07]. This prediction was also used in previous studies to predict the amount of hyperfragmentation produced at MAMI [Sch16]. Although $^{6}_{\Lambda}$He is inside the SpekA acceptance range, according to this prediction, the yield of $^{6}_{\Lambda}$He is several orders lower than the other candidates. The remaining isotopes are $^{3}_{\Lambda}$H, $^{4}_{\Lambda}$H and $^{7}_{\Lambda}$He. In this model, the yield of $^{3}_{\Lambda}$H is predicted to be about one-tenth

Table 2.2: Lambda hypernuclear candidates from fragmentation reaction with Lithium. The nuclear mass of the daughter nucleus and core nucleus is deduced from Reference [AWT03], and the mass of Λ and π^- are obtained from Reference [Ber+12]. Lambda binding energy of ${}^{7}_{\Lambda}$He is referenced from Reference [Gog+16] and for the others from Reference [EA+21]. The width of each daughter nuclei is from Reference [Int].

Hypernucleus	B_Λ	Decay modes	p_{π^-}	Width
${}^{3}_{\Lambda}$H	0.164 MeV	^{3}He $+ \pi^-$	114.32 MeV/c	–
${}^{4}_{\Lambda}$H	2.169 MeV	^{4}He $+ \pi^-$	132.85 MeV/c	–
${}^{5}_{\Lambda}$H	–	^{5}He $+ \pi^-$	–	0.6 MeV
${}^{6}_{\Lambda}$H	4.000 MeV	^{6}He $+ \pi^-$	135.27 MeV/c	$\simeq 0$
${}^{4}_{\Lambda}$He	2.347 MeV	^{4}Li $+ \pi^-$	98.23 MeV/c	6.0 MeV
${}^{5}_{\Lambda}$He	3.102 MeV	^{5}Li $+ \pi^-$	99.29 MeV/c	1.5 MeV
${}^{6}_{\Lambda}$He	4.180 MeV	^{6}Li $+ \pi^-$	108.47 MeV/c	–
${}^{7}_{\Lambda}$He	5.550 MeV	^{7}Li $+ \pi^-$	114.97 MeV/c	–

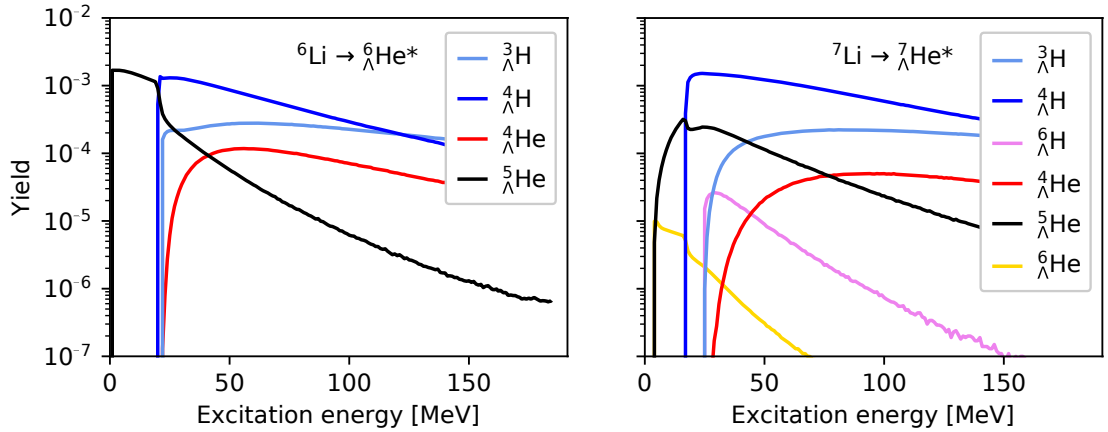

Figure 2.9: Predicted probability of hyperfragment production from a Lithium target [BP07]. The left panel shows the case of ^{6}Li, and the right panel shows ^{7}Li. In both cases, $^{4}_{\Lambda}$H and $^{3}_{\Lambda}$H are expected to be the most abundant hyperfragments, while the production of $^{6}_{\Lambda}$He is predicted to be several orders of magnitude lower. The yield of $^{7}_{\Lambda}$He is also negligible due to the low likelihood of direct transformation from a ^{7}Li nucleus. These results support the choice of natural lithium as a suitable target for obtaining s-shell hypernuclei, particularly $^{3}_{\Lambda}$H and $^{4}_{\Lambda}$H.

of that of $^{4}_{\Lambda}$H. Moreover, the direct production of a bound $^{7}_{\Lambda}$He from a ^{7}Li nucleus is considered highly unlikely [Von24], and thus this hypernucleus is not expected to be observed in the present experiment.

2.2.3 Setup of the experiment

Figure 2.10 shows a photo of the A1 hall in this experiment, and Figure 2.11 shows the spectrometer schematic layout when viewed from above. The target, natural lithium (Section 2.2.2), was placed in the target chamber in the center of the hall. The momentum of decay π^- emitted by Λ hypernuclei decaying in the target was measured by SpekA, which is installed at 95°. Since K^+, which is produced simultaneously with strange quark production, is emitted far forward, a dedicated spectrometer KAOS for tagging strangeness-produced events was installed at 0°. The orbit of the injected electron beam was adjusted by pre-chicane magnets (17°) so that the emitted particles entered KAOS at 0°.

The two spectrometer kinematic settings are summarized in Table 2.3. The following chapters will explain these spectrometers.

Table 2.3: Spectrometer settings

Spectrometer	Central momentum	Angle	Particle
SpekA	122.0 MeV/c	95°	π^-
KAOS	975.0 MeV/c	0°	K^+

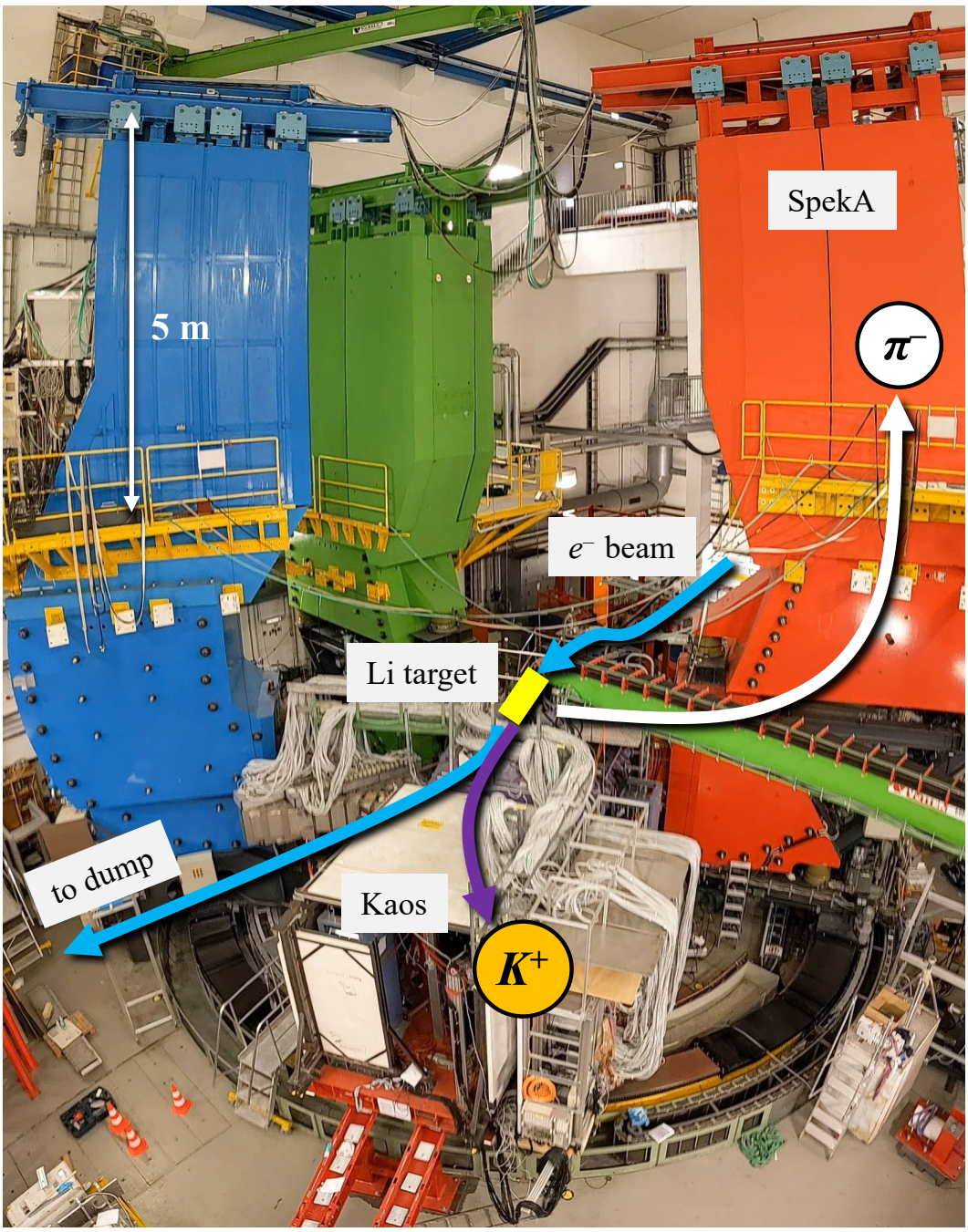

Figure 2.10: Picture of the A1 hall for decay pion spectroscopy experiment. An electron beam is sent from MAMI-C from the back of the picture and irradiates the lithium target placed in the center. The momentum of the pions emitted during Lambda hypernuclear decay is measured by SpekA installed at $95°$. K^+, which is generated at the same time as Lambda particle production, is emitted far forward, so the dedicated spectrometer KAOS installed at $0°$.

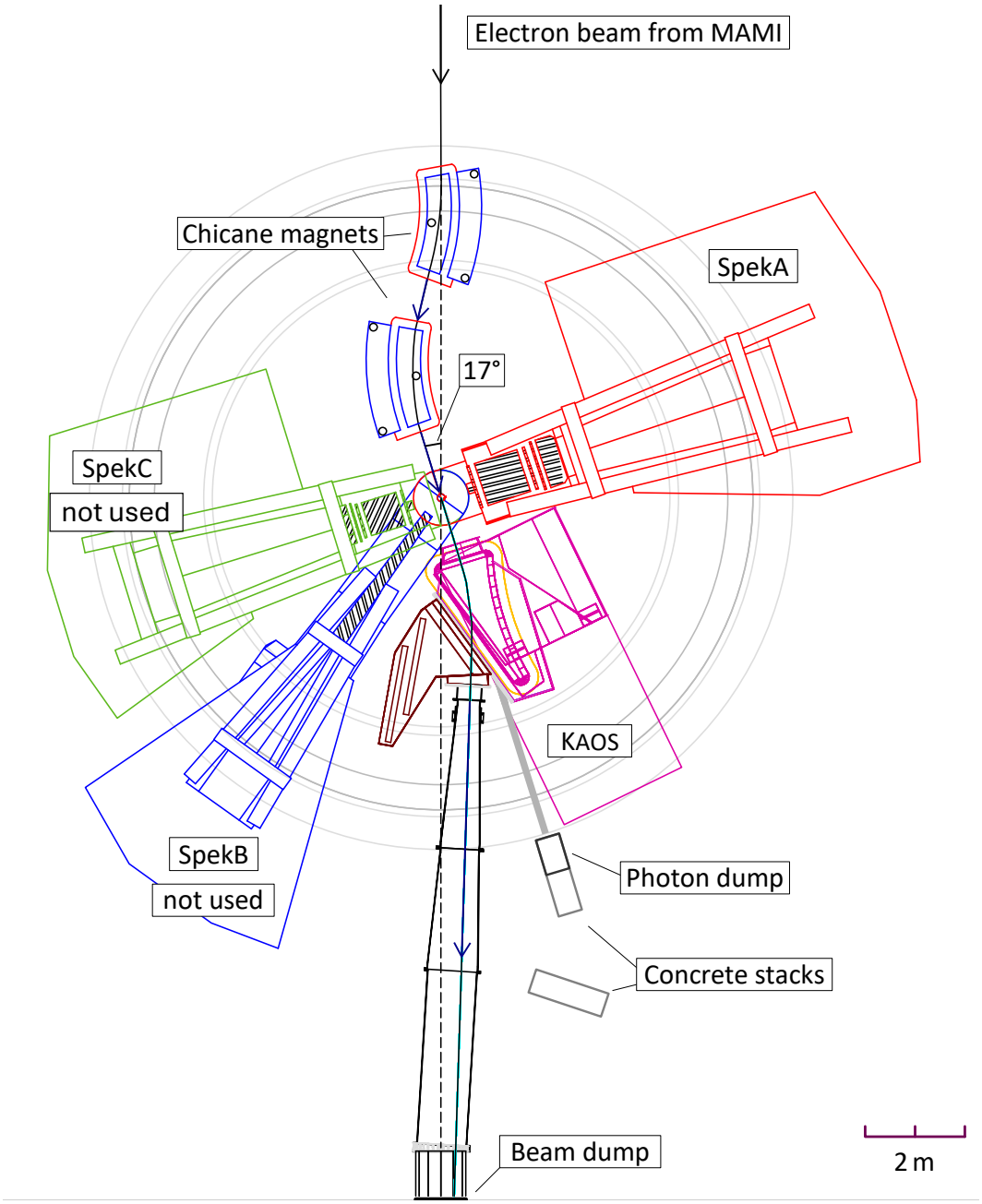

Figure 2.11: Top view of schematic drawing of the A1 hall [Von24]. The electron beam is injected from above. It is designed to be injected into KAOS at 0° through pre-chicane magnets that bend the orbit by 17° relative to the beam axis. Spek A is set at 95°.

2.3 Apparatus

2.3.1 Magnetic spectrometer A for decay pion momentum measurement

In this experiment, the momentum of decay π^- is measured by SpekA. Table 2.4 shows the main features of the spectrometer.

Table 2.4: Main property of the spectrometer A [Blo+98].

Maximum momentum	735 MeV/c
Momentum acceptance	20%
Solid angle acceptance	28 msr
Long target acceptance	50 mm
Dispersive angle coverage	± 70 mrad
Non-dispersive angle coverage	± 100 mrad
Length of the central trajectory	10.75 m
Momentum resolution	$\sim 10^{-4}$ [Sch16]

Figure 2.12 shows a schematic drawing of the magnet system of the SpekA. Spek A has a quadrupole, a sextupole, and two dipoles. The first two serve to focus the incoming particles, while the latter dipoles bend them upwards in a circular path, which separates them by momentum. By changing the magnetic field and current settings, the polarization and momentum region can be freely changed.

The dipole is equipped with an NMR probe (Caylar NMR20 Precision Teslameter). Two probes are equipped to cover the low field range ($0.1-0.5$ T) and the high field range ($0.45 - 2.1$ T), and the central magnetic field is constantly monitored.

The value of the central momentum p_{cent} is determined by the following equation [Sch16]:

$$p_{\text{cent}} = \frac{660.0 \text{ MeV}/c}{1.50101 \text{ T}} B_{\text{eff}} \times 1.0476203 \tag{2.3.1}$$

Here, B_{eff} is the effective magnetic flux density. The last factor, 1.0476203, is a correction factor defined in the design specification of SpekA to account for systematic offsets between the nominal and effective field settings. A more precise momentum calibration factor can be obtained experimentally through elastic electron scattering, as will be discussed in Section 2.3.2. The magnetic field is measured by NMR probes installed in both D1 and D2 dipole magnets; however, since the trajectory length in D1 is longer, the central magnetic field of D1 is referenced as B_{eff}. The difference in the magnetic field contributions between D1 and D2 has been taken into account in this study.

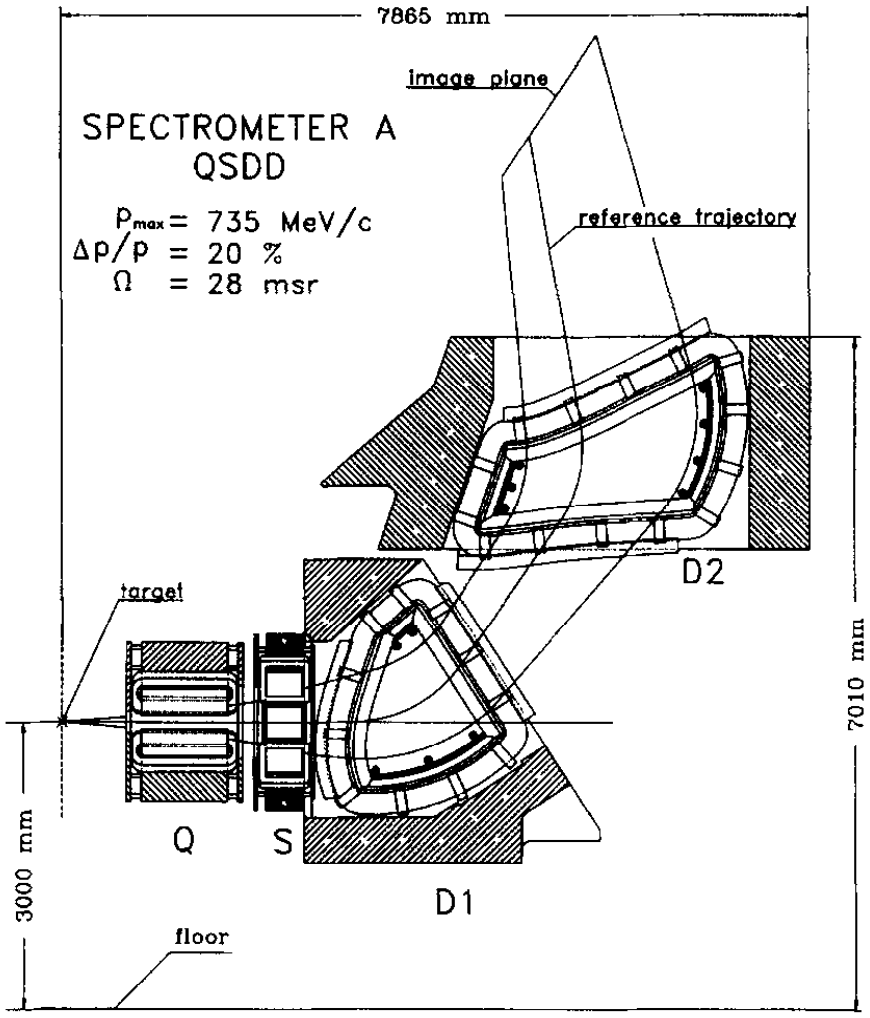

Figure 2.12: Schematic drawing of the magnet system of the SpekA [Blo+98]. The left side of the figure indicates the target position, where incoming particles pass through a quadrupole and sextupole magnet in sequence, which focus the trajectory. They are then momentum-dispersed by two dipole magnets (D1 and D2). NMR probes are installed in both D1 and D2 to monitor the magnetic field. By adjusting the dipole polarity and beam current, the central momentum can be set up to a maximum of 735 MeV/c.

Figure 2.13 shows the focal plane detector system of SpekA, which consists of vertical drift chambers, timing counters, and gas Cherenkov detectors.

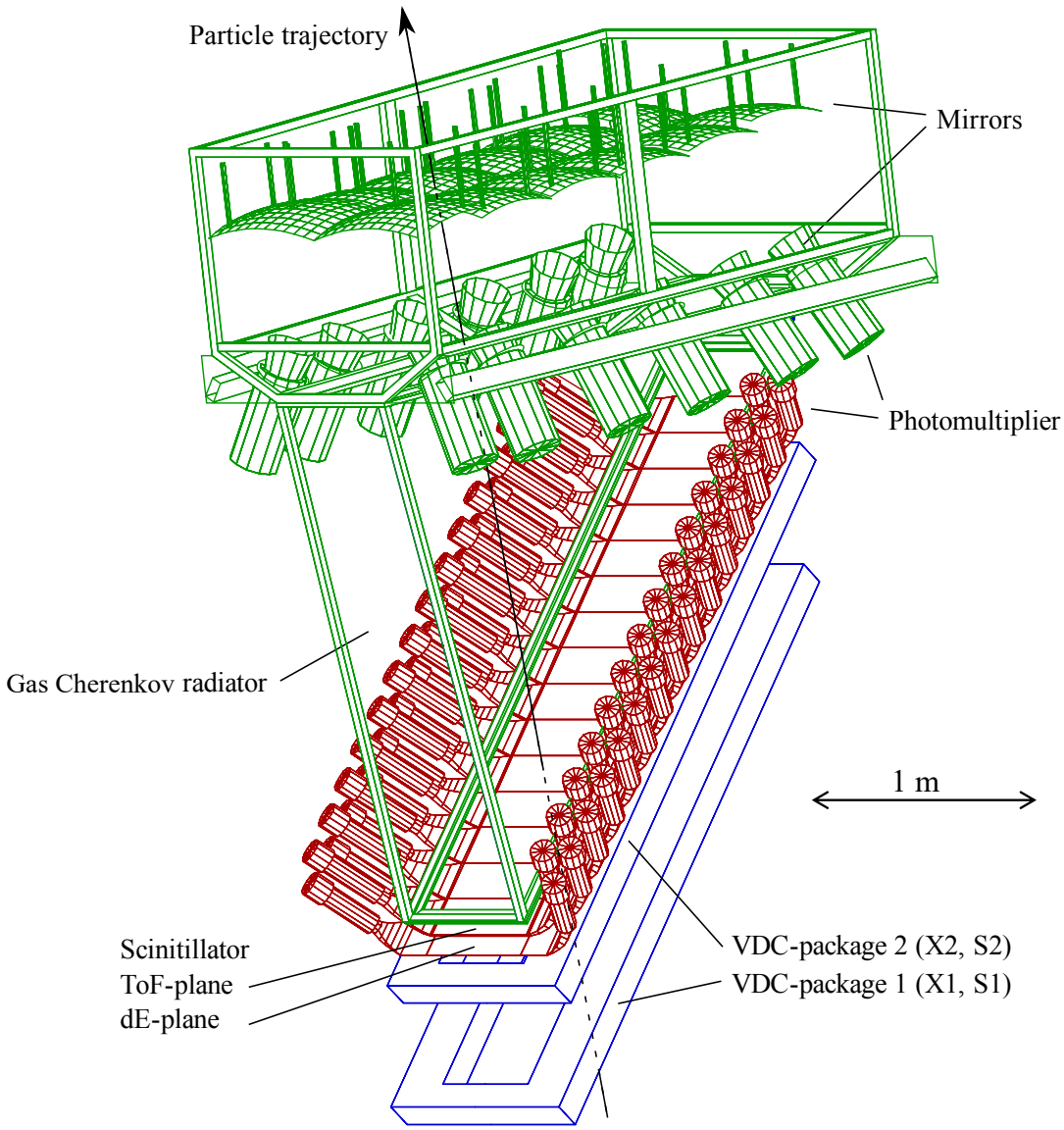

Figure 2.13: Detector system of the magnetic spectrometers [Ber10]. The arrows show the trajectory of the particles running from bottom to top. The first layer they pass is the four-layer VDC shown in blue. The next layer is the two-layer scintillator plane shown in red, named dE and ToF from bottom to top. A PMT is connected to both ends of each paddle. The last detector shown in green is a gas Cherenkov detector, which detects high-energy e^+/e^- and emits light. It was not used in this experiment.

The first detector encountered by the particles is a set of vertical drift chambers (VDCs), which allow two-dimensional tracking of the particle trajectory. These chambers provide a two-dimensional projection of the particle track in either the dispersive or non-dispersive plane. Figure 2.14 illustrates the operating principle of the VDCs.

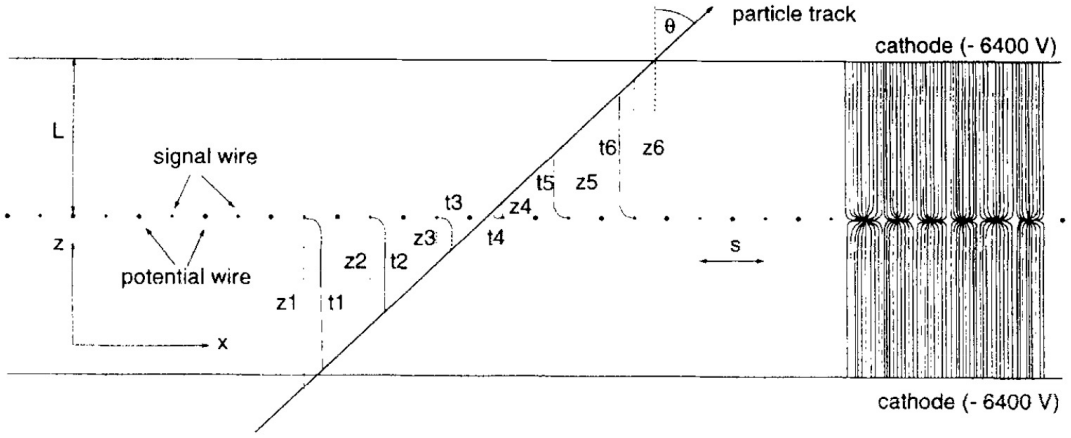

Figure 2.14: Operating principle of the vertical drift chamber (VDC). Charged particles passing through the chamber ionize the gas mixture. The ionization electrons drift toward the signal wires along the electric field lines, and their drift times are used to reconstruct the particle trajectory. The chamber consists of signal wires, potential wires, and cathode foils arranged with a spacing of 12 mm between wire planes and cathodes.

The potential wires are connected to ground, while both cathode foils are biased with negative high voltage. The gap L between the wire planes and cathode foils is 12 mm. The signal and potential wires have diameters of 15 μm and 50 μm, respectively. The applied high voltage, typically in the range of $5.6 - 6.5$ kV, is chosen such that the signal wires provide a high gas gain while the potential wires remain below the trigger threshold. The spacing between adjacent signal wires is 5 mm, and the distance between a signal wire and its neighboring potential wire is 2.5 mm. Consequently, each drift cell measures 24 mm in length and 5 mm in width. For particles with an incident angle of $45°$, a single track may pass through up to six drift cells.

To minimize aging effects, the VDCs are filled with a gas mixture of equal parts argon and isobutane, along with 1.5% pure ethanol. When a charged particle passes through the chamber, it ionizes the gas molecules. The primary and secondary electrons then drift toward the wires along paths t_1 to t_6, as shown in Figure 2.14. The drift distances z_1 to z_6 are calculated from the measured drift times,

which are typically around 200 ns. The particle trajectory is then reconstructed from these distances.

To reconstruct the trajectory of particles after passing over the dipole magnets, the VDCs are arranged in four wire planes: X1, S1, X2, and S2. The X1 and X2 planes measure the dispersive coordinate x and its corresponding angle θ, while the S1 and S2 planes measure the non-dispersive coordinate y and angle ϕ. Direct measurement of the y-coordinate over the more than 2 m length of the VDCs would be difficult, so this coordinate is inferred using the s-wire planes, which are tilted by an angle $\Gamma = 40^\circ$ with respect to the x-wires.

The position resolutions of the VDCs are approximately $\sigma_x \sim 50$ μm and $\sigma_y \sim 120$ μm, and the angular resolutions are $\sigma_\theta \sim 120$ μrad and $\sigma_\phi \sim 600$ μrad [Blo+98].

The next layer consists of timing counters, referred to as the dE and ToF planes [Blo+98]. Each plane contains 15 plastic scintillator paddles, with photomultiplier tubes (PMTs) attached to both ends—Philips XP2262B for the dE plane and XP2242B for the ToF plane. The paddle dimensions are 45 cm $\times$ 16 cm for the dE plane and 14 cm $\times$ 16 cm for the ToF plane. The dE paddles are 3 mm thick and made of NE102A, a widely used general-purpose plastic scintillator known for its high light yield and durability [Nuc70]. The ToF paddles are 1 cm thick and made of NE Pilot U, an ultra-fast scintillator with a short decay time of approximately 1.5 ns and high time resolution, well suited for precise time-of-flight measurements [Elj22]. Both planes serve to measure the energy loss of the particles and function as trigger counters. In this experiment, the coincidence of the timing signals from the ToF planes was used to define the trigger timing for SpekA.

At last, SpekA has gas Cherenkov counters for rejecting e^+/e^-, but these counters are not used for this experiment.

2.3.2 Spectrometer calibration method

The momentum calibration of the spectrometer SpekA is based on the kinematics of elastic scattering of electrons off stationary nuclei. In this process, both energy and momentum are conserved. Let an incident electron of energy E_b and momentum p_b scatter elastically from a target nucleus of mass M_t (at rest), resulting in a scattered electron with energy E' and momentum p' at an angle θ_m with respect to the incident direction.

Applying conservation of energy:

$$E_b + M_t = E' + E_t, \tag{2.3.2}$$

where E_t is the recoil energy of the target nucleus.

Similarly, conservation of momentum in vector form gives:

$$\vec{p_b} = \vec{p'} + \vec{p_t}, \tag{2.3.3}$$

where $\vec{p_t}$ is the recoil momentum of the target nucleus. Taking the magnitude squared of both sides and using the fact that the target is initially at rest, we obtain the invariant mass relation:

$$Q^2 = -q^2 = 4E_bE' \sin^2(\theta_m/2), \tag{2.3.4}$$

which is often used in high-energy scattering analysis, but for our calibration purpose, we seek the explicit expression for p' as a function of E_b, M_t, and θ_m.

From relativistic two-body kinematics, the scattered electron energy E' can be expressed as:

$$E' = \frac{E_b}{1 + \frac{E_b}{M_t}(1 - \cos\theta_m)}. \tag{2.3.5}$$

Then, the corresponding momentum is:

$$p_{\text{calc}} = \sqrt{E'^2 - m_e^2}, \tag{2.3.6}$$

where m_e is the electron rest mass.

In the actual experiment, the momentum p_m and scattering angle θ_m of the scattered electrons are measured by the spectrometer. The difference between the

calculated momentum p_{calc} and the measured momentum p_m is defined as:

$$\begin{aligned}\Delta p &= p_{\text{calc}} - p_m \\ &= \sqrt{\left(\frac{E_b}{1 + E_b/M_t(1-\cos\theta_m)}\right)^2 - m_e^2} - p_m.\end{aligned} \tag{2.3.7}$$

and used as a reference to calibrate the central momentum of SpekA. The quantities measured by the spectrometer are the scattering angle θ_m and the momentum p_m of the scattered electrons. The incident beam energy E_b is provided by MAMI's beam energy measurement or the nobel method of undulator interferometry, explained later.

The target materials used were ^{181}Ta and ^{12}C. The nuclear mass of ^{181}Ta is relatively large, so the effect of the scattering angle θ_m can be suppressed. In the case of ^{12}C, scattering peaks from each excited state are observed, so linear calibration can be performed from a single data set. This allows for the evaluation of the spectrometer's linearity over a wide energy range of approximately 16 MeV.

Figure 2.15 shows a photograph of the target used in the electron elastic scattering experiment.

The lithium target used for hypernuclei production has a physical target thickness of 45 mm in the z direction, which corresponds to the beam axis direction (Section 2.2.2). Five target foils were prepared to investigate the z-position dependence of Δp, with a spacing of 15 mm between each foil along the z axis. The target ladder was mounted on an automatic motorized stage movable in the x direction—perpendicular to the beam and defined in a left-handed coordinate system—allowing each foil to be irradiated one by one during the experiment. The y direction is defined opposite to gravity, and the full target control system is described in Section 2.2.2 and shown in Figure 2.16.

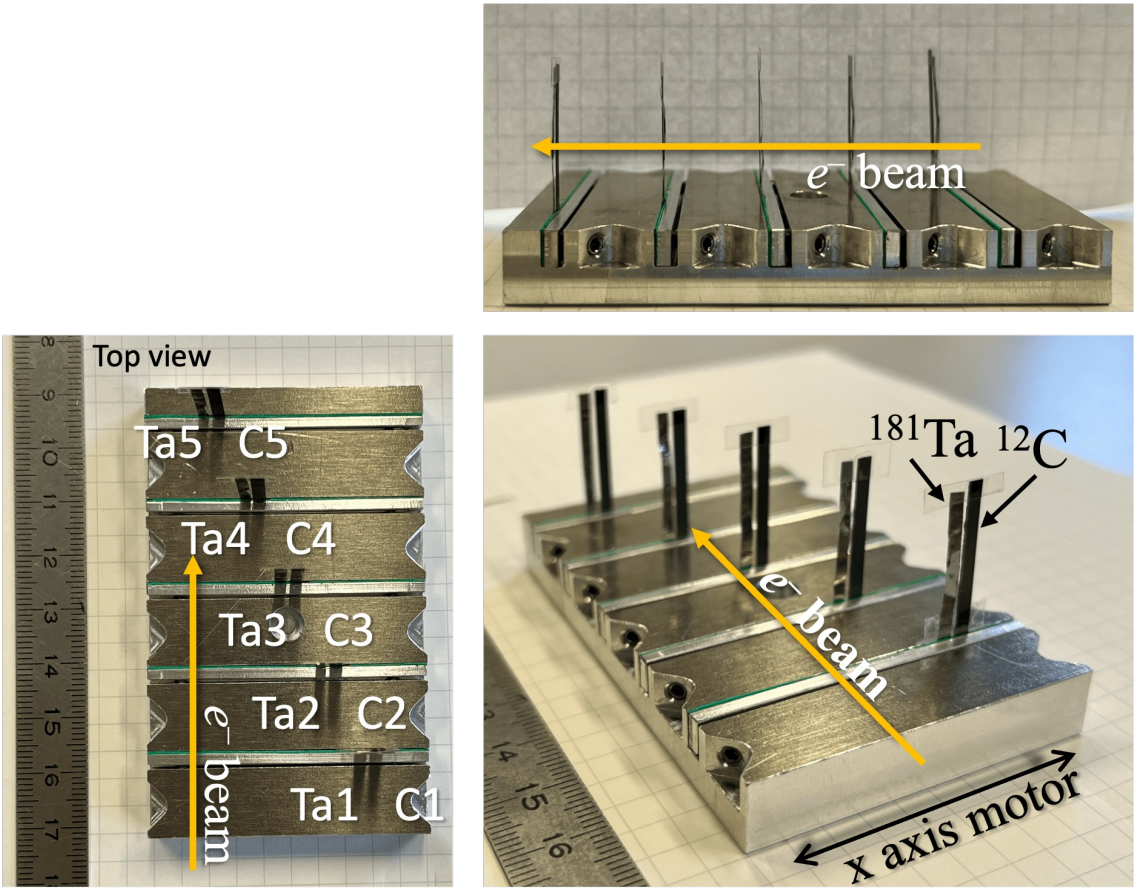

Figure 2.15: Targets for elastic electron scattering. Target foils with a width of approximately 1.5 mm and a height of approximately 15 mm were arranged in five layers at intervals of 15 mm in the z direction. In each layer, the left side viewed from the upstream side of the beam is ^{181}Ta, and the right is ^{12}C. Each x position was shifted so that the beam could be irradiated one by one, and the position was controlled using a theodolite so that the beam could be irradiated to the center. In the top view of the left figure, the foils are named Ta1, C1, Ta2, C2 ... from the upstream side of the beam.

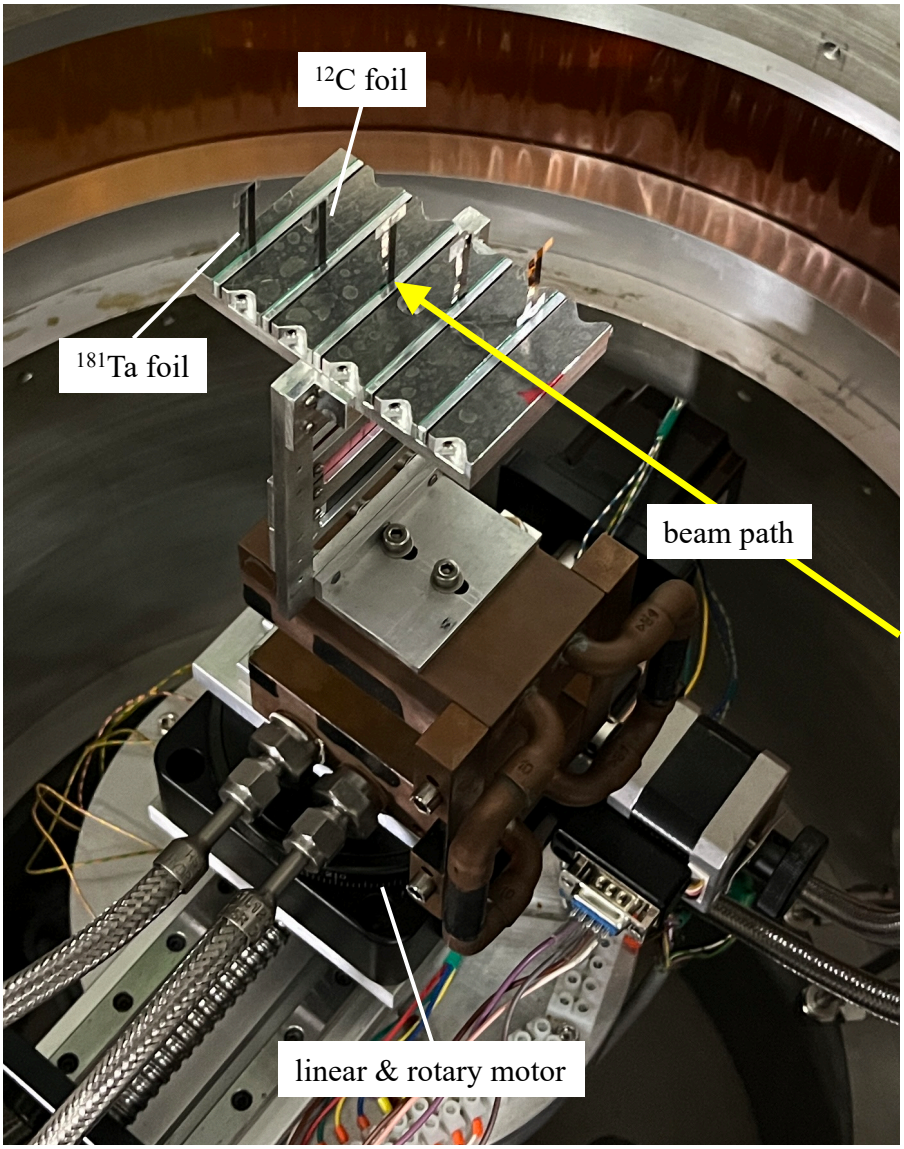

Figure 2.16: Picture of a mounted target for electron scattering. A photo of the inside of the target chamber. The target ladder was mounted on an automated motor that moved in the x-direction and along the rotation axis.

The ^{181}Ta target was a commercially available tantalum foil (Goodfellow Product Code: TA00-FL-000160) [Goo25b]. The foil size was determined by image analysis using a reference photo, with a pixel resolution of 468029 pixels per 2.5 cm. The mass was measured multiple times using a high-precision balance with a resolution of 10 μg. Using the density of tantalum $\rho = 16.654$ g/cm^3 from PDG [Gro22], the target thickness was calculated to be (7.39 ± 0.06) μm, which corresponds to (1.23 ± 0.01) mg/cm^2. The uncertainty reflects the variation in mass measurements. Monte Carlo simulations with GEANT4 [All+16] show that the energy loss uncertainty caused by a thickness error of 0.1 μm is approximately 0.25 keV, which is negligible in this analysis.

Similarly, the ^{12}C target was a carbon foil provided by Goodfellow (Product Code: C-00-FL-000108) [Goo25a]. The planar size was also determined via image analysis, and the thickness was measured using a micrometer with 0.1 μm resolution. The mass was measured using a 10 μg-precision scale, and the density was calculated from these measurements. The resulting areal density was (1.763 ± 0.028) g/cm^2, corresponding to a physical thickness of 128.0 μm. The uncertainty reflects the variation in both mass and thickness measurements. GEANT4 simulations show that a 0.1 g/cm^2 variation in the carbon target introduces an energy loss uncertainty of about 2 keV, which is also negligible.

Four types of incident electron beam energies are used: $180, 195, 210$, and 420 MeV. Ideally, the energy should be in the range close to the momentum of the decay pions ($100 - 150$ MeV/c); however, since the minimum energy that MAMI-C can supply to the A1 experimental hall is 180 MeV, we acquired several data points from 180 MeV and used the extrapolation method. In addition, we acquired several data points by changing the central momentum setting of the spectrometer for each beam energy so that the relative momentum (δp) of the elastic scattering peak covers the entire acceptance.

As mentioned above, the same method was used in the previous experiment to achieve a relative accuracy of 2×10^{-4}. In the present study, several important improvements were implemented to further reduce the systematic uncertainty in momentum calibration:

- In the previous study, only $^{4}_{\Lambda}$H was measured, so momentum calibration was required only over a limited portion of the spectrometer's momentum acceptance. In contrast, the present experiment aimed to measure both $^{4}_{\Lambda}$H and $^{3}_{\Lambda}$H, necessitating calibration over the full momentum acceptance. To achieve this, elastic scattering peaks were measured at multiple points across the acceptance by varying the central magnetic field setting of the spectrometer.

- To reduce the uncertainty associated with extrapolating the calibration curve, measurements were taken at five different beam energies instead of relying on a single energy point, as in the previous study.
- A unique z-position calibration was introduced by employing a multi-foil target and scanning the beam along the beam axis direction.
- Most notably, a new beam energy measurement technique using undulator interferometry was introduced. In the previous experiment, the beam energy was determined from the beam position and the RTM dipole magnetic field monitored by MAMI, which introduced a systematic uncertainty of approximately 160 keV. This directly affected the accuracy of the calculated momentum p_{calc} in Eq. 2.3.7, and ultimately dominated the total systematic uncertainty of 77 keV in the Λ binding energy.

As the analysis of the undulator-based measurement is still in progress, this thesis does not incorporate the results from that method in the subsequent analysis. Instead, a preliminary evaluation was carried out based on the conventional beam energy determination by MAMI. Nonetheless, the following section outlines the principle of the newly introduced technique—undulator synchrotron radiation interferometry—as a significant upgrade in this experiment.

Beam energy measurement by undulator's interference

A photo of the undulator used is shown in Figure 2.17. The coils are arranged one above the other, and the magnetic field is applied to them with alternating magnetic fields. When relativistic electrons pass between the upper and lower coils, the periodic deflection of the magnetic field causes the electrons' orbits to oscillate, generating synchrotron radiation.

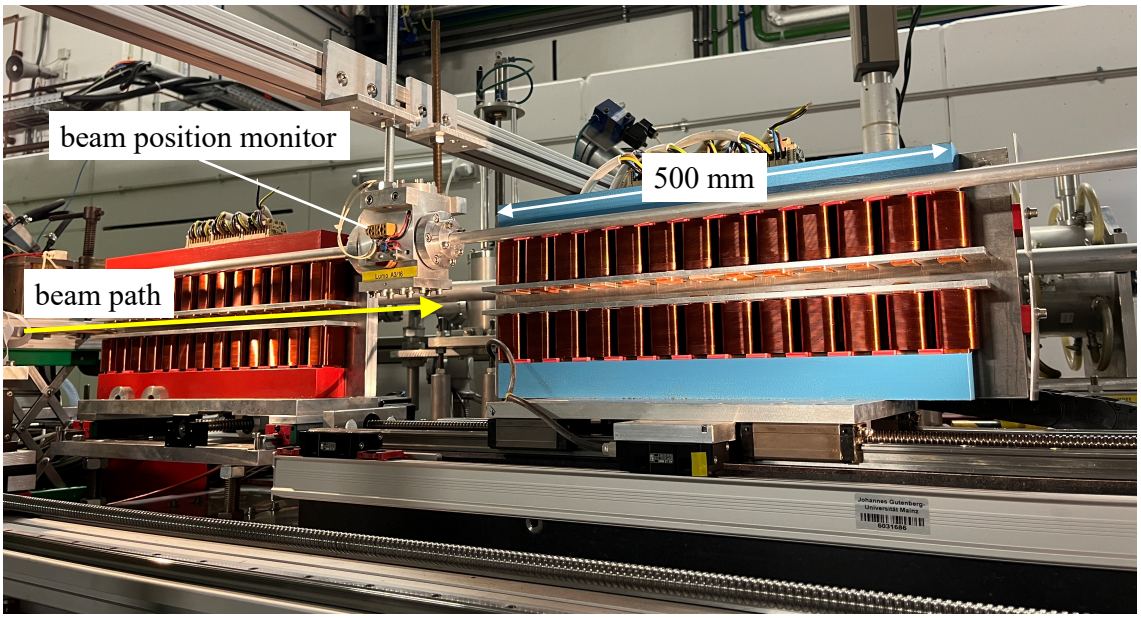

Figure 2.17: Picture of the undulators. The two undulators, red and blue, were installed on the beamline just after RTM3 (the photo shows them lowered from the beamline). A beam position monitor (XY monitor) is installed between the two undulators to measure the beam position.

Figure 2.18 shows a conceptual diagram of the beam energy measurement method using this undulator. Two undulators, S_1 and S_2, are placed at a distance d between them, and when an electron passes through them, synchrotron radiation T_1 and T_2 are generated from each undulator. Since the speed of the synchrotron radiation is faster than that of the electrons, the pulse generated by the upstream red undulator travels further.

The path difference between T_1 and T_2 is called Δ, and this quantity can be expressed as:

$$\Delta = \left(\frac{1}{\beta} - \cos\theta \right) d. \tag{2.3.8}$$

Here, $\beta = v/c$ is the normalized velocity of the electron, and θ is the observation angle. For ultra-relativistic electrons ($\gamma \gg 1$), the following approximations can

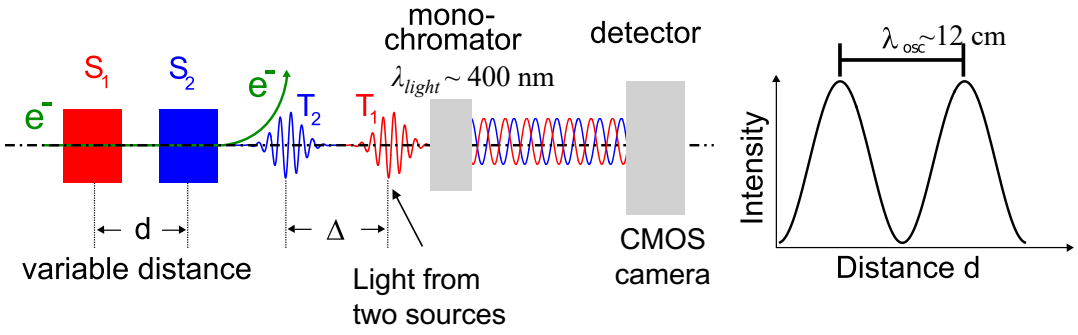

Figure 2.18: Principle of undulator interfeometry method [Kla+18]. Two undulators S_1 and S_2 are installed on the beamline, and when an electron beam passes between them, each undulator emits synchrotron radiation T_1 and T_2. At a certain wavelength of the interference light λ_{light}, the Lorentz factor of the electron is calculated by measuring the interference intensity while varying the distance d between the two undulators.

be used:

$$\frac{1}{\beta} \approx 1 + \frac{1}{2\gamma^2}, \qquad \cos\theta \approx 1 - \frac{\theta^2}{2}. \tag{2.3.9}$$

Substituting these into the expression for Δ gives:

$$\begin{aligned} \Delta &\approx \left(1 + \frac{1}{2\gamma^2} - \left(1 - \frac{\theta^2}{2}\right)\right) d \\ &= \left(\frac{1}{2\gamma^2} + \frac{\theta^2}{2}\right) d. \end{aligned} \tag{2.3.10}$$

Here, θ is the observation angle equivalent to the elevation angle. Thus, this path differenceΔ is a quantity that depends on the electron's Lorentz factor γ. The interference of the wave trains is obtained by Fourier analysis of the light using a monochromator. Finally, the interference intensity is measured using a pixel array CMOS camera detector. When this intensity is measured while changing the distance d between the undulators, the intensity of the interference light of a selected wavelength λ_{light} shows a periodic intensity change. The following equation holds between this oscillation period λ_{osc} and the selected wavelength of the interference light λ_{light}.

$$\begin{aligned} \frac{2\pi}{\lambda_{\text{osc}}} d &= \frac{2\pi}{\lambda_{\text{light}}} \Delta \\ \therefore\ \lambda_{\text{osc}} &= \frac{2\gamma^2 \lambda_{\text{light}}}{1 + \gamma^2 \theta^2} \end{aligned} \tag{2.3.11}$$

In case of $\theta = 0$,

$$\gamma = \sqrt{\frac{\lambda_{\text{osc}}}{2\lambda_{\text{light}}}}. \tag{2.3.12}$$

Therefore, the beam energy can be expressed as:

$$E_b = m_e c^2 \sqrt{\frac{\lambda_{\text{osc}}}{2\lambda_{\text{light}}}}. \tag{2.3.13}$$

In other words, the beam energy can be obtained by measuring the selected wavelength λ_{light} and the oscillation period λ_{osc} of the interference light intensity.

The two undulators were installed just after RTM3 and in front of the entrance to the X1 experimental hall. An optical spectroscopy system using gratings, dispersive lenses, and non-dispersive lenses was installed in the X1 hall to ensure that the appropriate elevation angle and wavelength measurement range of the interference light falls within the acceptance of the CMOS camera. Figure 2.19 shows a photo of the actual system.

In a proof-of-principle experiment of this method, it was demonstrated that the beam energy can be measured with a total error of $\Delta E/E \simeq 1.0 \times 10^{-4}$, which is about one-tenth of the error of conventional methods [Kla+18]. In a calibration experiment conducted in the spring of 2024, it was successful for the first time in combining the electron elastic scattering experiment and the beam energy measurement experiment using an undulator while switching the electron beam path.

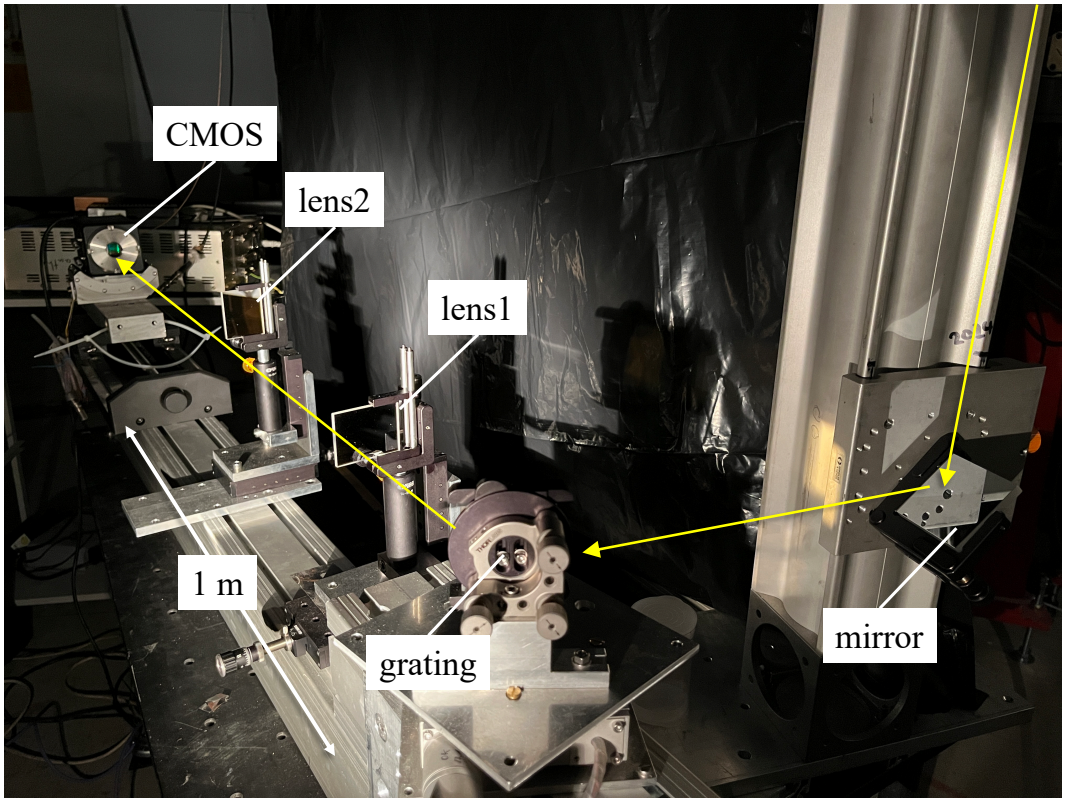

Figure 2.19: Picture of the optics spectrometer system in X1 hall. The interfering light was transported to the height of the optical spectrometer system using multiple mirrors, and the intensity was measured by a CMOS camera through two lenses. The yellow arrows indicate the path of the interfering light.

2.3.3 Kaon tagger spectrometer KAOS

At the very forward angle ($0°$) of the beam direction, a dedicated spectrometer called "KAOS" was installed to tag strangeness-produced events. KAOS was originally built at GSI in 1991 as a meson spectrometer for SIS (Schwer Ionen Synchrotron) [Sen+93]. It was brought to Mainz in 2007, and a completely new detector system was installed there [Ach10]. The schematic drawing of the KAOS is shown in Figure 2.20. KAOS is not a permanent part of the spectrometer system in the A1 hall, but is only installed when hypernuclear experiments are performed.

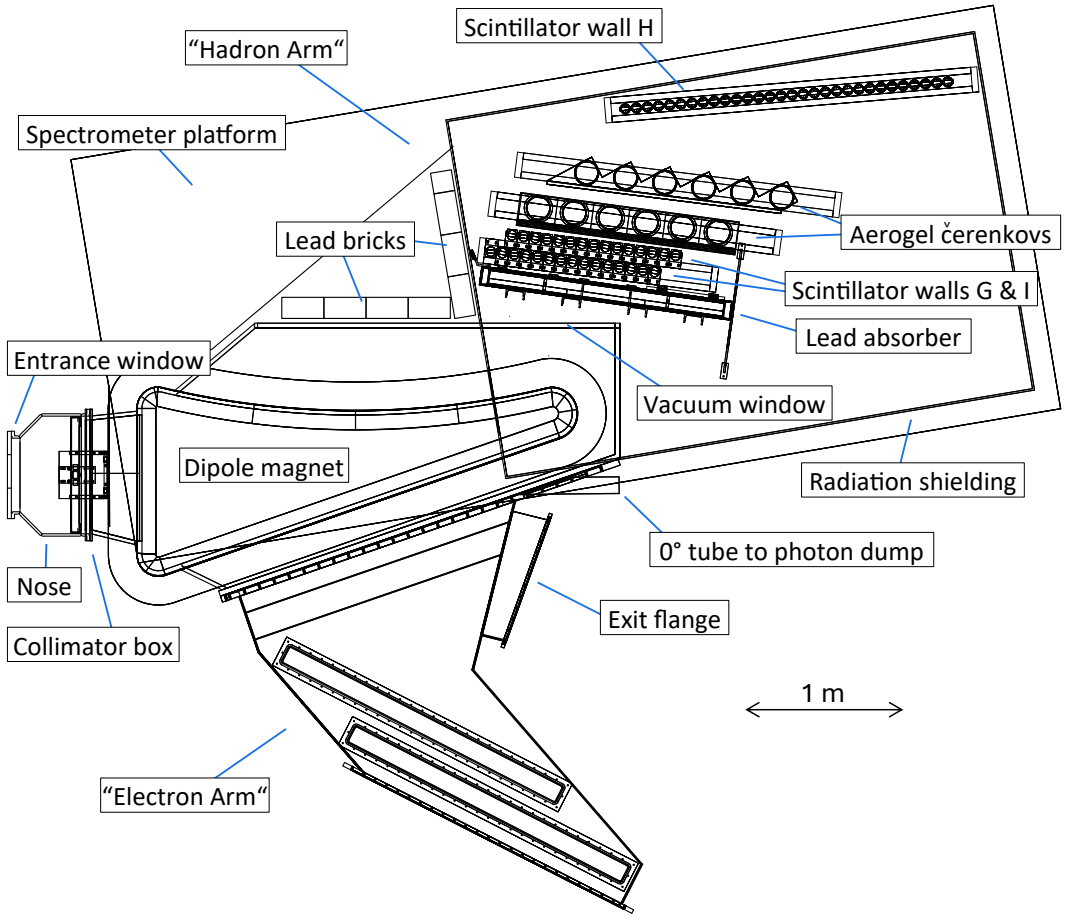

Figure 2.20: Schematic drawing of the KAOS spectrometer [Von24]. The K^+ entering from the entrance window on the left in the figure is bent toward the upper Hadron Arm. In this experiment, the Electron Arm and Aerogel Cherenkovs in the figure were not used.

The magnet-optical configuration of KAOS is straightforward, consisting of only one dipole. Charged K^+ has a lifetime of 12.3 ns, e.g., $c\tau = 3.7$ m. This dipole has a short central orbit length of only 5.3 m, which is much better suited for detecting K^+ than the SpekA, B, and C, which have orbit lengths of about 10 m. In addition, it is designed as an in-beamline spectrometer, so it can cover the 0° forward angle, where K^+ production is maximized.

The K^+ and other background particles, e^+, π^+, and protons entering through the left entrance window in Figure 2.20 are bent toward the upper hadron arm. Of the detectors in the figure, the three scintillator walls, G, I, and H, were used in this experiment. The Aerogel Cherenkov was not used in the analysis. Also, most of the electron beam irradiated to the target passes through the target and enters KAOS. In the same magnet, the electrons are bent towards the Electron Arm, where an exit beam pipe leads to the beam dump. The detectors (scintillation fibers) in the Electron Arm were removed and not used in the present experiment. Next to the exit flange is a 0° tube, which allows neutral particles such as γ-rays and neutrons to pass to a separate beam dump.

At the hadron arm exit of the dipole, lead blocks were placed to deal with the high detector counting rate due to a large amount of forward-angle background events, and a lead absorbing wall $10 - 12$ cm thick was placed. This wall has proven essential for suppressing the positron background [Nag15; Ess14]. This has almost deteriorated the momentum resolution of KAOS, which is now $\Delta p/p \sim 10^{-1}$ [Von24] from $\Delta p/p \sim 10^{-3}$ [Ach10].

Table 2.5 below shows the main parameters of KAOS.

Table 2.5: Properties of KAOS spectrometer [Ach10]

maximum momentum	2100 MeV
momentum acceptance	50%
solid angle acceptance	10.4 msr
dispersive angle acceptance	± 185 mrad
non-dispersive angle acceptance	± 14 mrad
length of central trajectory in the dipole magnet	5.3 m
momentum resolution	$\Delta p/p \sim 10^{-1}$ [Von24]

The absorbers installed on KAOS for radiation shielding

In order to detect the ${}^{3}_{\Lambda}$H in the momentum distribution of the final decay pions, it is necessary to reduce background events as much as possible. Due to the forward-angle design of KAOS, the spectrometer is closer to the beamline and the beam dump than the other A1 spectrometers. This required some shielding to keep radiation interference at a moderate level and limit the influx of radiation, including the large number of positrons coming from the beamline and neutrons from the beam dump.

Figure 2.21 shows a photograph of the protective absorber installed on KAOS. (a) shows a photograph of the hadron arm as seen from the beam dump side. In this experiment, two layers of 50 cm thick concrete blocks were placed behind KAOS (one layer is outside the photograph). This was installed to provide additional radiation shielding to the electron beam dump, which is a known source of background particles, especially neutrons. The block closer to KAOS also serves as the base for a dedicated photon beam dump. It was designed to capture uncharged particles coming from the 0° tube [Ess14].

The KAOS hadron arm is surrounded by a plastic wall containing boron, which absorbs neutrons. To provide additional protection, additional lead blocks were placed in the gap in the back wall facing the KAOS A1 beam dump.

Figure 2.21(b) shows the lead wall at the upstream end of the hadron arm. It is used to prevent positrons from entering the KAOS detector system. In previous

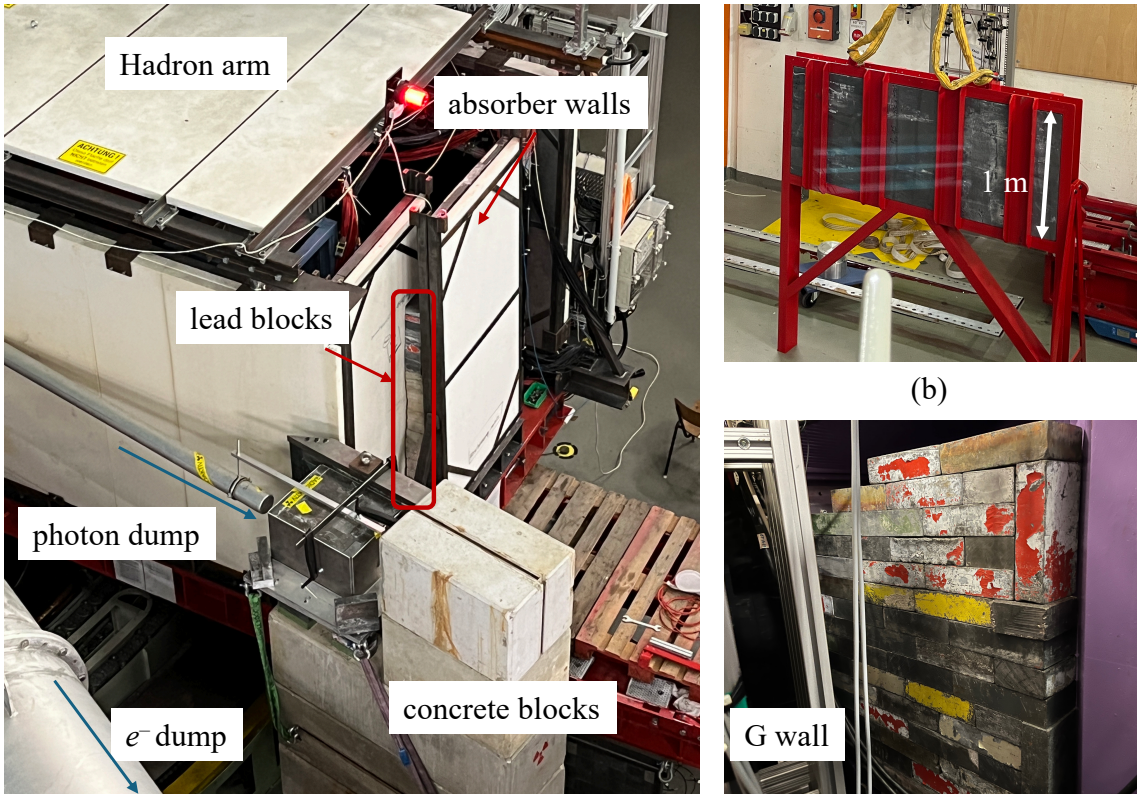

Figure 2.21: Picture of lead absorbers in KAOS. (a) A photograph of the Hadron arm is seen from the beam dump side. The concrete blocks that serve as the stand for the photon dump serve to suppress neutron background events caused by the e^- beam dump. The hadron arm is surrounded by an absorber containing boron, and lead blocks are also placed in the gaps in the wall. (b) The lead wall installed at the most upstream of the hadron arm. Its thickness is $10 - 12$ cm. (c) Lead blocks installed at the exit of the dipole on the hadron arm side. (b) and (c) were introduced to suppress positron background events.

studies, it was separated into three regions with different thicknesses to take into account the momentum-specific energy loss of K^+s. A thickness of 8 cm was chosen for the low momentum region, 10 cm for the center, and 12 cm for the high momentum end [Ess14]. However, as mentioned above, in the commissioning experiment in 2022, it was found that the count rate of the detector in the low momentum region was very high, so an additional 2 cm of lead was added to the thinnest section.

Figure 2.21(c) shows the lead blocks installed at the dipole exit on the hadron arm side. This was also added to suppress positrons in the low momentum region as much as possible based on the results of the commissioning experiment.

Furthermore, a large Kapton window [DuP] inside KAOS burst after the com-

missioning experiment, causing a vacuum leakage problem. This window needed to be replaced with a new window, and a solid aluminum plate was selected instead to improve reliability. This allowed the vacuum chamber to be successfully sealed, and 1 cm of aluminum was added to the total mass of the absorber.

Scintillator Walls G, I, and H

The G and I walls each consist of 15 scintillator paddles. Each paddle is made of BC408 plastic scintillator, with dimensions of $470^H \times 20^T \times 75^W$ mm^3. BC408 is a widely used polyvinyltoluene-based scintillator characterized by a fast decay time of 2.1 ns and high light output, making it suitable for timing measurements [Cry20]. Each paddle is read out from both the top and bottom ends using 2-inch photomultiplier tubes (PMTs), model R1828 by Hamamatsu Photonics. The PMTs are typically operated at a high voltage of approximately -2000 V supplied by a LeCroy 1440 HV power system [Nag15].

The G and I walls are installed adjacent to each other, just behind the lead wall, and are therefore the first detectors to be hit by particles. Their proximity to the 0° beam tube and the exit flange also subjects them to significant background radiation. To suppress background-induced single hits and enhance the identification of unphysical trajectories (i.e., double hits from non-target-originating particles), a double-wall configuration is employed [Nag15; Ess14].

During the KAOS commissioning run in 2022, the paddles located in the low-momentum region of the G and I walls exhibited hit rates $2-3$ times higher than those in the mid- to high-momentum regions. In particular, rates of several tens of counts per second were observed in the first paddle rows. This effect is attributed to residual positrons penetrating the lead wall, a phenomenon also reported in earlier experiments. Consequently, the first paddles of G and I were disabled to reduce background noise. The corresponding loss of acceptance can be compensated by operating at higher luminosity.

The H wall, installed approximately 1 m downstream of the G/I wall group, is the final detector in the KAOS setup. It consists of 30 larger paddles of size $580^H \times 20^T \times 70^W$ mm^3, made of the same BC408 material and read out by the same PMTs. Positioned near the focal plane of the spectrometer magnets, the H wall is less exposed to radiation compared to the G and I walls, allowing for stable operation and improved timing resolution. The spatial separation between the G/I and H walls permits time-of-flight (TOF) measurements.

KAOS determines particle momentum and TOF by identifying coincident hits between the G/I and H walls. In addition, energy loss (dE) information from

each paddle is recorded, enabling particle identification through combined TOF-dE analysis.

2.3.4 Data acquisition system

Trigger logic for KAOS

The coincidence of the three scintillator walls—G, I, and H—is used to generate the KAOS trigger signal for acquiring physical events. In order to reduce accidental background triggers, the paddle combinations among these walls were optimized in a previous experiment to reflect only physically possible hit patterns [Ess14].

Figure 2.22 shows the schematic diagram of the KAOS trigger logic. The readout signal from each photomultiplier tube (PMT) is split into two branches: one for time information via the Time-to-Digital Converter (TDC; GSI SU 1601), and one for charge information via the Analog-to-Digital Converter (ADC; LeCroy 1885F).

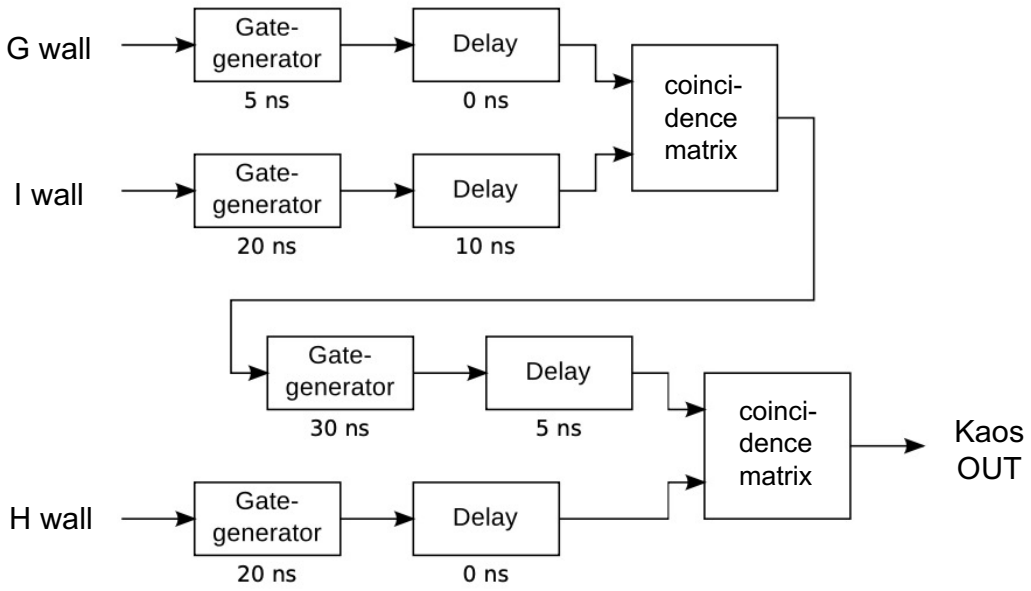

Figure 2.22: Diagram of the trigger logic of KAOS [Ess14] (modified).

In the TDC branch, the signal is first processed by constant fraction discriminators (CFDs; GSI CF 8105), then passed through a delay module (GSI DL 1610), and finally input into a logic module (VUPROM2), which incorporates a Xilinx Virtex-4 FPGA chip with 256 I/O channels. The logic firmware evaluates whether the observed hit combinations on the G and I walls are consistent with physical trajectories. If valid, it preselects the allowed combinations of hits on the H wall. In a second stage, the actual signal from the H wall is compared against the expected

pattern, thereby validating the event and minimizing the probability of random coincidences.

The output of this logic circuit, labeled “KAOS OUT”, generates the KAOS trigger signal, which is further processed in the global coincidence logic shared with SpekA (Section 2.3.4).

Meanwhile, the ADC branch is delayed using a separate delay module (GSI DP 1620) before being sent to the ADC for charge measurement.

Trigger logic for SpekA

Figure 2.23 shows a schematic diagram of SpekA trigger logic. In the SpekA spectrometer, the timing signal from each ToF paddle serves as the trigger for data acquisition. Similar to the KAOS setup, the signal is split into two branches: one for timing and one for charge measurement. The timing branch is processed by a leading-edge discriminator (LeCroy 4413), which generates a logic pulse. A logical AND is formed between the signals from both ends of the same ToF paddle, and the logical OR (SUM) of all ToF paddle signals produces the SpekA trigger.

The timing signals are digitized using a Time-to-Digital Converter (TDC; LeCroy 2228A), while the pulse height information is recorded by an Analog-to-Digital Converter (ADC; LeCroy 2249A). Additionally, the timing signal from the vertical drift chamber (VDC) is recorded by a separate TDC module (LeCroy 4291B).

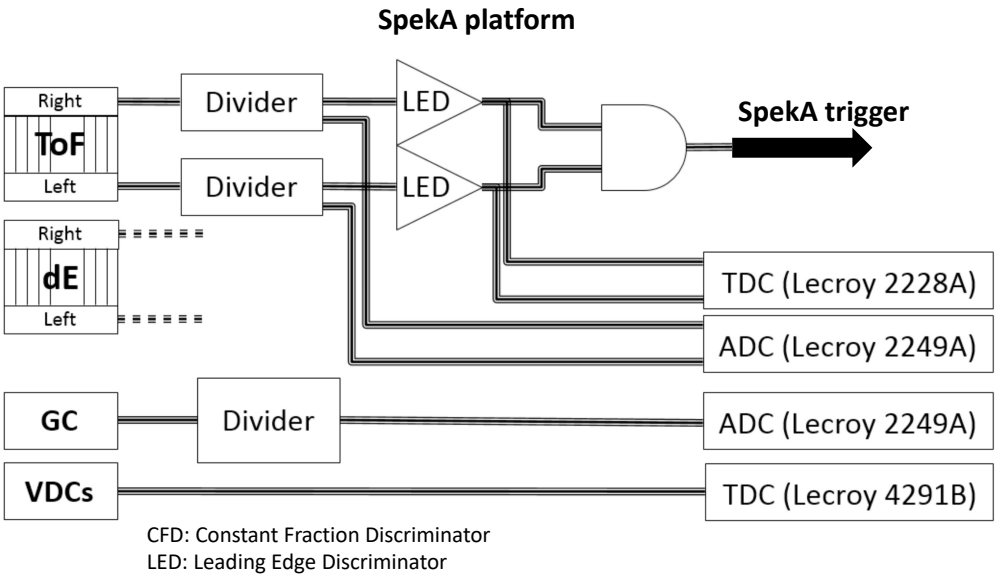

Figure 2.23: Diagram of the trigger logic of SpekA [Nag15] (modified).

DAQ system for coincidence events

Figure 2.24 shows a schematic diagram of coincidence logic. The complete logic diagram is shown in Appendix A.

The trigger signals from SpekA and SpekC were sent to the KAOS platform and logically combined with the KAOS trigger to form a coincidence condition. The logic condition was defined as $(\text{SpekA} \vee \text{SpekC}) \wedge \text{KAOS}$. Although data from SpekC were also recorded, they were not used in the present analysis. When this condition was satisfied and no busy signal was present from the data acquisition PC, a coincidence trigger was issued.

This coincidence signal was fed to the event builder module, which merged the data from all detectors and assigned a unique event number. The same signal was also used to generate the ADC gate, TDC stop, and arming signals for modules such as the LeCroy 1875.

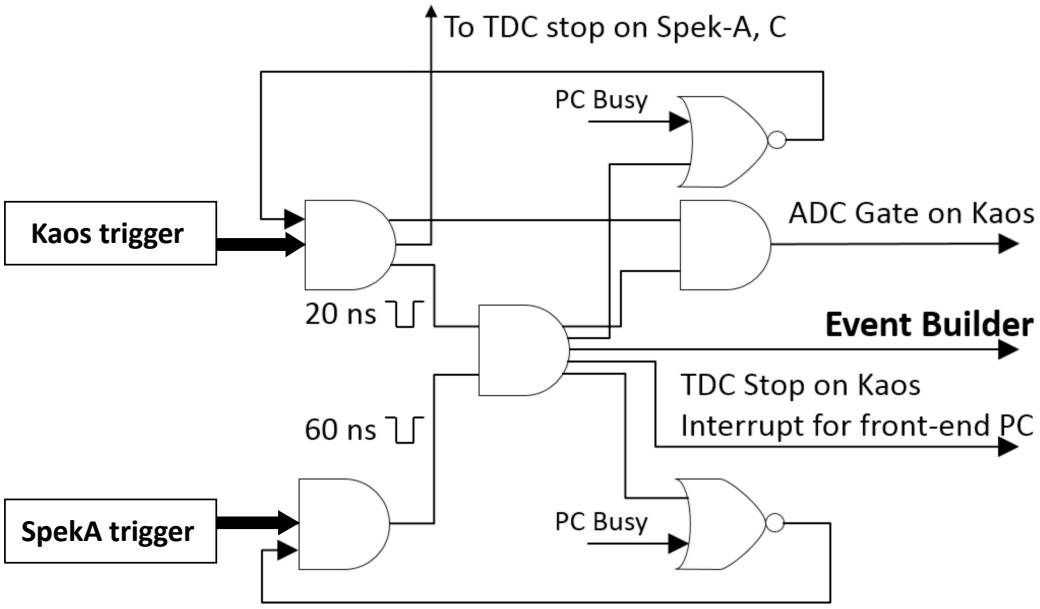

Figure 2.24: Diagram of the trigger logic of SpekA and KAOS coincidence [Nag15] (modified).

2.3.5 Target design

Finally, the newly developed target system for the present experiment is described. To observe rare events such as ${}^{3}_{\Lambda}$H, it is essential to suppress background contributions as much as possible. For this purpose, it is important to select target materials with low atomic numbers. Such materials offer fewer hyperfragment candidates and reduce background events originating from electromagnetic interactions.

Therefore, as previously mentioned, ${}^{\mathrm{nat}}$Li was chosen as the target material in this study, instead of ^{9}Be used in earlier experiments. However, lithium has a lower density and a lower melting point compared to beryllium. To overcome these disadvantages, a completely new target system had to be designed.

Concept of the new lithium target

Here, briefly introduce the beryllium target in the previous study to explain the new target system. Figure 2.25 shows the layout of the spectrometers and target: beryllium target in the 2014 experiment and lithium target in 2022.

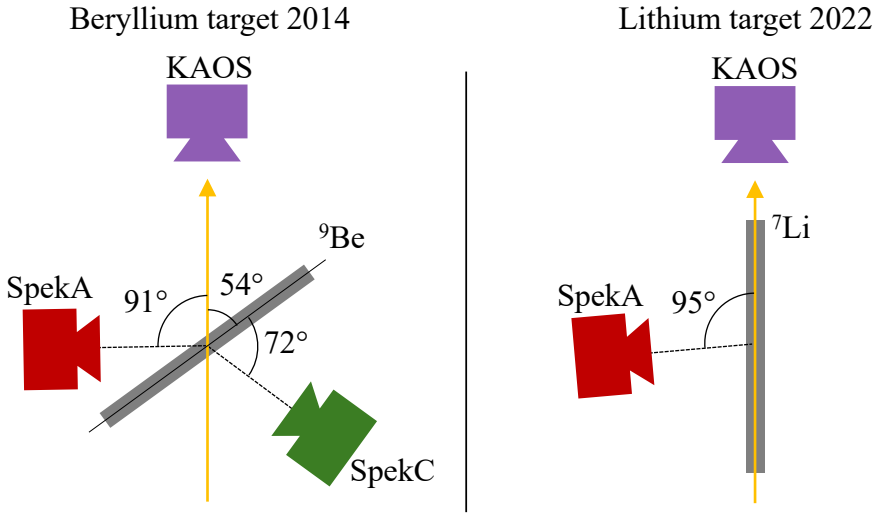

Figure 2.25: Comparison of the target designs used in 2014 (beryllium, left) and 2022 (lithium, right). Note that the scale, including target thickness and length, is not accurate.

The beryllium target plate was installed at an angle of 54° with respect to the beam axis. In 2014, both SpekA and SpekC were used to measure the momentum of decay π^-. Spek C was placed at $54^\circ + 72^\circ = 126^\circ$ from the beam axis to minimize the energy straggling effect of decay pions. SpekA was placed at 91° because part of the system interferes with KAOS. Two target material thicknesses were used:

$X = 23$ mg/cm^2 and $X = 47$ mg/cm^2. The beam current was set to $I = 43$ μA for the thin target and $I = 26$ μA for the thick target.

The luminosity L for a beryllium target can be calculated as follows:

$$\begin{aligned} L &= \frac{N_A}{m_{\text{mol}}} \cdot X \cdot I \\ L_{^9\text{Be}_{\text{thin}}} &= 5.10 \times 10^{35} \ /\text{cm}^2 \\ L_{^9\text{Be}_{\text{thick}}} &= 6.30 \times 10^{35} \ /\text{cm}^2 \end{aligned} \tag{2.3.14}$$

Here, Avogadro number $N_A = 6.022 \times 10^{23}$ mol^{-1}, the molar mass of beryllium $m_{\text{mol}} = 9.012$ g/mol are used. X is multiplied by a factor $1/\sin 54^\circ$ to estimate the effective target thickness. The beam current is converted to electrons per second 1 μA $= 6.24 \times 10^{12} e^-$/s.

The design of the new lithium target is completely different. In previous studies, relatively high beam current values were used, which caused technical problems such as increased radiation levels in the experimental hall, high background rates, and frequent crashes of surrounding equipment. To avoid this, it was necessary to enable steady data acquisition at low beam currents. Furthermore, since the density of lithium is small, $\rho = 0.534$ g/cm^3, we considered installing it at 0° in the beam direction to ensure maximum luminosity. To maximize the acceptance of the decay-pion spectrometer, the target length was extended to $l = 45$ mm, which corresponds to the coverage of approximately 95% of the spectrometer's acceptance and results in an areal density of $X = 2.4$ g/cm^2.

During the commissioning experiment in 2022, it was found that a beam current of 1.1 μA is the maximum that the detector can handle adequately. Above that, dead-time problems and accidental background events become dominant. As a result, the luminosity for the lithium target is calculated as follows:

$$L_{^7\text{Li}} = 8.47 \times 10^{35}/\text{cm}^2 \tag{2.3.15}$$

This design easily achieves luminosity exceeding that of beryllium while reducing the beam current by a factor of about $20-40$. The main advantage of the new design is the reduced beam intensity requirement. Fewer radiation sources suppress false trigger events in all spectrometer scintillators and reduce accidental events. In addition, the accelerator operation becomes more stable.

The horizontal (x-direction) width should be as narrow as possible to reduce the effects of energy straggling of decay π^-. On the other hand, it must be consid-

ered that a certain amount of electrons will be lost due to the Gaussian intensity distribution of the electron beam. For this dimension, the width of the lithium was chosen to be as thin as 0.75 mm. Monte Carlo simulations have confirmed that with this thickness, the most probable value of energy loss for decay π^- is approximately 20 keV, and the peak broadening due to energy straggling is about 18 keV (Section 3.6.1), representing a small and quantifiable part of the total momentum resolution ($\sim$ 70 keV/c). The beam size has been measured to be $\sigma \sim 0.3$ mm, and under this condition, the fraction of electrons passing through the target is estimated to be 78.9%. This transmission fraction is taken into account in the luminosity calculation shown in Eq. 2.3.15. This results in a larger geometric target thickness for SpekA through which the pions pass, but due to the low density of lithium, the material thickness is about the same as the previous beryllium target, about 20 mg/cm^2.

Mounting a lithium target composed of unstable material

Lithium is a chemically unstable material that reacts readily with oxygen, nitrogen, and moisture in the ambient air, making it difficult to handle as a target. To mitigate these risks during installation, the target chamber was continuously purged with argon gas, and a vacuum level of 10^{-5} mbar was maintained throughout the experiment.

Another critical concern is lithium's low melting point of 180 °C. Energy deposition from the beam can raise the target temperature significantly. To prevent thermal damage, a custom cooling frame was developed, incorporating water-cooled copper tubing.

Figure 2.26 presents photographs of the installed lithium target.

As shown on the left, the lithium plate is clamped into a copper frame using a copper holder. To facilitate temperature monitoring, half of the holder surface is painted black, allowing its orientation to be uniquely identified by a thermal camera, as described later. A cooling pipe connects the upper and lower base plates of the frame, enabling water circulation for effective heat removal from both ends. During beamtime, the cooling system operated at 5 °C using a water-isopropanol mixture. Mounted atop the copper frame is the standard A1 target ladder, which holds an Al_2O_3 screen for beam alignment and a carbon target for calibration. The entire system is actuated by two stepper motors—one for rotation and one for linear translation (Fig. 2.26, right).

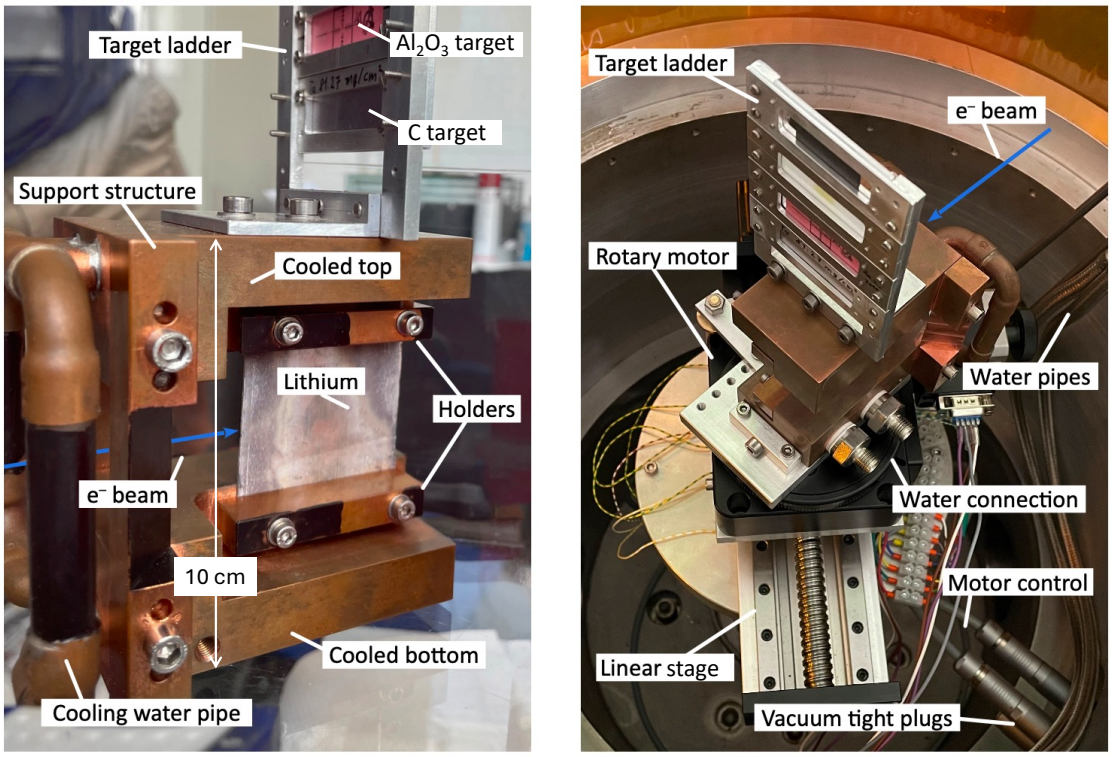

Figure 2.26: The lithium target mounted in the target chamber with a dedicated copper frame [Von24] (modified). Left: Close-up view of the frame and target holder. Right: View from above showing the complete assembly in the chamber.

Ensuring alignment of the beam with the lithium target

Due to the elongated and narrow geometry of the lithium target along the beam axis, precise alignment is essential to ensure the beam consistently passes through its center during data acquisition.

In the commissioning run, a thermal camera was employed to monitor temperature fluctuations in real time and prevent target melting. Details of the thermal monitoring setup can be found in Ref. [Von24]. Figure 2.27 shows a sample thermal image acquired during beam irradiation.

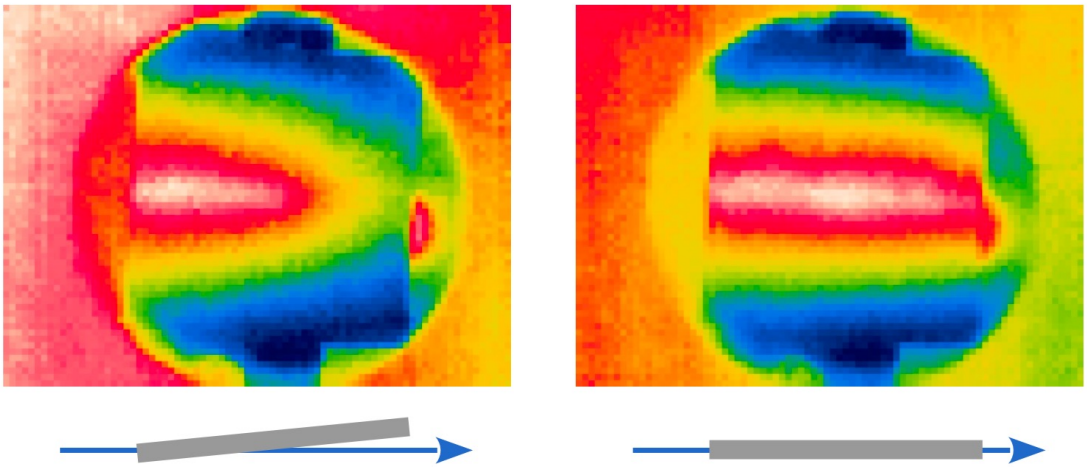

Figure 2.27: Thermal image of the lithium target [Von+22]. The left image shows that the beam is irradiating a part of the target. The right image shows the beam penetrating all the way to the end of the target. At the bottom, a conceptual diagram showing the target and beam positions from above is displayed to make each situation easier to understand. The maximum temperature was 28 °C when irradiated with a 1.5 GeV electron beam at 2 μA.

Below each thermal image, the corresponding beam path (indicated by a blue arrow) and target position are shown. In the left image, one can see that the target was not properly aligned, and only part of it was penetrated. In the right image, the beam penetrates all the way to the end of the target. In this test, a 1.5 GeV electron beam was irradiated at 2 μA, and it was confirmed that the maximum temperature reached 28 °C, which is above room temperature [Von+22].

In addition to monitoring beam penetration with a thermal camera, the single hit rate of each spectrometer was monitored throughout data acquisition. Figure 2.28 shows the target placement position and angle and the spectrometer single hit rate.

The target frame was placed on movable stages that could move in two directions, rotation and linear, as shown in the right figure of Figure 2.26. The rotary stage could be controlled at $1^\circ/10,000$ steps, and the linear stage could be controlled at 4 mm$/10,000$ steps, and they were remotely controlled. During the experiment, the single rate was constantly monitored, and the scan of Figure 2.28 was repeated, especially when the accelerator or beam conditions changed, and the movable stages were set to always maximize the single rate (Figure 2.29).

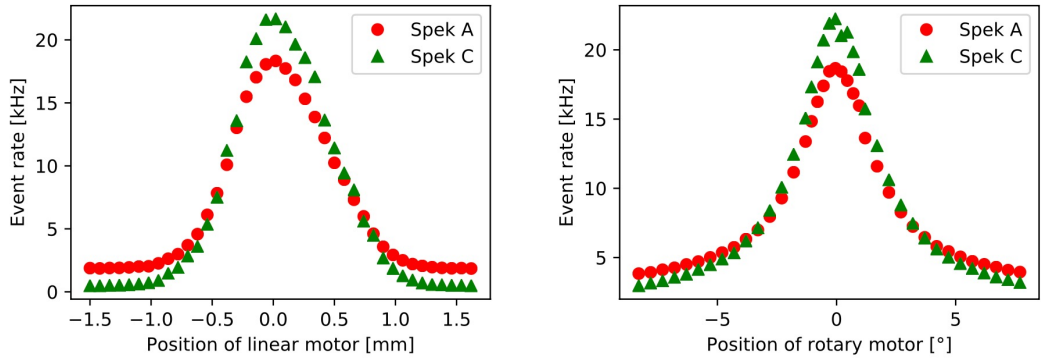

Figure 2.28: Spectrometer single hit rate vs. target placement position and angle [Von+22]. The red dots indicate SpekA and the green dots indicate SpekC. This scan shows that the electron beam intensity distribution is Gaussian.

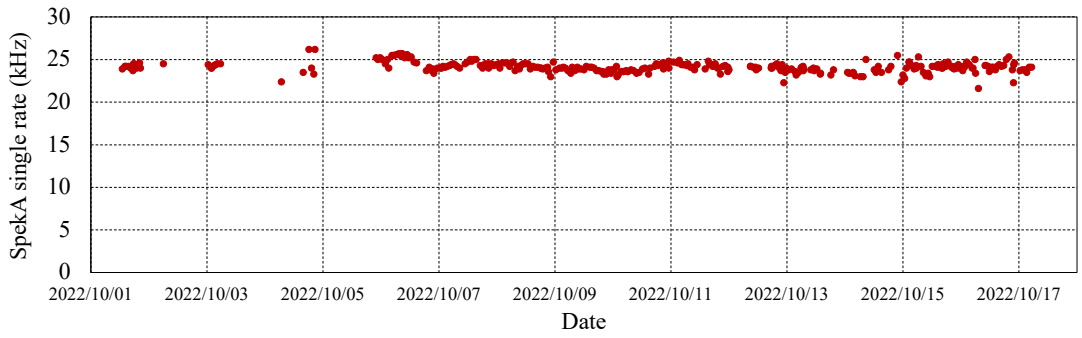

Figure 2.29: SpekA single hit rate during physics data taking. At beam currents of 1.1 μA, the single rate of SpekA was constant at approximately 24 kHz.

2.4 Summary of the experiment

There were three beamtime sessions in total: 1) commissioning from July to early August 2022, 2) physics data collection from September to October 2022, and 3) electron elastic scattering and undulator beam calibration experiments for spectrometer calibration from March to May 2024. This chapter summarizes the purpose of each beamtime and the data actually acquired.

2.4.1 Commissioning beamtime

The first beam time with the full experimental setup, including KAOS, was conducted from July 11 to August 1, 2022. The main objectives were: (1) to establish proper coincidence timing between SpekA and KAOS, and (2) to verify the operation of the detectors installed in KAOS.

For objective (1), the flight-time offset between the spectrometers was estimated based on the path length and momentum of the particles inside each spectrometer. The trigger timing was then adjusted at the hardware level by modifying the cable lengths accordingly. Figure 2.30 shows the final coincidence timing distribution between KAOS and SpekA.

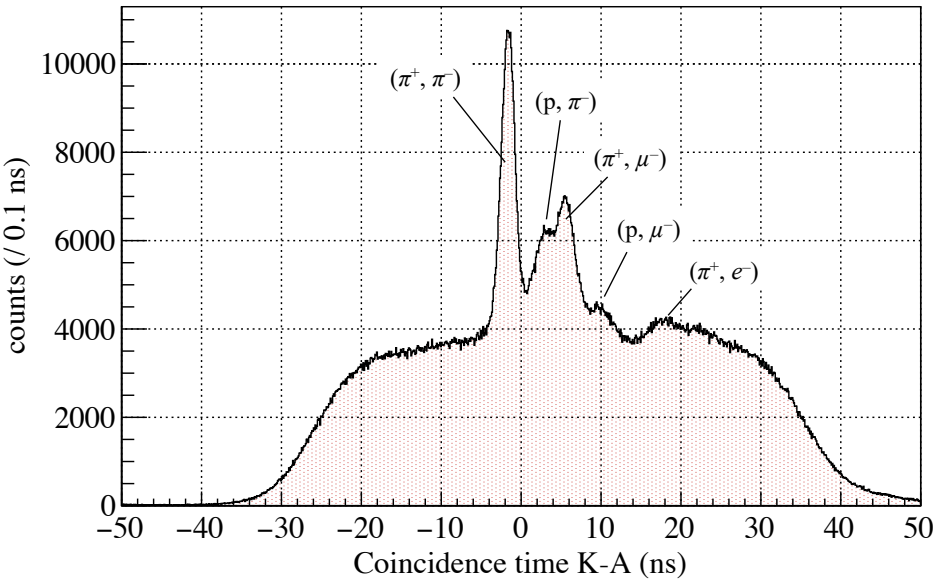

Figure 2.30: Coincidence time between KAOS and SpekA. The main peak corresponding to (π^+, π^-) events, and other specific peaks are labeled. The interested events, (K^+, π^-) coincidence peak is in between (π^+, π^-) and (p, π^-) peak. However, it is not visible in this figure.

The main peak is the (π^+, π^-) coincidence event. It is located almost in the center within the gate, and there are accidental coincidence events of 15 ns or more on both shoulders. Each of the other peaks is also labeled with the particle combination of the corresponding event. The interested (K^+, π^-) coincidence event exists between the (π^+, π^-) and (p, π^-) peaks, but it is not visible in this figure because it has few statistics compared to the π^+ event.

The width of the main $(\text{KAOS}, \text{SpekA}) = (\pi^+, \pi^-)$ coincidence peak was measured to be $\sigma = 0.61$ ns. The coincidence time resolution determined by the ToF trigger counters in SpekA is 1.2 ns (FWHM) [Blo+98], corresponding to $\sigma \sim 0.51$ ns. Considering that the time resolution of each paddle in the KAOS trigger counters (G, I, and H walls) is in the range of $0.1 - 0.2$ ns, the observed width is consistent with expectations.

Regarding objective (2), several scans were conducted on the high voltage ap-

plied to the PMTs of each detector, the digital conversion thresholds, and other parameters to determine their optimal settings. The main focus during this phase was the beam current. Figure 2.31 shows the results of the rate study for the spectrometer.

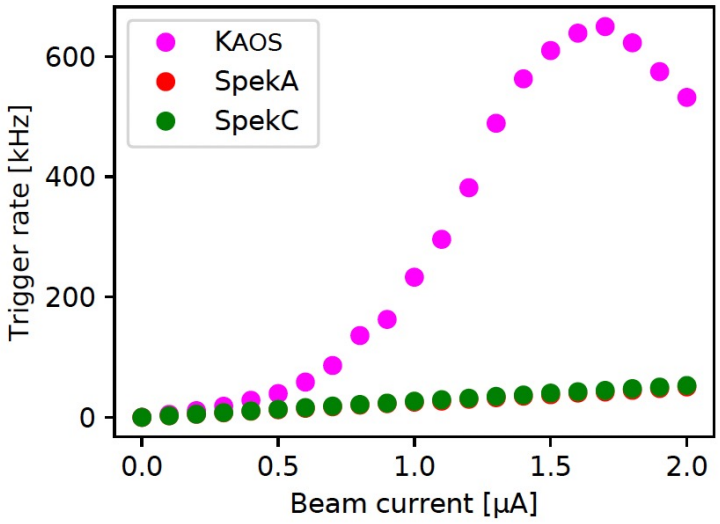

Figure 2.31: Beam current dependence of the spectrometer single rate [Von+22]. SpekA and SpekC overlap because they have almost the same rate. In KAOS, the rate peaks at about 1.5 μA, and then decreases due to dead time.

The figure records the electron beam current and the single hit rate of each spectrometer. SpekC, shown by the green dot, and SpekA, shown by the red dot, have almost the same value compared to SpekC, so they overlap. These two spectrometers show a linear dependence in this current region. In the case of KAOS, shown in pink, the rate of increase is remarkable, peaking at 1.5 μA. After that, it can be seen that it decreases due to the effect of the dead time of the KAOS trigger. Therefore, we evaluated the (π^+, π^-) event rate and the signal-to-noise ratio between 200 nA to 1.5 μA, and finally decided to collect data at 500 nA.

2.4.2 Physics data taking

The second beamtime was used to acquire physics data under the setup conditions determined during the commissioning process. The beamtime started on September 16th, 2022. There was an interruption on the September 24th for MAMI repairs. The beamtime resumed on September 30th, and ran until October 17th, 2022.

Beam current scans were performed again during the initial days of this beamtime. As described in Section 2.3.3, the scintillator paddles G0, I0, and H0—located in the low-momentum region of the KAOS spectrometer—were turned off to

optimize the signal-to-noise ratio. These scans confirmed that data quality comparable to that achieved at 500 nA during the commissioning run could be maintained even at a beam current of 1.1 μA. Accordingly, most of the data in this beamtime were acquired at 1.1 μA.

A summary of the data volumes used in the analysis, including the production run from the end of the commissioning experiment, is provided in Table 2.6.

Table 2.6: Summary of data amount from physics run.

Beam current (nA)	Run time (h)	Coulomb charge (C)	$\int Ldt$ (fb^{-1})
500	9.26	0.017	12.83
600	3.07	0.007	5.11
700	10.83	0.027	21.01
800	9.45	0.027	20.97
900	18.09	0.059	45.13
1000	10.26	0.037	28.43
1100	213.16	0.844	649.97
1200	13.07	0.056	43.49
total	287.19	1.074	826.94

2.4.3 Spectrometer calibration

The final beamtime was used to collect data for momentum calibration of the decay π^- spectrometer SpekA. As mentioned above, the electron elastic scattering peak is measured using ^{181}Ta target and ^{12}C target. In this experiment, a beam energy measurement experiment using undulator interferometry was also carried out in parallel to measure the beam energy with higher precision.

To determine the kinematic setup of the experiment, the differential cross section of the electron elastic scattering event was calculated. First, the Rutherford differential cross section is given by

$$\left(\frac{d\sigma}{d\Omega}\right)_{\mathrm{R}} = \frac{(Z_1 Z_2 e^2)^2}{16 E_1^2 \sin^4(\Theta/2)}, \tag{2.4.1}$$

where Z_1 is the charge of the incident electron (e^-), Z_2 is the charge of the target nucleus, E_1 is the energy of the incident electron (excluding its rest mass), and Θ is the scattering angle in the laboratory frame. Next, the Mott differential cross section is given by

$$\left(\frac{d\sigma}{d\Omega}\right)_{\mathrm{M}} = \left(\frac{d\sigma}{d\Omega}\right)_{\mathrm{R}} \cdot \left(1 - \beta_{\mathrm{CM}}^2 \sin^2(\Theta/2)\right), \tag{2.4.2}$$

where β_{CM}^2 is the relative velocity of the electron in Center-of-Mass frame. Finally, calculate the correction term that depends on the scattering wave number (q), taking into account the nuclear density distribution $(\rho(r))$.

$$F(q) = \frac{\int \rho(r) \frac{\sin(qr)}{qr} \cdot 4\pi r^2 dr}{\int \rho(r) \cdot 4\pi r^2 dr} \tag{2.4.3}$$

Here, r is the distance from the center of the nucleus. Therefore, the elastic scattering cross section σ_e can be calculated using the following formula.

$$\left(\frac{d\sigma}{d\Omega}\right)_{e} = \left(\frac{d\sigma}{d\Omega}\right)_{\mathrm{M}} \cdot F(q)^2 \tag{2.4.4}$$

Figure 2.33 shows the result of equation 2.4.4. The figure shows the angular dependence of the cross-section for each incident beam energy E_0 for the ^{181}Ta target (top) and the ^{12}C target (bottom). Depending on the installation angle of the spectrometer, the scattering probability may drop by several orders of magnitude locally. From the results of Figure 2.33, the installation angle of the spectrometer was determined to be 54° (black line in the figure), which is within the capable

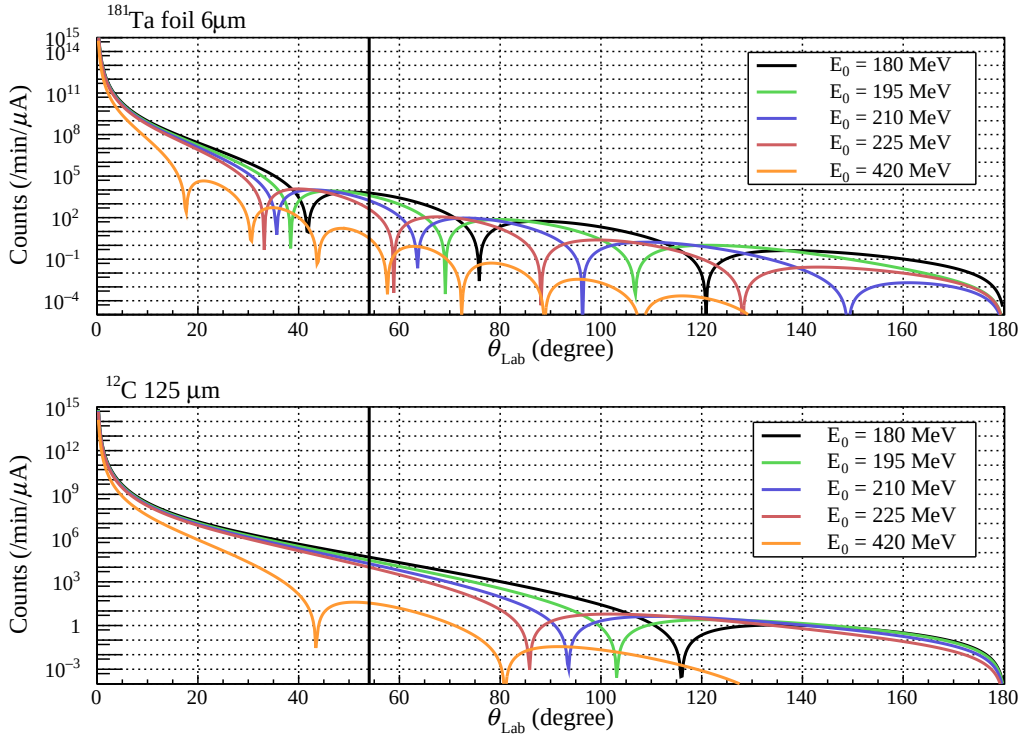

Figure 2.32: Angle dependence of electron elastic scattering cross-section. The top panel corresponds to the ^{181}Ta target case, while the bottom panel is the ^{12}C target.

range and allows a reasonable number of events to be obtained.

Figure 2.33 shows the image of the relative positions of the target and the spectrometer. The target was placed at $90°$ relative to the beam, and SpekA was placed at $54°$. The target chamber and the spectrometer were not connected by a vacuum extension pipe. Therefore, between the target and the spectrometer, there was a Kapton target chamber window with a thickness of 127 μm, an air layer of approximately 10 cm, and a Kapton spectrometer entrance window with a thickness of 127 μm. The effect of energy losses in these materials will be taken into account later in the energy calibration.

Experiments were conducted with this setup. Four beam energies E_b were used: $180, 195, 210$, and 420 MeV. As shown in Figure 2.2, in MAMI, the energy can be increased by 15 MeV per revolution with each increase in rotation number, so the energies were selected in 15 MeV increments from the minimum energy of 180 MeV. Data for 420 MeV were also acquired to ensure a more linear fit. Several central momenta $p_{\text{cent.}}$ were set for each beam energy E_b. The momentum peaks of decay π^-s of $^3_\Lambda$H and $^4_\Lambda$H predicted in Table 2.2 appear at the relative momentum $\delta p = -2.6\%$, 13.7%, respectively, at $p_{\text{cent.}} = 122.0$ MeV/c. The central momentum $p_{\text{cent.}}$ was selected so that the peaks of elastic electron scattering cover this region. The

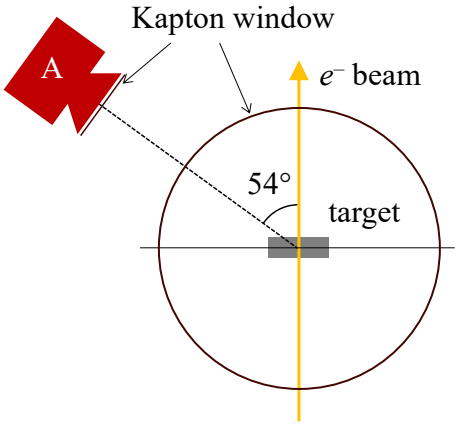

Figure 2.33: Geometrical image of the calibration experiment. The actual distance and size are not taken into consideration. The target is placed at $90°$ to the beam, and SpekA is placed at $54°$. Between the target and the spectrometer, there are a Kapton target chamber window, an air gap of approximately 10 cm, and a Kapton spectrometer entrance window.

targets were 10 patterns (Figure 2.15) of Ta1 - 5, C1 - 5, and five z positions were acquired for each target. The runtime was 15 minutes for ^{181}Ta and 30 minutes for ^{12}C per setup. For the data at $E_b = 420$ MeV, the cross-section is extremely small, so data was collected only on the centrally located Ta3 and C3. The run time is also long, 120 minutes each.

Table 2.7 shows a summary of the acquired data set.

In this experiment, beam energy measurements were performed in parallel using the undulator. Since constant measurements are important, beam energy measurements were performed once for every $2-3$ sets of central momentum $p_{\text{cent.}}$. As explained in Section 2.3.2, the undulator was installed at the exit of RTM3, and the optical system was installed in the X1 hall, so the beam was supplied to different locations for the elastic scattering experiment and the beam energy measurement. Therefore, the beamline was switched every time between the elastic scattering experiment and the beam energy measurement. Although this was the first attempt at beamtime management of two halls, it was successfully done.

Since the undulator-based beam energy measurement is only effective for beam energies below approximately 220 MeV, the conventional MAMI method was used for the 420 MeV dataset. As the analysis of the undulator data is still ongoing, the present work adopts a preliminary momentum calibration based solely on the 420 MeV elastic scattering data and the beam energy determined by the MAMI measurement.

Table 2.7: Summary of data sets for spectrometer calibration. The incident beam energy E_b, central momentum $p_{\text{cent.}}$, the predicted relative position δp of the elastic scattering peak for a ^{181}Ta target, and the target used are shown.

E_b (MeV)	$p_{\text{cent.}}$ (MeV/c)	δp (%)	Target
180	164.7	14.4	Ta1 - 5 & C1 - 5
	167.4	12.6	Ta1 - 5 & C1 - 5
	192.6	-2.1	Ta1 - 5 & C1 - 5
	194.4	-3.0	Ta1 - 5 & C2 - 4
195	179.0	14.1	Ta1 - 5 & C1 - 5
	195.0	4.7	Ta1 - 5 & C1 - 5
	208.3	-1.9	Ta2 - 3 & C1 - 5
210	193.2	13.8	Ta1 - 5 & C1 -5
	196.4	12.0	Ta1 - 5 & C1 -5
	201.6	2.0	Ta1 - 5 & C1 -5
	221.6	-0.8	Ta1 - 5 & C1 -5
	224.7	-2.1	Ta1 - 5 & C1 -5
420	387.7	13.4	Ta3 & C3
	445.2	-1.3	Ta3 & C3

Chapter 3

Analysis

This chapter provides a detailed description of the analysis. First, the analysis procedure is explained (Section 3.1), followed by the momentum analysis for the decay pion spectrometer SpekA (Section 3.2) and the spectrometer momentum calibration method using elastic electron scattering data (Section 3.3). In the momentum calibration, the beam energy measured by the MAMI facility is used instead of the result from the undulator interferometry, as the analysis of the latter is still ongoing. Therefore, the results presented in this thesis are considered preliminary. As the next step, the PID method using KAOS data (Section 3.4) will be discussed. Then, based on the electron elastic scattering data, an appropriate fitting function is evaluated, and finally, the fitting procedure for the momentum peak of the decay pion is described (Section 3.6).

3.1 Analysis procedure

Figure 3.1 shows a diagram of the analysis procedure. The red shaded area represents the SpekA data, and the purple shaded area represents the KAOS data analysis.

For the hypernuclear physics data, the KAOS and SpekA datasets are analyzed independently. In the SpekA analysis, the central magnetic field is first set based on the NMR readout. Subsequently, fundamental detector parameters such as TDC offsets and drift times are adjusted. Momentum reconstruction is then performed using VDC tracking data (Section 3.2).

In the KAOS analysis, basic parameters such as TDC offsets and ADC gains are initially calibrated. Momentum reconstruction is conducted using hit-paddle combinations on the scintillator walls. Finally, particle identification is performed based on the TOF, energy deposition, and momentum information from the KAOS

data (Section 3.4). Afterward, the KAOS and SpekA datasets are merged using the common event ID to extract the K^+-tagged momentum spectrum (Section 3.5).

Momentum calibration for SpekA is carried out using electron elastic scattering data (Section 3.3). The momentum analysis is performed following the same procedure as in the physics data. A peak fitting is then applied to determine the most probable value of the elastic peak. For this purpose, the absolute beam energy E_b, measured using an undulator-based interferometer, is typically used. However, in this work, the beam energy measured by the MAMI facility is adopted instead. A calibration function is constructed for the particle angle at the target, z-position, and relative momentum δp, and the momentum calibration factor is derived from the difference between the measured and calculated momenta for electron elastic scattering.

The final step involves fitting the momentum spectrum of the decay pion. Since the decay pion spectrum does not have sufficient statistics to determine the peak shape, the shape and width of the fitting function are evaluated using electron elastic scattering data (Section 3.6). This evaluation takes into account the effects of VDC-based position and angular resolutions as well as uncertainties in the transfer matrix. Furthermore, the energy loss of electrons/π^- in the target and other materials is estimated through simulation and incorporated into the analysis.

A final fitting of the decay pion momentum peak is performed (Section 3.6). Detailed explanations of each step are provided in the subsequent chapters.

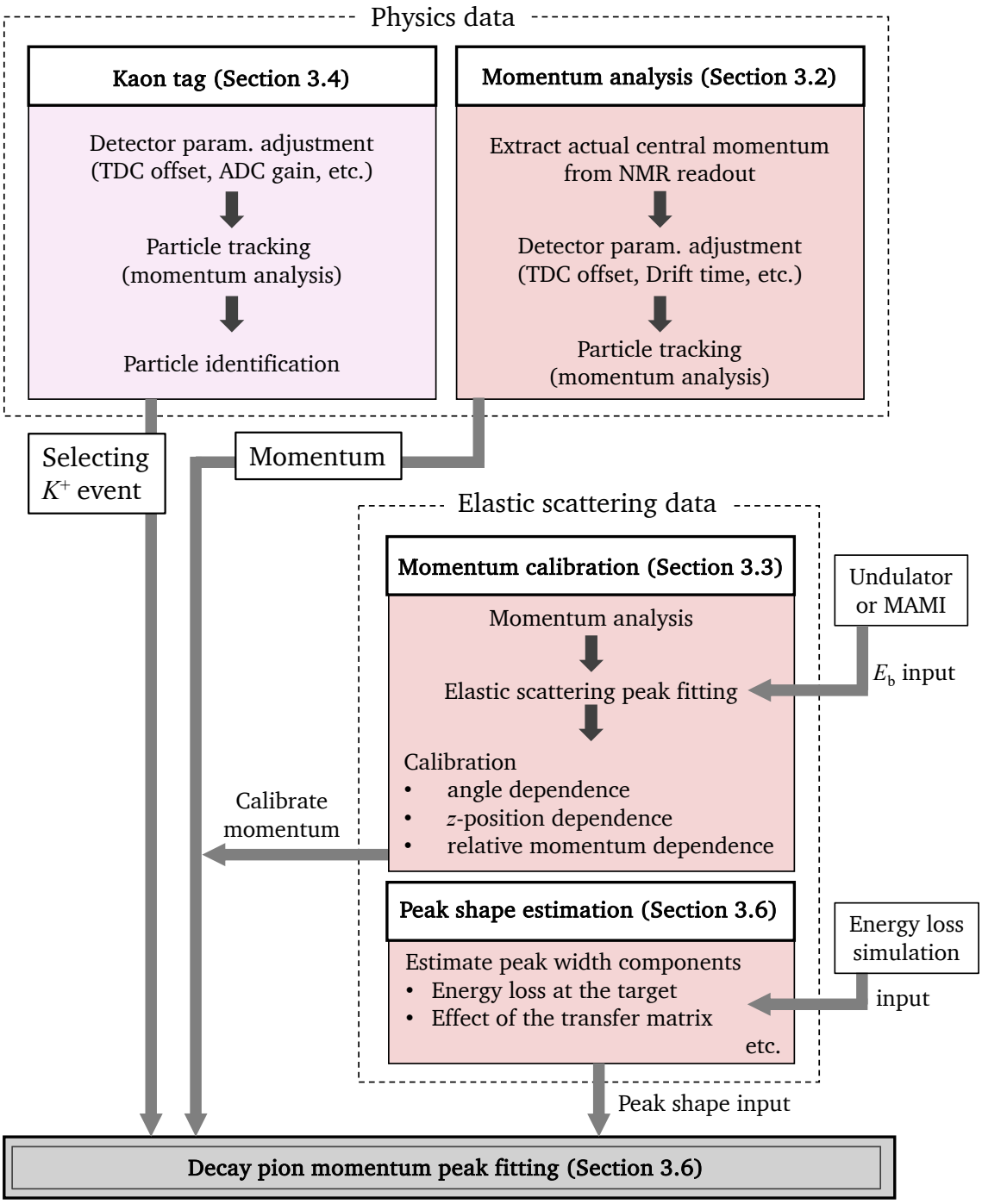

Figure 3.1: Diagram of analysis procedure. In the physics data analysis, the KAOS and SpekA data are analyzed independently to provide the tag of the K^+ event and momentum, respectively. Eventually, these are merged using the same event ID number. The electron elastic scattering data provide the momentum calibration information. The absolute beam energies by the undulator interferometry are used. The peak shape estimation is performed using not only elastic scattering data but also inputs from the Monte-Carlo simulation. Finally, the momentum peak of the decay pion is fitted.

3.2 Momentum analysis of decay pion spectrometer

The momentum of the decay π^- emitted from the hypernuclear decay is measured using the high-resolution magnetic spectrometer SpekA. This section presents an overview of the stability of the magnetic field in the dipole magnets, followed by a description of the basic analysis procedure and the achieved position and angle resolution of the vertical drift chambers (VDCs) located at the focal plane, which are used for momentum reconstruction.

3.2.1 Determination of central momentum and evaluation of the stability of the dipole magnetic field

Figure 3.2 shows the NMR readout magnetic field installed in the two dipole magnets of SpekA and the actual applied current value.

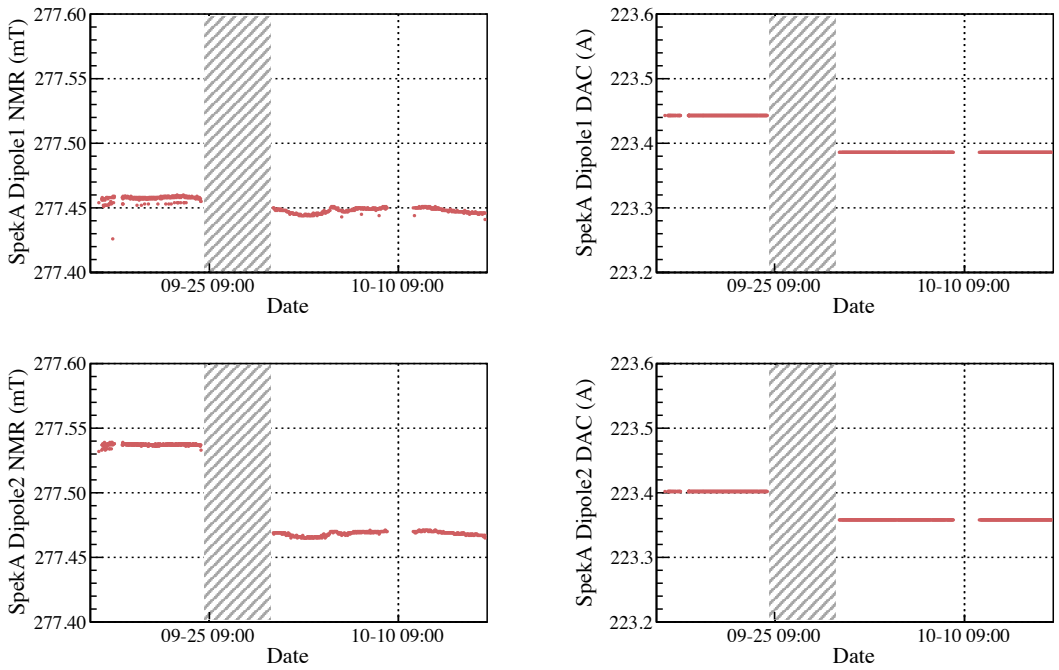

Figure 3.2: The NMR readout magnetic field installed in the two dipole magnets of SpekA (left column) and the actual current value. The top row corresponds to the first (upstream) dipole D1, and the bottom row corresponds to the second (downstream) dipole D2. The interruptions due to the MAMI problem from September 24th to October 1st are shown in the hatch.

During the beam time, there was a one-week interruption (the hatched area in the Figure 3.2) due to accelerator trouble, and the current value fluctuated before

and after that. The NMR readout value also reflects this fluctuation. The value of central momentum is calculated using the NMR readout magnetic field according to the formula 2.3.1. In the case of SpekA, the magnetic field of the first (upstream) dipole magnet (D1) is used as the reference. There is a difference of less than 10 μT between the magnetic fields read out by the two dipole magnets, especially in the first half of the beamtime, but the error is only 4 keV/c. This is taken into account as systematic uncertainty of the final results.

In the first half of the beamtime before the interruption, the central momentum variation was $\sigma \sim 1.18$ keV/c (Figure 3.3 (a)), i.e., $\Delta p/p \sim 9.7 \times 10^{-6}$, and in the second half of the beamtime it was $\sigma \sim 0.80$ keV/c (Figure 3.3 (b)), i.e., $\Delta p/p \sim 6.6 \times 10^{-6}$. The dipole magnetic field was stable during the whole data taking.

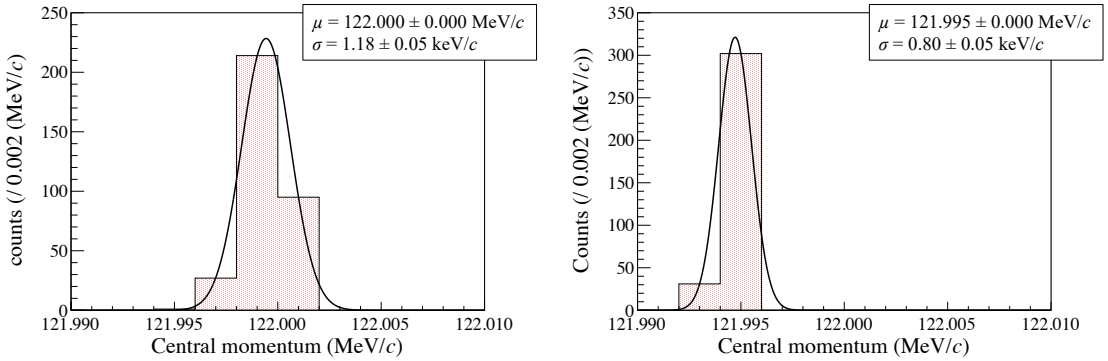

(a) first-half beamtime (b) second-half beamtime

Figure 3.3: Central momentum calculated from the magnetic field readout of the NMR probe installed on the D1 dipole magnet. Panel (a) shows the data before the interruption, and panel (b) shows the data after the interruption. Each distribution is fitted with a Gaussian function to extract the mean (μ) and standard deviation (σ).

3.2.2 Analysis for focal plane detectors

Charged particles with different momenta follow distinct trajectories in the magnetic field of the dipole magnets, and are subsequently detected by the downstream focal plane detector system comprising vertical drift chambers (VDCs), which measure both position and angle. Prior to performing tracking analysis, the timing offsets for each detector channel were calibrated. The trigger timing of SpekA was defined using signals from two layers of plastic scintillator detectors, ToF and dE, positioned downstream of the VDCs. Each layer consists of 15 channels, and their relative timing offsets were aligned based on the $(\mathrm{KAOS}, \mathrm{SpekA}) = (\pi^+, \pi^-)$ coincidence time peaks observed in correlation with the KAOS spectrometer.

Subsequently, the start timing (t_0) for the drift time (t_d) measurement in each wire of the VDCs was determined. Figure 3.4 presents the drift time distributions for each VDC layer. The horizontal axis indicates the TDC channel number, where one channel corresponds to 0.75 ns. Since the VDCs data acquisition operated in common stop mode, larger channel numbers represent earlier arrival times relative to the common trigger. The reference time t_0 was defined as the rising edge of the distribution, as indicated by the blue line in the figure. The timing of the rising edge was determined by fitting linear functions to both the continuous background distribution and the signal distribution, and extracting their intersection point.

Figure 3.5 illustrates the principle of the VDC tracking analysis. For each event, timing signals are recorded from multiple signal wires. The drift length L_d associated with each signal wire is calculated using the following relation:

$$L_d = t_d \times v \times C = (\mathrm{TDC} - t_0) \times v \times C. \tag{3.2.1}$$

where v is the drift velocity and C is the TDC conversion factor, $C = 0.75$ ns. Using the drift lengths obtained in this way, the particle trajectory is reconstructed by a linear fit, yielding the position and angle of the particle at the target.

The distributions of reconstruction errors for the position (x, y) and angle (θ, ϕ) on the focal plane obtained by this linear fitting are shown in Figure 3.6. These variables correspond to momentum, scattering angle, out-of-plane angle, and vertex position at the target, respectively.

The values of t_0 and the drift velocity for each VDC layer were adjusted to minimize the error in the linear track fitting. During this process, the values of Δx were used as references for optimizing t_0 and the drift velocity in the X1 and X2 layers, while Δy was used for optimizing t_0 in the S1 and S2 layers. A typical value of the obtained drift velocity was approximately 26 μm/ns, which falls within a realistic

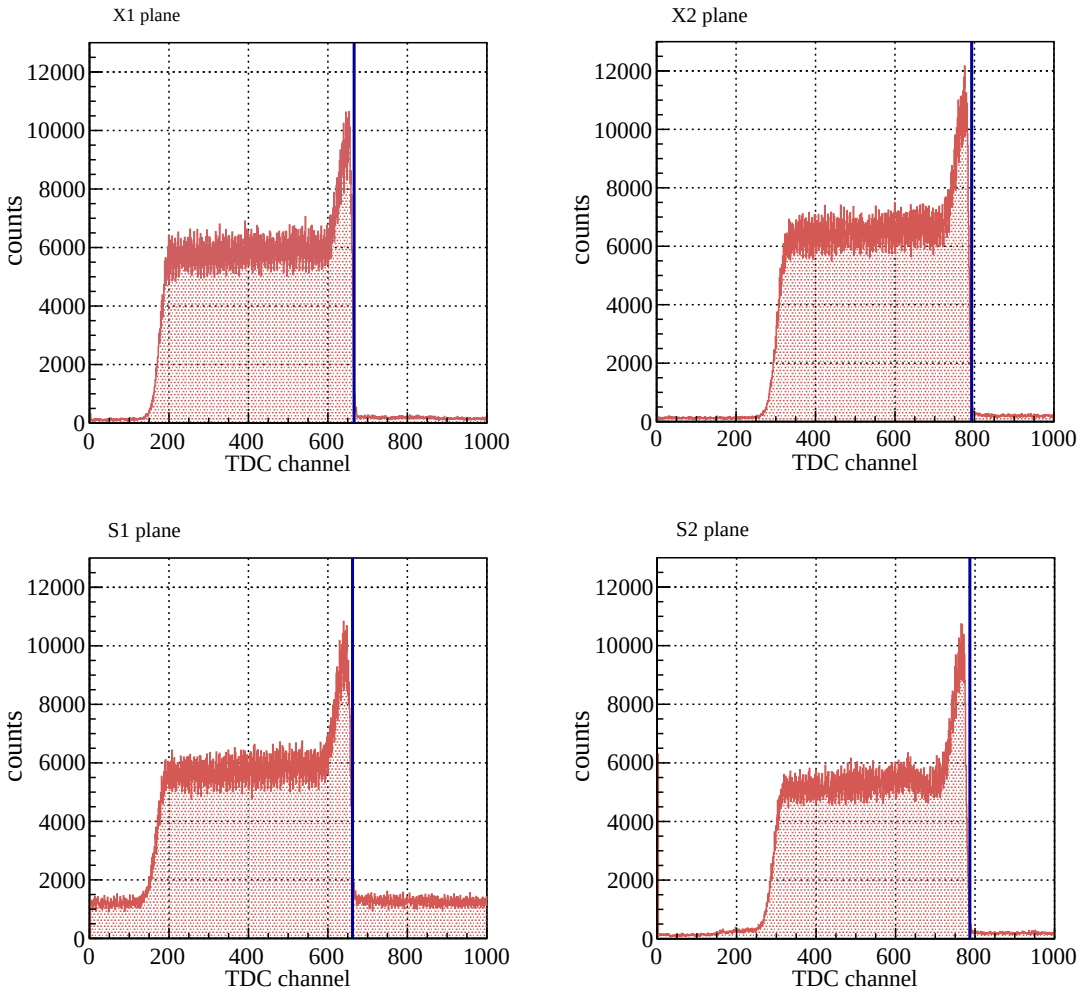

Figure 3.4: Drift time distribution of each layer of VDC. The horizontal axis is the TDC channel number, which corresponds to 0.75 ns per channel. The reference time t_0 for the drift time measurement of each layer is the rising edge of the distribution shown by the blue line.

and representative range for an Ar:i$C_4H_{10} = 50 : 50$ gas mixture in the VDCs, and is also consistent with the typical drift time of 200 ns reported in Ref. [Blo+98]. The resulting spatial resolutions after these optimizations are summarized in Table 3.1. The achieved performance is consistent in both magnitude and distribution shape with the reference values reported in Ref. [Blo+98].

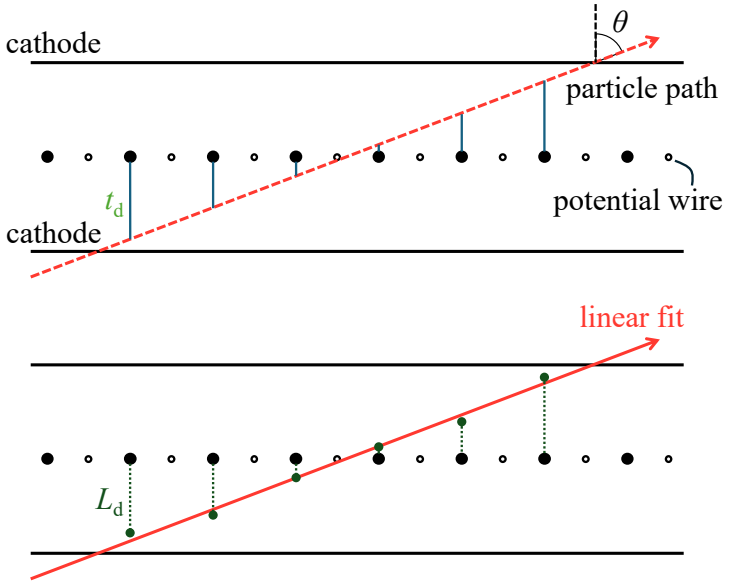

Figure 3.5: Principle of VDC tracking analysis. When a charged particle passes through the chamber, timing signals are obtained from several signal wires. The drift length for each wire is determined by the equation 3.2.1, and the particle tracking is obtained by a linear fit.

Table 3.1: Resolution of target coordinates reconstructed from the VDCs in the SpekA.

Focal-plane coordinate	x (μm)	y (μm)	θ (μrad)	ϕ (μrad)
Target coordinate	momentum	scattering angle	out-of-plane angle	vertex
Most probable error	73	173	178	925
Average error	115	239	243	1,175

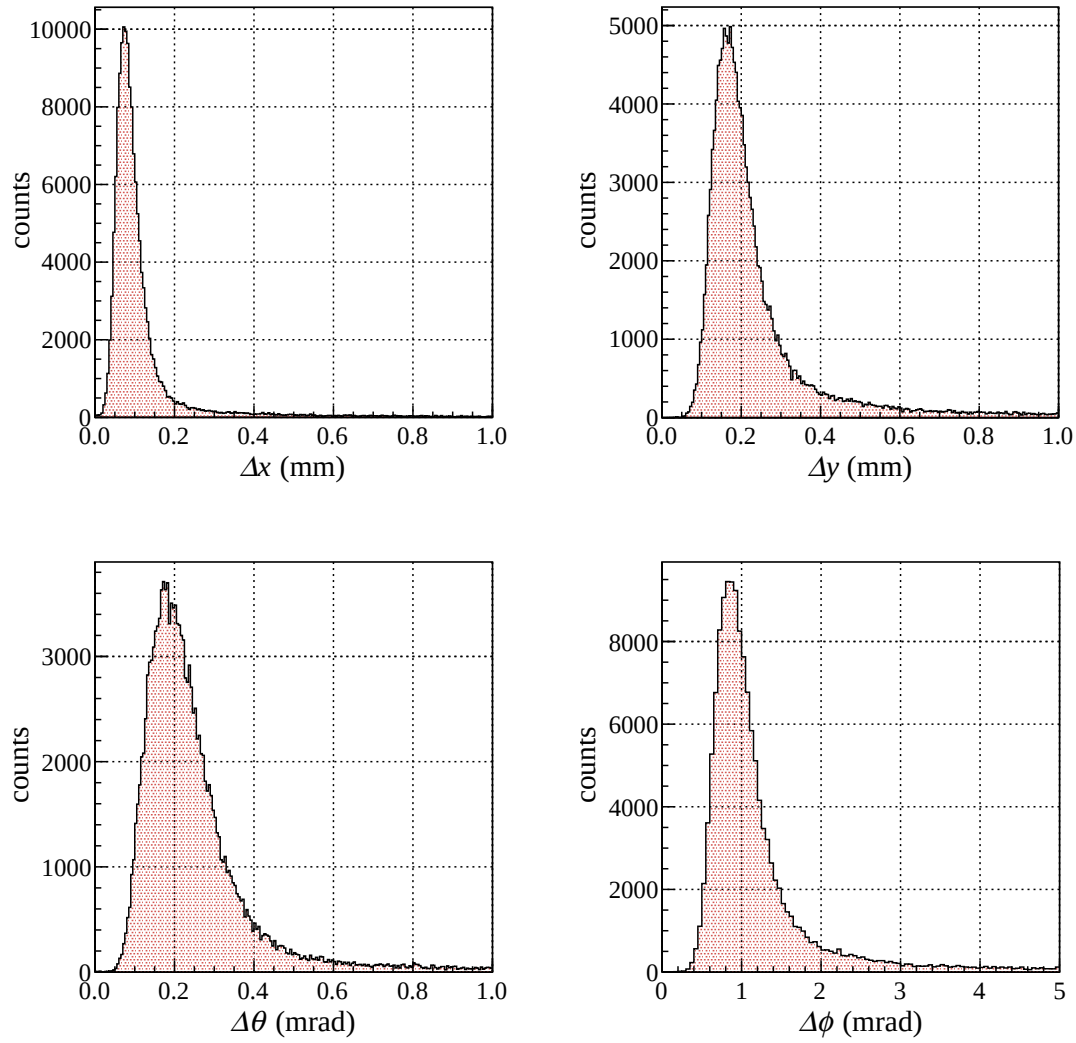

Figure 3.6: Distribution of errors of position (x, y) and angle (θ, ϕ) on the focal plane measured by VDC. The upper left is the error for x position, the upper right is the error for y position, the lower left is the error for θ, and the lower right is the error for ϕ, which are physical quantities corresponding to momentum, scattering angle, out-of-plane angle, and vertex at the target position, respectively.

3.3 Momentum calibration

The momentum measured by SpekA was calibrated by correcting the difference between the known momentum peak and the observed peak position using elastic electron scattering based on Eq. 2.3.7. This section begins with a description of the angular calibration of the spectrometer using the reconstructed sieve collimator's hole pattern (Subsection 3.3.1). The procedure for peak fitting, which is essential for momentum calibration, is then outlined (Subsection 3.3.2). Then, the fitting method is applied to evaluate the linearity within the momentum acceptance (Subsection 3.3.3) and to assess the z-position dependence (Subsection 3.3.4). Finally, the momentum calibration factor is deduced from the momentum difference. Noted that the electron beam energy is referenced from the results of MAMI's measurement instead of undulator interferometry in this thesis.

3.3.1 Angular calibration

The angular resolution of the spectrometer was evaluated by placing a sieve collimator at the spectrometer entrance during elastic scattering measurements and reconstructing the resulting hole pattern. Figure 3.7 shows a two-dimensional distribution of the reconstructed dispersion angle (θ) and non-dispersion angle (ϕ) of scattered electrons at the target position.

The sieve collimator is a 5 mm-thick heavy metal plate with symmetrically drilled holes [Blo+98]. It consists of seven rows in the θ direction and eleven rows in the ϕ direction, each with a hole radius of 2.5 mm (3.9 mrad). To avoid ambiguity in orientation, the central hole and one off-center hole are enlarged to a radius of 5 mm (7.8 mrad). The design positions and radii of the holes are plotted as black circles in Figure 3.7, showing good agreement with the reconstructed angular distribution of the scattered electrons.

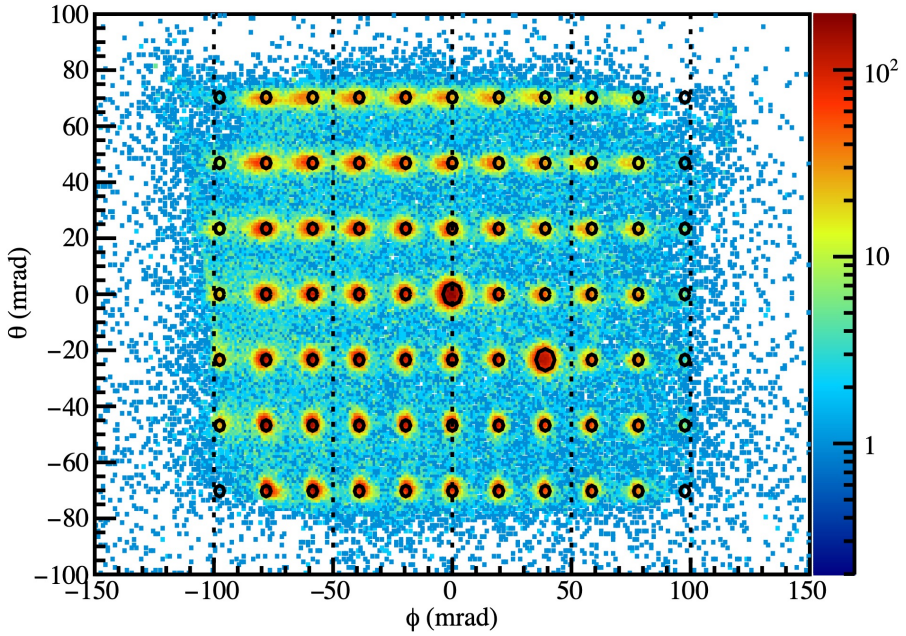

Figure 3.7: Two-dimensional distribution of the reconstructed dispersion angle (θ) and non-dispersion angle (ϕ) of scattered electrons at the target position. The black circles indicate the design values of the sieve collimator hole pattern, which are generally well reproduced in the measured distribution.

To evaluate the angular resolution, events passing through individual sieve holes were projected onto the θ and ϕ axes. Each projection was fitted with a Gaussian function and a constant function, as illustrated in Figure 3.8. The figure shows a representative example, where projections were taken for columns within the regions $10 \leq \theta\ (\text{mrad}) < 30$ and $10 \leq \phi\ (\text{mrad}) < 30$.

The measured Gaussian width σ_{measured} obtained from the fit was corrected for the finite hole size, and the intrinsic angular resolution σ_{res} was extracted using the following relation:

$$\sigma_{\text{res}} = \sqrt{\sigma^2_{\text{measured}} - \left(\frac{r_{\text{hole}}}{\sqrt{12}}\right)^2}, \tag{3.3.1}$$

where r_{hole} denotes the angular diameter of the hole in units of mrad, and the coefficient $\sqrt{12}$ represents the standard deviation of a uniform distribution across the hole width. Although even in the limit of infinitely good angular resolution, the particle distribution through the hole would not be exactly rectangular due to focusing toward the center, this approximation has a negligible impact in the present evaluation.

The average angular resolution obtained using this method was $\sigma_{\text{res}} = 1.76$ mrad. The accuracy of the hole center determination, defined as the RMS deviation be-

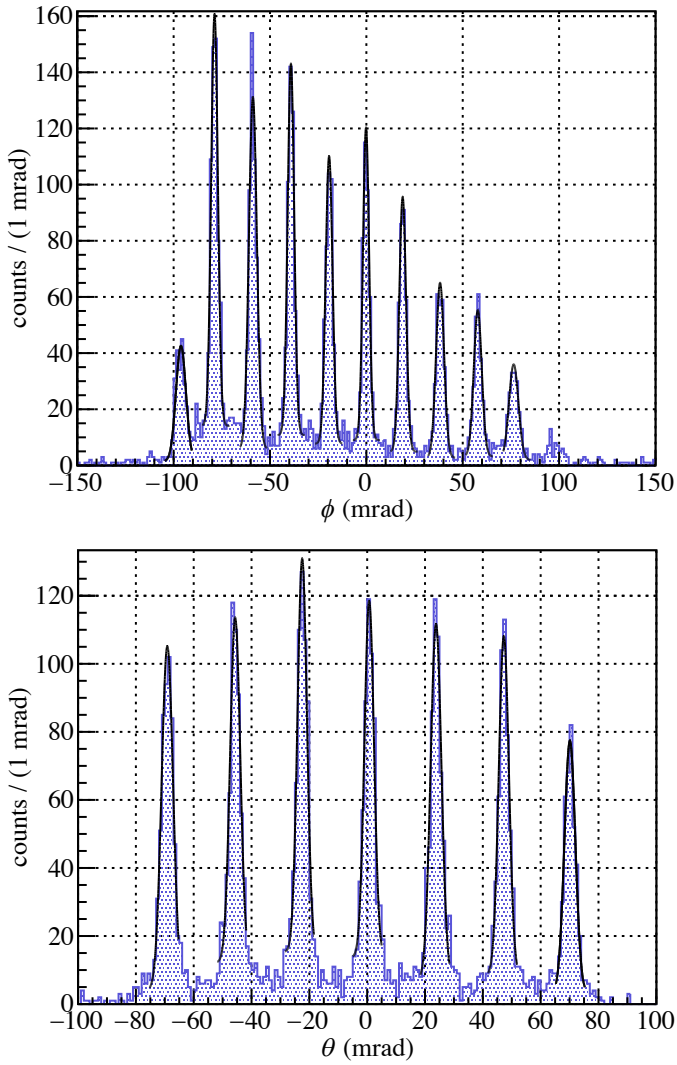

Figure 3.8: Fit to angular projection of hole events. Gaussian + constant fits to the projections of reconstructed angles at the target position: (top) dispersion angle θ, (bottom) non-dispersion angle ϕ. The selected regions are $10 \leq \theta$ (mrad) < 30 and $10 \leq \phi$ (mrad) < 30.

tween the measured hole positions and the design values of the sieve collimator, was estimated to be 1.85 mrad. The resulting momentum uncertainty due to this angular resolution was negligibly small: less than 1 keV/c for a ^{181}Ta target and less than 4 keV/c for a ^{12}C target at an incident beam energy of $E_b = 180$ MeV.

3.3.2 Peak fitting for elastic scattered electron momentum

Figure 3.9 shows an example of a measured elastic scattering peak from ^{181}Ta, along with fitting of response functions.

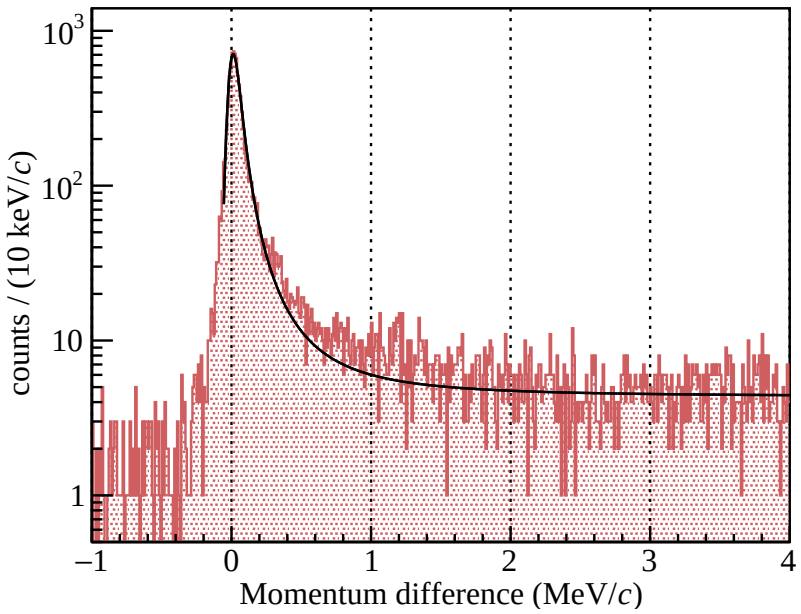

Figure 3.9: Deviation from the theoretical value of the elastic peak for a ^{181}Ta target. The beam energy was $E_b = 195$ MeV and the central momentum setting of the spectrometer was $p_{\text{cent}} = 208.3$ MeV/c. The Landau-Gaussian function is fitted to the elastic peak corresponding to the ground state $9/2^-$. A small structure from the excited state $11/2^+$ can be seen around $\sim +0.3$ MeV/c, but due to low statistics, its presence or absence causes a variation of approximately 2 keV/c in the fitted peak position.

The fitting function used is a convolution of the Landau and Gaussian distributions. This choice is justified because the target material is sufficiently thin, making the high-energy tail due to energy loss in the target non-negligible. The energy loss was calculated using the Bethe-Bloch formula [Leo94]:

$$-\frac{dE}{dx} = 2\pi N_a r_e^2 m_e c^2 \rho \frac{Z}{A}\frac{z^2}{\beta^2}\left[\ln\left(\frac{2m_e\gamma^2 v^2 W_{\max}}{I^2}\right) - 2\beta^2\right], \tag{3.3.2}$$

where

$$2\pi N_a r_e^2 m_e c^2 = 0.1535 \text{ MeV cm}^2/\text{g}. \tag{3.3.3}$$

The other variables are:

- r_e: classical electron radius $= 2.817 \times 10^{-13}$ cm,
- m_e: electron mass,

- N_a: Avogadro's number $= 6.022 \times 10^{23}$ mol^{-1},
- I: mean excitation potential,
- Z: atomic number of absorber,
- A: atomic mass of absorber,
- ρ: density of absorber,
- z: charge of incident particle in units of e,
- $\beta = v/c$, $\gamma = 1/\sqrt{1-\beta^2}$,
- W_{max}: maximum energy transfer in a single collision:

$$W_{\text{max}} = \frac{2m_e c^2(\beta\gamma)^2}{1 + 2(m_e/M)\sqrt{1+(\beta\gamma)^2} + (m_e/M)^2}. \tag{3.3.4}$$

The shape of the energy loss distribution is characterized by the parameter κ, defined as the ratio between the average energy loss $\bar{\Delta}$ and the maximum energy transfer W_{max}:

$$\begin{aligned} \kappa &= \bar{\Delta}/W_{\text{max}}, \\ \bar{\Delta} &= 2\pi N_a r_e^2 m_e c^2 \rho \frac{Z}{A}\frac{z^2}{\beta^2}. \end{aligned} \tag{3.3.5}$$

If $\kappa > 1$, the distribution approaches a Gaussian shape. If $\kappa < 1$, the distribution becomes asymmetric with a long, high-energy tail. In the extreme case $\kappa \lesssim 0.01$, the distribution follows the Landau form $\phi(\lambda)$:

$$f(\lambda, \Delta E) = \frac{\phi(\lambda)}{\xi}, \tag{3.3.6}$$

with

$$\begin{aligned} \phi(\lambda) =& \frac{1}{\pi}\int_0^\infty \exp(-u\ln u - u\lambda)\sin(\pi u)\, du, \\ \lambda =& \frac{1}{\xi}\left[\Delta E - \xi\left\{\ln\xi - \left(\ln\left(\frac{(1-\beta^2)I^2}{2m_e c^2\beta^2}\right) + \beta^2\right) + 1 - 0.577\right\}\right], \end{aligned} \tag{3.3.7}$$

where ξ is the mean energy loss and I is the mean excitation potential. In the both case of ^{181}Ta (average thickness: (12.3 ± 0.1) mg/cm^2) and ^{12}C (average thickness: (1.763 ± 0.028) g/cm^2), the κ is the order of 10^{-5} to 10^{-6}. There were also air ($\sim$ 10 cm thick) and two Kapton foils (127 μm thick [DuP]) between the target chamber and the spectrometer. These materials also have the same order of κ.

The Landau distribution $\phi(\lambda)$ is defined in a standard form with no explicit parameters such as mean or width. The most probable value (MPV) occurs at a fixed value of $\lambda = \lambda_{\text{mp}} = -0.22278298$ [KS84]. For practical fitting purposes, a parameterized Landau function is used, in which the MPV and width σ_L are treated as free parameters. The correspondence between the scaled λ and the physical MPV is:

$$\begin{aligned} \frac{x - MPV}{\sigma_L} &= \lambda_{\text{mp}} \\ \Rightarrow \quad MPV &= x - \lambda_{\text{mp}} \cdot \sigma_L. \end{aligned} \tag{3.3.8}$$

To decouple the MPV from the width parameter in fitting, we define a corrected MPV' as:

$$MPV', = MPV - \lambda_{\text{mp}} \cdot \sigma_L = MPV - 0.22278298 \cdot \sigma_L. \tag{3.3.9}$$

Therefore, the Landau-Gaussian convolution function used in this analysis is defined as:

$$\begin{aligned} f(x) &= A \int_{-\infty}^{\infty} \frac{1}{\sigma_L} L\left(u; \mu = MPV', \sigma_L\right) \cdot G(x - u; \sigma_G)\, \mathrm{d}u + C \\ &= A \int_{-\infty}^{\infty} \frac{1}{\sigma_L} L\left(u; \mu = MPV - \Delta, \sigma_L\right) \cdot G(x - u; \sigma_G)\, \mathrm{d}u + C, \end{aligned} \tag{3.3.10}$$

where

- $L(u; \mu, \sigma_L)$ is the Landau distribution,
- $G(x - u; \sigma_G) = \frac{1}{\sqrt{2\pi}\sigma_G} \exp\left(-\frac{(x-u)^2}{2\sigma_G^2}\right)$ is the Gaussian distribution,
- A is the amplitude,
- C is a constant offset (baseline),
- $\Delta = 0.22278298 \times \sigma_L$ is the shift between the most probable value (MPV) and the mean of the Landau distribution.

This function is evaluated numerically using a symmetric rectangle rule (midpoint approximation) over the range $\pm 5\sigma_G$ with $N = 250$ steps on each side (total 500 steps):

$$f(x) \approx A \cdot \frac{1}{\sqrt{2\pi}\sigma_G\sigma_L} \sum_{i=1}^{N} [L(u_i) \cdot G(x-u_i) + L(v_i) \cdot G(x-v_i)] \cdot \Delta u + C, \quad (3.3.11)$$

where

$$u_i = x - 5\sigma_G + \left(i - \frac{1}{2}\right) \cdot \Delta u,$$
$$v_i = x + 5\sigma_G - \left(i - \frac{1}{2}\right) \cdot \Delta u,$$
$$\Delta u = \frac{10\sigma_G}{N}.$$

Figure 3.10 shows an example of a Landau-Gaussian convolution function. In

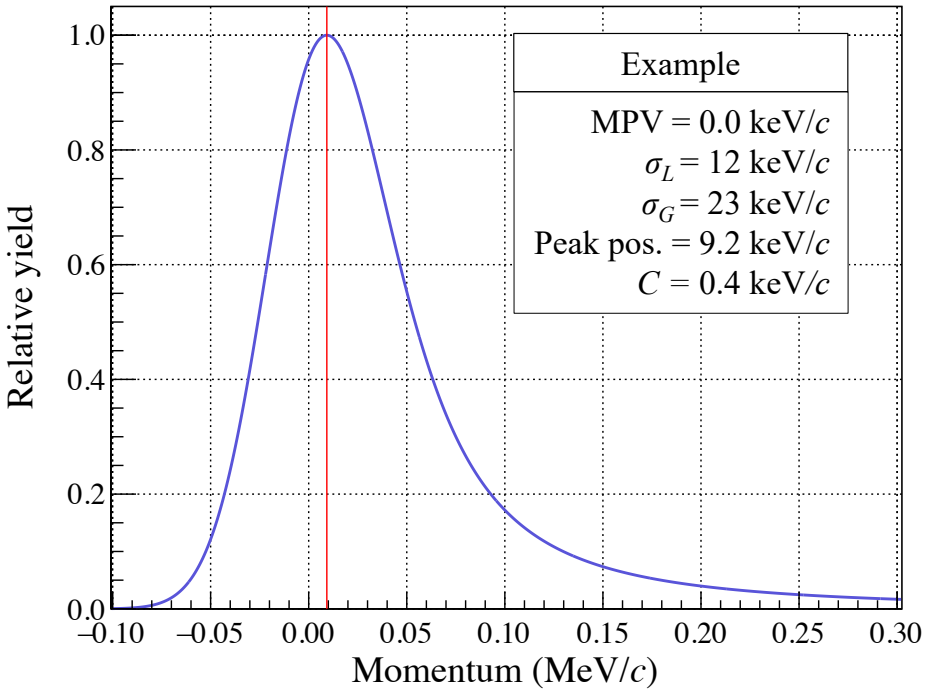

Figure 3.10: An example of the Landau-Gaussian convolution function used in fitting. Although the MPV' is set to zero, the actual peak position shifts rightward due to the width of the Gaussian component.

this example, the Landau width is set to $\sigma_L = 12$ keV/c and the Gaussian width to $\sigma_G = 23$ keV/c. As illustrated, the true peak position (where the derivative is zero) shifts from MPV' by an amount proportional to σ_G:

$$\begin{aligned} \text{Peak position} &= MPV' + C \cdot \sigma_G, \\ \delta_{\text{Peak position}} &= \sqrt{(\delta MPV')^2 + C^2 \cdot (\delta\sigma_G)^2}, \end{aligned} \quad (3.3.12)$$

where C is a numerical constant determined empirically.

Energy loss correction

In this analysis, the energy loss of the scattered electron in each material was corrected before calculating the momentum difference by fitting with Landau-Gaussian function. The following most probable value ΔE_{mp} was used for the actual calculation of the energy loss [Leo94].

$$\Delta E_{\mathrm{mp}} = \xi \left[\ln \xi - \left(\ln \frac{(1-\beta^2) I^2}{2 m_e c^2 \beta^2} + \beta^2 \right) + 0.198 - \delta \right] \tag{3.3.13}$$

As mentioned above, in this setup, the energy loss follows a Landau distribution, so a correction term of -0.198 is added. The density correction term δ is expressed as

$$\delta = \begin{cases} 0 & (X < X_0) \\ 4.6052X + C_0 + a(X_1 - X)^m & (X_0 \leq X \leq X_1) \\ 4.6052X + C_0 & (X > X_1), \end{cases}$$

where $X = \log_{10}(\beta\gamma)$. C_0, a, X_0, X_1, and m are parameters that depend on the absorbing material. The values for the target material used in this experiment are summarized in Table 3.2.

Table 3.2: Summary of each parameter for the target material used in this analysis [Ste84]

	C_0	a	X_0	X_1	m
^{181}Ta	5.5262	0.1780	-0.2117	3.4805	2.7623
^{12}C	2.8680	0.2614	-0.0178	2.3415	2.8697
^{7}Li	3.1221	0.9514	0.1304	1.6397	2.4993

Energy loss corrections were applied on an event-by-event basis by multiplying the material thicknesses (path lengths) of the target, air, and Kapton foils by the most probable energy loss rate, ΔE_{mp}. Ideally, the path length within the target for each event is calculated from the reconstructed z-position of the reaction point and the angles (θ_t, ϕ_t), obtained from the spectrometer measurement. However, in the case of the elastic scattering data, the z-position resolution (along the beam axis) is worse than the actual target thickness. Therefore, the z-position was fixed at the center of the target, and only the angular information was used to compute the path length. The resulting uncertainty in the energy correction was estimated to be less than 4 keV for the ^{181}Ta target and less than 10 keV for the ^{12}C target.

In the hypernuclear experiment, the target extended 45 mm along the z-direction, covering over 90% of the spectrometer acceptance. Accordingly, the path length was calculated solely based on the beam position and the emission angles (θ_t, ϕ_t) at the target vertex, independent of the z-position.

3.3.3 Linearity

The linearity of the momentum difference across the entire momentum acceptance of the spectrometer was evaluated using elastic scattering peaks measured with a ^{12}C target. The ^{12}C target allows clear identification of peaks corresponding to various excited states, and linearity can be assessed over a wide range of approximately 16 MeV within a single dataset.

The excitation energy E_x for each state was evaluated by calculating the missing mass according to the following equation:

$$E_x = M_{\text{miss}} - M_{^{12}\text{C}} = \sqrt{(E_e + M_{^{12}\text{C}} - E_{e'})^2 - (\overrightarrow{p_e} - \overrightarrow{p_{e'}})^2} - M_{^{12}\text{C}} \tag{3.3.14}$$

Figure 3.11 shows the missing mass spectrum measured with the ^{12}C target. The data were taken with a beam energy of $E_b = 210$ MeV and a central momentum setting of $p_{\text{cent}} = 193.2$ MeV/c. Five distinct peaks corresponding to the ground and excited states were observed and labeled in accordance with the level scheme shown in Figure 3.12. Each peak was fitted using a Landau-Gaussian function, following the same procedure used for the ^{181}Ta target.

The excitation energy shift ΔE_x for each ground and excited state spectrum was obtained by subtracting the literature value of the excitation energy [Ajz88], shown in the level scheme of Figure 3.12, from the measured value. The results are plotted in Figure 3.13. Panel (a) shows the dataset obtained in the present experiment, while (b) presents the datasets taken in 2014 [Nag15] and 2016 [Sch16] for comparison. In both panels, the horizontal axis represents the relative momentum δp with respect to the central momentum $p_{\text{cent.}}$, where the measured momentum p_{m} is defined as

$$p_{\text{m}} = p_{\text{cent.}} \times (1 + \delta p). \tag{3.3.15}$$

Figure 3.13(a) includes all datasets obtained using a ^{12}C target positioned at the center (z) labeled "C3"for each beam energy E_b and central momentum setting. For datasets with beam energies other than $E_b = 195$ MeV, the measured

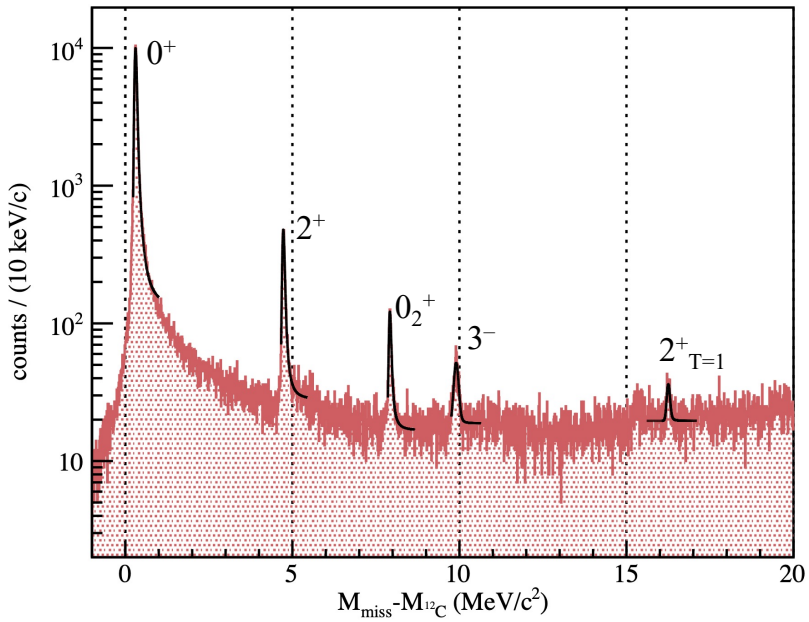

Figure 3.11: Missing mass distribution measured for the ^{12}C target. The beam energy was $E_b = 210$ MeV and the central momentum setting was $p_{\text{cent}} = 193.2$ MeV/c. Elastic scattering peaks corresponding to the ground state 0^+ and excited states 2^+, 0_2^+, 3^-, and the second 2^+ were observed and fitted using Landau-Gaussian functions.

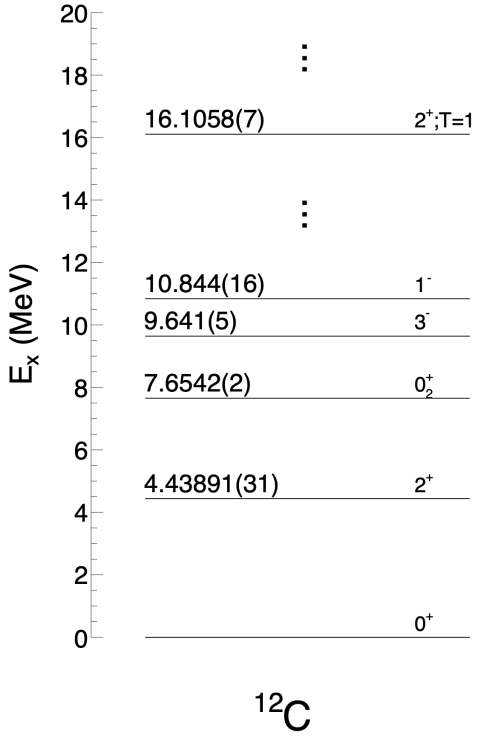

Figure 3.12: Level scheme of ^{12}C [Ajz88] (figure adapted from [Nag15])

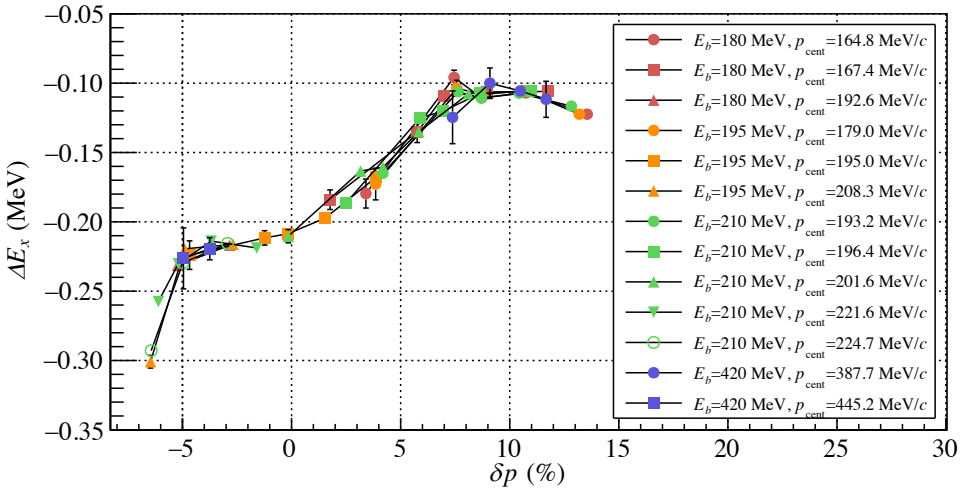

(a) Calibration 2024

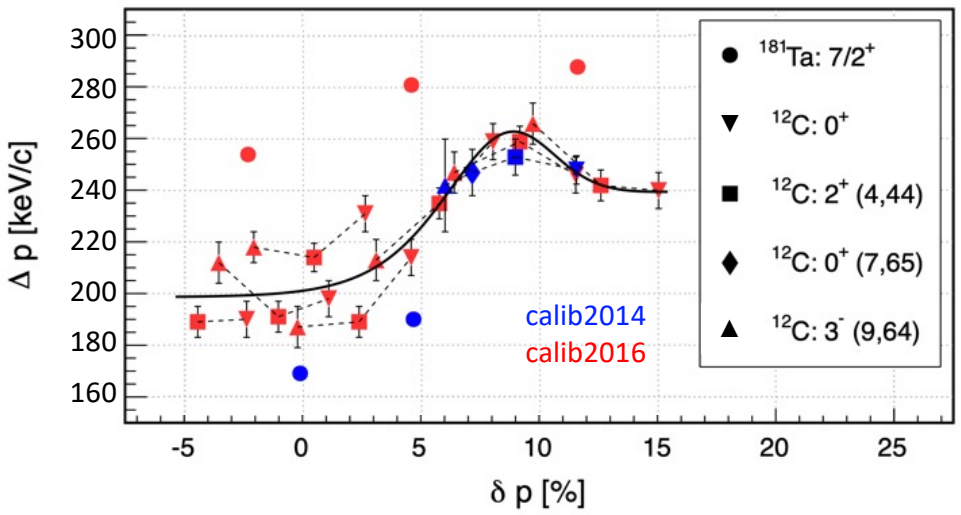

(b) Calibration 2014 2016

Figure 3.13: (a) Correlation between ΔE_x and relative momentum δp for $E_b = 195$ MeV. Error bars represent statistical uncertainties from the peak fitting. (b) Reference correlations from previous studies [Nag15; Sch16], measured at $E_b = 195$ MeV using the same target material. (Figure adapted from Ref. [Sch16], modified.) For the ^{12}C target, data points from a single dataset are connected by dashed lines. Although the vertical axes in (a) and (b) differ in units, the difference becomes less than 1 keV when Δp is converted into ΔE_x, allowing for direct comparison.

ΔE_x was scaled by a factor of $195/E_b$[1]. The vertical offsets of each curve were adjusted to align along the trend, reflecting stability of beam energy or systematic uncertainties in measurement methods. This adjustment does not affect the relative values of ΔE_x between peaks within each dataset. Therefore, the absolute values of ΔE_x in this figure have no physical significance due to the applied offset adjustment; only the relative values are meaningful. This operation, involving uniform scaling and offset adjustment for datasets with different beam energies, allows all datasets to reproduce a consistent behavior. This demonstrates that the relative-momentum-dependent behavior of the momentum deviation within the spectrometer acceptance is well described.

The observed trend is consistent with that of previous experiments shown in panel (b), exhibiting a rise from the low-momentum to high-momentum region and a slight decrease around $\delta p \sim 10\%$. In earlier studies, since only one decay-pion peak from a hypernucleus was detected, local calibration within a narrow acceptance region sufficed. However, in the present study, the decay-pion peaks from ${}^{4}_{\Lambda}$H and ${}^{3}_{\Lambda}$H are expected to appear around $\delta p \sim 13.7\%$ and $\delta p \sim -1.3\%$, respectively, necessitating correction over the full spectrometer acceptance.

To obtain a correction function for the correlation betweenΔE_x (or Δp) and δp, the vertical axis of Figure 3.13(a) was converted into $\Delta p/p_{\mathrm{m}}$, and a sixth-order polynomial was fitted to the data. The result is shown in Figure 3.14.

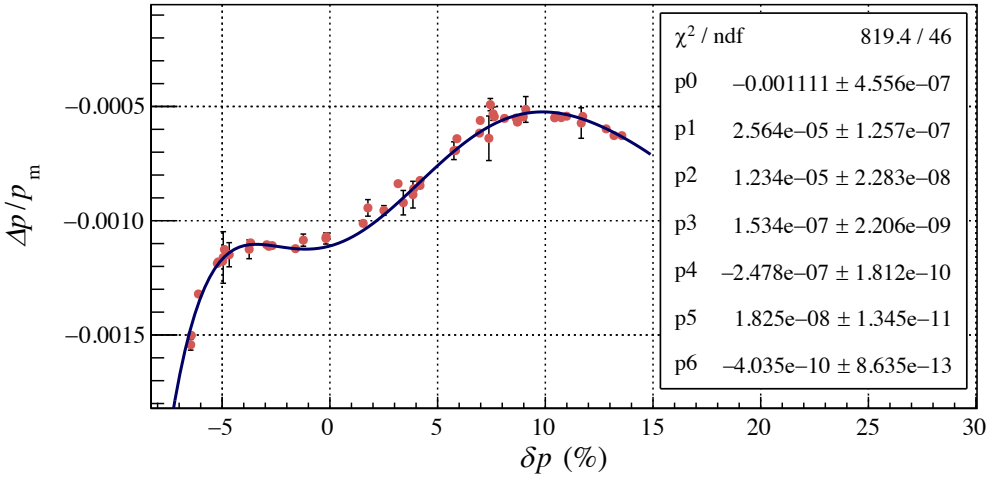

Figure 3.14: Correlation between $\Delta p/p_{\mathrm{m}}$ and δp from ^{12}C target data. A sixth-order polynomial was fitted to obtain the correction function.

[1]In the expression for Δp, Eq. 2.3.7, the contribution from second and higher-order terms is estimated to be only about 0.016%, which justifies the linear approximation.

Polynomial fits of fourth to eighth order were tested, and the sixth-order polynomial was selected because it provided a sufficiently good description of the data. The χ^2 values for the sixth-order and higher-order fits were nearly identical, indicating that the sixth-order fit was adequate. The fit results are summarized in Table 3.3.

Table 3.3: Fitted χ^2/NDF values for different polynomial orders used to model the $\Delta p/p_{\mathrm{m}} - \delta p$ correlation.

Function	χ^2/NDF
4th order polynomial	173.924
5th order polynomial	30.836
6th order polynomial	17.813
7th order polynomial	18.184
8th order polynomial	18.365

The resulting correction function is expressed as:

$$\begin{aligned} p_{\text{shift}} = &(2.56385 \times 10^{-5}) \times \delta p + (1.23367 \times 10^{-5}) \times \delta p^2 \\ &+ (1.53437 \times 10^{-7}) \times \delta p^3 - (2.47799 \times 10^{-7}) \times \delta p^4 \\ &+ (1.82476 \times 10^{-8}) \times \delta p^5 - (4.03546 \times 10^{-10}) \times \delta p^6 \end{aligned} \tag{3.3.16}$$

The correction to the measured momentum was then applied as:

$$p'_{\mathrm{m}} = (1 + p_{\text{shift}}) \times p_{\text{cent.}} \times (1 + \delta p) \tag{3.3.17}$$

Using the corrected momentum defined by Eq. 3.3.17, ΔE_x was re-evaluated from the ^{12}C data and plotted in Figure 3.15, with vertical offsets adjusted so that the central values are near zero, and the values scaled by $195/E_b$ as before.

Compared to the uncorrected plot in Figure 3.13 (a), the distortion in linearity was clearly mitigated. A projection of this plot onto the vertical axis is shown in Figure 3.16.

From the $\Delta E_x - \delta p$ correlation in the ^{12}C dataset, the remaining uncertainty after the spectrometer linearity correction over the entire acceptance was estimated to be $\sigma \sim 0.003$ MeV, corresponding to a relative precision of $0.003/195 \sim 1.5 \times 10^{-5}$. This corresponds to an impact of only about $\sigma \sim 2$ keV/c on the decay π^- momentum of hypernuclei (approximately 133 MeV/c).

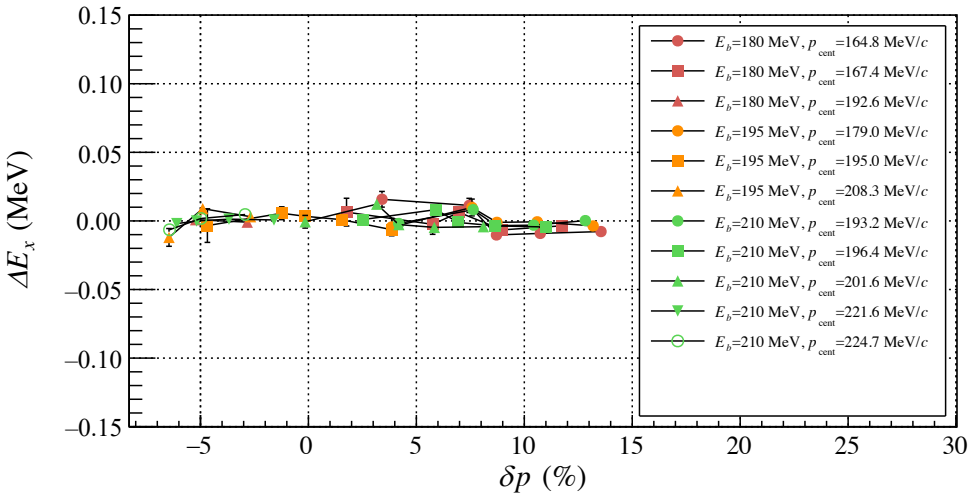

Figure 3.15: Corrected ΔE_x vs. δp plot after applying the momentum linearity correction function. The values are scaled by $195/E_b$ and offset-adjusted so that the central values are near zero.

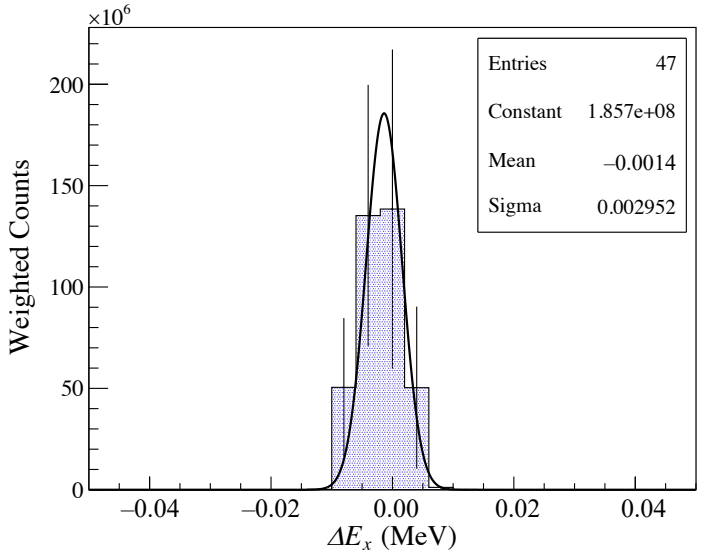

Figure 3.16: Projection of the corrected ΔE_x vs. δp plot onto the vertical axis of Figure 3.15. The Gaussian function is fitted to evaluate the deviation the result of this linearity correction. The deduced uncertainty is $\sigma \sim 0.003$ MeV which corresponds to $\sigma \sim 2$ keV/c on the decay π^- momentum of hypernuclei.

3.3.4 z position calibration

After correcting the linearity as described in the previous section, the z position dependence is also calibrated. As shown in Figure 2.15, five foils of ^{181}Ta and ^{12}C targets were placed at intervals of 15 mm along the z-axis, which is defined along the beam direction. By measuring the positions of the elastic scattering peaks from each of these targets, the z-position dependence of the reconstructed momentum can be evaluated. This calibration is essential because the lithium target used for hypernuclear production has a significant longitudinal extent of 45 mm along the beam axis. The derived dependence is used to correct for systematic shifts and to estimate associated systematic uncertainties.

Figure 3.17 shows the reconstructed z-vertex positions of electrons scattered elastically from the ^{181}Ta target, based on the particle positions and angles measured at the focal plane of SpekA. To account for the broad background distribution, the data were fitted with a sum of two Gaussian functions. Although the effective thickness of the target foil in the z-direction is approximately 7.4 μm, the reconstructed z-vertex distribution exhibited a peak width of $\sigma \sim 7 - 8$ mm due to limitations in resolution. Nevertheless, thanks to the sufficient statistics obtained for each dataset, the peak center was determined with a precision of 0.06 mm.

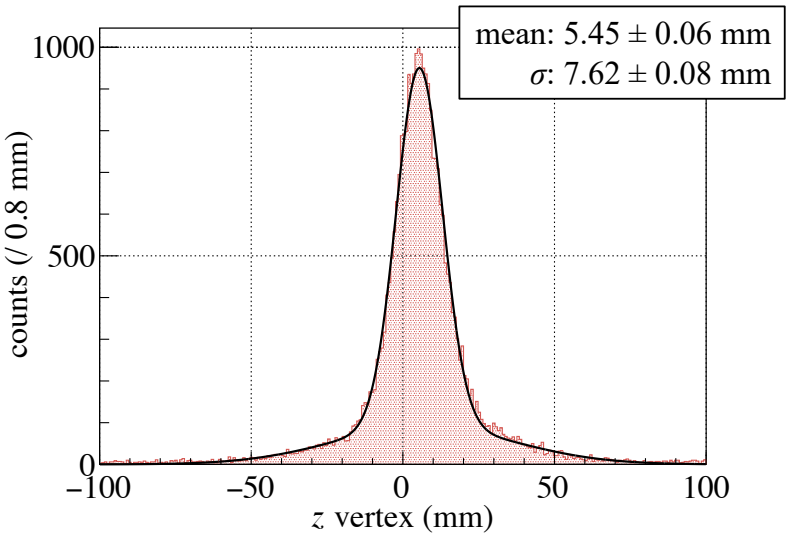

Figure 3.17: Reconstructed z-vertex distribution for elastic scattering events from the ^{181}Ta target. The distribution was fitted with a sum of two Gaussian functions to account for the background component. The center of the peak was extracted with a precision of approximately 0.06 mm, while the width was $\sigma \sim 7 - 8$ mm.

The momentum shift Δp was evaluated for each target foil (Ta1-Ta5) and plotted against the reconstructed z-vertex position, as shown in Figure 3.18. These results were obtained from data taken at a beam energy of $E_b = 180$ MeV. The upper panel of Figure 3.18 corresponds to a momentum setting of $\delta p \sim 14\%$ ($p_{\text{cent}} = 167.4$ MeV/c), which is relevant to decay π^- from ${}^{4}_{\Lambda}$H. The lower panel corresponds to $\delta p \sim -1\%$ ($p_{\text{cent}} = 192.6$ MeV/c), corresponding to decay π^- from ${}^{3}_{\Lambda}$H. The error bars represent statistical uncertainties from peak fitting for Δp, and the sum of statistical uncertainty and the Gaussian width σ for the z-vertex.

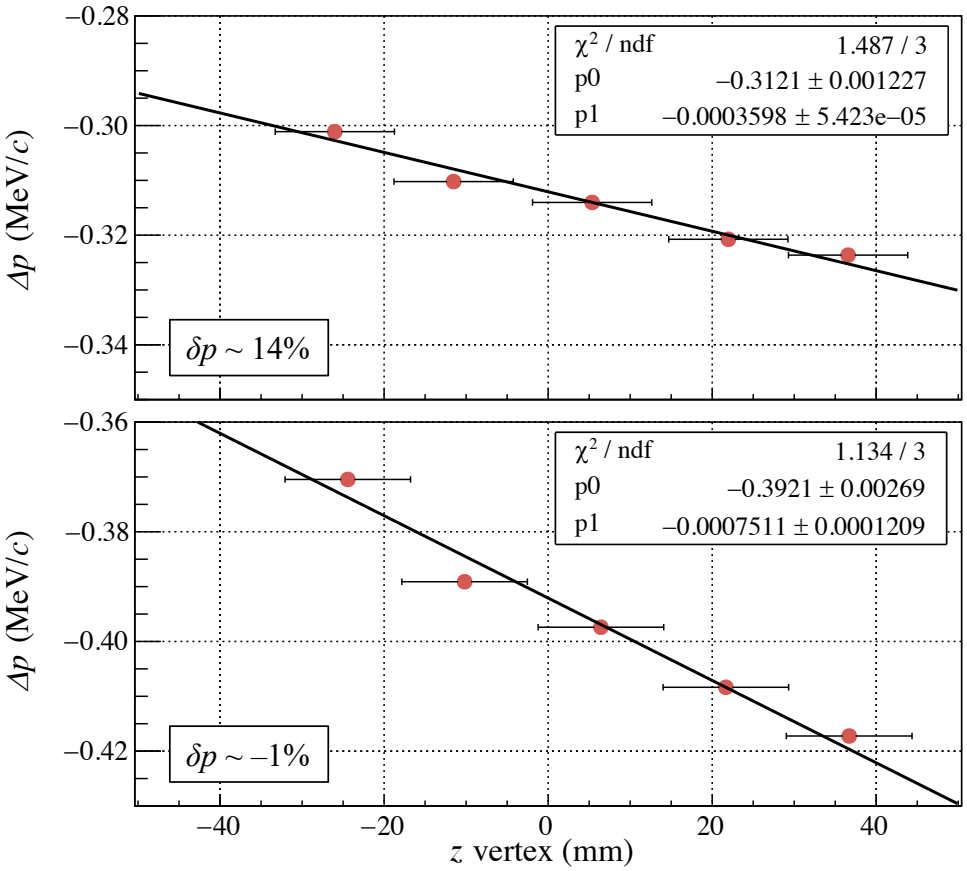

Figure 3.18: Correlation between the reconstructed z-vertex and the elastic peak momentum shift Δp for each target position at $E_b = 180$ MeV. Top: $\delta p \sim 14\%$ ($p_{\text{cent}} = 167.4$ MeV/c), corresponding to ${}^{4}_{\Lambda}$H decay π^-. Bottom: $\delta p \sim -1\%$ ($p_{\text{cent}} = 192.6$ MeV/c), corresponding to ${}^{3}_{\Lambda}$H decay π^-. Linear fits were applied to extract the z-dependence slope.

The figure clearly shows that the measured momentum exhibits a dependence on the z-position of the particle. Linear fits to each distribution yield a shift of approximately 3.6 keV/c per 10 mm in z for the $\delta p \sim 14\%$ case (upper panel), and approximately 7.5 keV/c per 10 mm in z for the $\delta p \sim -1\%$ case (lower panel).

The slope of the momentum shift exhibits a dependence on the relative momentum δp within the spectrometer acceptance. Figure 3.19 shows the correlation between the slope (where Δp is normalized by p_{m}) and δp, as obtained from this analysis.

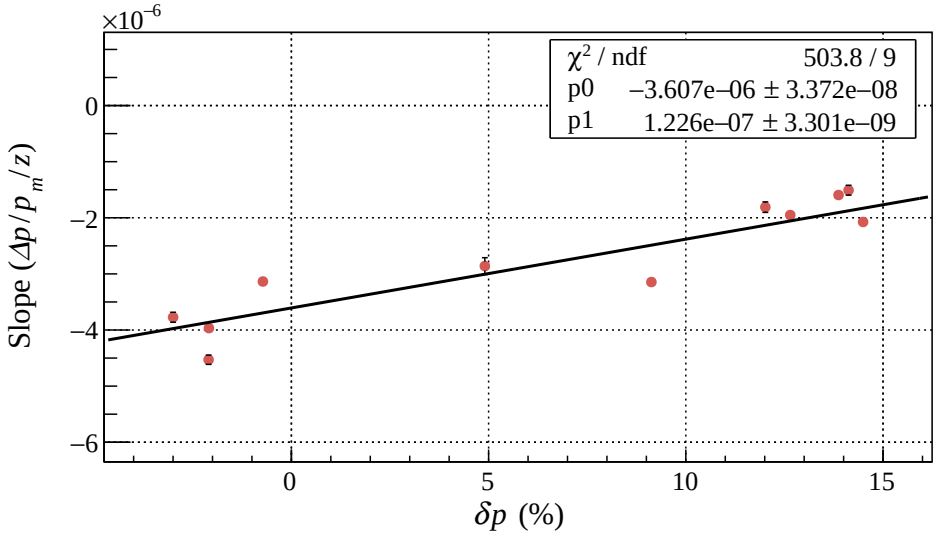

Figure 3.19: Correlation between the slope of $\Delta p/p_{\mathrm{m}}$ versus z-vertex and the relative momentum δp. A linear function was fitted to the data.

The magnitude of the slope is smaller in the higher momentum region compared to the lower momentum region and exhibits an approximately linear dependence over the entire momentum range. A linear function was fitted to the distribution, and the slope z_{slope} obtained from the fitting and the corresponding correction term z_{shift} were as follows:

$$\begin{aligned} z_{\mathrm{slope}} &= (1.22591 \times 10^{-7}) \times \delta p, \\ z_{\mathrm{shift}} &= z_{\mathrm{slope}} \times z_{\mathrm{vertex}}. \end{aligned} \tag{3.3.18}$$

The final correction term was incorporated into the momentum calculation as:

$$p''_{\mathrm{m}} = (1 + p_{\mathrm{shift}} + z_{\mathrm{shift}}) \times p_{\mathrm{cent.}} \times (1 + \delta p). \tag{3.3.19}$$

To evaluate the effectiveness of the z-position correction defined in Eq. 3.3.19, the width of the z-dependence in momentum was assessed before and after applying the correction, as shown in Figure 3.20. This histogram includes the full ^{181}Ta dataset (Ta1-Ta5) across all beam energies from $E_b = 180$ to 420 MeV. The mea-

sured Δp values were normalized by p_{m}, and the offsets were adjusted such that the central value is aligned to zero. Panel (a) shows the distribution before the z-position correction, while panel (b) shows the result after applying the correction.

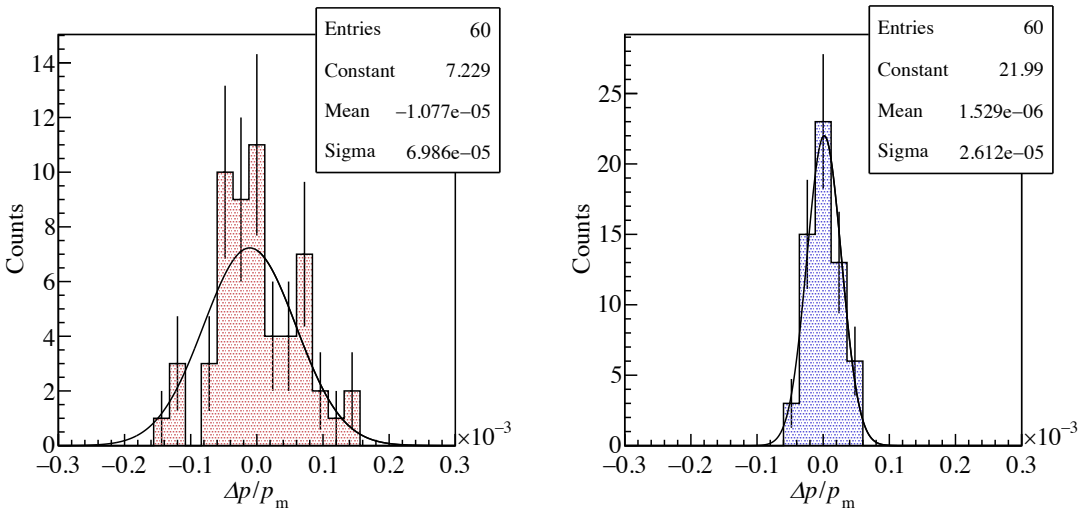

(a) Before correction (b) After correction

Figure 3.20: Evaluation of the momentum spread with respect to z-vertex position, (a) before and (b) after applying the z-dependent correction.

As a result of the z-position-dependent correction, the momentum spread was improved from $\sigma \sim 7.0\times10^{-5}$ to $\sigma \sim 2.6\times10^{-5}$. This corresponds to the uncertainty of $\sigma \sim 3.5$ keV/c to the hypernuclear decay π^- momentum (~ 133 MeV/c). This is also included as the final systematic error.

3.3.5 Calibration of absolute momentum

Finally, the absolute momentum is calibrated. The beam energy measurement using synchrotron radiation interferometry from the undulator is still in progress. Therefore, alternatively, the beam energy measured by MAMI is referenced as the same as that of the previous experiment at this moment. Beam energy measurement by MAMI was carried out only for $E_b = 420$ MeV data sets because the undulator method was not available for energies higher than around 220 MeV.

The reported value was $E_b = 420.18 \pm 0.160$ MeV, with an uncertainty of 0.160 MeV, consistent with previous measurements. Although the elastic scattering cross section is small at this energy (as described in Section 2.4.3), several hours of beam exposure were secured for each setup (combination of target and central momentum of the spectrometer), allowing the statistical error in peak fitting to be reduced to a few keV/c.

For each target, the difference $\Delta p = p_{\text{calc.}} - p_{\text{m}}$, as defined in Eq.2.3.7, was evaluated for the elastic scattering peak. The data set with ^{181}Ta target was used for the determination of the absolute value.

The calibration factor F_{calib} was defined, following previous work [Sch16], as:

$$F_{\text{calib}} = 1 + \frac{\Delta p}{p_{\text{m}}} \tag{3.3.20}$$

where p_{m} is the actual measured momentum of the elastic electrons. The corrected momentum is defined by multiplying the measured momentum by the calibration factor as

$$p_{\text{calibrated}} = F_{\text{calib}} \times p_{\text{m}}. \tag{3.3.21}$$

The resulting calibration factor for each momentum region is summarized in Table 3.4.

Table 3.4: Calibration factors derived from $E_b = 420$ MeV elastic scattering peaks.

Momentum region	$\delta p \sim -1.3\%$
p_{m} (MeV/c)	419.499 ± 0.004
Δp (MeV/c)	0.273 ± 0.004
Calibration factor	$1.000652(10)$

The obtained values of Δp is 0.273 ± 0.004 MeV/c at $\delta p \sim -1.3\%$. The calibration factor $F_{\text{calib}} = 1.000652(10)$, was adopted.

3.4 Tagging strangeness-produced events

The following section describes the analysis of the KAOS spectrometer, with the objective of identifying K^+ events. The KAOS detector consists of only scintillator walls, and the time and energy information was calibrated using the main background π^+ events. First, the calibration process and the basic resolution obtained as a result are summarized (Section 3.4.1). Next, the particle tracking method is described (Section 3.4.2), followed by an explanation of the particle identification procedure and the selection of strangeness production events (Section 3.4.3).

3.4.1 Time and energy calibration of KAOS detector

First, the time and energy information of the scintillator wall was calibrated using π^+ events, which constitute the main background. Figure 3.21 shows a simplified schematic view of the detector setup inside the KAOS spectrometer (a), along with a conceptual illustration of the TOF scintillator paddles. In the KAOS analysis, a coordinate system defined specifically within the spectrometer is employed. The particle emission direction is defined as the z_{Kaos} axis, the upward vertical direction (against gravity) as y_{Kaos}, and the x_{Kaos} axis is defined according to a left-handed coordinate system. The TOF wall consists of three layers–G, I, and H walls–each comprising scintillator paddles arranged along the x_{Kaos} direction. Paddle channels are numbered from 0 to 14 for G and I, and up to 29 for the H wall.

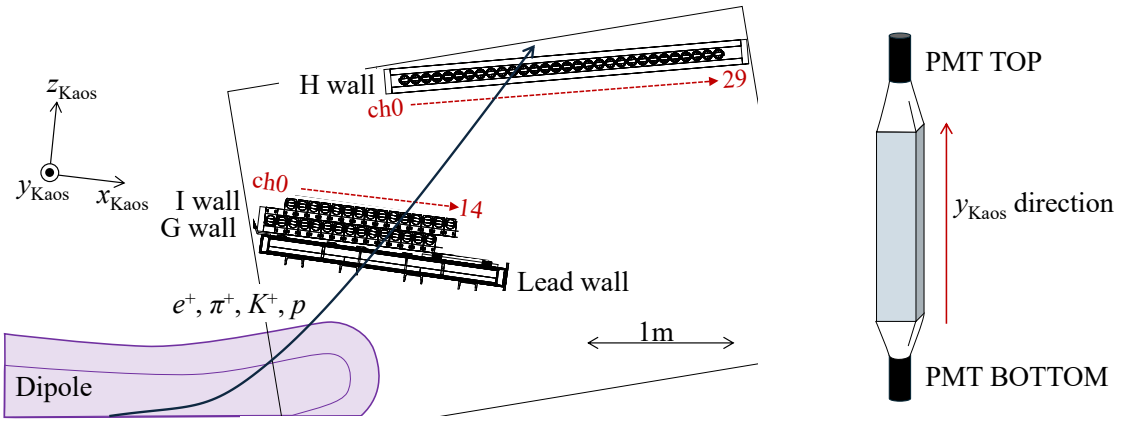

(a) Schematic view of KAOS (b) TOF Scintillator image

Figure 3.21: Schematic view of the KAOS detector and the TOF scintillator paddles. (a) Overview of the detector configuration inside KAOS. (b) Conceptual image of the TOF scintillator paddle, equipped with photomultiplier tubes (PMTs) at both the top and bottom ends.

For the time calibration, two parameters were adjusted: the TDC offset and a parameter related to the hit position along the y_{Kaos} direction (see Figure 3.21 (b)), calculated from the time difference between the signals from the upper and lower PMTs. The TDC offset for each paddle was calibrated such that the mean value of the time-of-flight (TOF, Δt) distribution per meter for π^+ events corresponds to $\beta = 1$, i.e., $\Delta t \sim 3.33$ ns/m. Figure 3.22 shows the time-of-flight distributions for paddle No. 3 of the G wall and paddle No. 5 of the H wall.

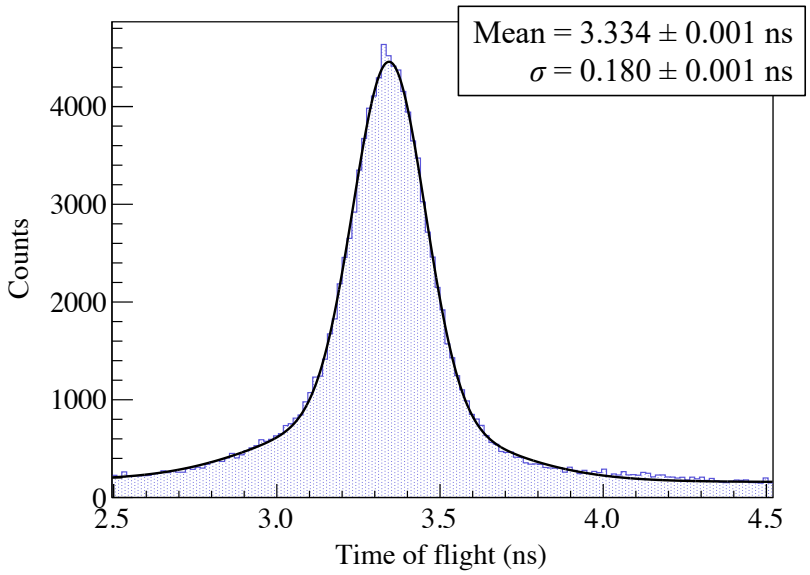

Figure 3.22: Time-of-flight distribution of KAOS TOF paddles. The figure shows the time-of-flight distributions for G wall paddle no. 3 and H wall paddle no. 5. Events with small energy loss are selected as π^+ event candidates. The fit function consists of a double Gaussian function and a linear function, with a central value of 3.33 ns/m. The obtained width from fitting is $\sigma = 180$ ps.

The depicted events correspond to π^+ event candidates with an energy loss of approximately 2 MeV/cm, which corresponds to the Minimum Ionization Particle (MIP). The distribution was fitted using a combination of a double Gaussian and a linear function. The center value is 3.33 ns, with $\beta = 1$. The TDC offset for each PMT was adjusted to ensure that this center value remains 3.33 ns for all possible TOF paddle combinations in the design.

In parallel, the y_{Kaos} hit position was also calibrated. The position is defined as:

$$\begin{aligned} y_{\text{Kaos}}\ \text{position} &= (t_{\text{TOP}} - t_{\text{BOTTOM}}) * \text{slope}, \\ \text{slope} &= \text{paddle size}/6\sigma \end{aligned} \tag{3.4.1}$$

where “TOP”and “BOTTOM”denote the TDC values from the upper and lower PMTs, respectively. The TDC offsets of the top and bottom PMTs were adjusted such that the hit position of particles was centered within the paddle. The slope parameter was further tuned so that the 6σ spread of the hit distribution matched the full length of the scintillator paddle. The calibration procedure involved iterating the adjustment of the inter-paddle TDC offsets using the time-of-flight (TOF) of π^+ events and the alignment of the y_{Kaos}-position distribution. Additionally, as the data were acquired using a constant fraction discriminator (CFD) module (GSI CF 8105), which generates timing signals at a constant fraction of the input pulse height, the timing was effectively independent of signal amplitude. This minimized the time-walk effect and eliminated the need for slewing correction. As a result, no significant second-order correlation was observed between TDC and ADC values.

Figure 3.23 shows the distributions of hit positions in the y_{Kaos}-direction for each calibrated TOF scintillator wall. The red lines indicate the physical boundaries of the scintillator paddles. While the hit positions for the G and I walls are concentrated near the center, the distribution for the H wall is more diffuse. This broadening is attributed to multiple scattering as particles pass through the two-layer aerogel cerenkov detector and the intervening air layer, both located downstream of the G and I walls. The time resolution of each TOF paddle is approximately $\sigma \sim 0.1$ ns. Taking into account the corresponding spatial uncertainty (position leakage) due to this timing resolution, events falling within the shaded region were selected for further analysis.

The energy was also calibrated using the π^+ event. After the pedestal position was determined for the ADC information from each PMT, a factor was determined so that the MIP peak of π^+ would be 2 MeV/cm.

The data acquisition was performed by switching runs approximately every hour. The calibration parameters for time and energy were individually determined for each run, ensuring stability throughout the entire beam time.

Figure 3.24 shows the final time and energy resolutions obtained for each scintillator paddle after the calibration procedure. The time resolution was approximately $\sigma \sim 0.1$ ns. The time resolution of each paddle was determined by measuring the time-of-flight (TOF) for all combinations of the GI, IH, and HG wall pairs. The energy resolution was approximately 0.20 MeV/cm for the G and I walls, and about 0.12 MeV/cm for the H wall. Both the time and energy resolutions achieved in this work are comparable to those reported in a previous study [Nag15].

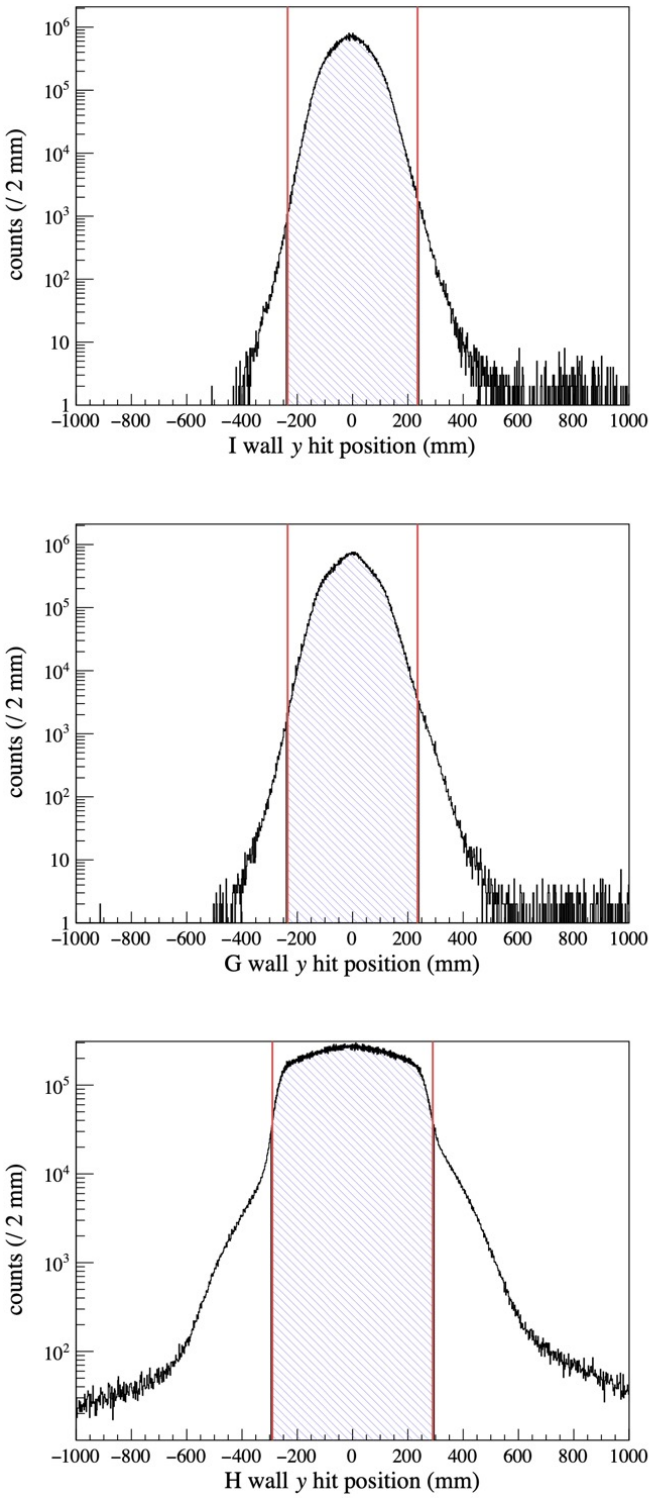

Figure 3.23: y hit position distribution for each scintillator walls. The red line indicates the actual size of the paddle. The shaded area is the event used in subsequent analyses. The area of $+5$ mm was selected, taking into account blunting due to time resolution.

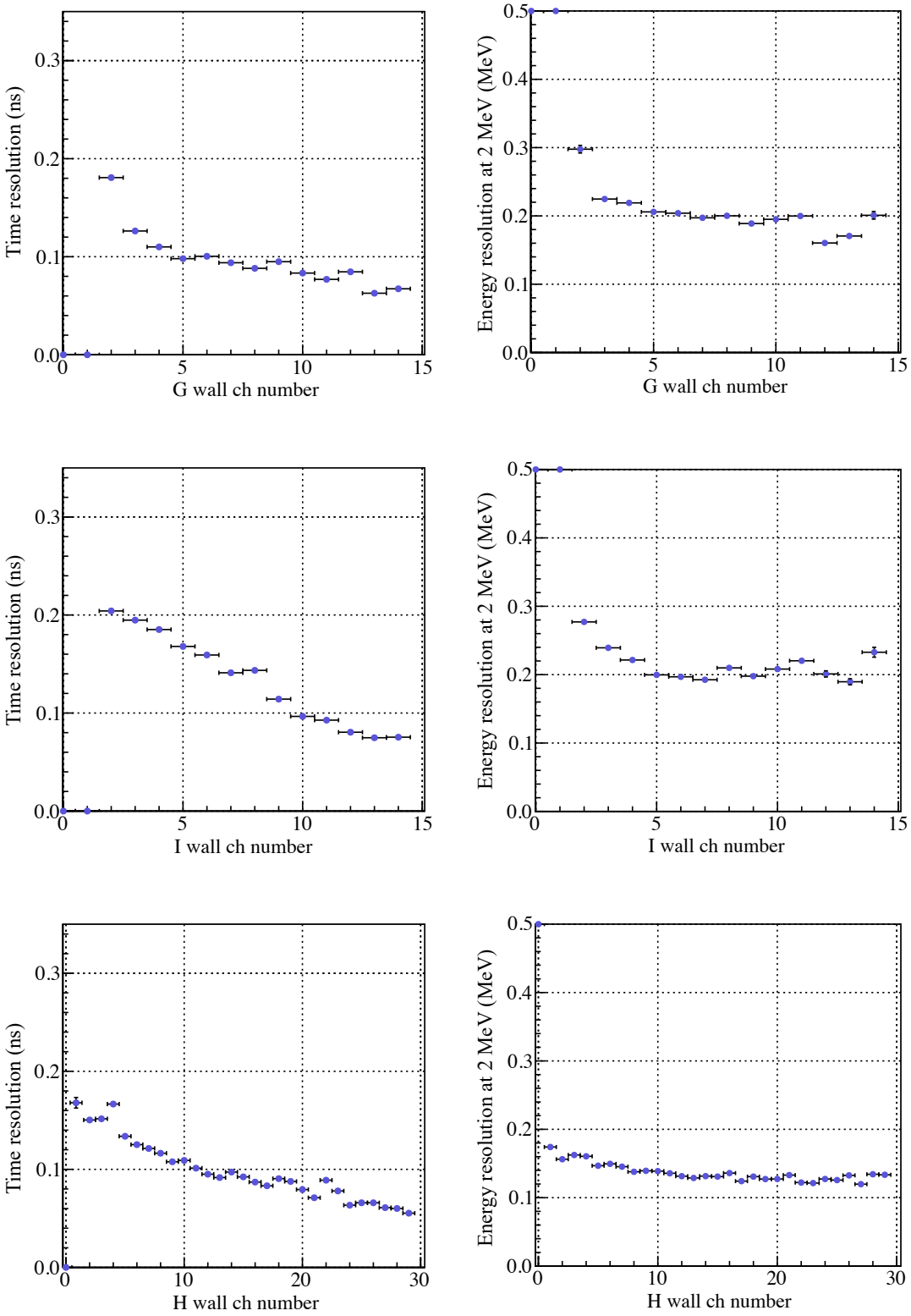

Figure 3.24: Time and energy resolution for each scintillator paddle in KAOS. The left column shows the time resolution for π^+ events at $\beta = 1$, and the right column shows the energy resolution for π^+ events at 2 MeV/cm.

3.4.2 Particle tracking

Particle position and angle were reconstructed using hit information from the G, I, and H scintillator walls in the KAOS spectrometer. All possible combinations of hits across the three walls were considered. For each combination, a straight-line fit was performed in both the $x_{\text{Kaos}} - z_{\text{Kaos}}$ and $y_{\text{Kaos}} - z_{\text{Kaos}}$ planes, and the goodness of fit was evaluated using the χ^2 value.

Figure 3.25 shows the resulting χ^2 distribution. Events with χ^2 values smaller than the threshold indicated by the blue dashed line were selected for further analysis. In this analysis, three hit points were used to fit a straight line, leading to one degree of freedom ($ndf = 3 - 2 = 1$) since the fit involved two parameters. Therefore, the resulting χ^2 distribution follows a χ^2 distribution with one degree of freedom, with an expected value around 1. A commonly used selection criterion is $\chi^2 < 4$, which corresponds to approximately 95% confidence level for one degree of freedom.

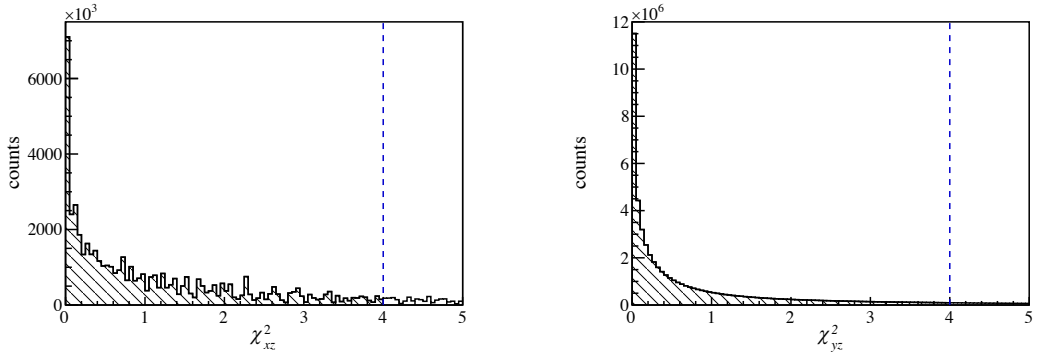

Figure 3.25: Chi-square distribution of particle tracking in KAOS. The left figure shows the distribution for tracking in the $x-z$ direction, and the right figure shows the distribution for tracking in the $y - z$ direction. The area smaller than the blue dotted line was used in later analysis.

3.4.3 Kaon identification

Figure 3.26 shows the correlation between β, averaged energy loss at G, I, and H paddle, and momentum obtained by KAOS. In the correlation between β and momentum, a clear π^+ locus appears around $\beta = 1$. Proton events form a separate locus in the region $0.4 < \beta < 0.8$. These major background components were efficiently removed using this correlation. In the correlation between energy loss and momentum, π^+ events are distributed around 2 MeV/cm, and proton events

are distributed in the region of $dE/dx > 3$ MeV/cm. This correlation was also used as an auxiliary means to remove background events, along with β and momentum correlation.

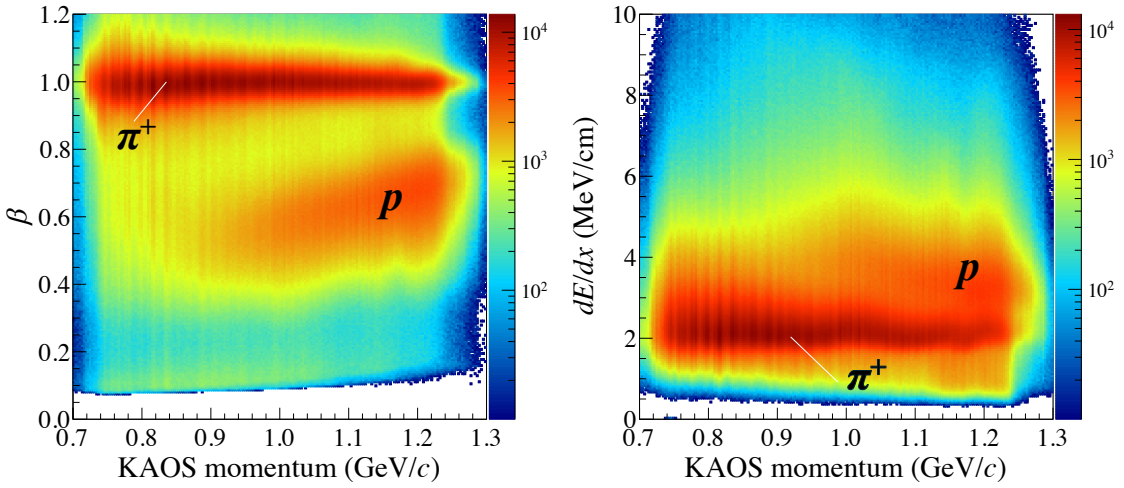

Figure 3.26: Correlation between β, energy loss and momentum in KAOS. The left figure shows the correlation between β and momentum, and the right figure shows the correlation between energy loss and momentum. π^+ and proton event distributions are clearly visible and effectively removed using these correlations.

K^+ should also be selected using the same correlation distribution. However, because there is not enough resolution to see a clear K^+ distribution and there are too many background events, an indirect event selection method was adopted instead of a direct one.

Two types of cut conditions are defined for K^+ event selection. The first is the likelihood cut:

$$\begin{aligned}\chi^2_{\text{likeli}} = &\left(\frac{\beta - \beta_{K^+}}{w_\beta}\right)^2 + \left(\frac{dE/dx - dE/dx_{K^+}}{w_{dE/dx}}\right)^2_G \\ &+ \left(\frac{dE/dx - dE/dx_{K^+}}{w_{dE/dx}}\right)^2_I + \left(\frac{dE/dx - dE/dx_{K^+}}{w_{dE/dx}}\right)^2_H\end{aligned} \tag{3.4.2}$$

Here, the subscript K^+ denotes the mean value of the K^+ event distribution, and the denominator w represents the width of the distribution, which reflects the detector resolution in time and energy. In this cut, events are selected based on their consistency with the expected mean values of TOF (dt) and the energy loss (dE/dx) in each scintillator paddle, with smaller deviations contributing to lower χ^2_{likeli} values.

The second is the threshold cut:

$$\left(\frac{\beta-\beta_{K^+}}{w_\beta}\right)^2 < 1 \otimes \left(\frac{dE/dx-dE/dx_{K^+}}{w_{dE/dx}}\right)^2_G < 1 \\ \otimes \left(\frac{dE/dx-dE/dx_{K^+}}{w_{dE/dx}}\right)^2_I < 1 \otimes \left(\frac{dE/dx-dE/dx_{K^+}}{w_{dE/dx}}\right)^2_H < 1 \tag{3.4.3}$$

Each term has the same meaning as in the likelihood cut. In this cut, only events lying within one standard width of the K^+ mean values in all observables are accepted, and any events falling outside are excluded.

The width parameters w represent the spread of each observable around its mean due to the intrinsic time and energy resolution of the detectors. Note that the width parameters w appearing in both the likelihood and threshold cuts refer to the same quantities and are consistently defined based on the detector resolution. Their values are chosen based on a balance between maximizing signal retention and minimizing background contamination. A detailed discussion on the determination of these widths is provided later.

To select K^+ events according to these cut conditions, the mean value of the K^+ distribution for each physical quantity was first determined. First, the mean value for TOF, i.e., β, was determined. This is because it has a better resolution compared to the energy loss. As mentioned above, it is difficult to directly see the distribution of K^+ events, so the mean value was determined relatively. Figure 3.27 shows how the mean value of the K^+ distribution for β was determined.

First, the mean β values for π^+ and p were determined via slice fitting (Figures 3.27 (a), (b)). To isolate the precise distribution for each particle species, selection cuts were applied to the energy loss regions: $1.8 < dE/dx$ (MeV/cm) < 2.2 for π^+, and $3 < dE/dx$ (MeV/cm) < 8 for p. Each error bar represents a 1σ uncertainty. Since protons lose energy while passing through the scintillator paddles, the measured β corresponds to a momentum lower than the initial value. This implies that the reconstructed velocity reflects an effective momentum, $p_{\text{eff}} = p_{\text{in}} - \Delta p$, where Δp represents the momentum loss along the particle trajectory.

Assuming that K^+ particles undergo a similar energy loss, their effective momentum can be estimated based on the relative shift observed between the π^+ and p distributions. Using this, the expected $\beta-$momentum correlation for K^+ was plotted in Figure 3.27 (c). A theoretical curve based on the expression $\beta = p_{\text{eff}}/\sqrt{p^2_{\text{eff}} + m^2_{K^+}}$ was fitted to the numerical center positions obtained from this correlation. From this fit, the mean value β_{K^+} was deduced.

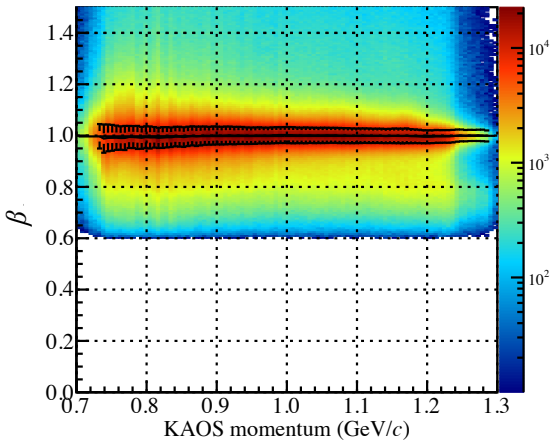

(a) π^+ peak fit

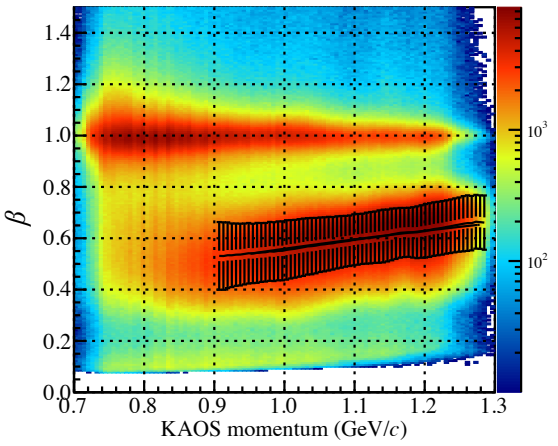

(b) proton peak fit

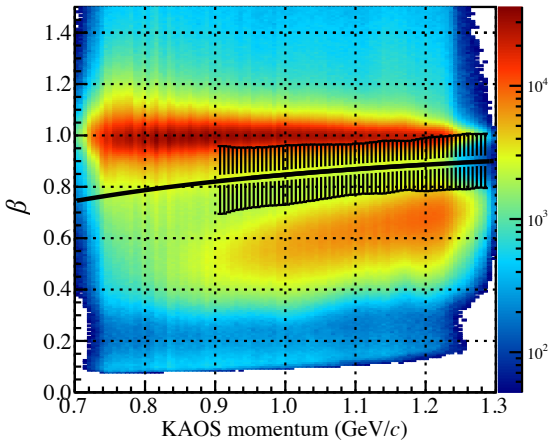

(c) K^+ mean value plot

Figure 3.27: Determination of the central $\beta-$momentum correlation for each charged particle. (a) Slice fitting was performed for $^+$ events selected in the energy loss region $1.8 < dE/dx$ (MeV/cm) < 2.2. (b) Slice fitting was performed for proton events selected in the energy loss region $3 < dE/dx$ (MeV/cm) < 8. (c) The $\beta-$momentum correlation for K^+ was estimated based on the relative positions of the $^+$ and p distributions obtained in (a) and (b), taking into account energy loss in the scintillator. The resulting numerical center positions for K^+ were plotted, and a theoretical curve defined by $\beta = p_{\text{eff}}/\sqrt{p_{\text{eff}}^2 + m_{K^+}^2}$ was fitted to them. The error bars in (c) reflect the propagated 1σ uncertainties derived from the $^+$ and proton distributions.

Next, the mean energy loss in the scintillator paddles was determined. Since the energy loss distribution for protons spans a broad region, fitting procedures to extract peak centers are not suitable for reliably identifying each particle species. Instead, the mean dE/dx value for K^+ was uniquely determined from the $dE/dx-\beta$ correlation.

Figure 3.28 shows the measured $dE/dx - \beta$ correlation for all charged particles. As described in Eq. 3.3.2, the Bethe-Bloch formula predicts that, for particles with the same charge, the energy loss dE/dx follows a curve:

$$\frac{dE}{dx} \propto \frac{1}{\beta^2}. \tag{3.4.4}$$

Since π^+, p, and K^+ all have electric charge $+1$, they are distributed along a common curve. To quantify this correlation, slice fitting was performed on the distribution, and the extracted mean values were fitted with a function of the form a/β^2, where a is a free parameter. This procedure allowed for the determination of a representative $dE/dx - \beta$ correlation function.

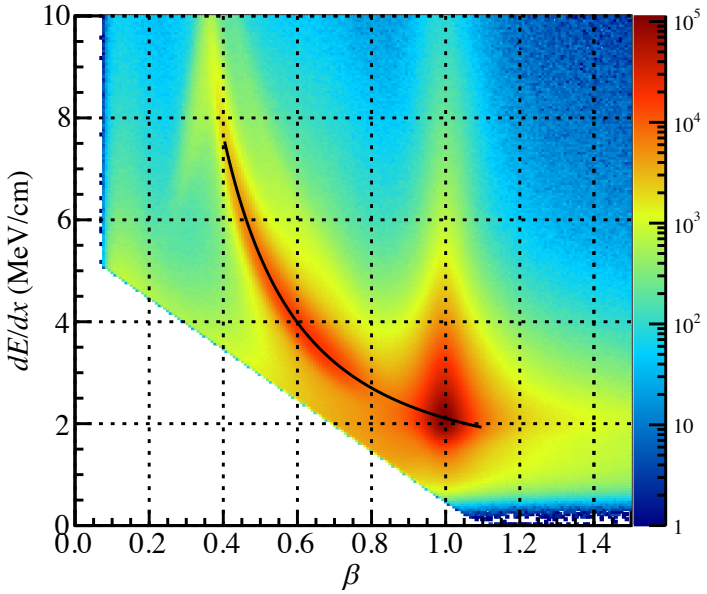

Figure 3.28: Measured correlation between energy loss (dE/dx) and β for all charged particles. Since π^+, K^+, and p all have charge $+1$, they follow a common $1/\beta^2$ trend as predicted by the Bethe-Bloch formula. Slice fitting was applied to the distribution to extract mean values, and a curve of the form a/β^2 was fitted to these points to obtain the $dE/dx - \beta$ correlation. To simplify the fit, events in the low-momentum region with large background contributions were removed in advance.

Based on the obtained $dE/dx - \beta$ correlation, the expected dE/dx values for K^+ were estimated from its momentum and β_{K^+}. Figure 3.29 shows the correlation between particle momentum and scintillator paddle channel. From this figure, it can be seen that for the G and I walls, there is no clear correlation between channel number and particle momentum, indicating that all paddles cover a wide

momentum range. Therefore, for the G and I walls, the average momentum was calculated for each paddle channel, and the corresponding dE/dx was estimated using this mean momentum and the previously obtained β_{K^+}.

In contrast, a clear correlation between momentum and paddle channel was observed for the H wall. Hence, for the H wall, the most probable momentum value was taken for each channel, and the corresponding dE/dx was estimated in the same manner using the previously determined β_{K^+}.

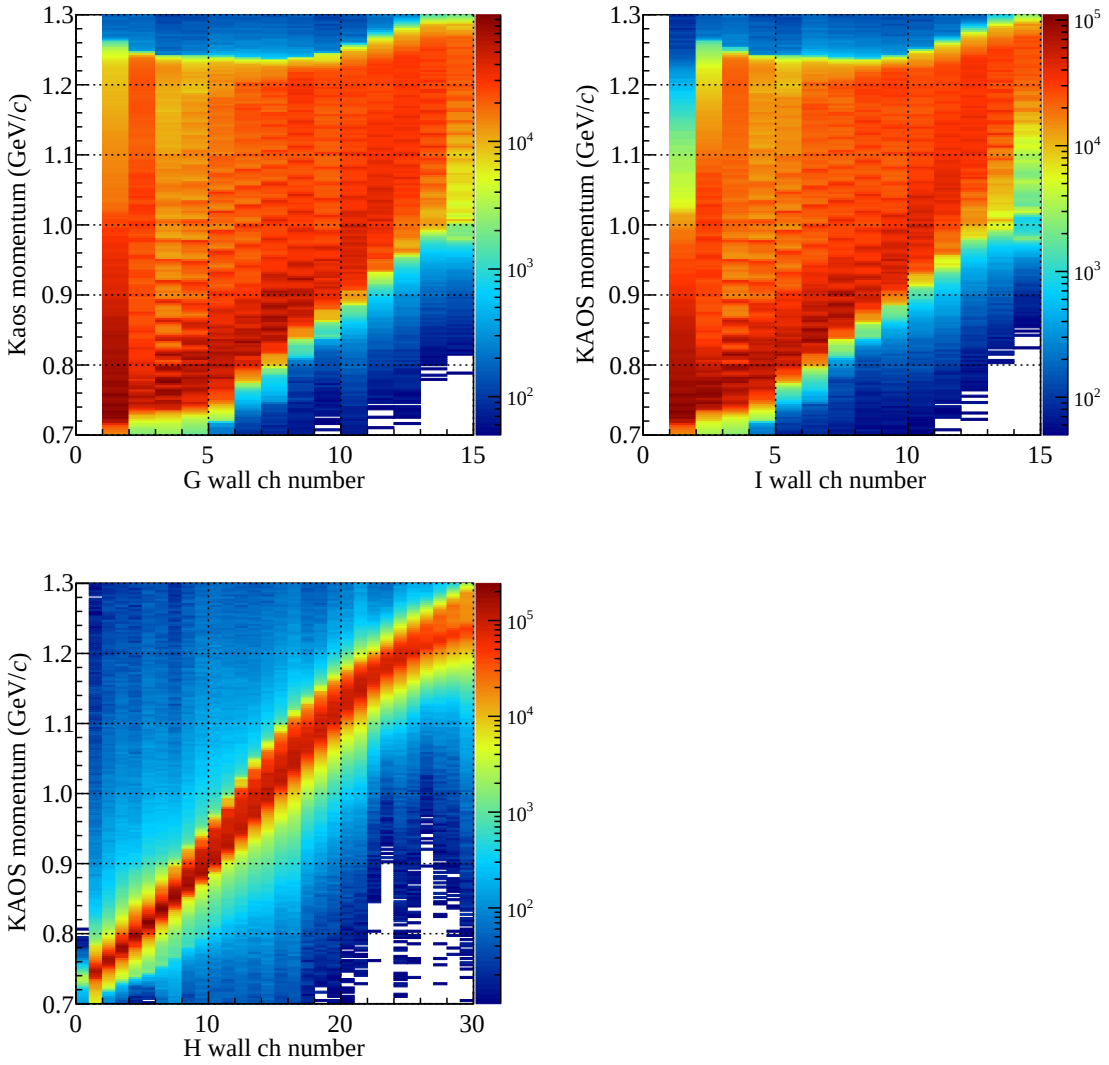

Figure 3.29: Correlation between momentum and TOF paddle numbers. For the G and I walls, no clear correlation is observed, and most channels cover a broad range of momenta. In contrast, the H wall exhibits a distinct correlation between paddle number and momentum.

The estimated dE/dx values for each channel are plotted in Figure 3.30. For the G and I walls, where no significant correlation between channel number and momentum exists, a standard second-order polynomial was used as the fitting function. For the H wall, where such a correlation is present, the function

$$\begin{aligned} \frac{dE}{dx} \propto \frac{1}{\beta^2} &= \left(\frac{\sqrt{p^2+m^2}}{p} \right)^2, \\ f &= C \cdot \left(\frac{\sqrt{p^2+m_{K^+}^2}}{p} \right)^2 + \text{const.} \end{aligned} \tag{3.4.5}$$

was adopted to reflect the momentum dependence of energy loss. From this analysis, the mean energy loss dE/dx_{K^+} was determined.

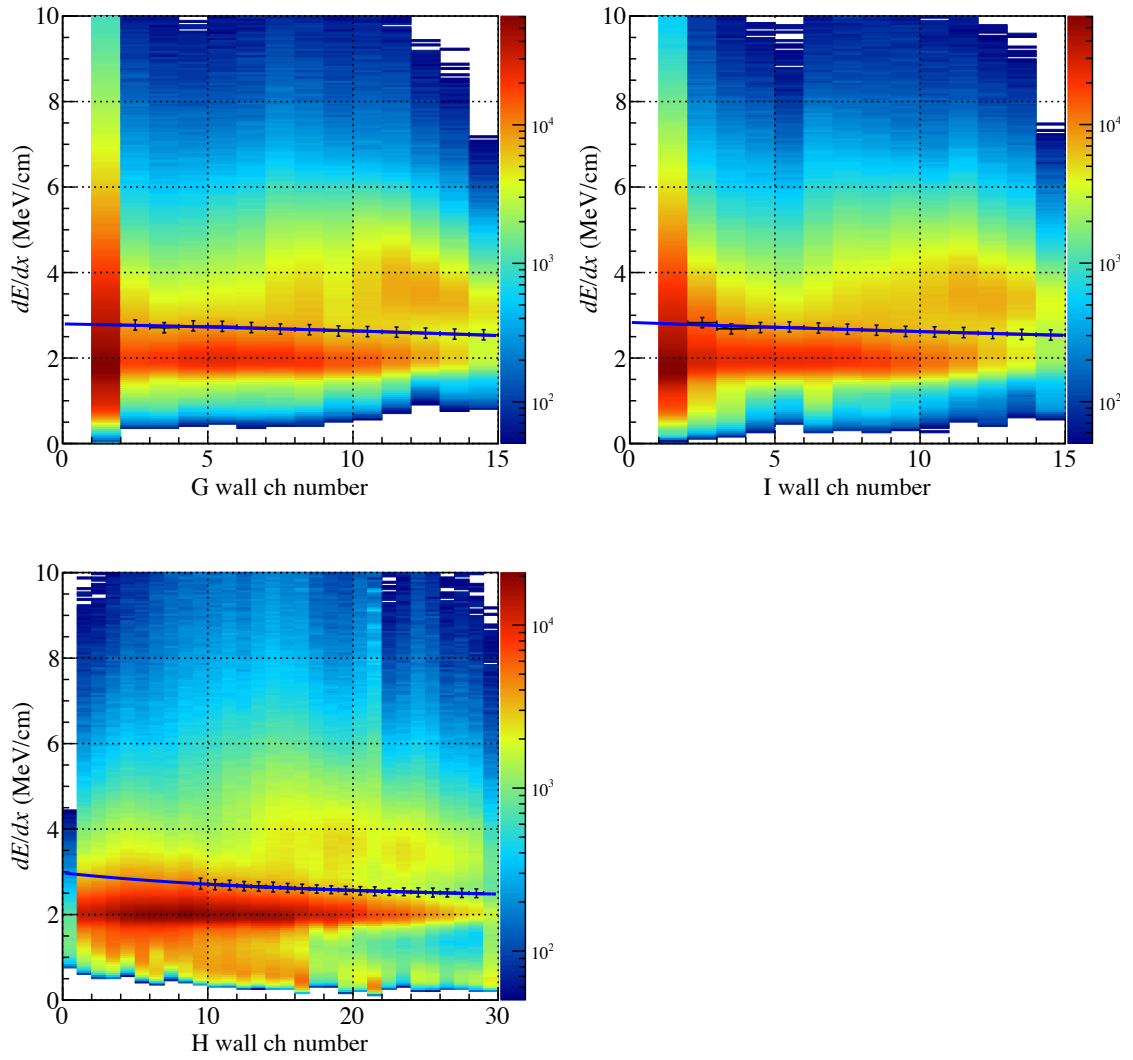

Figure 3.30: Correlation between dE/dx and paddle channel number for each TOF wall. Estimated dE/dx values were plotted using the $dE/dx - \beta$ correlation function, the β_{K^+} value for each channel, and the average momentum (or the most probable value in the case of the H wall). The error bars reflect the uncertainty derived from the fit of the $dE/dx - \beta$ correlation. A second-order polynomial was fitted to the G and I wall data, while a mass-momentum relation function was fitted to the H wall data. The fitted curves are shown in blue.

The widths w_β and $w_{dE/dx}$ associated with the previously determined mean values were then evaluated. Figure 3.31 presents the correlations among each parameter used in the cut conditions, where β has been converted to the time-of-flight per meter (dt). In all panels, the zero point on the vertical axis corresponds to the mean value of K^+.

Because the mass difference between π^+ and K^+ is smaller than that between

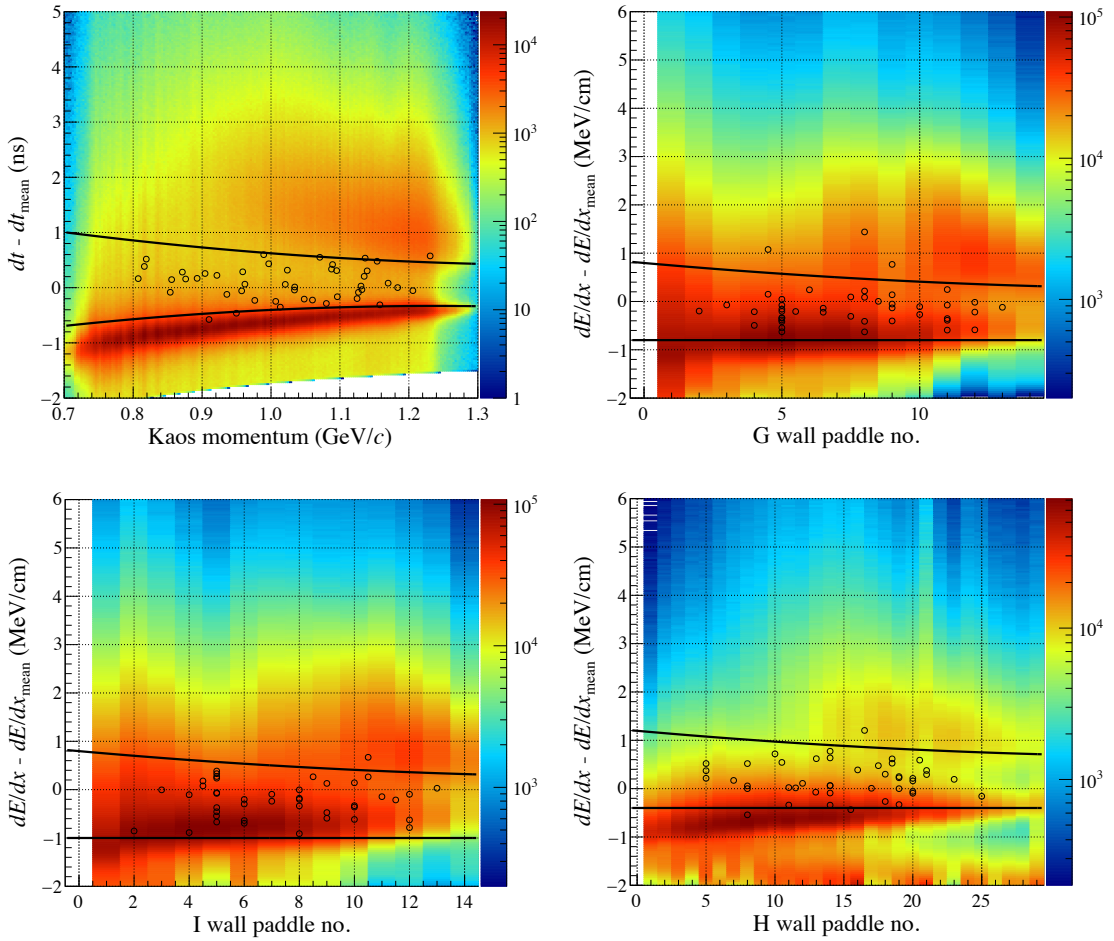

Figure 3.31: Width for each cut condition element. The correlation between β and momentum (top left) and the energy loss distributions in each scintillation wall are shown. In all figures, the zero point on the vertical axis ($y = 0$) corresponds to the mean value of K^+ events, as determined in Figures 3.27 and 3.30. After all PID analyses were completed, candidate events for ${}^{4}_{\Lambda}$H—identified as described in Section 3.5—were used to validate the adequacy of the cut conditions. These events are overlaid as circles in each plot.

p and K^+, narrower widths were applied on the π^+ side for both TOF and dE/dx. For β (or dt), where the resolution is relatively good, the width was chosen to effectively suppress contamination from π^+ and proton distributions. In contrast, for dE/dx, where the resolution is limited, a wider range was selected to avoid excessive signal loss.

Circles overlaid in the plots show the distribution of ${}^{4}_{\Lambda}$H candidate events, which were used after the main PID analysis to validate the adequacy of the cut conditions. These events were selected using a threshold cut where three of the four variables were fixed to their respective K^+ widths, and only the parameter under inspection

was varied. Here, the "four variables" refer to the four terms included in the K^+ selection criteria defined in Eqs. 3.4.2 and 3.4.3: the TOF-based velocity β and the energy losses dE/dx measured in the G, I, and H scintillator paddles. The events were further required to have momenta measured by SpekA around 132.70 ± 0.05 MeV/c, and to be in proper coincidence timing between SpekA and KAOS. The resulting distribution confirms that the adopted cut conditions effectively identify K^+ events.

After determining the appropriate widths, a final selection of K^+ events was made using the logical AND of the likelihood cut and the threshold cut. Figure 3.32 shows the dE/dx distributions for the identified K^+, π^+, and p candidate events. For better visibility, the π^+ events are scaled by a factor of $1/100$, and the proton events by a factor of $1/50$. Despite the overlap in the energy loss distributions caused by limited resolution, a clustering structure is visible around the expected dE/dx value for K^+, due to the additional constraint from the β-based cuts.

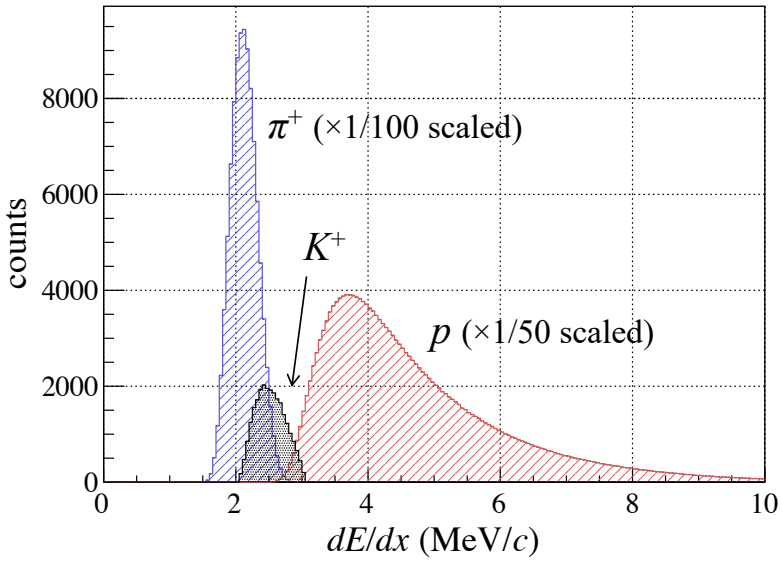

Figure 3.32: Final dE/dx distributions for identified K^+, π^+, and p events after applying both likelihood and threshold cuts. The π^+ and proton events are scaled by factors of $1/100$ and $1/50$, respectively, to improve visibility. A clustering structure is observed near the expected dE/dx value for K^+, indicating successful separation despite overlapping distributions due to limited energy resolution.

3.5 Coincidence time and momentum distribution

After the preceding analyses, the data from SpekA and KAOS were merged based on matching event IDs, and events with the correct particle combinations were selected by identifying the peak position in the trigger coincidence time distribution between the two spectrometers.

3.5.1 Evaluation of particle identification purity

By applying the particle identification (PID) procedure for KAOS described in the previous section, it was confirmed that the coincidence time distribution between SpekA and KAOS, shown in Figure 2.30, exhibits distinct peak positions corresponding to the mass differences of each particle species, as illustrated in Figure 3.33.

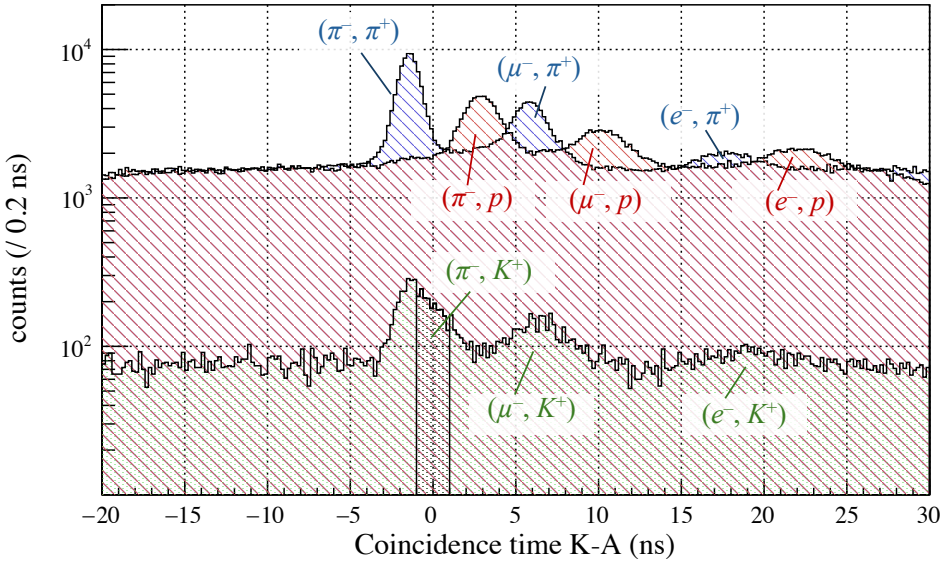

Figure 3.33: Coincidence time distribution between SpekA and KAOS for different particles. Blue shaded areas represent π^+ events, red represent protons (p), and green represent K^+ events. Additional peaks corresponding to μ^- and e^- emitted from π^- decays are also observed in SpekA. The $(\text{SpekA}, \text{KAOS}) = (\pi^-, K^+)$ coincidence peak is partially contaminated by π^+ events.

In the figure, events identified as π^+ by KAOS are shown as blue shaded areas, protons (p) as red shaded areas, and K^+ as green shaded areas. On the SpekA side, additional peaks corresponding to μ^- and e^- emitted from π^- decay are observed. Events identified as K^+ include residual π^+ contamination, which could not be completely removed due to the limited time resolution, as evidenced by a peak structure to the left of the $(\text{SpekA}, \text{KAOS}) = (\pi^-, K^+)$ coincidence peak, coinciding with the timing of the (π^-, π^+) coincidence peak.

The purity of particle identification was evaluated for the (π^-, K^+) coincidence peak. Figure 3.34 shows the coincidence time distribution between SpekA and KAOS for events identified as K^+. To account for contamination from (π^-, π^+) and (μ^-, π^+) coincidence events near 0 ns, the distribution was modeled by fitting a function (black line) composed of Gaussian components (green and blue lines) representing the (π^-, K^+) and (π^-, π^+) coincidences, exponential components (red dashed lines) representing (μ^-, π^+) coincidences, and a linear background component accounting for accidental coincidences.

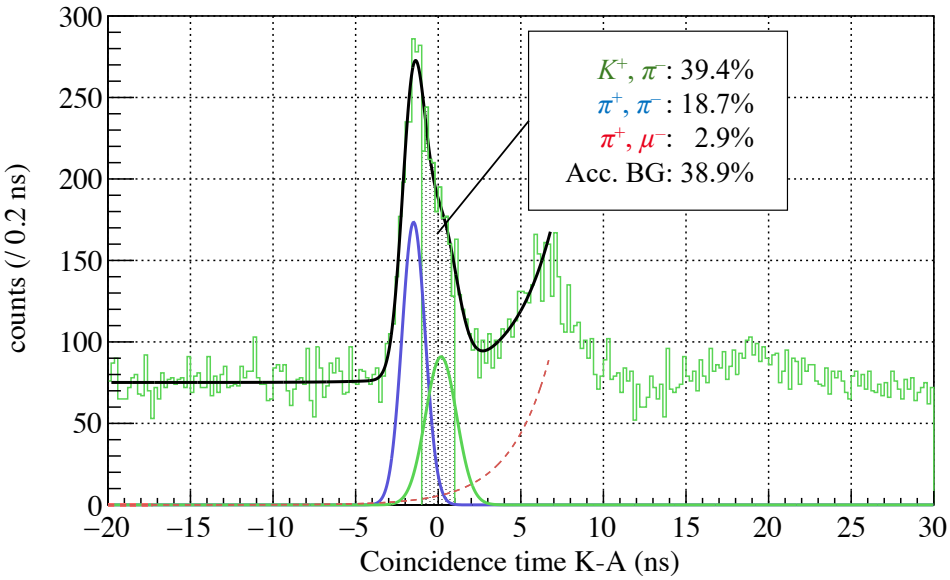

Figure 3.34: Coincidence time distribution between SpekA and KAOS for K^+ events. The fitting includes Gaussian components for (π^-, K^+) and (π^-, π^+) coincidences, an exponential component for (μ^-, π^+) coincidences, and a linear component for accidental background.

Selecting the region within ± 0.98 ns (shaded area in the figure) as the (π^-, K^+) coincidence window, the fraction of each contribution was evaluated based on the fitted areas. The resulting composition was as follows: (π^-, K^+): 39.4%, (π^-, π^+): 18.7%, (μ^-, π^+): 2.9%, and accidental background: 38.9%. Based on this estimation, the number of events identified as K^+ in this study was 618 events.

3.5.2 Final momentum distribution

Figure 3.35 shows the coincidence time distributions between SpekA and KAOS (left column) and the corresponding momentum distributions measured by SpekA (right column) for each particle species: K^+ (a), π^+ (b), and p (c). For each particle, the filled black regions in the coincidence time spectra indicate the main

peaks selected for analysis, and the corresponding momentum distributions are shown in the right column. Additionally, accidental backgrounds, selected from the sideband regions (shaded areas), are plotted as black dots. The accidental distributions are scaled to match the width of the coincidence time window used for the main peak selection.

As shown in the figure, the momentum distributions for π^+ and p events are relatively flat and do not exhibit distinct peak structures. In contrast, the momentum distribution for K^+ events shows clear peaks around 114 MeV/c and 133 MeV/c.

To validate that the observed peak structures are not due to artifacts introduced by the binning process, a p-value scan was conducted, as shown in Figure 3.36.

In this evaluation, the background within the range of $115 - 130$ MeV/c was modeled by a linear function. The statistical significance at each point was defined as $S/\sqrt{S+N}$, where S is the number of signal events and N is the number of background events within a 100 keV/c bin. The p-value was evaluated by scanning the momentum range in 40 keV/c steps.

As a result, the peak near 114 MeV/c was found to exceed 3σ, and the peak near 133 MeV/c exceeded 5σ, confirming that these structures are statistically significant and not artifacts of binning.

By comparing the observed peaks with the decay π^- momenta of hyperfragment candidates listed in Table 2.2, the peak near 133 MeV/c is uniquely identified as originating from the decay of ${}^{4}_{\Lambda}\mathrm{H}$, while the peak near 114 MeV/c is identified as that of ${}^{3}_{\Lambda}\mathrm{H}$.

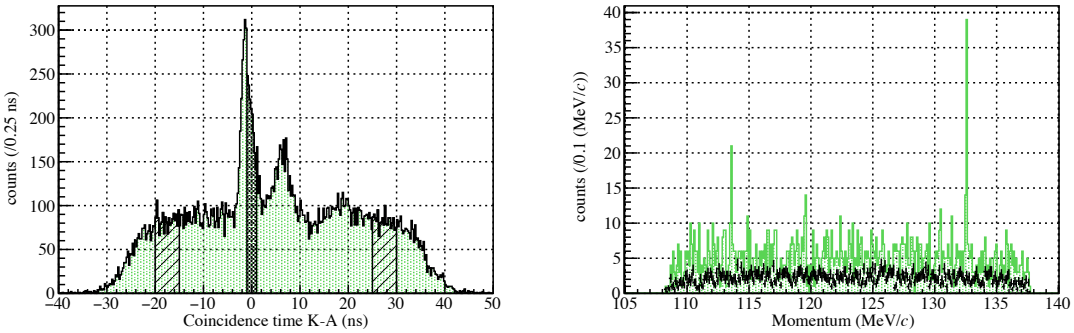

(a) (π^-, K^+) event selected

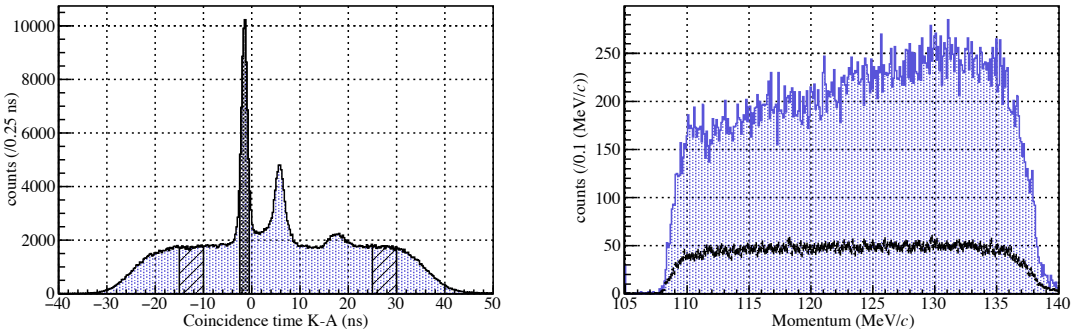

(b) (π^-, π^+) event selected

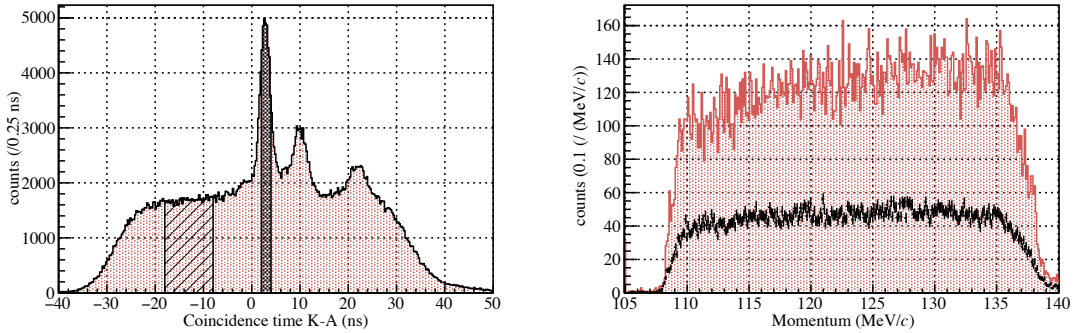

(c) (π^-, p) event selected

Figure 3.35: Coincidence time distributions (left column) and corresponding momentum distributions measured by SpekA (right column) for each particle species: (a) K^+ events, (b) π^+ events, and (c) p events. The black filled regions indicate the main coincidence peaks selected for analysis. The accidental backgrounds, selected from the sidebands (shaded areas), are shown as black dots and scaled to match the main peak window. A clear peak structure is observed for the K^+ events.

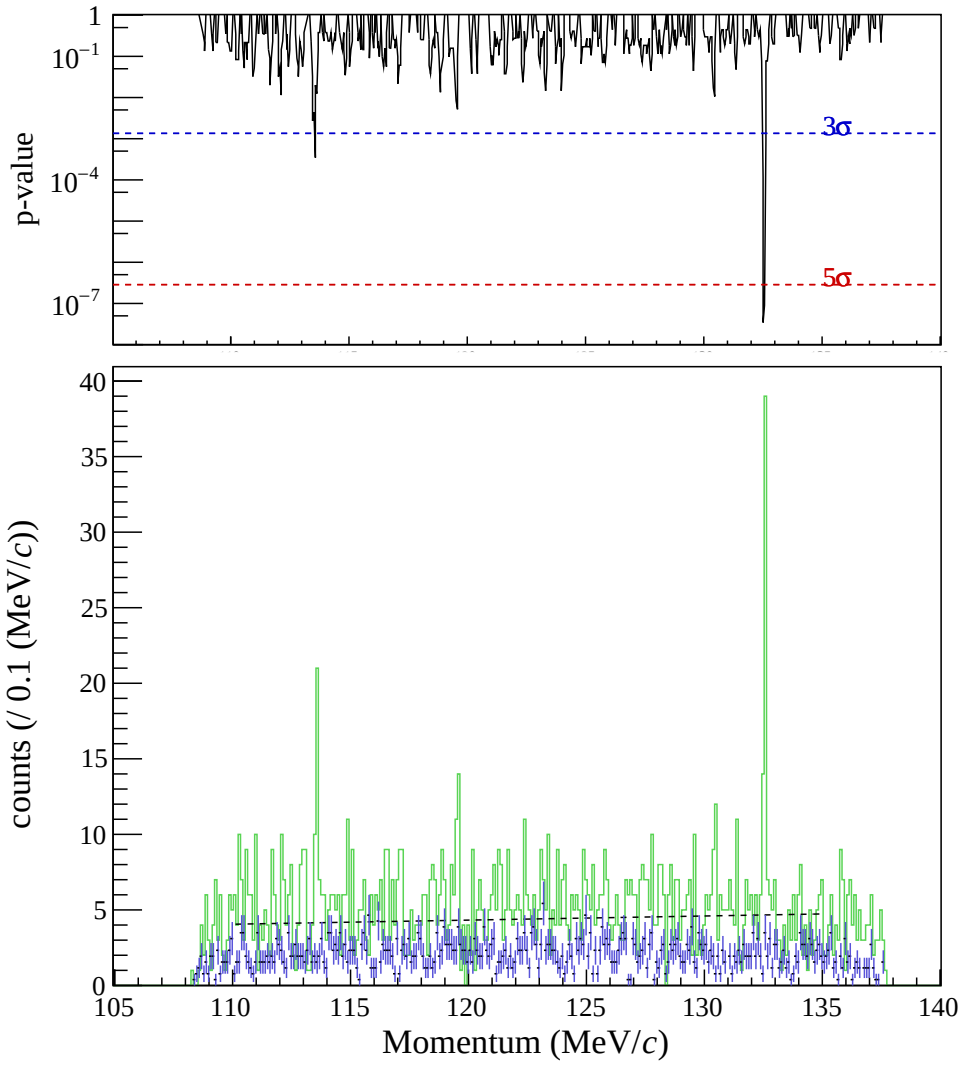

Figure 3.36: Result of the p-value scan evaluating the statistical significance of the peak structures in the momentum distribution. This scan was performed to validate that the observed structures are not artifacts introduced by the binning procedure. The background in the range of $115 - 130$ MeV/c was modeled using a linear function, and the significance was calculated as $S/\sqrt{S+N}$, where S and N denote the number of signal and background events, respectively, within a 100 keV/c bin. The scan was conducted in steps of 40 keV/c across the momentum range.

3.6 Decay pion momentum fitting

This section describes the fitting procedure to determine the center of the momentum distribution obtained. First, the effective shape of the response function is determined (section 3.6.1). Because the momentum distribution of the decay π^- has limited statistics, this study was carried out using simulations and elastic electron scattering data. Second, fitting to the observed peak structure is performed to determine the final momentum of the decay π^- (section 3.6.2).

3.6.1 Estimation of the shape of the response function

Before fitting functions to the momentum distribution of decay π^- from hypernuclei, it is necessary to constrain the parameters of the response function, such as its width, to reasonable values. This constraint is required because the available statistics for decay π^- events are insufficient to determine the function shape solely from the experimental data.

As explained in Section 3.3.2, the path length of decay π^- in the ^{7}Li target used in this experiment is extremely short. Therefore, the energy loss distribution is expected to follow a Landau distribution. Accordingly, the same Landau-Gauss convolution function used for fitting the electron elastic scattering data can be applied to the momentum distribution of the decay π^-.

The Landau-Gausssian fitting function involves four parameters: the most probable value (MPV', Eq. 3.3.9), the Landau width σ_L, the Gaussian width σ_G, and a scaling factor corresponding to the overall yield. Among these, σ_L and σ_G must be determined based on reasonable physical assumptions, reflecting the spectrometer resolution, energy loss in the target, and other factors.

The following seven components are considered as contributions to the widths σ_L and σ_G:

F_1 Energy loss in the absorbers

F_2 Multiple scattering effects

F_3 Detector resolution

F_4 Angular resolution at the target position

F_5 Ambiguity in the momentum reconstruction matrix

F_6 Uncertainty in momentum due to the vertical beam size

F_7 Effect of the beam energy spread

Among these, the first five components ($F_1 - F_5$) follow the approach adopted in a previous study [Nag15]. In the present work, F_6 and F_7 are additionally included to account for experimental conditions specific to this measurement.

Each contribution is evaluated in detail below. First, Monte Carlo simulations and elastic scattering data are used to examine whether these factors can account for the observed width of the electron elastic scattering peak. The results are then applied to the case of decay π^- from hypernuclei with a ^{7}Li target, where only F_1 through F_6 are considered to determine the final shape of the response function.

F_1: Energy loss in the absorbers

The energy loss distribution within the absorbers is expected to follow a Landau distribution, contributing primarily to the Landau width σ_L in the final momentum distribution. In the energy loss correction for the momentum analysis, the path length through the target was calculated using only the measured angular parameters (θ_t, ϕ_t), as described in Section 3.3.2. However, for a more realistic evaluation, the energy loss distribution was simulated using the GEANT4 Monte Carlo simulation [All+16].

The simulation procedure is straightforward and illustrated in Figure 3.37. As shown, a ^{181}Ta target is placed at $(x, y, z) = (0, 0, 0)$. The target thickness along the z direction was set to 7.39 μm (12.3 mg/cm^2), matching the experimental condition. Note that the thickness is exaggerated in the figure for clarity and is not drawn to scale. The z-axis corresponds to the beam direction, and the spectrometer is positioned at an angle of $54°$ relative to the beam axis.

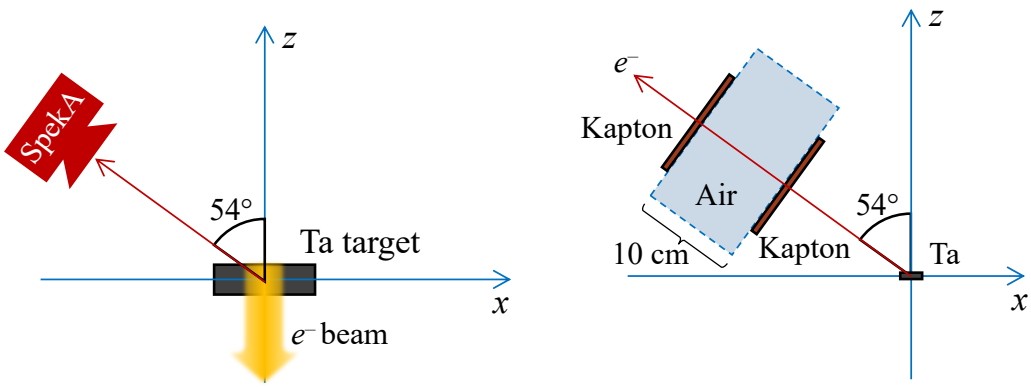

(a) Step 1 (b) Step 3

Figure 3.37: Schematic view of the simulation setup used to evaluate the energy loss distribution in the target. The ^{181}Ta target is placed at $(0, 0, 0)$, and the spectrometer is positioned at $54°$ relative to the beam axis.

The simulation consists of three steps:

Step 1: Electrons are generated at random positions within the target and propagated in the $-z$ direction (opposite to the beam) with an initial energy $E_i = 180$ MeV (Figure 3.37 (a)). The initial position distribution follows a Gaussian profile with $\sigma = 0.3$ mm in the x and y directions, consistent with the beam profile measured in the experiment, and is uniform in the z direction across the target thickness. The energy loss E_{loss} within the target is recorded, and the residual energy $E_1 = E_i - E_{\text{loss}}$ is calculated for each event.

Step 2: Using E_1, the scattered electron energy E_2 is calculated event-by-event according to the elastic scattering formula (Eq. 2.3.7), assuming scattering at angles uniformly distributed within the spectrometer acceptance around 54°. The values of E_2 and the initial vertex positions are saved into a seed file for further simulation.

Step 3: Additional energy loss after scattering is simulated. As shown in Figure 3.37 (b), two Kapton foils [DuP] and a vacuum gap (10 cm) are placed between the target and the spectrometer entrance. The vacuum chamber and the spectrometer entrance window are covered with Kapton foils of thickness 127 μm each. The electrons, using the initial parameters from the seed file, are propagated through these materials, and the cumulative energy loss is recorded.

The simulation results are shown in Figure 3.38. The same procedure was also applied to a ^{12}C target with a material thickness of 125 μm (1.763 g/cm^2).

The resulting energy loss distributions were fitted with a Landau-Gauss convolution function. The extracted width parameters for each target were:

- ^{181}Ta: $\sigma_L = (5.82 \pm 0.01)$ keV/c, $\sigma_G = (6.34 \pm 0.01)$ keV/c,
- ^{12}C: $\sigma_L = (9.31 \pm 0.01)$ keV/c, $\sigma_G = (12.79 \pm 0.01)$ keV/c.

The uncertainties represent the statistical errors from the fitting procedure. Due to the large number of simulated events, the resulting uncertainties are small. The most probable values obtained from the fits were consistent with the expectations calculated using the Landau correction formula (Eq. 3.3.13).

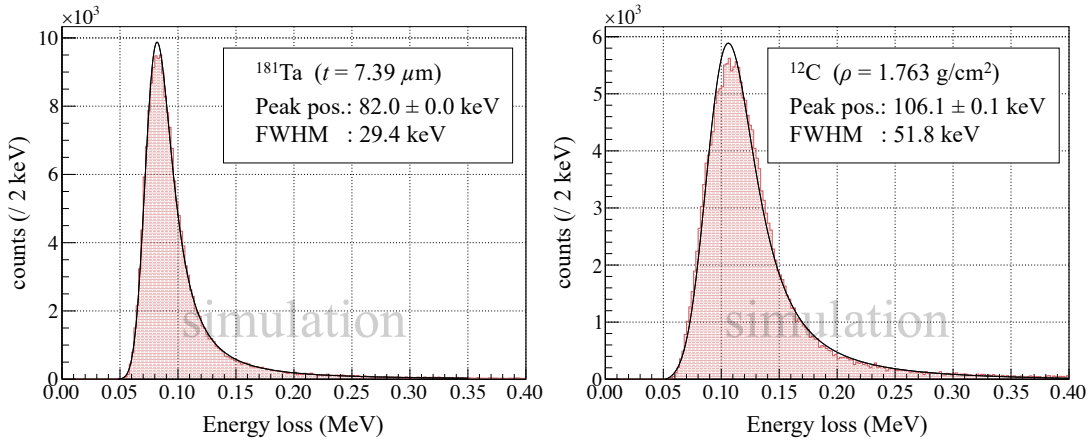

Figure 3.38: Simulated energy loss distributions for electrons traversing ^{181}Ta (left) and ^{12}C (right) targets, including energy loss within the target, Kapton foils, and vacuum gaps.

F_2: Multiple Scattering Effects

The measured position and angle of the electron at the detector are broadened due to multiple scattering in the absorber materials. These absorbers can be broadly categorized into two regions: (1) the spectrometer entrance, consisting of the air layer between the target chamber and the spectrometer as well as two Kapton foils with thickness of 127 μm covering their entrances; and (2) the spectrometer exit, including the 12 μm thick mylar windows and the gas filling of the VDCs.

According to the documentation on the design and performance of SpekA [Blo+98], the impact of multiple scattering for 495 MeV electrons corresponds to a momentum resolution of $\Delta p/p = 0.5 \times 10^{-4}$ (FWHM). This corresponds to:

$$\Delta p_{\text{FWHM}} = 0.5 \times 10^{-4} \times 495 \text{ MeV}/c = 24.75 \text{ keV}/c. \tag{3.6.1}$$

To scale this to $p = 180$ MeV/c, using the standard dependence $\sigma \propto 1/p \Rightarrow \sigma_{180} = \sigma_{495} \cdot \left(\frac{495}{180}\right)$.

$$\sigma_{495\to180} = \frac{24.75}{2.355} \cdot \left(\frac{495}{180}\right) \approx 29 \text{ keV}/c. \tag{3.6.2}$$

In addition, Ref. [Nag15] conducted Monte Carlo simulations to evaluate the effect of multiple scattering for 195 MeV electrons passing through each absorber. In their approach, distortions were introduced into the elements of the simplified transfer matrix to assess the resultant momentum broadening. The findings

showed that, for SpekA, the multiple scattering contribution was $\sigma_{\text{in}} = 21$ keV/c at the entrance and $\sigma_{\text{out}} = 9$ keV/c at the exit. These values are scaled to 180 MeV using the standard dependence $\sigma \propto 1/p$:

$$\sigma_{\text{in}}^{195\to180} = \left(\frac{195}{180}\right)\cdot 21\ \text{keV}/c \approx 23\ \text{keV}/c, \quad \sigma_{\text{out}}^{195\to180} = \left(\frac{195}{180}\right)\cdot 9\ \text{keV}/c \approx 10\ \text{keV}/c.$$

Combining these in quadrature gives:

$$\sigma_{\text{total}}^{195\to180} = \sqrt{(23\ \text{keV}/c)^2 + (10\ \text{keV}/c)^2} \approx 25\ \text{keV}/c.$$

These two independent estimates for 180 MeV electrons —$\sim$ 29 keV/c from Ref. [Blo+98] and ~ 25 keV/c from the simulation-based approach in Ref. [Nag15] —are in reasonable agreement. Taking their mean value yields $\sigma_G = 27$ keV/c. To account for uncertainties arising from the simplified transfer matrix model, the energy scaling approximation, and the variation between literature sources, a systematic uncertainty of 20 % is assigned. Thus, the contribution from multiple scattering is taken to be:

$$\sigma_G = (27 \pm 5)\ \text{keV}/c.$$

F_3: Detector resolution

The contribution of the detector's position and angular resolutions has been studied in a previous work [Nag15]. In that study, the effect was evaluated by using the GEANT4 Monte Carlo simulation, where momentum reconstruction from the focal plane measurements was compared between cases with and without the smearing due to the measured VDC resolutions. The result showed that the contribution to the momentum resolution is approximately $\sigma_G \sim 1$ keV/c, which is sufficiently small to be considered negligible.

F_4: Angular resolution at the target position

As explicitly shown in Eq. 2.3.7, the scattering angle directly affects the energy of the elastically scattered electrons. As discussed in Section 3.3.1, the angular resolution was $\sigma = 1.76$ mrad, and the angular accuracy was 1.85 mrad.

Here, the angular *resolution* refers to the event-by-event fluctuation in the reconstructed scattering angle, primarily limited by the intrinsic resolution of the detector system and multiple scattering. In contrast, the angular *accuracy* denotes the systematic deviation of the reconstructed angle from the true value, which may arise from misalignments or imperfections in the tracking calibration.

The resulting uncertainty in momentum was found to be less than 1 keV/c for ^{181}Ta targets and less than 4 keV/c for ^{12}C targets.

F_5: Ambiguity in the momentum reconstruction matrix

The momentum reconstructed from the detected position and angle by the VDC is broadened due to uncertainties in the transfer matrix. In particular, distortions are observed in the edge regions of the spectrometer acceptance. To evaluate the impact of this ambiguity, a comparison was made between the momentum distributions of elastically scattered electrons selected over the full acceptance and those restricted to events passing through the central hole of the sieve collimator, where the ambiguity is minimized. Figure 3.39 shows this comparison for 180 MeV electrons scattered from a ^{181}Ta target. The elastic peaks obtained from the full acceptance (left) and the central hole (right) were each fitted with a Landau-Gaussian function. The broadening effect was quantified by the difference in the Landau widths, $\sigma^L_{\text{all}} - \sigma^L_{\text{cut}}$, and by the square root of the difference in the squares of the Gaussian widths, $\sqrt{(\sigma^G_{\text{all}})^2 - (\sigma^G_{\text{cut}})^2}$.

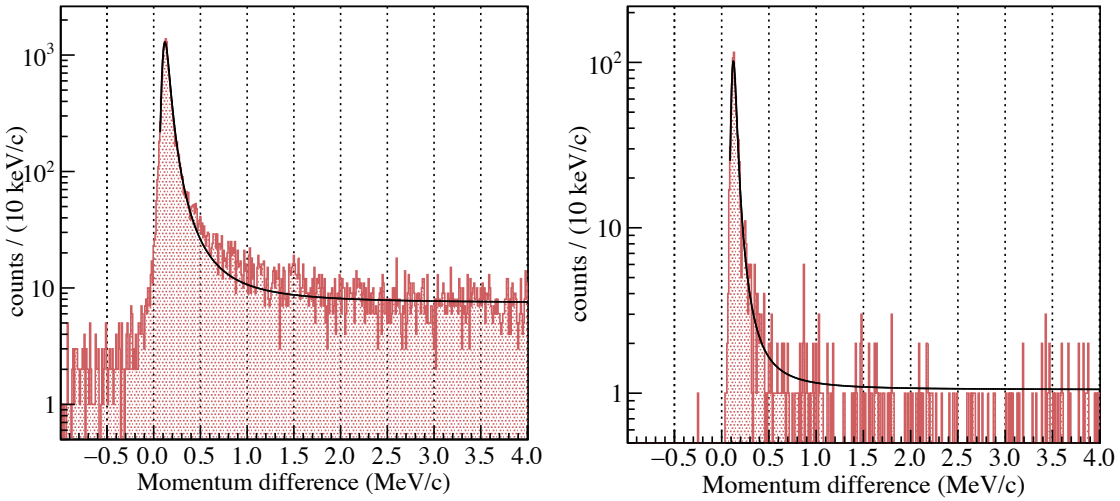

(a) With whole acceptance

(b) One-hole acceptance

Figure 3.39: Comparison of the momentum distributions of elastically scattered electrons from a ^{181}Ta target at 180 MeV. Left: events selected over the full spectrometer acceptance. Right: events restricted to those passing through the central hole of the sieve collimator. Each distribution is fitted with a Landau-Gauss function to evaluate the broadening effect caused by the ambiguity in the transfer matrix.

F_6: Uncertainty in momentum due to the vertical beam spot and size

Since the bending magnet in SpekA analyzes momentum by deflecting particles in the vertical direction, the y-position of the vertex (along the direction of gravity) directly affects the momentum reconstruction. The vertex positions in x and y correspond to the beam position. The beam position was adjusted with sub-millimeter precision using the beam image projected onto a ruled Al_2O_3 screen (Figure 3.40, left).

In practice, the beam has a finite spatial extent, and this beam size must also be taken into account. The beam size was measured by scanning a 15 μm-diameter aluminum wire oriented along the y-direction across the beam in the horizontal (x) direction, while recording the single rates of each spectrometer. The measured rate distribution was fitted with a Gaussian function plus a constant offset:

$$f(x) = p_0 \exp\left(-\frac{(x-p_1)^2}{2p_2^2}\right) + p_3,$$

where p_0 is the peak amplitude, p_1 is the beam center, p_2 corresponds to the beam width σ_x, and p_3 represents the constant background level. These measurements were routinely performed for each setup (central magnetic field of the dipole and beam energy conditions).

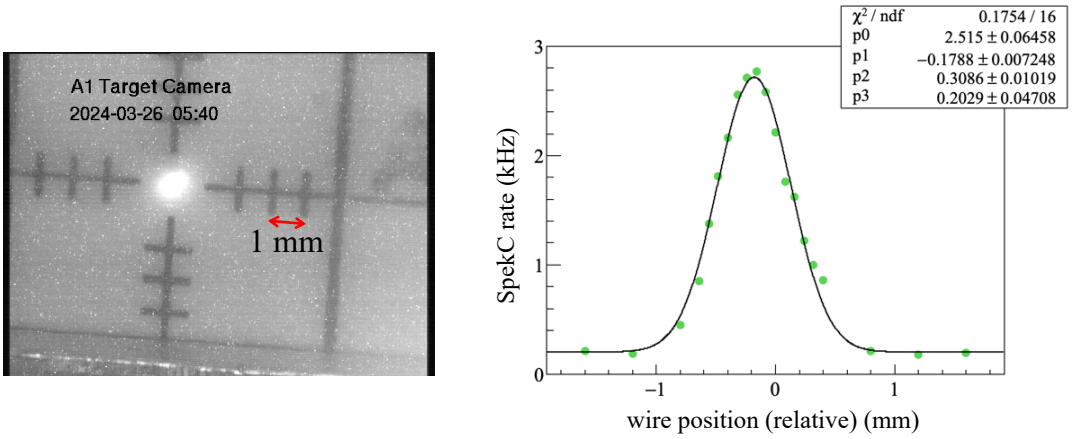

Figure 3.40: Evaluation of the beam position and size. Left: Beam spot on the marked Al_2O_3 screen used for beam position tuning. Right: Beam profile obtained by scanning an aluminum wire across the beam. The rate distribution was fitted with a Gaussian function plus a constant offset: $f(x) = p_0 \exp\left(-\frac{(x-p_1)^2}{2p_2^2}\right) + p_3$, where p_2 represents the beam size σ_x. The wire position in the right figure does not represent the absolute position.

The measured beam size in the x direction was approximately $\sigma_x \sim 0.3$ mm and remained nearly constant. Although the y-direction beam spread σ_y was not

measured, the beam spot on the screen (Figure3.40, left) appears nearly circular, suggesting $\sigma_y \sim 0.3$ mm as well.

To evaluate the effect of the vertex y-position (i.e., beam position) on the momentum reconstruction, measurements were performed by intentionally shifting the beam vertically and observing the corresponding shift in the elastic scattering peak. The results are summarized in Figure 3.41.

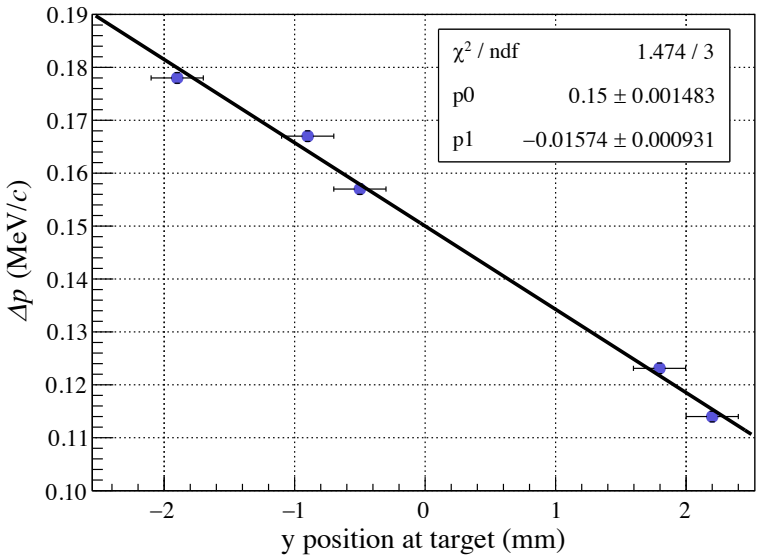

Figure 3.41: Momentum shift of the elastic scattering peak as a function of the vertical beam position.

This measurement was conducted using incident electrons with an energy of 195 MeV. The results indicate that a vertical shift of $y = \pm 2$ mm leads to a momentum shift of approximately ± 30 keV/c. Accordingly, for a beam spread of $\sigma_y \sim 0.3$ mm, the resulting contribution to the momentum uncertainty is estimated to be $\sigma_G \sim 4$ keV/c, assuming a beam energy of 180 MeV.

F_7: Beam energy spread

When evaluating the momentum peak width of electron elastic scattering, the intrinsic energy spread of the beam must be taken into account, as it directly contributes to the elastic scattering momentum. According to Ref. [Jan06], the 180 MeV electron beam is accelerated through RTM1 and RTM2, and the associated energy spread at this stage is reported to be $\sigma = 2.8$ keV.

Summary of the response function for electron elastic scattering data

Table 3.5 summarizes the contributions from the evaluated factors F_1 through F_7. The table presents the expected resolution, where the Landau components are added linearly and the Gaussian components are combined in quadrature. For comparison, the experimental values obtained from actual data are also shown.

This comparison indicates that, for the Landau component, the combined effect of the estimated factors successfully reproduces the energy width observed in the experimental data. For the Gaussian component, the expected resolution is overestimated by a factor of $1.3 - 1.5$, which is likely due to an overestimation of the multiple scattering contribution. Nevertheless, it is shown that the measured peak width can be explained by the sum of these contributing factors.

Table 3.5: Contributions of each effect to the momentum width.

Component	^{181}Ta		^{12}C	
	σ_L (keV/c)	σ_G (keV/c)	σ_L (keV/c)	σ_G (keV/c)
F_1 (Energy loss)	6	6	9	13
F_2 (Multiple scattering)	–	27 ± 5	–	27 ± 5
F_3 (Detector resolution)	–	< 1	–	< 1
F_4 (Angular resolution)	–	< 1	–	< 4
F_5 (Matrix ambiguity)	6 ± 2	13 ± 3	5 ± 1	18 ± 4
F_6 (Beam size)	–	4	–	4
F_7 (Beam energy spread)	–	2.8	–	2.8
Expected resolution	12 ± 2	31 ± 5	14 ± 2	35 ± 4
Experimental data	12 ± 1	23 ± 2	15 ± 1	23 ± 2

Response function for the decay pion momentum distribution

The elements of the response function evaluated for the electron elastic scattering momentum peak in the previous sections are applied to the momentum distribution of the decay π^- from hypernuclei. For F_1 (Energy loss in the absorbers), a dedicated simulation was performed using the same setup as the physics experiment with a ^{7}Li target and π^- particles. The results are shown in Figure 3.42.

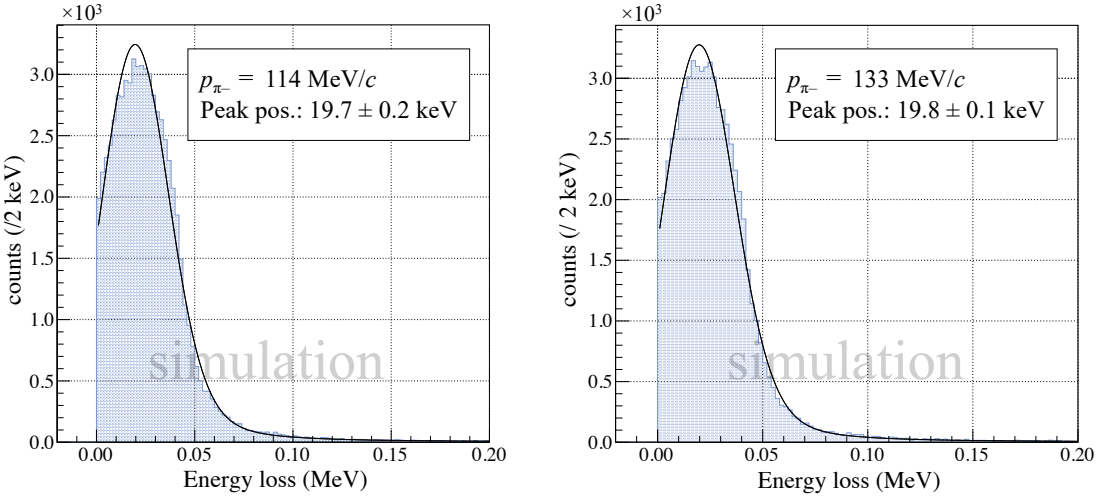

Figure 3.42: Simulation of energy loss effects for decay π^- in a ^{7}Li target. The left panel corresponds to 114 MeV/c (for ${}^3_\Lambda$H decay) and the right panel to 133 MeV/c (for ${}^4_\Lambda$H decay).

Simulations were conducted for momentum values corresponding to ${}^3_\Lambda$H decay (114 MeV/c) and ${}^4_\Lambda$H decay (133 MeV/c). In both cases, the peak position, defined using the Landau MPV' and $_G$ as described in Eq. 3.3.12, was located at approximately 20 keV. The extracted peak widths were $\sigma_L = (1.52 \pm 0.02)$ keV, $\sigma_G = (16.2 \pm 0.1)$ keV for 114 MeV/c, and $\sigma_L = (1.54 \pm 0.03)$ keV, $\sigma_G = (16.1 \pm 0.1)$ keV for 133 MeV/c.

For F_2 (Multiple scattering effects), the contributions were scaled to match the corresponding momentum values of the π^- particles. In this experimental setup, the target chamber and spectrometer were connected by a vacuum pipe, and therefore, only the effects of multiple scattering at the spectrometer exit were considered. The uncertainty of this evaluation was also estimated to be 20%.

F_3 (Detector resolution) was found to have negligible impact, similar to the electron scattering case. F_4 (Angular resolution at the target position) was not considered, since the momentum of the decay π^- does not depend on the scattering angle. F_5 (Matrix ambiguity) and F_6 (Beam size in y direction) were also scaled to the momentum values corresponding to the π^- case. F_7 (Beam energy spread)

was not considered for the decay π^- case, as it's momentum is independent of the initial beam energy.

The summary of the contributions to the momentum resolution for decay π^- is provided in Table 3.6.

Table 3.6: Contributions of each effect to the momentum width.

Component	$p_{\pi^-} = 114$ MeV/c		$p_{\pi^-} = 133$ MeV/c	
	σ_L (keV/c)	σ_G (keV/c)	σ_L (keV/c)	σ_G (keV/c)
F_1 (Energy loss)	2	16	2	16
F_2 (Multiple scattering)	–	21 ± 4	–	18 ± 3
F_3 (Detector resolution)	–	< 1	–	< 1
F_4 (Angular resolution)	–	0	–	0
F_5 (Matrix ambiguity)	3 ± 2	10 ± 3	3 ± 1	13 ± 3
F_6 (Beam size)	–	4	–	4
Expected resolution	$5 \pm 2 \pm 2$	$29 \pm 3 \pm 10$	$5 \pm 1 \pm 2$	$28 \pm 3 \pm 10$

Since the estimated peak shape serves only as an approximation, an uncertainty of 30% is assigned to each contributing component. The final response function shapes estimated for the decay π^- peaks are shown in Figure 3.43.

In the figure, the most probable value (MPV') of the Landau distribution was set to zero for plotting. The peak position shifts toward higher momentum relative to the MPV' depending on the Gaussian width σ_G, as defined in Eq. 3.3.12. This shift directly impacts the momentum calibration. The difference in peak positions between the elastic scattering and decay π^- distributions, arising from differences in peak widths, was estimated to contribute a systematic uncertainty of $2-6$ keV/c.

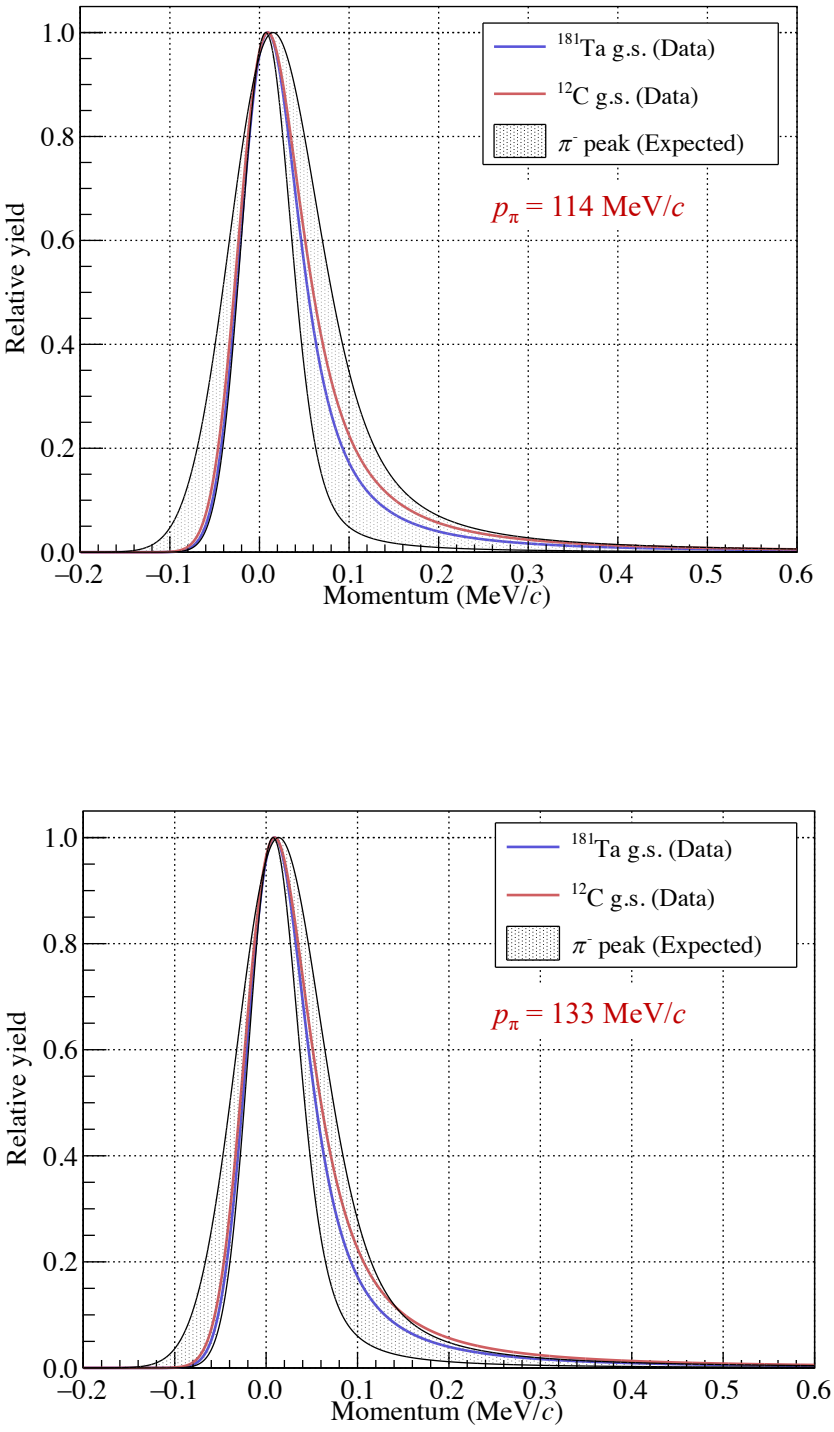

Figure 3.43: Estimated response functions for the decay π^- momentum distributions. The top panel shows the case for ${}^{3}_{\Lambda}$H (114 MeV/c) and the bottom panel for ${}^{4}_{\Lambda}$H (133 MeV/c). The shaded regions represent the response functions for the decay π^-, and the blue and red lines correspond to the elastic scattering data from ^{181}Ta and ^{12}C targets, respectively.

3.6.2 Momentum fitting

Finally, the decay π^- momentum spectra were fitted using a Landau-Gaussian function. The free parameters in the fit were the most probable value of the Landau distribution (MPV'), and the widths of the Landau and Gaussian components, σ_L and σ_G, respectively. Based on the response function estimated in the previous section, the parameter ranges were constrained as follows: for π^- from ${}^{3}_{\Lambda}\mathrm{H}$ decay (approximately 114 MeV/c), $\sigma_L = 1-9$ keV/c and $\sigma_G = 16-42$ keV/c; for ${}^{4}_{\Lambda}\mathrm{H}$ decay (approximately 133 MeV/c), $\sigma_L = 5-18$ keV/c and $\sigma_G = 15-41$ keV/c. Within these constraints, MPV' was treated as a free parameter and determined through fitting. To ensure consistency with the momentum calibration analysis, the peak position was defined according to Eq. 3.3.12, and was calculated using the fitted values of MPV' and σ_G.

Because of the limited number of events, the unbinned maximum likelihood method was employed, avoiding histogram binning to preserve the statistical information of each individual event. The data were assumed to follow Poisson statistics, and parameter estimation was performed by minimizing the negative logarithm of the likelihood (NLL), rather than maximizing the likelihood function L directly. This approach improves numerical stability and is formulated as:

$$-\ln L(\vec{p}) = -\sum_i \ln F(m_i;\vec{p}). \tag{3.6.3}$$

For the Landau-Gaussian distribution, the probability density function $F(m; p_{\pi^-}, \sigma_L, \sigma_G)$ is expressed in terms of the observable momentum m, and the approximation parameters are given by $\vec{p} = (p_{\pi^-}, \sigma_L, \sigma_G)$. The parameter estimation was performed by minimizing the negative log-likelihood (NLL) of the likelihood function for each event.

Minimization was performed using the MIGRAD algorithm provided by the MINUIT package [JR75]. The uncertainty of each parameter was determined from the point where the NLL increases by 0.5 above its minimum value.

Peak fitting with peak shape limitation

First, an unbinned fit was performed under the condition that the peak widths, σ_L and σ_G, were constrained. In this fit, the background distribution was modeled using a first-order polynomial.

Figure 3.44 presents the result of the unbinned maximum likelihood fit for the decay π^- momentum from ${}^{3}_{\Lambda}\mathrm{H}$ (approximately 114 MeV/c), and Figure 3.45 shows the result for ${}^{4}_{\Lambda}\mathrm{H}$ (approximately 133 MeV/c). In these figures, the momentum distributions are superimposed with Poisson error bars using bin widths of 0.060 MeV/c for ${}^{3}_{\Lambda}\mathrm{H}$ and 0.040 MeV/c for ${}^{4}_{\Lambda}\mathrm{H}$. Note that the fitting was performed without binning the data.

Figure 3.46 shows the distributions of the negative log-likelihood (NLL) values obtained by scanning each parameter—Landau MPV, Landau width σ_L, and Gaussian width σ_G—within their allowed ranges. For each plot, one of the three parameters was fixed at the value that minimized the NLL, while the remaining two were scanned. The resulting NLL values were plotted as a 2D surface with respect to the two scanned parameters, setting the global minimum to zero.

From these results, the most probable values of the decay π^- momentum were obtained as $p_{\pi^-}({}^{4}_{\Lambda}\mathrm{H}) = 132.718 \pm 0.007$ MeV/c for ${}^{4}_{\Lambda}\mathrm{H}$ and $p_{\pi^-}({}^{3}_{\Lambda}\mathrm{H}) = 113.661 \pm 0.020$ MeV/c for ${}^{3}_{\Lambda}\mathrm{H}$.

Regarding the width parameters, the following values were obtained: for ${}^{4}_{\Lambda}\mathrm{H}$ decay, $\sigma_L = 0.007 \pm 0.003$ MeV/c and $\sigma_G = 0.027 \pm 0.007$ MeV/c; for ${}^{3}_{\Lambda}\mathrm{H}$ decay, $\sigma_L = 0.009 \pm 0.007$ MeV/c and $\sigma_G = 0.042 \pm 0.006$ MeV/c.

However, as shown in Figure 3.46, the fit for ${}^{3}_{\Lambda}\mathrm{H}$ decay exhibits a tendency for the width parameters σ_L and σ_G to converge to the upper limits of their allowed ranges. To investigate whether this constraint affects the determination of the peak position, an alternative fit was performed without applying parameter limits.

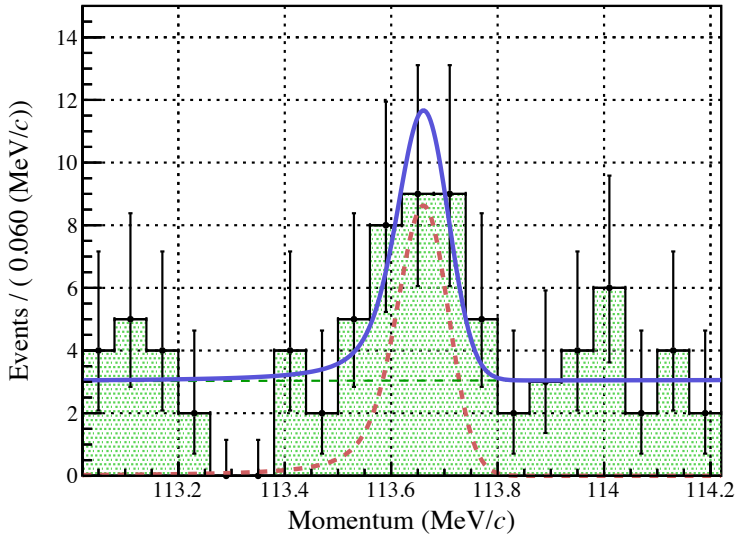

Figure 3.44: Result of the unbinned maximum likelihood fit to the decay π^- momentum distribution from ${}^{3}_{\Lambda}$H. The fit employs a Landau-Gaussian convolution function, with the Landau width σ_L and Gaussian width σ_G limited based on the estimated detector response. The most probable value of the Landau component (MPV') was treated as the sole free parameter.

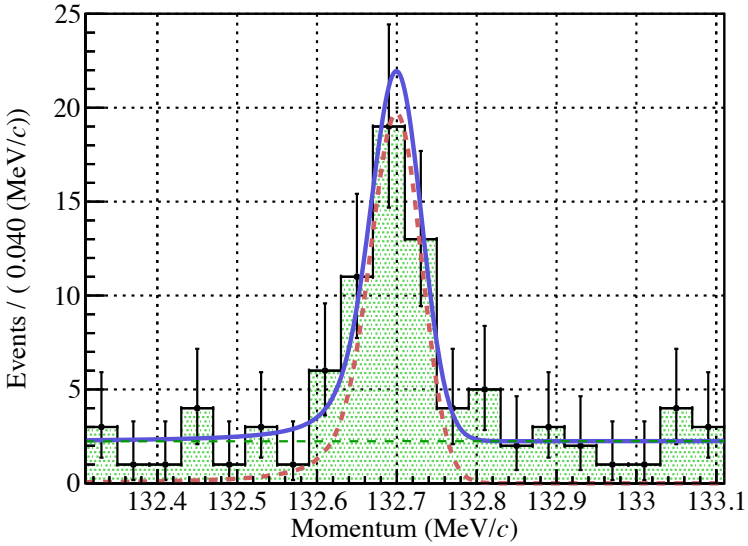

Figure 3.45: Result of the unbinned maximum likelihood fit to the decay π^- momentum distribution from ${}^{4}_{\Lambda}$H. The same Landau-Gaussian function was used, with the widths σ_L and σ_G constrained as in the ${}^{3}_{\Lambda}$H case. The only floating parameter was the most probable value (MPV') of the Landau distribution.

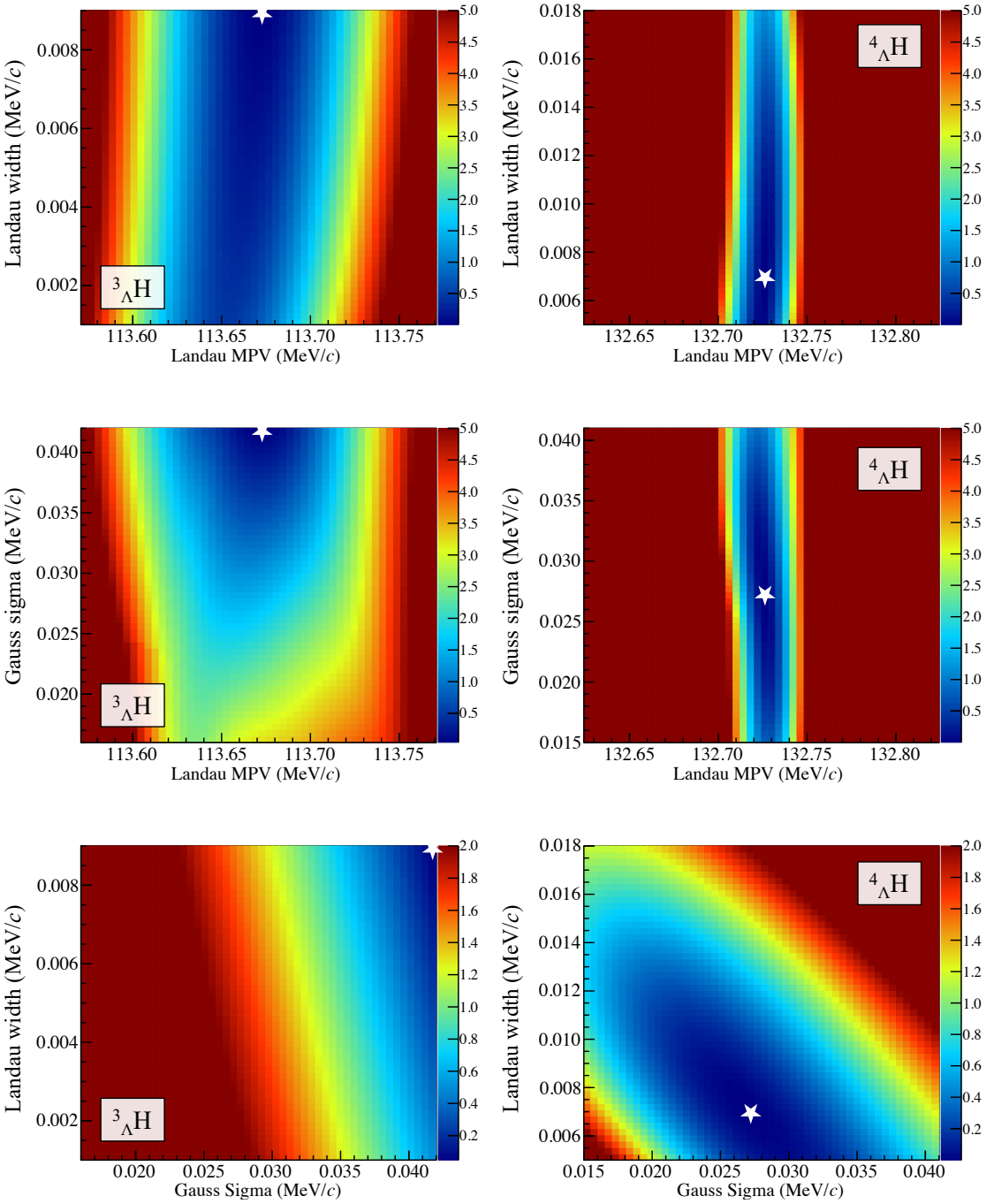

Figure 3.46: Two-dimensional scans of the negative log-likelihood (NLL) surface for the Landau MPV, Landau width σ_L, and Gaussian width σ_G in the unbinned fit. In each panel, one parameter is fixed at its optimal value, and the other two are scanned within their allowed ranges. The minimum NLL is normalized to zero.

Peak fitting without peak shape limitation

Next, unbinned maximum likelihood fits were performed without imposing constraints on the peak widths. Specifically, the Landau width σ_L and Gaussian width σ_G were allowed to vary freely within sufficiently broad limits. As before, the background distribution was modeled using a first-order polynomial.

Figure 3.47 shows the result for the decay π^- momentum distribution from ${}^{3}_{\Lambda}\mathrm{H}$ (approximately 114 MeV/c), and Figure 3.48 presents the corresponding result for ${}^{4}_{\Lambda}\mathrm{H}$ (approximately 133 MeV/c). Poisson error bars are overlaid for visualization, using bin widths of 0.060 MeV/c for ${}^{3}_{\Lambda}\mathrm{H}$ and 0.040 MeV/c for ${}^{4}_{\Lambda}\mathrm{H}$, while the fitting was performed on unbinned data.

The NLL distributions obtained by scanning the Landau MPV, Landau width σ_L, and Gaussian width σ_G are shown in Figure 3.49. Each plot was generated by fixing one of the three parameters to the value that minimizes NLL, and scanning the remaining two within their allowed ranges. The minimum NLL was normalized to zero.

From these results, the most probable momentum values were obtained as $p_{\pi^-}({}^{4}_{\Lambda}\mathrm{H}) = 132.718 \pm 0.007$ MeV/c for ${}^{4}_{\Lambda}\mathrm{H}$ and $p_{\pi^-}({}^{3}_{\Lambda}\mathrm{H}) = 113.651 \pm 0.026$ MeV/c for ${}^{3}_{\Lambda}\mathrm{H}$.

The corresponding width parameters were obtained as follows: for ${}^{4}_{\Lambda}\mathrm{H}$ decay, $\sigma_L = 0.007 \pm 0.006$ MeV/c and $\sigma_G = 0.027 \pm 0.012$ MeV/c; for ${}^{3}_{\Lambda}\mathrm{H}$ decay, $\sigma_L = 0.001 \pm 0.018$ MeV/c and $\sigma_G = 0.068 \pm 0.019$ MeV/c.

In the fit to the ${}^{3}_{\Lambda}\mathrm{H}$ decay momentum distribution, the Landau width converged to the lower limit, while the Gaussian width increased. Nevertheless, the combined width is consistent with that obtained from the previous fit with constraints. Furthermore, the most probable value (MPV) remained consistent within uncertainties regardless of whether the parameter constraints were applied. It is therefore concluded that the parameter constraints do not affect the final determination of the Λ binding energy.

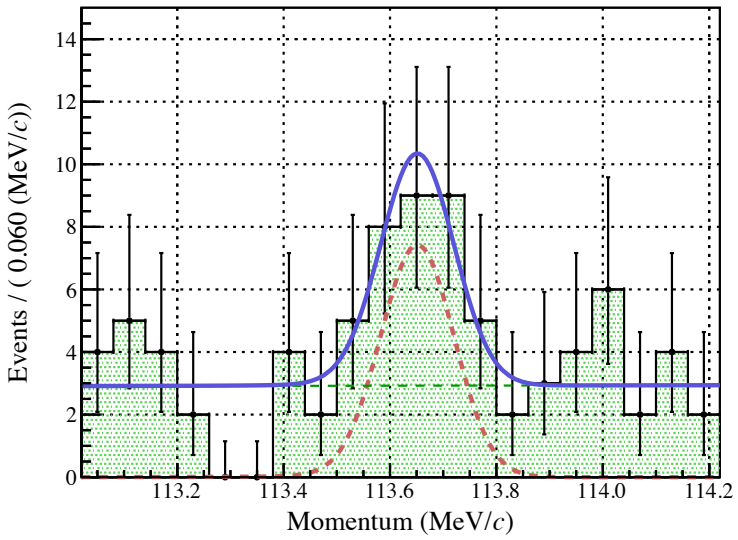

Figure 3.47: Unbinned maximum likelihood fit to the decay π^- momentum distribution from ${}^{3}_{\Lambda}\mathrm{H}$, performed without constraints on the Landau-Gaussian shape parameters. The Landau width σ_L and Gaussian width σ_G were treated as free parameters within wide bounds. Poisson error bars are shown using 0.060 MeV/c bins.

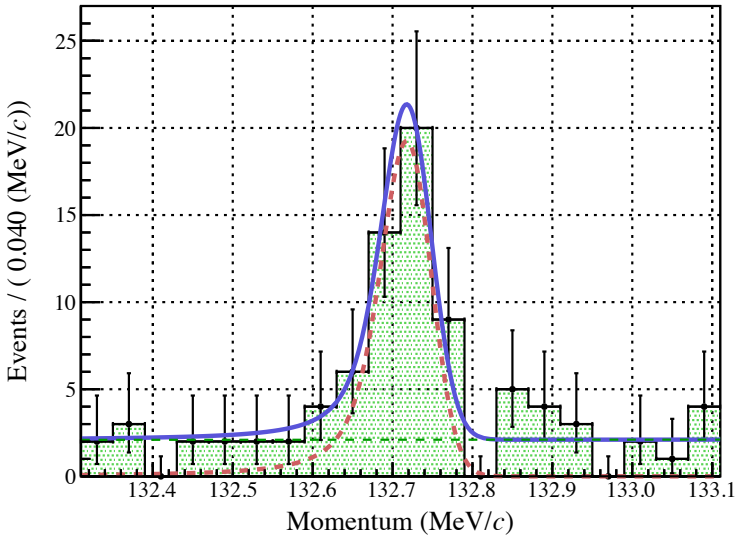

Figure 3.48: Unbinned maximum likelihood fit to the decay π^- momentum distribution from ${}^{4}_{\Lambda}\mathrm{H}$, using a Landau-Gaussian function with unconstrained shape parameters. Both σ_L and σ_G were floated independently during the fit. Poissonian error bars are overlaid using 0.040 MeV/c bins.

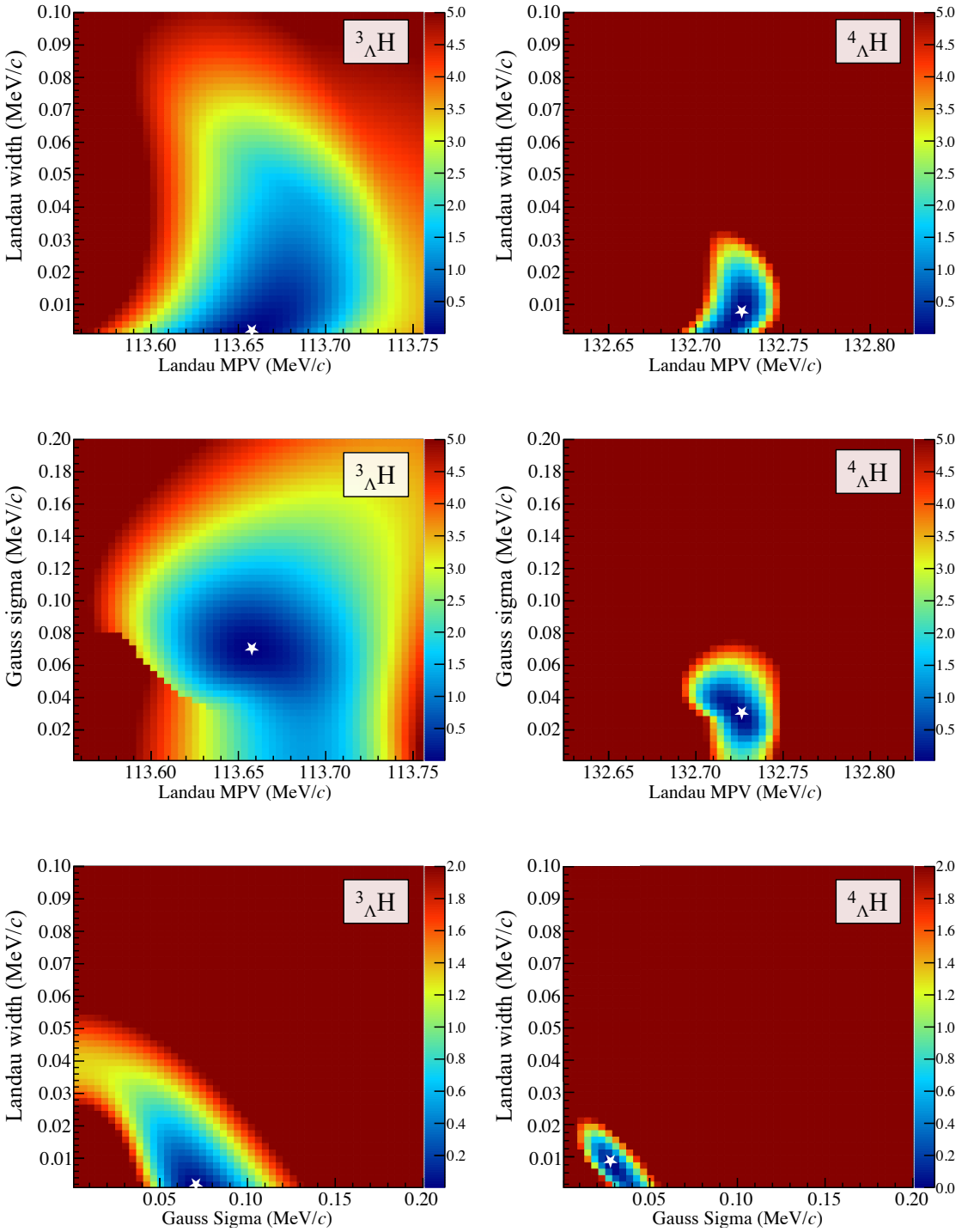

Figure 3.49: Two-dimensional scans of the negative log-likelihood (NLL) surface in the unbinned fit without peak shape constraints. In each panel, one parameter is fixed at its optimal value, and the other two are scanned within their allowed ranges. The minimum NLL is normalized to zero.

Summary of peak fitting

The parameter constraints applied during the peak fitting, along with the resulting fitted values, are summarized in Table 3.7. The table also lists the total negative logarithm of the likelihood (NLL) for each fit.

Table 3.7: Summary of the parameter constraints and fit results. All values are given in units of MeV/c.

	Limitations		Results			
	σ_L	σ_G	σ_L	σ_G	p_{π^-}	NLL
${}^{3}_{\Lambda}\mathrm{H}$	$0.001 - 0.009$	$0.016 - 0.042$	$0.009(7)$	$0.042(6)$	$113.661(20)$	537.77
	$0.001 - 0.100$	$0.001 - 0.200$	$0.001(18)$	$0.068(19)$	$113.651(26)$	462.22
${}^{4}_{\Lambda}\mathrm{H}$	$0.005 - 0.018$	$0.015 - 0.041$	$0.007(3)$	$0.027(76)$	$132.718(7)$	3285.05
	$0.001 - 0.100$	$0.001 - 0.200$	$0.007(7)$	$0.027(12)$	$132.718(9)$	3533.71

As discussed above, the peak position of the decay π^- momentum remained unchanged regardless of whether constraints on the peak widths were imposed. The two results are consistent within their respective uncertainties. Therefore, the final values of the decay π^- momenta were determined as follows:

- $p_{\pi^-}({}^{4}_{\Lambda}\mathrm{H}) = 132.718 \pm 0.007$ MeV/c
- $p_{\pi^-}({}^{3}_{\Lambda}\mathrm{H}) = 113.661 \pm 0.020$ MeV/c

The statistical significance of these peaks was evaluated using a method that employed a likelihood ratio approach based on the definition in Ref. [Cou+08]. The signal significance S_L was computed using

$$S_L = \sqrt{-2\ln(L_{\mathrm{BG}}/L_{\mathrm{S+BG}})}, \tag{3.6.4}$$

where L_{BG} and $L_{\mathrm{S+BG}}$ denote the likelihoods under the background-only and signal+background hypotheses, respectively. This approach provides a rigorous hypothesis test grounded in the actual fit model, including the signal and background shapes and parameters, and is thus considered more reliable. The resulting significances were:

- $S_L({}^{4}_{\Lambda}\mathrm{H}) = 8.36$
- $S_L({}^{3}_{\Lambda}\mathrm{H}) = 4.21$

These results demonstrate that the observed spectra exhibit statistically significant peaks. The significance evaluation using simple formula $S/\sqrt{S+B}$ is discussed in Appendix B.

However, the obtained decay π^- momentum for ${}^{4}_{\Lambda}\mathrm{H}$ is approximately 0.2 MeV/c lower than the value reported in a previous study, $p_{\pi^-}({}^{4}_{\Lambda}\mathrm{H}) = 132.867 \pm 0.013\,(\mathrm{stat.}) \pm 0.098\,(\mathrm{syst.})$ MeV/c [Sch+16]. It should be noted that the momentum calibration in this study was based on elastic scattering at $E_b = 420$ MeV, which introduces non-negligible systematic uncertainty due to extrapolation in beam energy. The observed discrepancy lies within the quoted systematic uncertainty and is therefore considered consistent with the previous measurement. A more detailed discussion of systematic uncertainties is provided in the following section.

3.6.3 Calibrate using decay pion momentum from ${}^{4}_{\Lambda}$H decay

In the calibration method using the electron elastic scattering peak at a beam energy of $E_b = 420$ MeV, the uncertainty arising from extrapolation in beam energy is non-negligible. Therefore, the most precise and currently effective method is to use the previously reported high-precision value of the decay π^- momentum peak from ${}^{4}_{\Lambda}$H at this moment.

An unbinned fit using a Landau-Gaussian convolution function was performed for the spectrum before applying momentum calibration, as shown in Figure 3.50.

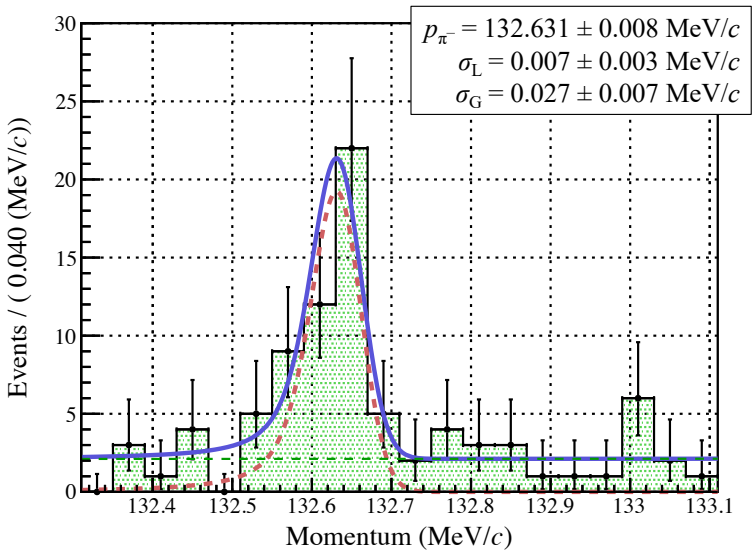

Figure 3.50: Unbinned fit to the momentum spectrum of the ${}^{4}_{\Lambda}$H decay π^- before applying momentum calibration. The data were fitted with a Landau-Gaussian convolution function, with constraints imposed on the Landau and Gaussian widths as described in Section 3.6.2.

The fit was carried out with constraints on the Landau and Gaussian widths, in the same manner as described in Section 3.6.2. As a result, the obtained peak position was $p_{\pi^-} = 132.631 \pm 0.008$ MeV/c. This value was then compared with the reference momentum previously remeasured at MAMI in 2014, which was $p_{\pi^-} = 132.867 \pm 0.013$ (stat.) ± 0.107 (syst.) MeV/c [Sch+16]. This value represents the weighted average of the results from unbinned fits of multiple measurements performed in 2012 and 2014 using different thickness targets and spectrometers, as presented in that paper. It corresponds to a binding energy of $B_\Lambda({}^{4}_{\Lambda}\mathrm{H}) = 2.157 \pm 0.005$ (stat.) ± 0.077 (syst.) MeV. Using this value as the reference, the calibration factor for the ${}^{4}_{\Lambda}$H decay π^- momentum was calculated as follows:

$$\begin{aligned} \Delta p &= p_{\text{ref.}} - p_{\text{m}} = 132.867 - 132.631 = 0.236 \\ F'_{\text{calib}}({}^{4}_{\Lambda}\text{H}) &= 1 + \frac{\Delta p}{p_{\text{m}}} = 1 + \frac{0.236}{132.631} = 1.00178(12) \end{aligned} \tag{3.6.5}$$

The calculation of the uncertainty took into account the statistical errors associated with each value.

The obtained calibration factor F' was applied, and unbinned fits using a Landau-Gaussian function were performed for each spectrum in the same manner. As in Section 3.6.2, constraints were imposed on the widths of both the Landau and Gaussian components during the fitting. The result is shown in Figure 3.51.

Based on the obtained peak position, the decay π^- momentum from ${}^{3}_{\Lambda}\text{H}$ is as follows.

- $p_{\pi^-}({}^{3}_{\Lambda}\text{H}) = 113.789 \pm 0.020$ MeV/c
- $S_L = 4.33$

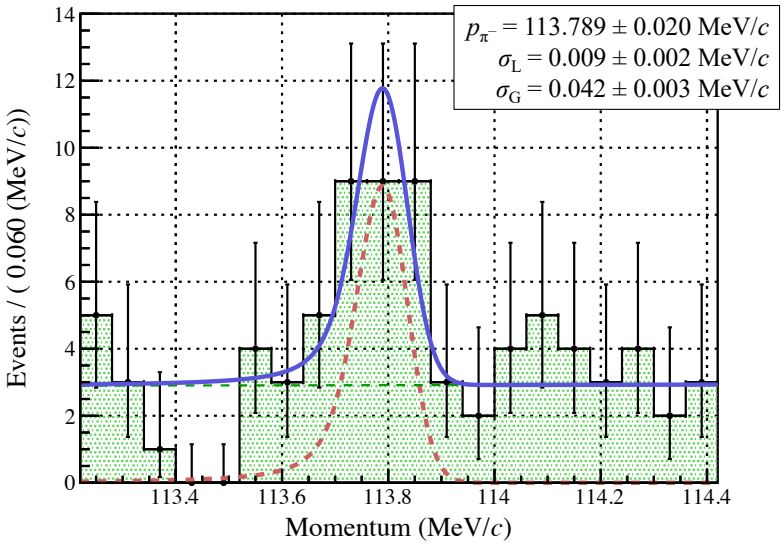

Figure 3.51: Spectrum calibrated using the relative momentum value based on the ${}^{4}_{\Lambda}\text{H}$ momentum peak, along with the result of the unbinned fit.

3.7 Evaluation of Systematic Error

Finally, the systematic uncertainties associated with the measured decay π^- momenta are discussed. Ten sources of systematic uncertainty were considered in this study:

- Effect of the energy loss within the target
- Stability of the central magnetic field of the spectrometer dipole
- Effect of the beam position on momentum reconstruction
- Effect of the z position on momentum reconstruction
- Uncertainty in the spectrometer installation angle
- Momentum non-linearity
- Peak position shift due to the peak width
- Uncertainty in the beam energy
- Uncertainty due to extrapolation in the beam energy
- Uncertainty in the referenced decay π^- momentum of ${}^{4}_{\Lambda}\mathrm{H}$

The last three sources are specific to the calibration method used. In the case of calibration using elastic scattering data at $E_b = 420$ MeV, systematic uncertainties arise from the beam energy measurement by MAMI and from extrapolation beyond the measured energy range. For the calibration method using the π^- peak from ${}^{4}_{\Lambda}\mathrm{H}$ decay reported in previous studies, the uncertainty in the referenced value contributes to the final results.

Each of these sources is discussed in detail below, followed by a summary of the total systematic uncertainty.

Effect of the energy loss within the target

As described in Section 3.3.2, the energy loss of the decay π^- and of elastically scattered electrons for momentum calibration was evaluated on an event-by-event basis using the Bethe-Bloch equation, with the path length through the target calculated for each event. For the decay π^-, the z vertex and angles (θ_t, ϕ_t) at the target were reconstructed from the particle's position and angle measured at the

spectrometer focal plane, while the beam position (x, y) was provided as an external input. These parameters were then used to calculate the path length through the target.

Although the z vertex resolution was insufficient ($\sigma_z = 7 - 8$ mm, see Section3.3.4), the long lithium target (45 mm) covered nearly the full acceptance of SpekA, making the path length effectively independent of the z vertex. On the other hand, since the spectrometer is installed at an angle of 95° with respect to the beam axis, the x position effectively influences the path length of the π^- within the target. Considering the spectrometer installation angle of 95°, angular acceptance of $\theta_t \leq \pm 70$ mrad (dispersive) and $\phi_t \leq \pm 100$ mrad (non-dispersive), target width in the x-direction of 0.75 mm, and a target orientation angle of 0°, the possible path length varies up to $0 - 0.775$ mm.

The beam position was regularly monitored using the Al_2O_3 screen shown in Figure 3.40 (left), and the automatic stage system controlled both position and angle to ensure the beam passed through the target center $(x, y) = (0, 0)$, as confirmed in Figure 2.29. Assuming the beam center at $(0, 0)$ and a beam size of $\sigma_x \sim 0.3$ mm (Figure 3.40), the resulting uncertainties in energy loss were estimated to be 14 keV for $p_{\pi^-} = 133$ MeV/c ($^4_\Lambda$H) and 16 keV for $p_{\pi^-} = 114$ MeV/c ($^3_\Lambda$H). Potential non-uniformity in target thickness was considered negligible compared to the beam position effect.

For the calibration using elastically scattered electrons, the uncertainty in energy loss was 4 keV for the ^{181}Ta target, as detailed in Section 3.3.2. This was due to the small target thickness compared to the z vertex resolution, which allowed the z vertex to be fixed at the center of the target in the path length calculation.

In summary, the systematic uncertainties due to energy loss in the target were estimated to be 15 keV for $^4_\Lambda$H and 17 keV for $^3_\Lambda$H.

Stability of the central magnetic field of the spectrometer dipole

In this study, the central magnetic field of the spectrometer dipole was continuously monitored using an NMR probe. As evaluated in Section 3.2.1, the field stability was $\sigma_{\text{1st}} \sim 1.18$ keV/c during the first half of the beamtime (September 16-24, 2022) and $\sigma_{\text{2nd}} \sim 0.80$ keV/c during the second half (October 1-17, 2022). Normalizing by the number of days in each period, the combined uncertainty from magnetic field stability is estimated as:

$$\sigma = \sqrt{\frac{9}{26} \cdot \sigma^2_{\text{1st}} + \frac{17}{26} \cdot \sigma^2_{\text{2nd}}} \sim 1 \text{ keV}/c \tag{3.7.1}$$

In addition, during the first half of the beamtime, a discrepancy of approximately 4 keV/c was observed between the two dipole magnets, D1 and D2, of SpekA. This discrepancy was scaled according to the number of days, resulting in an estimated uncertainty of $4 \times 9/26 \approx 1.4$ keV/c.

Effect of the beam position on momentum reconstruction

As discussed in Section 3.6.1, due to the vertical bending of the dipole spectrometer, the beam y position directly affects momentum reconstruction. The beam position was regularly confirmed on the viewer screen (Figure 3.40, left), and visually remained within $y = \pm 0.1$ mm. According to Section3.6.1, a y shift of ± 2 mm leads to a momentum change of approximately ± 30 keV/c at $E_b = 195$ MeV. Extrapolating from this, a y variation of ± 0.1 mm corresponds to a momentum uncertainty of approximately 1 keV/c for both ${}^{4}_{\Lambda}$H and ${}^{3}_{\Lambda}$H.

Effect of the z position on momentum reconstruction

As shown in Section 3.3.4, the measured momentum depends on the z vertex of the particle in the target, and a z-dependent momentum correction was applied during calibration. The correction was performed across the full acceptance, and as a result, variations of $\sigma = 4$ keV/c for ${}^{4}_{\Lambda}$H and $\sigma = 3$ keV/c for ${}^{3}_{\Lambda}$H are considered in the analysis.

Uncertainty in the spectrometer installation angle

The momentum of elastically scattered electrons depends on the scattering angle (see Eq. 2.3.7). The spectrometer was installed with an angular accuracy of 0.1° [Nag15], which affects the momentum measurement by less than 1 keV/c for the heavy ^{181}Ta target. Therefore, the uncertainty due to the spectrometer installation angle is negligible.

Momentum non-linearity

As described in Section 3.3.3, the momentum linearity over the full spectrometer acceptance was evaluated using the excitation spectrum of a ^{12}C target. By correcting the non-linearity across the full acceptance range, the resulting uncertainty was reduced to approximately $\sigma \sim 2$ keV/c.

Peak position shift due to peak width

In both the momentum calibration using elastic scattering electrons and the analysis of the decay π^- from hypernuclei, the momentum peaks were fitted using a Landau-Gaussian convolution function. As discussed in Section 3.3.2, the extracted peak position tends to shift toward the Landau tail, depending on the Gaussian width σ_G. Since the Landau and Gaussian widths differ between the calibration data and the hypernuclear decay π^-, the peak position exhibits a systematic shift. As noted in Section 3.6.1, this shift was quantified to be 6 keV/c in both the high- and low-momentum regions.

Uncertainty in the beam energy

When using the elastic scattering peak for momentum calibration, the beam energy uncertainty directly affects the determination of the momentum difference via Eq. 2.3.7. The beam energy measured at MAMI was $E_b = 420.180 \pm 0.160$ MeV. This uncertainty, $\delta E_b = 0.160$ MeV, corresponds to a systematic error of approximately $0.160 \times 132.7/419.8 \approx 0.051$ MeV/c for ${}^{4}_{\Lambda}$H and $0.160 \times 113.7/419.8 \approx 0.043$ MeV/c for ${}^{3}_{\Lambda}$H, after scaling to the measured momenta.

Uncertainty due to extrapolation in the beam energy

The momentum calibration factor derived from the elastic scattering peak at $E_b = 420$ MeV was directly applied to the momentum of the decay π^- from hypernuclei. In the dipole magnet of SpekA, deviation from linear response due to magnetic saturation was observed only above 1.2 T [Kra95]. Since the maximum magnetic field setting at $E_b = 420$ MeV was 1.004 T (corresponding to a central momentum of 445 MeV/c), the magnet was operating within the linear regime. Nevertheless, due to the broad range of extrapolation, careful consideration of linearity is required.

Figure 3.52 shows the central momentum calculated from the dipole current settings and the magnetic field values measured via NMR, using Eq. 2.3.1.

The left panel shows D1 and the right panel shows D2. Red points represent data recorded during the calibration period from March 22 to May 10, 2024, while blue points represent data from the hypernuclear experiment from September 16 to October 17, 2022. Linear fits were applied across the full range for both cases. The top panels show residuals from the linear fits. The RMS spread of the residuals was 240 keV, which was adopted as the systematic uncertainty due to extrapolation from the $E_b = 420$ MeV calibration data.

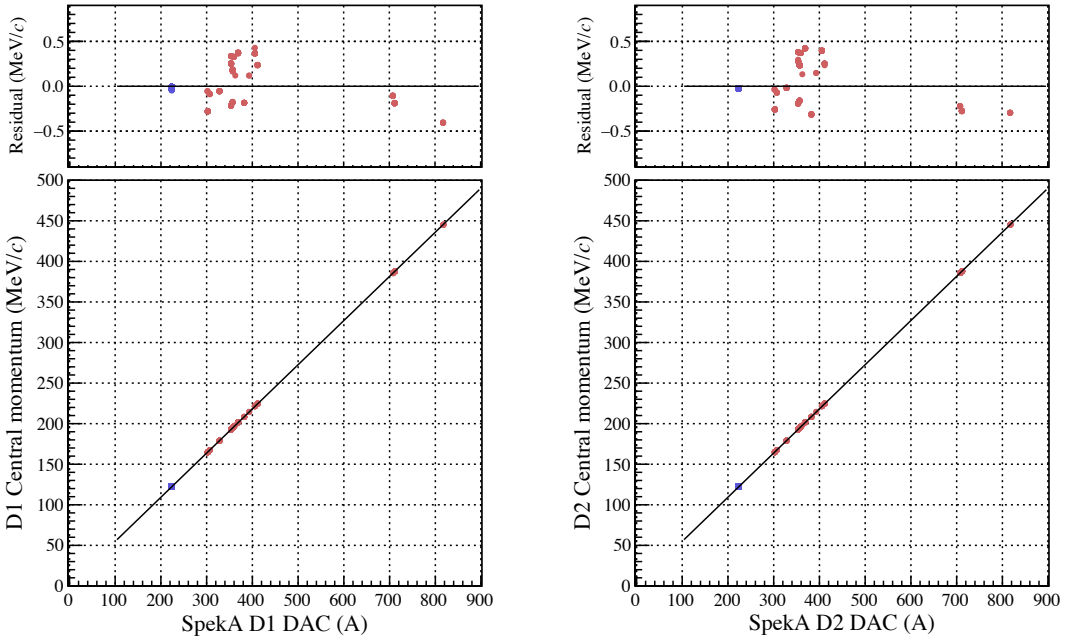

Figure 3.52: Central momentum calculated from the dipole magnet current settings and magnetic field values measured with NMR, plotted according to Eq.2.3.1. The left and right panels show data from D1 and D2, respectively. Red points indicate calibration data recorded between March 22 and May 10, 2024, while blue points correspond to hypernuclear data recorded between September 16 and October 17, 2022. Solid lines represent linear fits. The top panels display the residuals from the linear fits. The RMS of the residuals was 240keV and was adopted as the systematic uncertainty due to extrapolation from the $E_b = 420$ MeV calibration.

3.7.1 Summary of the systematic error

All of the above-mentioned components are summarized in Table 3.8. For each calibration method, the systematic uncertainties from individual sources as well as the total systematic uncertainty are listed for each hypernucleus. In addition, for the method using the ${}^{4}_{\Lambda}$H peak, the total error of 85 keV from the reference value $p_{\pi^-} = 132.867 \pm 0.013\ (\text{stat.}) \pm 0.107\ (\text{syst.})$ MeV/c reported in [Sch+16], and the uncertainty of Λ mass [Gro22] is included.

Table 3.8: Summary of the systematic errors

Component	**Calibration method**			
	Elastic scattered electron		$^{4}_{\Lambda}$H peak	
	$^{4}_{\Lambda}$H	$^{3}_{\Lambda}$H	$^{4}_{\Lambda}$H	$^{3}_{\Lambda}$H
Effect of the energy loss within the target (keV)	15	17	15	17
Stability of the central magnetic field (keV/c)	1	1	1	1
Effect of the beam position on momentum reconstruction (keV/c)	1	1	1	1
Effect of the z position on momentum reconstruction (keV/c)	4	3	4	3
Uncertainty in the spectrometer installation angle (keV/c)	< 1	< 1	< 1	< 1
Momentum non-linearity (keV/c)	2	2	2	2
Peak position shift due to the peak width (keV/c)	6	6	6	6
Uncertainty in the beam energy (keV/c)	51	43	–	–
Uncertainty due to extrapolation in the beam energy (keV/c)	240	240	–	–
Uncertainty of referenced $^{4}_{\Lambda}$H decay π^- momentum (keV/c)	–	–	108	108
Uncertainty of Λ mass (keV/c^2)	6	6	6	6
Total systematic error in p_{π^-} (keV/c)	246	245	110	112
Total systematic error in B_Λ (keV)	178	165	80	75

Chapter 4

Experimental Results and Discussions

4.1 Lambda binding energy of ${}^{3}_{\Lambda}$H and ${}^{4}_{\Lambda}$H

The peak position of momenta of decay π^- obtained from ${}^{3}_{\Lambda}$H and ${}^{4}_{\Lambda}$H in this experiment are summarized in Table 4.1. The table lists the results derived using three different calibration methods, including their associated statistical and systematic uncertainties.

Table 4.1: Summary of decay π^- momenta p_{π^-} for ${}^{3}_{\Lambda}$H and ${}^{4}_{\Lambda}$H obtained using different calibration methods. Both electron elastic scattering data ($E_b = 420$ MeV) and the referenced ${}^{4}_{\Lambda}$H peak are used. All numbers are described with a unit of MeV/c.

Calibration method	Hypernucleus	p_{π^-}	Statistical error	Systematic error
Elastic scattered electron	${}^{4}_{\Lambda}$H	132.718	0.007	0.246
	${}^{3}_{\Lambda}$H	113.661	0.020	0.245
${}^{4}_{\Lambda}$H peak	${}^{4}_{\Lambda}$H	132.867[*1]	0.007	0.110
	${}^{3}_{\Lambda}$H	113.789	0.020	0.112

[*1]The value for ${}^{4}_{\Lambda}$H obtained using the ${}^{4}_{\Lambda}$H peak calibration is same as referenced value [Sch+16].

Substituting these decay π^- momenta into Eq. 2.2.10 and Eq. 2.2.11, the resulting Λ binding energies B_Λ are calculated. The mass values used for the calculation are listed in Table 4.2. The obtained B_Λ are summarized in Table 4.3.

Although some variation is observed depending on the calibration method, all results are mutually consistent within their respective systematic uncertainties. For ${}^{4}_{\Lambda}$H, the method using the elastic scattering peak at $E_b = 420$ MeV yields a slightly deeper binding energy by approximately 0.15 MeV, but this difference remains

Table 4.2: Mass values used in the calculation of B_Λ.

Particle	Mass [MeV/c^2]	Reference
^{2}H	1875.612946	AME 2020 [Wan+21]
^{3}H	2808.921138	AME 2020 [Wan+21]
^{3}He	2808.391608	AME 2020 [Wan+21]
^{4}He	3727.379409	AME 2020 [Wan+21]
Λ	1115.683	PDG 2022 [Gro22]
π^-	139.5706	PDG 2022 [Gro22]

Table 4.3: Summary of Λ binding energies B_Λ for ${}^3_\Lambda$H and ${}^4_\Lambda$H obtained using different calibration methods. All numbers are described with a unit of MeV.

Calibration method	Hypernucleus	B_Λ	Statistical error	Systematic error
Elastic scattered electron	${}^4_\Lambda$H	2.265	0.005	0.178
	${}^3_\Lambda$H	0.609	0.013	0.165
${}^4_\Lambda$H peak	${}^4_\Lambda$H	2.157*1	0.005	0.080
	${}^3_\Lambda$H	0.523	0.013	0.075

*1The value for ${}^4_\Lambda$H obtained using the ${}^4_\Lambda$H peak calibration is same as referenced value [Sch+16].

within the uncertainty range due to energy extrapolation. For ${}^3_\Lambda$H, the present study has revealed that the Λ binding energy is significantly deeper than previously suggested by nuclear emulsion experiments and heavy-ion collision measurements by the ALICE Collaboration.

Figure 4.1 summarizes the reported values of B_Λ for ${}^3_\Lambda$H, and Figure 4.2 shows those for ${}^4_\Lambda$H, as measured in previous experiments. Including the result from the present data, the weighted mean was calculated for each case.

The relative difference between the ${}^4_\Lambda$H and ${}^3_\Lambda$H decay π^- momenta is a robust result derived from the present data and remains unaffected by the undulator calibration. The relative momentum, $p_{\pi^-}({}^4_\Lambda\mathrm{H}) - p_{\pi^-}({}^3_\Lambda\mathrm{H})$, is obtained as:

- 19.057 ± 0.021 (stat.) ± 0.036 (syst.) MeV/c (with elastic scattering data)
- 19.078 ± 0.021 (stat.) ± 0.036 (syst.) MeV/c (with ${}^4_\Lambda$H decay π^- momentum)

The observation of a statistically significant peak in the ${}^3_\Lambda$H decay π^- momentum using the well-established method of decay-pion spectroscopy represents the first such measurement in the world. This constitutes a major advancement, successfully achieving a direct and spectroscopic determination of the Λ binding energy of ${}^3_\Lambda$H.

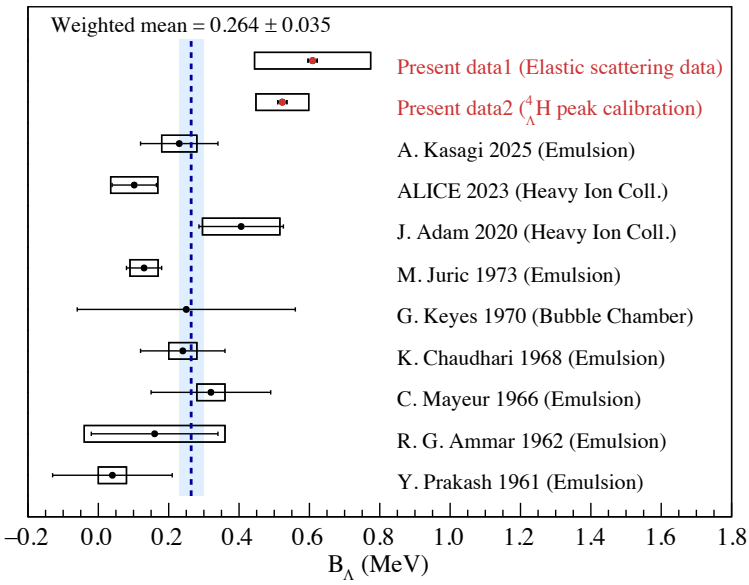

Figure 4.1: A summary of the reported values of the B_Λ for $^{3}_{\Lambda}$H. The present result is plotted together, and the weighted average is indicated by the blue dashed line, with its uncertainty shown as a light blue band. Each data point is referenced from the corresponding publication: [Pra+61; Amm+62; May+66; Cha+68; Key+70; Jur+73; Ada+20; Ach+23; Kas+25].

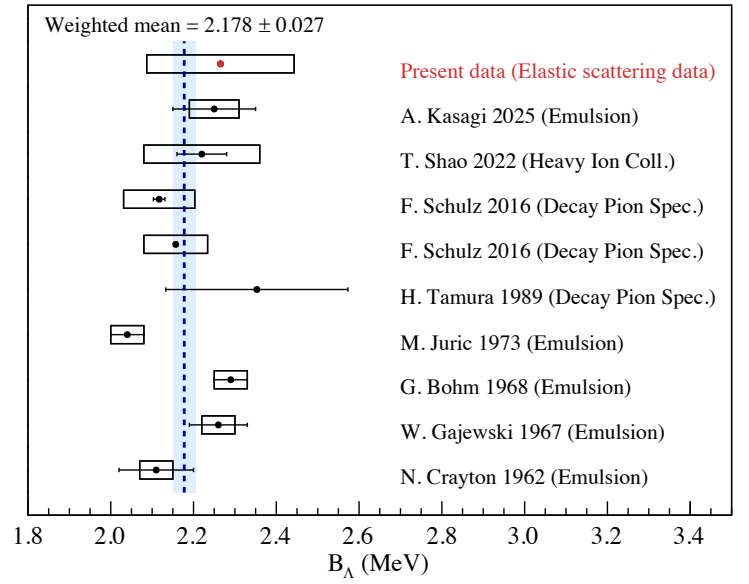

Figure 4.2: A summary of the reported values of the B_Λ for $^{4}_{\Lambda}$H. The present result is plotted together, and the weighted average is indicated by the blue dashed line, with its uncertainty shown as a light blue band. Each data point is referenced from the corresponding publication: [Cra+62; Gaj+67; Boh+68; Jur+73; Tam+89; Sch+16; T S22; Kas+25].

4.2 Discussion

The present study suggests that the Λ binding energy of ${}^{3}_{\Lambda}$H may be significantly deeper than previously reported. In contrast, the value obtained for ${}^{4}_{\Lambda}$H is consistent with prior experimental results. In the following, we discuss the possible implications of these findings for the structure of s-shell hypernuclei and the nature of the $\Lambda - N$ interaction.

4.2.1 Input for the nature of $\Lambda - N$ interaction

As introduced in Section 1.2.1, there have been discrepancies among experimental values for the Λ binding energy of ${}^{3}_{\Lambda}$H. Although theoretical calculations employing various approaches are generally consistent with the results from early nuclear emulsion experiments and heavy-ion collision measurements by the ALICE Collaboration, the interpretation remains model-dependent.

The present study yields a value of $B_{\Lambda}({}^{3}_{\Lambda}\mathrm{H}) = 0.523 \pm 0.013\,(\mathrm{stat.}) \pm 0.075\,(\mathrm{syst.})$ MeV, which is consistent with the value reported by the STAR Collaboration, $B_{\Lambda} = 406 \pm 120\,(\mathrm{stat.}) \pm 110\,(\mathrm{syst.})$ keV [Ada+20] while significantly deeper than previously reported other results. This suggests the presence of a stronger interaction between the Λ and the deuteron core.

Theoretical investigations have been conducted to explore how the hyperon-nucleon (YN) interaction must be modified to reproduce such a deeply bound state. For example, a study by H. Le *et al.* [Le+20] employed chiral effective field theory (χEFT) interactions (NLO13 and NLO19) and solved the Faddeev equation to evaluate B_{Λ} of ${}^{3}_{\Lambda}$H. They found that enhancing the singlet ${}^{1}S_{0}$ Λp scattering length from the conventional value of -2.91 fm to approximately -4.5 to -5.0 fm, while reducing the strength of the spin-triplet ${}^{3}S_{1}$ interaction maintained consistency with existing Λp scattering data, could reproduce a binding energy of $0.4 - 0.5$ MeV. This modification was also applied to other hypernuclei, such as ${}^{4}_{\Lambda}$He and ${}^{7}_{\Lambda}$Li. For ${}^{4}_{\Lambda}$He, the Λ binding energy of the 0^{+} state increased and approached the experimental value of 2.39 MeV, while the separation energy of the 1^{+} state – being sensitive to the spin-triplet interaction – decreased, resulting in an improved reproduction of the observed $0^{+} - 1^{+}$ spin splitting. For ${}^{7}_{\Lambda}$Li, the Λ binding energy slightly increased as well, but the shift remained within the theoretical uncertainty due to three-body force (3BF) effects (on the order of ~ 300 keV). These results demonstrate that the observed deep binding energy can be understood by considering the spin dependence of the YN interaction.

However, several theoretical models for the YN interaction developed over the past decades encounter inconsistencies with other hypernuclear systems when modified to reproduce the present result.

For instance, E. Hiyama $et\ al.$ [Hiy+14] performed high-precision three-body calculations using the Gaussian Expansion Method (GEM) to investigate whether the $nn\Lambda$ system can form a bound state. Their model employed the AV8 potential for the NN interaction and a realistic YN interaction that incorporates $\Lambda N - \Sigma N$ coupling and reproduces the phase shifts of the NSC97f potential.

In their analysis, the strength of the tensor component of the YN interaction —particularly the ${}^3V_T^{\Sigma N-\Lambda N}$ term—was scaled to test the sensitivity of the $nn\Lambda$ binding. Simultaneously, they evaluated whether the same interaction parameters could reproduce the Λ binding energies of ${}^3_\Lambda$H, ${}^4_\Lambda$H, and ${}^4_\Lambda$He. Their results showed that although a 20% enhancement of the tensor term could marginally bind the $nn\Lambda$ system, it led to an overbinding of the other hypernuclei compared to experimental values. Based on this, they concluded that the $nn\Lambda$ system is unlikely to be bound within the framework of realistic YN interactions.

Notably, within their model, a deeper binding energy of ${}^3_\Lambda$H in the range of $0.5 - 0.6$ MeV, as suggested by the present measurement, would imply a bound $nn\Lambda$ state. This highlights the critical role of precise $B_\Lambda({}^3_\Lambda\mathrm{H})$ determinations in constraining the possible existence of exotic hypernuclei such as $nn\Lambda$.

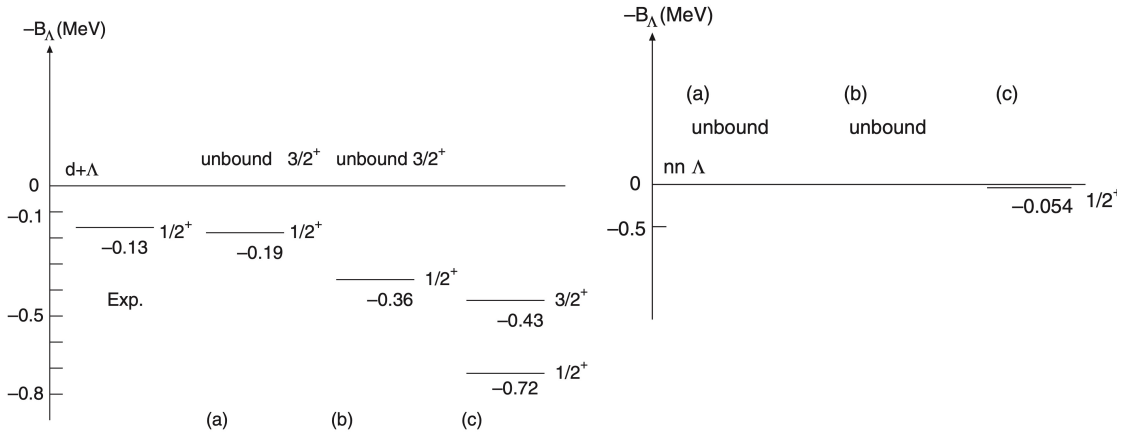

(i) Calculated B_Λ for ${}^3_\Lambda$H (ii) Calculated B_Λ for ${}^3_\Lambda n$

Figure 4.3: Calculated Λ-separation energies of (i) ${}^3_\Lambda$H and (ii) the $nn\Lambda$ system for various strengths of the tensor component ${}^3V_T^{\Sigma N-\Lambda N}$ in the YN interaction (adapted from Ref. [Hiy+14]). Panels (a), (b), and (c) correspond to scaling factors of 1.00, 1.10, and 1.20, respectively.

Furthermore, D. L. Mihaylov $et\ al.$ [Mih+24] imposed stringent constraints on the $p\Lambda$ interaction by combining traditional low-energy scattering data—characterized by limited statistics and large systematic uncertainties—with femtoscopic $p\Lambda$ correlation functions measured in 13 TeV pp collisions by the ALICE Collaboration. This analysis offers one of the most precise characterizations of low-energy YN interactions to date.

In their study, both the phenomenological Usmani potential and the chiral EFT NLO19 interaction (modified to account for SU(3) symmetry breaking) were employed. The authors utilized the CATS framework to solve the Schrödinger equation numerically while varying the singlet and triplet scattering lengths, f_0 and f_1, to reproduce the correlation function $C(k)$. The source function $S(m_T, r)$ was modeled using the CECA framework, and the correlation function was computed through the Koonin-Pratt formalism.

As a result, assuming $f_0 = 2.1$ fm, they obtained $f_1 = 1.56 \pm 0.08$ fm, indicating that the $p\Lambda$ interaction is less attractive than previously thought. This finding appears to contradict the present result, which implies a significantly more attractive ΛN interaction as required to produce a deeply bound ${}^{3}_{\Lambda}\mathrm{H}$ state.

In parallel, the present result for the Λ binding energy of ${}^{4}_{\Lambda}\mathrm{H}$ is consistent with the previous measurements performed at MAMI within the range of systematic uncertainties, albeit indicating a relatively larger binding energy. Notably, it is in good agreement with the values recently reported by the STAR collaboration in heavy-ion collision experiments [T S22] as well as by the J-PARC E07 experiment using nuclear emulsion techniques [Kas+25]. This consistency may suggest a smaller value of $\Delta B^{4}_{\Lambda}(0^{+}_{\mathrm{g.s.}}) = B_{\Lambda}({}^{4}_{\Lambda}\mathrm{H}(0^{+})) - B_{\Lambda}({}^{4}_{\Lambda}\mathrm{He}(0^{+}))$ in the ground state.

4.2.2 Effect for the hypertriton puzzle

Regarding the lifetime τ of ${}^{3}_{\Lambda}\mathrm{H}$, several theoretical interpretations have been proposed in relation to the increase in B_{Λ}. Calculations based on chiral effective field theory by Pérez-Obiol $et\ al.$ [Pér+20] indicate that the lifetime τ exhibits a strong dependence on the Λ binding energy. Specifically, for $B_{\Lambda} \sim 0.1$ MeV, they predict $\tau/\tau_{\Lambda} \sim 0.8$ (τ_{Λ}: lifetime of the Λ hyperon, ~ 263 ps), while for $B_{\Lambda} \sim 0.4$ MeV, the ratio can decrease to $\tau/\tau_{\Lambda} \sim 0.6$. This implies that the shorter lifetime of around 150 ps reported in the 2010s could be explained by a stronger Λd interaction.

On the other hand, calculations based on a pion-exchange model by M. Rayet and R.H. Dalitz [RD66], and those using pionless EFT by F. Hildenbrand and H.W. Hammer [HH20], suggest that the ${}^{3}_{\Lambda}\mathrm{H}$ lifetime is largely independent of the Λ binding energy and consistently remains close to $\tau/\tau_{\Lambda} \sim 1$.

Currently, a direct high-statistics measurement of the ${}^{3}_{\Lambda}\mathrm{H}$ lifetime is under analysis in the J-PARC E73 experiment, and new high-precision data are expected to provide further insight.

4.2.3 Future prospects

As discussed above, precision measurements of the beam energy using synchrotron radiation interferometry from the undulator are currently in progress. The analysis of the data obtained in both the undulator validation experiment and the present study has demonstrated that the absolute beam energy can be determined with a statistical uncertainty of approximately 1.0×10^{-4} [Nis25]. At present, the primary focus is on evaluating the systematic uncertainty arising from the wavelength calibration of the interference fringes.

In the future, further improvements in the absolute energy calibration using this technique are expected to reduce the current systematic uncertainty to below 30 keV. This will enable the determination of the Λ binding energies for both hypernuclei with world-leading precision, independent of prior measurements.

Through the progression from earlier experiments at MAMI to the present study, the method of high-precision B_Λ determination via decay pion spectroscopy has been firmly established for light hypernuclei. Future experiments at Jefferson Lab, which offers higher beam current and is equipped with detector systems capable of handling high-rate environments, are being planned to apply decay pion spectroscopy for high-precision B_Λ measurements. This will make it possible to extend the technique to p-shell hypernuclei, where the mesonic weak decay rate is lower, thus opening up further opportunities for advancing hypernuclear spectroscopy.

Chapter 5

Summary and Conclusion

In this study, we conducted a high-precision measurement of the Λ binding energy B_Λ of ${}^{3}_{\Lambda}$H using the decay pion spectroscopy method at the Mainz Microtron (MAMI), where the world's most precise B_Λ measurement of ${}^{4}_{\Lambda}$H had previously been achieved. The hypertriton ${}^{3}_{\Lambda}$H, as a bound system of a deuteron and a Λ hyperon, is the simplest Λ hypernucleus and has thus served as a benchmark in hypernuclear physics. Nevertheless, its fundamental properties, including B_Λ and lifetime, remain experimentally considerable, and theoretical interpretations are model-dependent. In particular, recent heavy-ion collision experiments have reported conflicting B_Λ values, and its lifetime—despite its shallow binding energy —has been reported to be shorter than those of medium and heavy hypernuclei. These puzzles have brought renewed attention to the so-called hypertriton puzzle.

Decay pion spectroscopy offers a direct and highly precise approach to measuring the ground-state B_Λ. Building on the experimental methods established in our ${}^{4}_{\Lambda}$H measurements conducted at MAMI in 2012 and 2014, we aimed to directly measure B_Λ of ${}^{3}_{\Lambda}$H with improved accuracy, thereby contributing critical experimental input toward resolving the hypertriton puzzle and constraining the $\Lambda - N$ interaction.

This experiment featured two major advancements. First, the target material was changed from ^{9}Be to ${}^{\text{nat.}}$Li. A target with a lower atomic number helps suppress not only electromagnetic background events but also background from other hyperfragments. Despite its lower density, a high luminosity was achieved by designing the lithium target to be 45 mm long along the beam axis. Moreover, to minimize the effective target thickness traversed by the decay π^-, the spectrometer was placed at 95° relative to the beam axis, and the target width was narrowed to 0.75 mm. This unique design was made possible by mounting the target on a remotely controllable stage with a few micrometers of precision, combined with a

primary electron beam steerable to sub-millimeter level.

Second, a new method for measuring the beam energy using synchrotron radiation interferometry from an undulator was introduced. Since spectrometer momentum calibration is based on electron elastic scattering, the absolute value of the incident beam energy critically affects the accuracy. In conventional methods, an uncertainty of 160 keV in beam energy dominated the systematic error. The new method achieved a tenfold improvement in precision, significantly reducing this source of systematic uncertainty.

This dissertation introduced these updates and explained in detail the physical and calibration experiments conducted, along with the analysis methods. The experiment was carried out in autumn 2022, achieving a luminosity of $\int Ldt = 826.94$ (fb^{-1}), comparable to that of the previous ${}^{4}_{\Lambda}$H study. For the calibration experiment, a multi-foil target was designed to investigate the z-dependence of particle production, and a richer dataset in beam energy and spectrometer momentum settings was acquired.

The momentum calibration analysis accounted for both the nonlinearity over the full spectrometer acceptance and the z-dependence of the reconstruction, with uncertainties suppressed to the level of a few keV/c. Due to the ongoing analysis of the synchrotron radiation data, the beam energy provided by the MAMI facility was used as a reference in this work.

In the tagging strangeness produced events analysis using the KAOS spectrometer, K^+ mesons were identified based on their β values and energy loss measured by TOF counters, combined with momentum information. Despite limited resolution and without relying on simulation, the background from abundant π^+ and protons was separated through a data-driven approach. As a result, 618 K^+ events were identified.

The momentum distribution of SpekA for selected K^+ events exhibited two distinct peaks: one near 114 MeV/c, corresponding to decay π^- from ${}^{3}_{\Lambda}$H, and another near 133 MeV/c, attributed to decay π^- from ${}^{4}_{\Lambda}$H. These peaks were fitted using Landau-Gaussian convolution functions, whose shapes were determined from the calibration data and simulation. The obtained peak significances were studied with a likelihood ratio test, resulting in 4.21 for ${}^{3}_{\Lambda}$H and 8.36 for ${}^{4}_{\Lambda}$H, indicating statistically significant observations.

The decay π^- momenta obtained from calibration with electron elastic scattering data were:

- $p_{\pi^-}({}^{4}_{\Lambda}\mathrm{H}) = 132.718 \pm 0.007\ (\mathrm{stat.}) \pm 0.246\ (\mathrm{syst.})$ MeV/c
- $p_{\pi^-}({}^{3}_{\Lambda}\mathrm{H}) = 113.661 \pm 0.020\ (\mathrm{stat.}) \pm 0.245\ (\mathrm{syst.})$ MeV/c

The corresponding Λ binding energies were:

- $B_\Lambda(^4_\Lambda\mathrm{H}) = 2.265 \pm 0.005\ (\text{stat.}) \pm 0.178\ (\text{syst.})$ MeV
- $B_\Lambda(^3_\Lambda\mathrm{H}) = 0.609 \pm 0.013\ (\text{stat.}) \pm 0.165\ (\text{syst.})$ MeV

When calibrated using the known $^4_\Lambda$H decay π^- momentum from previous studies at MAMI [Sch+16], $p_{\pi^-}(^4_\Lambda\mathrm{H}) = 132.867 \pm 0.013\ (\text{stat.}) \pm 0.107\ (\text{syst.})$ MeV/c, the results were:

- $p_{\pi^-}(^3_\Lambda\mathrm{H}) = 113.789 \pm 0.020\ (\text{stat.}) \pm 0.112\ (\text{syst.})$ MeV/c
- $B_\Lambda(^3_\Lambda\mathrm{H}) = 0.523 \pm 0.013\ (\text{stat.}) \pm 0.075\ (\text{syst.})$ MeV

The calibration based on elastic scattering data includes systematic uncertainties arising from the beam energy uncertainty at MAMI and extrapolation errors due to the higher beam energy ($E_b = 420$ MeV). In contrast, the calibration using the $^4_\Lambda$H decay π^- from previous work primarily inherits the statistical and systematic errors from that measurement. These uncertainties are expected to be reduced below 30 keV once the undulator-based beam energy analysis is complete.

In this study, both $^3_\Lambda$H and $^4_\Lambda$H decay π^- peaks were successfully observed, enabling a precise determination of the momentum difference between the two, $p_{\pi^-}(^4_\Lambda\mathrm{H}) - p_{\pi^-}(^3_\Lambda\mathrm{H})$:

- $19.057 \pm 0.021\ (\text{stat.}) \pm 0.036\ (\text{syst.})$MeV/$c$ (elastic scattering calibration)
- $19.078 \pm 0.021\ (\text{stat.}) \pm 0.036\ (\text{syst.})$ MeV/c (using $^4_\Lambda$H decay π^-)

This study marks the first observation of the $^3_\Lambda$H decay π^- peak using decay pion spectroscopy. The statistical significance exceeds 4σ, and the statistical uncertainty of 13 keV surpasses the precision of all previously reported measurements by approximately an order of magnitude. The systematic uncertainty is expected to be further reduced once the analysis of the undulator-based beam energy measurement is completed in the near future.

Appendix A

DAQ system for hypernuclear experiment at A1

Figure A.1 shows the complete DAQ diagram used in the present experiment. Here, all the modules involved are shown as rectangular boxes, and signals coming from (or going to) external modules are shown as rhombuses. Many modules unique to the MAMI and GSI facilities are used here. The description of the role of each module is assigned a letter linked to the box below. In the figure, two trigger signals enter from the left: KAOS and SpekA. The top half is for KAOS, and the bottom half is for SpekA; both have their own branches, but the basic principle is almost the same.

First, the trigger is distributed through the FAN-IN FAN-OUT (FIFO), modules A and V. From there, the trigger branches to the VUCAM D and U for single events, and to the first AND modules B and P that lead to the coincidence section. Both of these modules get their secondary input from the micro-Busy module (ξ). In the case of the SpekA arm, the busy signal from the read logic of SpekA is explicitly taken. If there is no interruption due to the busy signal, it reaches the main coincidence module O. The SpekA trigger signal is defined to be 80 ns long. This opens a coincidence window, and the module waits for the KAOS trigger to arrive. This pulse is 20 ns long. From there, it reaches the OR modules (F and Q), which trigger the data readout and set the spectrometer busy. The emitted coincidence signal was sent to the Event Builder module and labeled with an event number.

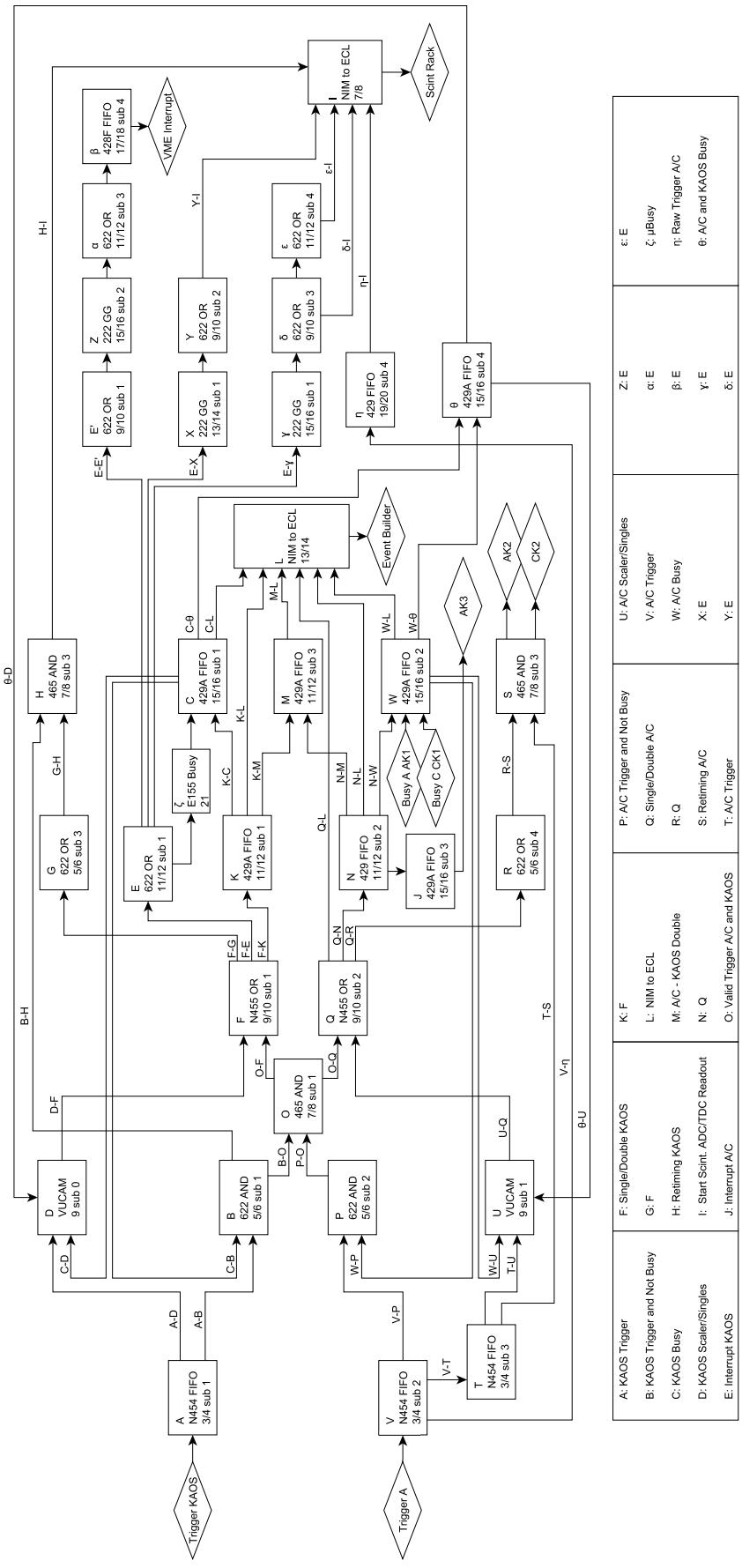

Figure A.1: Diagram of the trigger logic for SpekA and KAOS [Von24] (modified).

Appendix B

Simple peak significance evaluation

From the fitting with the Landau-Gaussian function, the statistical significance of peaks was also evaluated using a simple analytical approximation based on the simple significance formula. The peak significance N_σ was defined as

$$N_\sigma = \frac{S}{\sqrt{S + BG}}, \tag{B.0.1}$$

where S and BG are the integrals of the signal component (Landau-Gaussian) and background component (first-order polynomial), respectively, over the region of $\pm 3\sigma$ around the peak. The calculated values of N_σ were:

- $N_\sigma({}^{4}_{\Lambda}\mathrm{H}) = 5.73\sigma$
- $N_\sigma({}^{3}_{\Lambda}\mathrm{H}) = 3.09\sigma$

Bibliography

[Ach+23] S. Acharya *et al.* "Measurement of the Lifetime and Λ Separation Energy of ${}^{3}_{\Lambda}$H". In: *Phys. Rev. Lett.* 131 (10 Sept. 2023). DOI: https://link.aps.org/doi/10.1103/PhysRevLett.131.102302, p. 102302.

[Ach10] P. Achenbach. "The KAOS Spectrometer at the Mainz Microtron and First Measurements of Kaon Electro-Production". DOI: http://doi.org/10.25358/openscience-6535. PhD thesis. Johannes Gutenberg-Universität Mainz, 2010.

[Ada+16] J. Adam *et al.* "${}^{3}_{\Lambda}$H and ${}^{3}_{\Lambda}\bar{\text{H}}$ production in Pb–Pb collisions at $\sqrt{s_{NN}} = 2.76$ TeV". In: *Physics Letters B* 754 (2016). DOI: https://doi.org/10.1016/j.physletb.2016.01.040, pp. 360–372.

[Ada+18] L. Adamczyk *et al.* "Measurement of the ${}^{3}_{\Lambda}$H lifetime in Au+Au collisions at the BNL Relativistic Heavy Ion Collider". In: *Physical Review C* 97.5 (2018). DOI: https://doi.org/10.1103/PhysRevC.97.054909, p. 054909.

[Ada+20] J. Adam *et al.* "Measurement of the mass difference and the binding energy of the hypertriton and antihypertriton". In: *Nature Physics* 16.4 (2020). DOI: https://doi.org/10.1038/s41567-020-0799-7, pp. 409–412.

[Agn+12] M. Agnello *et al.* "First observation of the hyper superheavy hydrogen ${}^{6}_{\Lambda}$H". In: *Nuclear Physics A* 881 (2012). DOI: https://doi.org/10.1016/j.nuclphysa.2012.02.015, pp. 269–287. ISSN: 0375-9474.

[Ajz88] Fay Ajzenberg-Selove. "Energy levels of light nuclei A= 5 - 10". In: *Nuclear Physics A* 490.1 (1988), pp. 1–225.

[Aka+00] Y. Akaishi *et al.* "Dynamical supersymmetry in hypernuclei and the role of $\Lambda - \Sigma$ coupling". In: *Phys. Rev. Lett.* 84 (2000), p. 3539.

[All+16] J. Allison *et al.* "Recent developments in Geant4". In: *Nuclear Instruments and Methods in Physics Research Section A: Accelerators, Spectrometers, Detectors and Associated Equipment* 835 (2016). Geant4 version 10, pp. 186–225. DOI: 10.1016/j.nima.2016.06.125.

[Amm+62] R. G. Ammar *et al.* "On the Spin and Binding of ${}^{3}_{\Lambda}$H". In: *Il Nuovo Cimento (1955-1965)* 26 (1962). DOI: https://doi.org/10.1007/BF02781808, pp. 840–843.

[AWT03] G. Audi, A. H. Wapstra, and C. Thibault. "The AME2003 atomic mass evaluation: II. Tables, graphs and references". In: *Nuclear Physics A* 729 (2003), pp. 337–676.

[BCS78] RA Brandenburg, SA Coon, and PU Sauer. "Nuclear charge asymmetry in the A= 3 nuclei". In: *Nuclear Physics A* 294.3 (1978), pp. 305–320.

[Bed+76] M. Bedjidian *et al.* "Observation of a γ transition in the ${}^{4}_{\Lambda}$H hypernucleus". In: *Physics Letters B* 62.4 (1976). DOI: https://doi.org/10.1016/0370-2693(76)90686-9, pp. 467–470.

[Bed+79] M. Bedjidian *et al.* "Further investigation of the γ-transitions in ${}^{4}_{\Lambda}$H and ${}^{4}_{\Lambda}$ hypernuclei". In: *Physics Letters B* 83.2 (1979). DOI: https://doi.org/10.1016/0370-2693(79)90697-X, pp. 252–256.

[Ber+12] J. Beringer *et al.* "Review of Particle Physics". In: *Physical Review D* 86 (1 July 2012). DOI: https://doi.org/10.1103/PhysRevD.86.010001, p. 010001.

[Ber10] J. C. Bernauer. "Measurement of the elastic electron-proton cross section and separation of the electric and magnetic form factor in the Q2 range from 0.004 to 1 (GeV/c^2)". PhD thesis. Johannes Gutenberg-Universität Mainz, 2010.

[BGI90] AS Botvina, Ye S Golubeva, and AS Iljinov. "Statistical simulation of the break-up of light nuclei in hadron-nucleus reactions". In: *preprint INR P-0657, Moscow* (1990).

[Bha+98] H. Bhang *et al.* "Lifetime Measurement of ${}^{12}_{\Lambda}$C, ${}^{28}_{\Lambda}$Si, and ${}_{\Lambda}$Fe Hypernuclei". In: *Physical review letters* 81.20 (1998). DOI: https://link.aps.org/doi/10.1103/PhysRevLett.81.4321, p. 4321.

[Blo+98] K. I. Blomqvist *et al.* "The three-spectrometer facility at the Mainz microtron MAMI". In: *Nuclear Instruments and Methods in Physics Research Section A: Accelerators, Spectrometers, Detectors and Associated Equipment* 403.2 (1998). DOI: https://doi.org/10.1016/S0168-9002(97)01133-9, pp. 263–301. ISSN: 0168-9002.

[Boh+68] G. Bohm *et al.* "A determination of the binding-energy values of light hypernuclei". In: *Nuclear Physics B* 4.6 (1968). DOI: https://www.sciencedirect.com/science/article/pii/0550321368901090, pp. 511–526.

[BP07] A. S. Botvina and J. Pochodzalla. "Production of hypernuclei in multifragmentation of nuclear spectator matter". In: *Physical Review C* 76 (2 Aug. 2007). DOI: https://doi.org/10.1103/PhysRevC.76.024909, p. 024909.

[BU85] A.R. Bodmer and Q.N. Usmani. "Coulomb effects and charge symmetry breaking for the A = 4 hypernuclei". In: *Physical Review C* 31.4 (1985). DOI: https://journals.aps.org/prc/abstract/10.1103/PhysRevC.31.1400, p. 1400.

[Cha+68] K. N. Chaudhari *et al.* "Binding energy and π^- decay of light hyperfragments". In: *Proceedings of the Indian Academy of Sciences - Section A* 68 (1968). DOI: https://doi.org/10.1007/BF03046429, pp. 228–243.

[Coo+99] S.A. Coon *et al.* "Particle Mixing and Charge Asymmetric Lambda N Forces". In: *arXiv preprint nucl-th/9903034* (1999).

[Cou+08] R.D. Cousins *et al.* "Evaluation of three methods for calculating statistical significance when incorporating a systematic uncertainty into a test of the background-only hypothesis for a Poisson process". In: *Nuclear Instruments and Methods in Physics Research Section A: Accelerators, Spectrometers, Detectors and Associated Equipment* 595.2 (2008), pp. 480–501.

[Cra+62] N. Crayton *et al.* "Compilation of Hyperfragment Binding Energies". In: *Rev. Mod. Phys.* 34 (2 Apr. 1962). DOI: https://link.aps.org/doi/10.1103/RevModPhys.34.186, pp. 186–189.

[Cry20] Saint-Gobain Crystals. *BC408 Premium Plastic Scintillator - Technical Data Sheet*. https://www.crystals.saint-gobain.com/sites/imdf.crystals.com/files/documents/bc400-404-408-data-sheet_0.pdf. 2020.

[Dal+72] R.H. Dalitz *et al.* "Phenomenological study of s-shell hypernuclei with ΛN and ΛNN potentials". In: *Nuclear Physics B* 47.1 (1972), pp. 109–137.

[DP53] M. Danysz and J. Pniewski. "Delayed disintegration of a heavy nuclear fragment: I". In: *The London, Edinburgh, and Dublin Philosophical Magazine and Journal of Science* 44.350 (1953), pp. 348–350.

[DuP] DuPont. *Kapton® Polyimide Film*. https://www.dupont.com/electronics-industrial/kapton-polyimide-film.html. Accessed: 2025-06-07.

[EA+21] P. Eckert, P. Achenbach, *et al. Chart of hypernuclides—Hypernuclear structure and decay data*. URL: https://hypernuclei.kph.uni-mainz.de. 2021.

[Elj22] Eljen Technology. *EJ-228 Plastic Scintillator —Ultra-fast timing grade equivalent to NE Pilot U*. https://eljentechnology.com/products/plastic-scintillators/ej-228. Eljen Technology, accessed 2025. Equivalent to NE Pilot U and BC-418. 2022.

[ENS+15] A. Esser, S. Nagao, F. Schulz, *et al.* "Observation of ${}^{4}_{\Lambda}$H Hyperhydrogen by Decay-Pion Spectroscopy in Electron Scattering". In: *Physical Review Letters* 114.23 (2015), p. 232501.

[Ess14] Anselm Esser. "Zerfallspionenspektroskopie leichter Hyperkerne in der Elektroproduktion". DOI: http://doi.org/10.25358/openscience-4222. PhD thesis. Johannes Gutenberg-Universität Mainz, 2014.

[Fri70] J.L. Friar. "The ^{3}He-^{3}H charge form factor and the ^{3}He coulomb energy". In: *Nuclear Physics A* 156.1 (1970), pp. 43–52.

[FSN07] Y Fujiwara, Y Suzuki, and C Nakamoto. "Baryon–baryon interactions in the SU6 quark model and their applications to light nuclear systems". In: *Progress in Particle and Nuclear Physics* 58.2 (2007), pp. 439–520.

[Fuj+08] Y. Fujiwara *et al.* "Addendum to triton and hypertriton binding energies calculated from SU (6) quark-model baryon-baryon interactions". In: *Physical Review C—Nuclear Physics* 77.2 (2008), p. 027001.

[Gaj+67] W. Gajewski *et al.* "A compilation of binding energy values of light hypernuclei". In: *Nuclear Physics B* 1.3 (1967). DOI: https://doi.org/10.1016/0550-3213(67)90095-8, pp. 105–113. ISSN: 0550-3213.

[GG16] Daniel Gazda and Avraham Gal. "Ab initio calculations of charge symmetry breaking in the A= 4 hypernuclei". In: *Physical Review Letters* 116.12 (2016), p. 122501.

[GG19] A. Gal and H. Garcilazo. "Towards resolving the ${}^{3}_{\Lambda}$H lifetime puzzle". In: *Physics Letters B* 791 (2019). DOI: https://www.sciencedirect.com/science/article/pii/S037026931930108X, pp. 48–53.

[GGM12] D. Gazda, A. Gal, and J. Mares. "$\Lambda\Lambda$ hypernuclei and the onset of stability for strange matter". In: *Nucl. Phys. A* 881 (2012). DOI: https://doi.org/10.1016/j.nuclphysa.2012.01.007, pp. 159–170.

[Gog+16] T. Gogami *et al.* "Spectroscopy of the neutron-rich hypernucleus ${}^{7}_{\square}$He from electron scattering". In: *Phys. Rev. C* 94 (2 Aug. 2016). DOI: 10.1103/PhysRevC.94.021302, p. 021302.

[Goo25a] Goodfellow. *Carbon Foil, C-00-FL-000108*. https://www.goodfellow-japan.jp/en/product/carbon-foil-C-00-FL-000108.htm. Accessed: 2025-06-04. 2025.

[Goo25b] Goodfellow. *Tantalum Foil, TA00-FL-000160*. https://www.goodfellow-japan.jp/en/product/tantalum-foil-TA00-FL-000160.htm. Accessed: 2025-06-04. 2025.

[Gro+22] R.L. Workman (Particle Data Group) *et al.* "REVIEW OF PARTICLE PHYSICS". In: *Prog. Theor. Exp. Phys* 2022.083C01 (8 2022). DOI: https://doi.org/10.1093/ptep/ptac097.

[Gro22] Particle Data Group. "Review of Particle Physics". In: *Progress of Theoretical and Experimental Physics* 2022.8 (2022), p. 083C01. DOI: 10.1093/ptep/ptac097. URL: https://academic.oup.com/ptep/article/2022/8/083C01/6651666.

[Hai+20] J. Haidenbauer *et al.* "Hyperon–nucleon interaction within chiral effective field theory revisited". In: *The European Physical Journal A* 56.3 (2020), p. 91.

[Hai+21] J. Haidenbauer *et al.* "Constraints on the Λ-neutron interaction from charge symmetry breaking in the ${}^{4}_{\Lambda}$He-${}^{4}_{\Lambda}$H hypernuclei". In: *Few-Body Systems* 62.4 (2021), p. 105.

[Hay+21] S.H. Hayakawa *et al.* "Observation of Coulomb-Assisted Nuclear Bound State of Ξ^{-}—^{14}N System". In: *Physical Review Letters* 126.6 (2021), p. 062501.

[HH20] F. Hildenbrand and H.W. Hammer. “Lifetime of the hypertriton”. In: *Physical Review C* 102.6 (2020), p. 064002.

[Hiy+00] E. Hiyama *et al.* “Four-body cluster structure of ${}^{7}_{\Lambda}$Li”. In: *Phys. Rev. Lett.* 85 (2000). DOI: https://doi.org/10.1103/PhysRevLett.85.270, pp. 270–273.

[Hiy+01] E. Hiyama *et al.* “$\Lambda - \Sigma$ conversion in ${}^{4}_{\Lambda}$He and ${}^{4}_{\Lambda}$H based on a four-body calculation”. In: *Phys. Rev. C* 65 (2001), 011301(R).

[Hiy+14] E. Hiyama *et al.* “Three-body model study of $nn\Lambda$ with realistic YN and NN interactions”. In: *Physical Review C* 89.6 (2014). DOI: https://doi.org/10.1103/PhysRevC.89.061302, p. 061302.

[Hiy+96] E. Hiyama *et al.* “Three-body model study of ${}^{3}_{\Lambda}$H, ${}^{4}_{\Lambda}$H, and ${}^{4}_{\Lambda}$He”. In: *Phys. Rev. C* 53 (1996). DOI: https://doi.org/10.1103/PhysRevC.53.2075, pp. 2075–2091.

[Hon+17] R. Honda *et al.* “Missing-mass spectroscopy with the ^{6}Li$(\pi^-, K^+)X$ reaction to search for ${}^{6}_{\square}$H”. In: *Physical Review C* 96 (1 July 2017). DOI: https://link.aps.org/doi/10.1103/PhysRevC.96.014005, p. 014005.

[IAH07] Noriyoshi Ishii, Sinya Aoki, and Tetsuo Hatsuda. “Nuclear force from lattice QCD”. In: *Physical review letters* 99.2 (2007), p. 022001.

[Int] International Atomic Energy Agency (IAEA). *LiveChart of Nuclides*. https://nucleardata.iaea.org/livechart/. Accessed: 2024-01-08.

[Jan06] A. Jankowiak. “The Mainz Microtron MAMI – Past and future”. In: *European Physical Journal A* 28 (2006). DOI: https://doi.org/10.1140/epja/i2006-09-016-3, pp. 149–160.

[JR75] F. James and M. Roos. “MINUIT —a system for function minimization and analysis of the parameter errors and correlations”. In: *Computer Physics Communications* 10 (1975). DOI: 10.1016/0010-4655(75)90039-9, pp. 343–367.

[Jur+73] M. Jurič *et al.* “A new determination of the binding-energy values of the light hypernuclei (A<15)”. In: *Nuclear physics B* 52.1 (1973). DOI: https://www.sciencedirect.com/science/article/pii/0550321373900849, pp. 1–30.

[Kai+08] K.-H. Kaiser *et al.* "The 1.5 GeV harmonic double-sided microtron at Mainz University". In: *Nuclear Instruments and Methods in Physics Research Section A: Accelerators, Spectrometers, Detectors and Associated Equipment* 593.3 (2008). DOI: https://doi.org/10.1016/j.nima.2008.05.018, pp. 159–170. ISSN: 0168-9002.

[Kam+23] H. Kamada *et al.* "Faddeev calculation of ${}^{3}_{\Lambda}$H incorporating the 2 π-exchange ΛNN interaction". In: *Physical Review C* 108.2 (2023), p. 024004.

[Kam+98] H. Kamada *et al.* "π-mesonic decay of the hypertriton". In: *Physical Review C* 57.4 (1998). DOI: https://link.aps.org/doi/10.1103/PhysRevC.57.1595, p. 1595.

[Kas+25] A. Kasagi *et al.* "Binding energy of ${}^{3}_{\Lambda}$H and ${}^{4}_{\Lambda}$H via image analyses of nuclear emulsions using deep-learning". In: *Progress of Theoretical and Experimental Physics* 2025.8 (July 2025). DOI: https://doi.org/10.1093/ptep/ptaf097, p. 083D01. ISSN: 2050-3911.

[Kaw97] A. Kawachi. "Hyperfragment Production from Stopped K^- Absorption". PhD thesis. University of Tokyo, 1997.

[Key+70] G. Keyes *et al.* "Properties of ${}^{3}_{\Lambda}$H". In: *Phys. Rev. D* 1 (1 Jan. 1970). DOI: https://link.aps.org/doi/10.1103/PhysRevD.1.66, pp. 66–77.

[Kla+18] P. Klag *et al.* "Novel optical interferometry of synchrotron radiation for absolute electron beam energy measurements". In: *Nuclear Instruments and Methods in Physics Research Section A* 910 (2018). DOI: https://doi.org/10.1016/j.nima.2018.09.072, pp. 147–156.

[Kra95] H. Kramer. "Grundlagen für das Steuerungs- und Überwachungssystem der Drei-Spektrometer-Anlage am Elektronenbeschleuniger MAMI". Dissertation. PhD thesis. Johannes Gutenberg-Universität Mainz, 1995.

[KS84] K. S. Kölbig and B. Schorr. "Numerical algorithms for the computation of the complex error function". In: *Computer Physics Communications* 32 (1984). DOI: https://doi.org/10.1016/0010-4655(84)90031-0, pp. 121–132.

[Le+20] H. Le *et al.* "Implications of an increased Λ-separation energy of the hypertriton". In: *Physics Letters B* 801 (2020), p. 135189.

[Leo94] W. R. Leo. *Techniques for Nuclear and Particle Physics Experiments*. 2nd. DOI: https://doi.org/10.1007/978-3-642-57920-2. Berlin, Heidelberg: Springer, 1994.

[LP17] D. Lonardoni and F. Pederiva. "Medium-mass hypernuclei and the nucleon-isospin dependence of the three-body hyperon-nucleon-nucleon force". In: *arXiv preprint arXiv:1711.07521* (2017).

[May+66] C. Mayeur *et al.* "A determination of the B_Λ values of light hypernucleivalues of light hypernuclei". In: *Il Nuovo Cimento A (1971-1996)* 43 (1966), pp. 180–192.

[Mih+24] D. L. Mihaylov *et al.* "Constraints on the $p\Lambda$ interaction at low relative momenta from femtoscopy in pp collisions at $\sqrt{s} = 13$ TeV". In: *Physics Letters B* 850 (2024). DOI: https://doi.org/10.1016/j.physletb.2024.138550, p. 138550.

[Mil94] G.A. Miller. "Charge independence and symmetry of nuclear forces". In: *arXiv preprint nucl-th/9406023* (1994).

[Miy+95] K. Miyagawa *et al.* "Properties of the hypertriton in the Faddeev approach with YN interactions". In: *Phys. Rev. C* 51 (1995), p. 2905.

[Nag15] S. Nagao. "Decay pion spectroscopy of electro-produced hyper nuclei". PhD thesis. Tohoku University, 2015.

[NAM03] H. Nemura, Y. Akaishi, and K. S. Myint. "ΛN interaction from the ${}^{3}_{\Lambda}$H binding energy". In: *Phys. Rev. C* 67 (2003). DOI: https://doi.org/10.1103/PhysRevC.67.051001, p. 051001.

[Nis25] K. Nishi. 電子ビームエネルギー精密測定のためのアンジュレータ放射光干渉法 *(in Japanese)*. 2025.

[Nog+02] A. Nogga *et al.* "The Hypernuclei ${}^{4}_{\Lambda}$He and ${}^{4}_{\Lambda}$H: Challenges for Modern Hyperon-Nucleon Forces". In: *Physical Review Letters* 88.17 (2002), p. 172501.

[Nog13] A. Nogga. "Light hypernuclei based on chiral and phenomenological interactions". In: *Nuclear Physics A* 914 (2013), pp. 140–150.

[Nuc70] Nuclear Enterprises Ltd. *Plastic Scintillator NE 102A —Technical Data Sheet*. Available from standard scintillator material handbooks and manufacturer datasheets. See also Saint-Gobain BC-408 equivalence. 1970.

[OY81] Makoto Oka and Koichi Yazaki. “Short Range Part of Baryon-Baryon Interaction in a Quark Model. I: —Formulation—”. In: *Progress of Theoretical Physics* 66.2 (1981), pp. 556–571.

[Pér+20] A. Pérez-Obiol *et al.* “Revisiting the hypertriton lifetime puzzle”. In: *Physics Letters B* 811 (2020). DOI: https://doi.org/10.1016/j.physletb.2020.135916, p. 135916. DOI: 10.1016/j.physletb.2020.135916.

[Pra+61] Y. Prakash *et al.* “On the binding energies of mesic hypernuclei”. In: *Il Nuovo Cimento (1955-1965)* 21 (1961). DOI: https://doi.org/10.1007/BF02832551, pp. 235–248.

[Rap+13] C. Rappold *et al.* “Hypernuclear spectroscopy of products from ^{6}Li projectiles on a carbon target at 2A GeV”. In: *Nuclear Physics A* 913 (2013). DOI: https://doi.org/10.1016/j.nuclphysa.2013.05.019, pp. 170–184. ISSN: 0375-9474.

[RD66] M. Rayet and R.H. Dalitz. “The lifetime of $^{3}_{\Lambda}$H”. In: *Nuovo Cimento A (1965-1970)* 46 (1966), pp. 786–794. DOI: 10.1007/BF02857527.

[RI18] V. Della Rocca and F. Iachello. “Cluster shell model: I. Structure of ^{9}Be, ^{9}B”. In: *Nuclear Physics A* 973 (2018), pp. 1–32.

[RNY10] Thomas A Rijken, MM Nagels, and Yasuo Yamamoto. “Baryon-Baryon Interactions:—Nijmegen Extended-Soft-Core Models—”. In: *Progress of Theoretical Physics Supplement* 185 (2010), pp. 14–71.

[Sch+16] F. Schulz *et al.* “Ground-state binding energy of $^{4}_{\Lambda}$H from high-resolution decay-pion spectroscopy”. In: *Nuclear Physics A* 954 (2016). DOI: https://doi.org/10.1016/j.nuclphysa.2016.03.015, pp. 149–160.

[Sch16] F. Schulz. “Präzisionsmessung der Lambda-Separationsenergie von Lambda-vier-H am Mainzer Mikrotron”. DOI: http://doi.org/10.25358/openscience-4548. PhD thesis. Johannes Gutenberg-Universität Mainz, 2016.

[Sen+93] P. Senger *et al.* “The kaon spectrometer at SIS”. In: *Nuclear Instruments and Methods in Physics Research Section A: Accelerators, Spectrometers, Detectors and Associated Equipment* 327.2 (1993), pp. 393–411. ISSN: 0168-9002. DOI: https://doi.org/10.1016/0168-9002(93)90706-N. URL: https://www.sciencedirect.com/science/article/pii/016890029390706N.

[Ste84] R. M. Sternheimer. “Density effect for the ionization loss of charged particles in various substances”. In: *Atomic Data and Nuclear Data Tables* 30 (1984). DOI: https://doi.org/10.1016/0092-640X(84)90002-4, pp. 261–271.

[T S22] The STAR Collaboration T. Shao. “Measurement of ${}^{4}_{\Lambda}$H and ${}^{4}_{\Lambda}$He binding energy in Au+ Au collisions at $\sqrt{s_{NN}} = 3$ GeV”. In: *Physics Letters B* 834 (2022). DOI: https://doi.org/10.1016/j.physletb.2022.137449, p. 137449. ISSN: 0370-2693.

[Tak+01] H. Takahashi *et al.* “Observation of a ${}^{6}_{\Lambda\Lambda}$He Double Hypernucleus”. In: *Physical review letters* 87.21 (2001), p. 212502.

[Tam+89] H. Tamura *et al.* “Formation of ${}^{4}_{\Lambda}$H hypernuclei from K^{-} absorption at rest on light nuclei”. In: *Physical Review C* 40.2 (1989), R479.

[Tam08] H. Tamura. “Gamma-ray spectroscopy of hypernuclei at K1.1”. In: *Proposals for the 4th PAC meeting* (2008). URL: https://j-parc.jp/researcher/Hadron/en/pac_0801/pdf/LOI_Tamura_gamma.pdf.

[Von+22] P. Eckert (Vonwirth) *et al.* “Commissioning of the hypertriton binding energy measurement at MAMI”. In: *EPJ Web of Conferences*. Vol. 271. DOI: https://doi.org/10.1051/epjconf/202227101006. EDP Sciences. 2022, p. 01006.

[Von24] P. Vonwirth. “Preparation and realization of a new hypertriton mass experiment at MAMI”. DOI: http://doi.org/10.25358/openscience-9899. PhD thesis. Johannes Gutenberg-Universität Mainz, 2024.

[Wan+21] M. Wang *et al.* “The AME 2020 atomic mass evaluation (II). Tables, graphs and references”. In: *Chinese Physics C* 45.3 (2021). Atomic mass unit: NIST (2022 CODATA), p. 030003. DOI: 10.1088/1674-1137/abddaf.

[Yam+15] T.O. Yamamoto *et al.* “Observation of Spin-Dependent Charge Symmetry Breaking in ΛN Interaction: Gamma-Ray Spectroscopy of ${}^{4}\Lambda$He”. In: *Physical review letters* 115.22 (2015). DOI: https://journals.aps.org/prl/abstract/10.1103/PhysRevLett.115.222501, p. 222501.

List of Figures

List of Tables